Streaming virtual reality : learning for attentional models and network optimization

Miguel Fabián Romero Rondón

UNIVERSITÉ CÔTE D'AZUR

ÉCOLE DOCTORALE
SCIENCES ET TECHNOLOGIES DE L'INFORMATION ET DE LA COMMUNICATION

Streaming de Réalité Virtuelle: Apprentissage pour Modèles Attentionnels et Optimisation Réseau

Miguel Fabian ROMERO RONDON

Laboratoire d'Informatique, Signaux et Systèmes de Sophia Antipolis (I3S)

Présentée en vue de l'obtention du grade de docteur en Informatique **d'**Université Côte d'Azur
Dirigée par : Frédéric PRECIOSO / Lucile SASSATELLI
Soutenue le : 23/09/2021

Devant le jury composé de :
Alberto DEL BIMBO, Professeur, University of Firenze
Ngoc Q. K. DUONG, Chercheur Senior, InterDigital R&D
Président: Patrick LE CALLET, Professeur, Université de Nantes
Laura TONI, Maîtresse de conférence, University College London

Streaming Virtual Reality: Learning for Attentional Models and Network Optimization

Jury :

Rapporteurs :

Prof. Alberto DEL BIMBO, Professeur des universités, University of Firenze, Italy

Dr. Ngoc Q. K. DUONG, Chercheur senior, InterDigital R&D, France

Examinateurs :

Prof. Patrick LE CALLET, Professeur des universités, Université de Nantes, France

Dr. Laura TONI, Maîtresse de conférence, University College London, United Kingdom

Directeurs :

Prof. Frédéric PRECIOSO, Professeur des universités, Université Côte d'Azur, France

Dr. Lucile SASSATELLI, Maîtresse de conférence HDR, Université Côte d'Azur, France

Invités :

Dr. Hui-Yin WU, Chargée de recherche, INRIA, France

Dr. Ramón APARICIO-PARDO, Maître de conférence, Université Côte d'Azur, France

Abstract

Virtual Reality (VR) has taken off in the last years thanks to the democratization of affordable head-mounted displays (HMDs), giving rise to a new market segment along with sizable research and industrial challenges. However, the development of VR systems is persistently hindered by the difficulty to access immersive content through Internet streaming. To decrease the amount of data to stream, a solution is to send in high resolution only the position of the sphere the user has access to at each point in time, named the Field of View (FoV).

We develop a foveated streaming system for an eye-tracker equipped headset, which adapts to the user's fovea position by focusing the quality in the gaze target and delivering low-quality blurred content outside, so as to reproduce and help the natural focusing process while reducing bandwidth waste. This approach however requires to know the user's head position in advance, that is at the time of sending the content from the server.

A number of recent approaches have proposed deep neural networks meant to exploit the knowledge of the past positions and of the 360° video content to periodically predict the next FoV positions. We address the strong need for a comparison of existing approaches on common ground with the design a framework that allows to prepare a testbed to assess comprehensively the performance of different head motion prediction methods. With this evaluation framework we re-assess the existing methods that use both past trajectory and visual content modalities, and we obtain the surprising result that they all perform worse than baselines we design using the user's trajectory only.

We perform a root-cause analysis of the metrics, datasets and neural architectures that allows us to uncover major flaws of existing prediction methods (in the data, the problem settings and the neural architectures). The dataset analysis helps us to identify how and when should the prediction benefit from the knowledge of the content. The neural architecture analysis shows us that only one architecture does not degrade compared to the baselines when ground-truth saliency is given to the model. However, when saliency features are extracted from the content, none of the existing architectures can compete with the same baselines.

From the re-examination of the problem and supported with the concept of Structural-RNN, we design a new deep neural architecture, named TRACK. TRACK achieves state-of-the-art performance on all considered datasets and prediction horizons, outperforming competitors by up to 20% on focus-type videos and prediction horizons of 2 to 5 seconds.

We also propose a white-box predictor model to investigate the connection between the visual content and the human attentional process, beyond above Deep Learning models, often referred to as "black-boxes". The new model we design is built on the physics of rotational motion and gravitation, and named HeMoG.

The prediction error of the head position might be corrected by downloading again the same segments in higher quality. Therefore, the consumed data rate depends on the prediction error (user's motion), which in turn depends on the user's attentional process and on possible attention-driving techniques.

Film editing with snap-cuts can benefit the user's experience both by improving the streamed quality in the FoV and ensuring the user sees important elements of the content plot. However, snap-cuts should not be too frequent and may be avoided when not beneficial to the streamed quality. We formulate the dynamic decision problem of snap-cut triggering as a model-free Reinforcement Learning. We design Imitation Learning-based dynamic triggering strategies, and show that only knowing the past user's motion and video content, is possible to outperform the controls without and with all cuts.

Keywords: Virtual reality, 360° videos, multimedia streaming, machine learning, deep learning, sequential decision making, imitation learning, visual attention prediction, gravitational physics.

Résumé

La réalité virtuelle (VR) a décollé ces dernières années grâce à la démocratisation des visiocasques, donnant naissance à un nouveau segment de marché ainsi qu'à d'importants défis industriels et de recherche. Cependant, le développement des systèmes de VR est constamment entravé par la difficulté d'accéder à du contenu immersif via le streaming sur Internet. Pour réduire la quantité de données à diffuser, une solution consiste à n'envoyer en haute résolution que la zone correspondant au champ de vision.

Nous développons un système de streaming pour un casque équipé d'un dispositif d'oculométrie, qui s'adapte à la position de la fovéa de l'utilisateur en focalisant la qualité dans la cible du regard et en fournissant un contenu flou de faible qualité à l'extérieur, afin de reproduire et d'aider le processus naturel de focalisation tout en réduisant le gaspillage de bande passante. Cette approche nécessite cependant de connaître à l'avance la position de la tête de l'utilisateur.

Un certain nombre d'approches récentes ont proposé des réseaux neuronaux pour prédire périodiquement les prochaines positions du champ visuel. Nous répondons au fort besoin de comparer les approches existantes sur un terrain commun en concevant un cadre qui permet de préparer un banc d'essai pour évaluer de manière exhaustive les performances des différentes méthodes de prédiction du mouvement de la tête. Nous réévaluons les méthodes existantes, et nous obtenons le résultat surprenant qu'elles sont toutes moins performantes que les lignes de base que nous concevons sans utiliser la modalité du contenu visuel.

Nous effectuons une analyse approfondie des causes qui nous permet de découvrir les principaux défauts des méthodes de prédiction existantes. L'analyse des ensembles de données nous aide à identifier comment et quand la prédiction doit bénéficier de la connaissance du contenu. L'analyse de l'architecture neuronale nous montre qu'une seule architecture ne se dégrade pas par rapport aux lignes de base lorsque la vraie saillance est donnée au modèle. Cependant, lorsque les caractéristiques de saillance sont extraites du contenu, aucune des architectures existantes ne peut rivaliser avec les mêmes lignes de base.

À partir du réexamen du problème et en nous appuyant sur le concept de RNN-structurel, nous concevons une nouvelle architecture neuronale profonde, appelée TRACK. TRACK atteint des performances de pointe sur tous les ensembles de données et horizons de prédiction considérés, surpassant ses concurrents jusqu'à 20% sur des vidéos de type focus et des horizons de prédiction de 2 à 5 secondes.

Nous proposons également un modèle prédictif fondé sur la physique du mouvement de rotation et de la gravitation pour étudier le lien entre le contenu visuel et le processus attentionnel humain, au-delà des modèles souvent appelés "boîtes noires".

L'erreur de prédiction de la position de la tête peut être corrigée en téléchargeant à nouveau les mêmes segments dans une qualité supérieure. Par conséquent, le débit de données consommé

dépend de l'erreur de prédiction, qui dépend à son tour du processus attentionnel de l'utilisateur et d'éventuelles techniques de stimulation de l'attention.

L'édition vidéo avec des coupures rapides peut être bénéfique pour l'expérience de l'utilisateur en améliorant la qualité du streaming dans le champ visuel et en garantissant que l'utilisateur voit les éléments importants de la trame du contenu. Cependant, les coupures rapides ne doivent pas être trop fréquentes et peuvent être évitées lorsqu'elles ne sont pas bénéfiques pour la qualité du streaming. Nous concevons des stratégies de déclenchement dynamique des coupures rapides basées sur l'apprentissage par imitation, et nous montrons qu'il est possible de surpasser la performance des contrôles sans et avec toutes les coupures uniquement en connaissant le mouvement passé de l'utilisateur et le contenu vidéo.

Mots-Clé: Réalité virtuelle, vidéos 360°, streaming multimédia, apprentissage automatique, apprentissage profond, prise de décision séquentielle, apprentissage par imitation, prédiction de l'attention visuelle, physique gravitationnelle.

Acknowledgements

First of all, I would like to express my very great appreciation to my PhD advisors. Professors Lucile Sassatelli and Frédéric Precioso. I want to thank you for all the time invested, the patience and the support you gave me throughout the whole process of my PhD. I feel lucky of having you leading my work during these years and I appreciate that, even if your schedule was busy, you were constantly checking that everything was all right not only in my research but also in my life. Thank you for your valuable and constructive suggestions during the development of my research work and thanks for always having the perfect words to encourage me in difficult times, and to cheer me up during each of our achievements. I admire you and I will always be inspired by your work.

I would like to thank Professors Alberto Del Bimbo and Ngoc Q. K. Duong for accepting to review my dissertation despite the amount of work this requires. I would also like to thank Dr. Dario Zanca, for the openness to work and the willingness to help that made smoother and more fruitful our collaboration. I wish to acknowledge Professors Patrick Le Callet and Laura Toni, your research always reveals new paths to investigate, and it has been a constant inspiration throughout my PhD.

My colleagues and unconditional friends Thomas, Eva, Ninad, Melissa and Fernando, thank you so much for the deep and shallow conversations, for the unforgettable times we spent together. The pubs in Berlin, Genova, Valencia, New Delhi and Nice (special mention to Akathor and Pompei) will remember the epic stories that developed there and how the bond of our friendship grew stronger. Lola, Carlos and Margarita, my arrival and my life in Nice was much easier thanks thanks to your help, I will always be grateful for all the support. I will try not to leave anyone that helped me to forget how stressful a PhD can be: Davide, Pedro, Antonio, Panchito, Mohit, Jean-Marie, Melpo, Vasilina, Quentin, Diana, Alessio, Andrea, Lucy, Yao, Amina and Henrique. I tried to list the people that helped me during the development of my PhD, I'm sorry if your name is not here, to include the contribution of everyone would be impossible.

My love Gaëlle, thank you for being with me during the roller coaster of emotions that is a PhD. Thank you for believing in me and comforting me when the results were not as expected and for all the love and care that helped me get through it. Thank you for the happiness you brought in my life. Thank you also for all the sweet moments we shared together with your family. Florence, Stéphane, Boris, Loriane and Elodie thanks for being there to celebrate vehemently each of my achievements.

My sincere thanks to my parents Miguel Angel and Sandra. Thank you for your unconditional support, your wise words and loving advice encouraged me to undertake this journey. Thank you for accompanying me in each of my achievements and for believing in me when I felt down. My siblings Silvia and Gabriel, every time I look up, I see the stars, and above

them I see you. You are a source of inspiration for me and you never cease to surprise me with your achievements. The admiration I feel for you fills me with energy that keeps me pushing forward. To the rest of my family, my sister Leidy and my nieces. my *tías* Lili, Ivonne, Adriana, Martha, Esther and Lucila, my *nonos* Ligia and Jesús, my cousins Maria Alejandra, Isabella, Mauricio, Pedro, Claudia, Leidy, my uncles Lucho and Eduardo, my siblings-in-law Mauricio and Maribel, because despite the distance I always felt your support as if you were next to me.

Contents

List of Figures

List of Acronyms

12K 11520×6480 pixels

2D Two Dimensional

3D Three Dimensional

4K 4096×2048 pixels

API Application Programming Interface

AVC Advanced Video Coding

BC Behavioral Cloning

CB Content-Based

CB-sal Content-Based Saliency

CDF Cumulative Distribution Function

CPU Central Processing Unit

CSV Comma-Separated Values

DASH Dynamic Adaptive Streaming over HTTP

DHP Deep Head Prediction

DL Deep Learning

DoF Degrees of Freedom

DRL Deep Reinforcement Learning

DT Decision Tree

EEG Electroencephalogram

FC Fully Connected

FoV Field of View

FFmpeg Fast Forward Motion Picture Experts Group

GPU Graphics Processing Unit

GT Ground-Truth

GT-Sal Ground-Truth Saliency

HAS HTTP Adaptive Streaming

HEVC High Efficiency Video Coding

HMDs Head Mounted Displays

HQ High Quality

HVS Human Visual System

IL Imitation Learning

IoU Intersection over Union

LQ Low Quality

LQ Low Quality

MI Mutual Information

MP4 MPEG-4

MPD Media Presentation Description

OS Operating System

QoE Quality of Experience

QP Quantization Parameter

RAM Random Access Memory

RL Reinforcement Learning

RNN Recurrent Neural Networks

RoI Regions of Interest

SDK Software Development Kit

Seq2Seq Sequence-to-Sequence

SLERP Spherical Linear Interpolation

SRD Spatial Relationship Description

TE Transfer Entropy

URL Uniform Resource Locator

VAS Viewport Adaptive Streaming

VE Virtual Environment

VM Virtual Machine

VR Virtual Reality

XML Extensible Markup Language

Chapter 1

Introduction

1.1 Context

Immersive media are on the rise: the global market for Virtual Reality (VR) is projected to continue growing from US$21.83 Billion in 2021 to US$69.6 Billion by 2028 [19]. VR has taken off in the last years thanks to the democratization of affordable head-mounted displays (HMDs) provided by almost all high-tech device companies, giving rise to a new market segment along with sizable research and industrial challenges which are all increasing the interest for stable, comfortable and enjoyable systems. 360° videos are an important modality of the Virtual Reality ecosystem, providing the users the ability to freely explore an omnidirectional scene and also providing a feeling of immersion when watched in a VR headset, with applications in story-telling, journalism or remote education.

1.2 Challenge

Despite the exciting prospects and the multiple applications of VR, the technology is still nascent and immature, entailing poor to downright sickening experience. The full rise of Virtual Reality systems is persistently hindered by multiple hurdles, and can be cast into two categories.

On the one hand, a number of problematic components are intrinsic to the VR display systems. The currently fast-developing products for the general public deal with 360° framed video content displayed on a virtual sphere, an inch away from the eyes through magnifying glasses. The challenge in the design of HMDs comes mainly from the Induced Symptoms and Effects of Virtual Reality. If the feeling of immersion is not sufficient, VR users could experience discomfort to a distressing level, possibly yielding disorientation and nausea [20].

On the other hand, another set of problems for the VR experience is the difficulty to access immersive content through Internet streaming. A key aspect to ensure a high level of immersion is the video resolution which must be at least 11520×6480 pixels (12K) [14]. Given the closer proximity of the screen to the eye and the width of the content (2π steradians in azimuth and π in elevation angles), the required data rate is two orders of magnitude that of a regular video

[21]. Given the human eye acuity, fooling our visual perception to give a feeling of immersion would require a data rate of 5.2 Gbps considering the latest compression standards [22]. These data rates cannot be supported by the current Internet accesses when the content is streamed from remote servers. Furthermore, while such data rates are employed to send the video, most of the delivered video signal is not displayed in the Head-Mounted Display (HMD).

1.3 Motivation and Research Questions

As mentioned above, the challenges of Virtual Reality systems can be cast into two categories. One is the discomfort yielded by current VR display systems and the other is the difficulty to access immersive content through Internet streaming. Our motivation lies in the multiple solutions that can arise, benefiting not only the multimedia streaming community but also the filmmaking or gaming industry. For example, to reduce discomfort, 360° videos can be stereoscopic to create a 3D effect, but those on main distribution platforms (YouTube 360, Facebook 360, etc.) are mostly monoscopic to date. While the absence of a 3D effect limits the sense of immersion, it also prevents a major hurdle to the proper rendering of stereoscopic views in near-eye displays, which lies in the vergence/accommodation conflict [11]. A main set of solutions to contribute to the feeling of immersion relies on so-called foveated rendering, where clear content is rendered in a restricted radius around the fovea, while the rest is blurred away to reproduce the natural focusing process in a real scene, thereby lowering the visual discomfort and cognitive load [23]. This requires to constantly locate the gaze direction with an eye-tracker integrated within the HMD and render the content in radially-decreasing quality from the fovea to the eye's periphery.

Likewise, as 360° video streaming is projected to require a network throughput of 1Gbps (100 times higher than current throughput) [24], the multimedia network community has proposed several solutions to cope with the discrepancy between the required video rate for best quality and the available network bandwidth. A simple principle is to send the non-visible part of the video sphere with lower quality. To do so, recent works have proposed to either segment the video spatially into tiles and set the quality of the tiles according to their proximity to the Field of View (FoV), or use projections enabling high resolutions of regions intersecting the FoV and lower resolution in regions far from the viewers' FoV. These approaches however require to know the user's head position in advance, that is at the time of sending the content from the server. This can go from a few tens of milliseconds (low network delay) to a few seconds (extreme network delay or presence of a video playback buffer at the client to absorb network rate variations). It is therefore crucial for an efficient 360° video streaming system to embed an accurate head motion predictor which can periodically inform where the user will be likely looking at over a future time horizon based on the past trajectory and on the 360° video content.

To be able to model the way people explore virtual environments, it is key to understand the connection between the audio-visual content and the human attentional process. The Human Visual system consists of a set of complex mechanisms that we have evolved to guide the movement of our head and eyes to filter relevant areas in our visual field and center the fovea towards certain locations [25]. Predicting the user's head motion is difficult and can be done accurately only over short horizons. The prediction error might be corrected when time progresses by downloading again the same segments in higher quality to replace their low quality version close to the playout deadline. This however yields redundant transmissions and hence a higher consumed network rate. The consumed data rate therefore depends on the prediction error (user's motion), which in turn depends on the user's attentional process. Instead of adapting *reactively* by predicting the user's attention, another solution is to *proactively* drive the users' viewing direction towards the areas the director wants them to explore. Driving the user's attention is critical for a director to ensure the story plot is understood. Film editing can be helpful for streaming 360° videos by directing the user's attention to specific pre-defined Regions of Interest (RoI), thereby lowering the randomness of the user's motion. Using the a-priori knowledge of the RoIs in the streaming decisions can hence improve the degree of delight of the user in the immersive experience, namely, the Quality of Experience (QoE). This has raised the interest of attention driving techniques to the multimedia network community [26].

Virtual Reality systems raise several multidisciplinary questions centered at improving the Quality of Experience.

From the perspective of the multimedia networking community important questions include:

• To define a protocol to stream VR content: Which algorithm should be used to decide the frame rates and qualities transmitted for each region of the video sphere?

• How to anticipate the users' trajectory in order to improve the transmission of VR content, and how to compare the existing prediction techniques to find the best model of attention prediction?

From the filmmaking industry the questions are:

• To help to identify the impact of current storytelling techniques: How does the categorization of VR content (e.g. exploration, moving focus, static focus, rides) impact the trajectories of the users?

• To help to investigate new storytelling techniques: How to model the Human Visual System and its attentional process?

• To optimize user-centered film editing techniques: How to automate and control the editing of VR content centered at the user's exploration?

• To help to model Quality of Experience: How to identify the spatial and temporal relationships between the emotions provoked in an immersive experience and the exploration of users in a VR setting?

The challenge consists in providing solutions that reconcile all these multi-disciplinary questions. From the questions above, the present dissertation contributes to all but the last. However,

the last question on modeling the quality of experience with emotional maps is planned as future work together with improvements to the approaches proposed in this thesis.

1.4 Contributions and Organization of the Manuscript

Our research goal is to build high-performing Virtual Reality streaming systems. In this work we consider the problem of streaming stored 360° videos to a VR headset. The contributions of this manuscript are gathered into three main topics: (Part 1) adapt to, (Part 2) predict and (Part 3) guide the attentional and emotional trajectory of the user. For Part 1 (Chapter 3) we use foveated streaming to help the natural focusing process in virtual scenes, enhancing the feeling of immersion while improving bandwidth utilization. In Part 2 (Chapters 4, 5 and 6) prediction techniques are proposed for viewport-adaptive streaming to anticipate the user's attention and potentially improve the QoE. In Part 3 (Chapter 7) we present attention driving techniques based on foveal manipulation and rotational snap-cuts with a mechanism of control to ensure that the story plot is understood and that the streaming process is optimal. Finally, Chapter 8 concludes this dissertation.

Foveated Streaming of VR Videos (Chapter 3).

We developed a streaming system based on the FOVE HMD that adapts to the user's gaze position by blurring away the regions not in the gaze's target to reproduce and help the natural focusing process while reducing the bandwidth waste. Instead of sending the whole frame from the server to the client, we used different resolution levels to stream and project the content, (i) a High-Resolution segment corresponding to the foveal area, (ii) a radially increasing blurred area (blending area) covering the FoV and (ii) a Low-Resolution area that corresponds to the places outside the FoV to avoid having blank sections in the sphere. Our specific contribution is:
• We build on the FOVE's Unity API to design a gaze-adaptive streaming system. The client is designed to inform the server of the current gaze position, receives the video sphere in low-resolution and additionally the foveal region in high-resolution, and is responsible for the merging of textures. The server prepares the content upon reception of a request. It computes the equirectangularly projected mask, crops the frame of the segment and formats the resulting piece for transmission without overhead. To enable full freedom in future design, we provide the ability to apply different masks over each frame of a segment, and verify that the whole system can work online.

A Unified Evaluation Framework for Head Motion Prediction Methods in 360° Videos (Chapter 4).

A complementary option to the foveated streaming system is to use prediction models to estimate the future FoV positions. In the last years, several approaches have been proposed for head motion prediction, none of them however compares with their counterparts aiming at the

same prediction problem. We proposed a software framework to address the strong need for a comparison of existing approaches on common ground, thus we made the following contribution:

• We built a framework that allows researchers to study the performance of their head motion prediction methods and compare them with existing approaches on the same evaluation settings (dataset, prediction horizon, and test metrics). This software framework therefore contributes to progress towards efficient and reproducible results in 360° streaming systems.

A Critical Comparison of Deep Architectures for Head Motion Prediction in 360° Videos (Chapter 5).

We used our framework to study several head motion prediction models from the state-of-the-art. We show that the relevant existing methods have hidden flaws, that we thoroughly analyze to overcome with a new proposal establishing state of the art performance. We hence make two main contributions.

• Uncovering hidden flaws of existing methods and performing a root-cause analysis:
After a review and taxonomy of the most relevant and recent methods (PAMI18 [1], CVPR18 [5], MM18 [3], ChinaCom18 [4] and NOSSDAV17 [2]), we compare them to common baselines. First, comparing against the *trivial-static baseline*, we obtain the intriguing result that they all perform worse, on their exact original settings, metrics and datasets. Second, we show it is indeed possible to outperform the *trivial-static baseline* (and hence the existing methods) by designing a stronger baseline, named the *deep-position-only baseline*: it is an LSTM-based architecture considering only the positional information, while the existing methods are meant to benefit both from the history of past positions and knowledge of the video content. From there, we carry out a thorough root-cause analysis to understand why the existing methods perform worse than baselines that do not consider the content information. Looking into the metrics and the data, we show that: (i) evaluating only on some specific pieces of trajectories or specific videos, where the content is proved useful, does not change the comparison results, and that (ii) the content can indeed inform the head position prediction, but for prediction horizons longer than 2 to 3 sec (all these existing methods consider shorter horizons). Looking into the neural network architectures, we identify that: (iii) when the provided content features are the ground-truth saliency, the only architecture not degrading away from the baseline is the one with a Recurrent Neural Network (RNN) layer dedicated to the positional input, but (iv) when fed with saliency estimated from the content, the performance of this architecture degrades away from the *deep-position-only baseline* again.

• Introducing a new deep neural architecture achieving state-of-the-art performance on all the datasets of compared methods and all prediction horizons (0-5 sec.):
To overcome this difficulty, we re-examine the requirements on how both modalities (past positions and video content) should be considered given the structure of the problem. We support our reasoning with the concept of Structural-RNN, modeling the dynamic head motion prediction

problem as a spatio-temporal graph. We obtain a new deep neural architecture, that we name TRACK. TRACK establishes state-of-the-art performance on all the prediction horizons 0-5 sec. and all the datasets of the existing competitors. In the 2-5 sec. horizon, TRACK outperforms the second-best method by up to 20% in orthodromic distance error on focus-type videos, i.e., videos with low-entropy saliency maps.

HeMoG: A White-Box Model to Unveil the Connection Between Saliency Information and Human Head Motion in Virtual Reality (Chapter 6).

Deep Learning models, often referred to as "black-boxes" do not provide any insight on the dependence and the interplay between head motion and the visual content. To further investigate and explain the performance improvements of Deep Learning models, and to study the connection between saliency information and human head motion. In Chapter 6, we address 2 research questions:

Q1: To which extent can we investigate the inner workings of these DL models with a white-box model?

Q2: What knowledge can we obtain from a white-box model regarding the connection between saliency information and head motion?

We made the following contribution:

• We design a new white-box model to predict head motion from the past head trajectories and the 360° content. This model is built on the assumption that the head motion can be described by gravitational physics laws driven by virtual masses created by the content. This model is named HeMoG (Head Motion with Gravitational laws of attention). We evaluate the performance of HeMoG in comparison with reference DL models to predict head motion from the exact same inputs. When the prediction is made from past motion only (i.e., without content information), we show that HeMoG and the reference DL models achieve comparable performance. We interpret this as the DL model learning the curvature and friction dynamics of head motion that HeMoG is explicitly built on (1st answer to Q1). When HeMoG is fed with saliency information, it can achieve comparable or better performance than the reference DL model TRACK. We interpret this as the state-of-the-art DL models performing a similar type of fusion as HeMoG, which enables to benefit from both input modalities, past positions and visual content (2nd answer to Q1). We discuss in which case the representation learning of the DL models is key. In order to answer Q2, we take a closer look to the optimal hyper-parameters for HeMoG w.r.t. (i) the semantic category of the 360° video and (ii) the *prediction horizon*. On videos where the saliency maps render attractive areas (videos of categories *Static Focus*, *Moving Focus* and *Rides*), the optimal weight assigned in the motion equation to the content masses is higher than that when the video does not feature specific attractive areas (videos of category *Exploration*). Furthermore, analyzing the evolution of the saliency weight over the *prediction horizon* of 5 sec., we identify that the head motion momentum is most important first, and the content information starts being relevant only after 3 sec.

Control Mechanism for User-Adaptive Rotational Snap-Cutting in Streamed 360° Videos (Chapter 7).

Instead of adapting in a reactive manner to the estimated users' gaze position, we explore ways to proactively change the viewing direction towards areas we want them to explore. A direct and effective guidance technique is to add rotational snap-cuts in the 360° video. Whether or not a cut will be beneficial depends on the user's motion and on the network conditions, this trade-off involves: (i) a snap-change guarantees that the user will see the FoV desired by the director, and that High-Quality is displayed in this FoV, while (ii) not having a snap-change may preserve the level of presence and keep low the probability of disorientation.

We consider the network conditions being fixed and investigate how to optimize cut triggering to obtain the best from this trade-off, by designing a user-adaptive control mechanism for attention guidance techniques in 360° video streaming. Hence our contribution is:

• We model the dynamic decision problem of snap-change triggering as a model-free Reinforcement Learning (RL), for which we model the user's quality of experience as a reward function based on the quality in FoV penalized by the cut frequency. We express the optimum cut triggering decisions computed offline with dynamic programming, when the user's motion is known before but also after the cut decision time. We adopt a machine learning framework from the realm of Imitation Learning, namely Behavioral Cloning, to train different strategies aimed at approaching optimal decisions. We show that it is possible to improve the quality of experience by dynamically deciding to trigger snap-cuts, only knowing the past user's motion and video content, compared to the controls without and with all cuts.

Conclusion and Publications.

Chapter 8 concludes this dissertation. The subject of this thesis is multi-disciplinary, involving concepts from Multimedia Communication and Networking, Machine Learning and Deep Learning, Attentional Models and Perception. Our work has been proven to be relevant in the context of international research. This work resulted in six publications. The complete list of publications is presented in Appendix C.

Chapter 2

Related Work

The aim of this Chapter is to briefly describe the terminology used throughout the text concerning the different approaches to improve the quality of experience with a proper modeling of the human visual system and the different computational techniques to perform streaming of immersive content.

2.1 Human Visual System

A number of problematic components are intrinsic to the VR display systems. Up to now, almost all the solutions for Virtual Reality remain rarely pleasant after a few dozen of minutes, current systems do not handle properly the cognitive overload.

When wearing a VR headset, unlike in the real world, users look at every detail of the VR environment around them, which after a while may lead them to lose their sense of direction and balance, and to feel nausea [27].

Understanding the connection between the audio-visual content and the human attentional process is key for the design of immersive environments. In this section we introduce some contents related to the Human Visual System (HVS) together with details of how the feeling of immersion is provided by VR headsets.

Natural visual scenes are cluttered with objects and information that we cannot perceive simultaneously. To efficiently perceive our environment, we have evolved different biological mechanisms in our visual system. The HVS includes the eyes (as sensory organ) and a set of complex mechanisms located in the central nervous system.

2.1.1 Structure of the Eye

The human eye is an almost spherical sensory organ that contains the structures responsible for vision [28]. The eyeball can be divided in three layers as shown in Fig. 2.1.

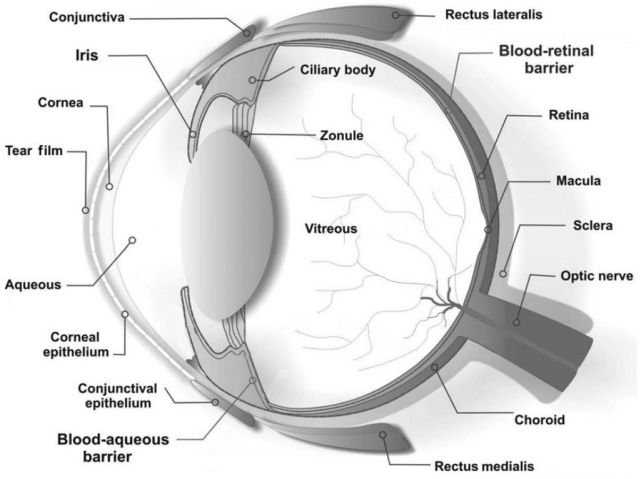

FIGURE 2.1: Schematic diagram of the different layers of the human eye. Image from [6].

The outermost layer is composed in its majority of a fibrous tissue (sclera) that provides attachment to the muscles outside the eye that are responsible of its motion. However, the front of this layer is a transparent tissue (cornea) that allows light rays to enter the eye.

The vascular layer is located immediately beneath the sclera and includes the iris, the ciliar body and the choroid. The iris is a structure able to control the size of the pupil, the pupil is an aperture at the centre of the iris; The ciliar body includes a set of muscles that control the shape of the lens; and the choroid contains blood vessels that nourish the outer layers of the retina.

The inner layer is formed by the retina and contains light-sensitive neurons capable of transmitting visual signals to the central nervous system. In Fig. 2.2 we present the distribution of photoreceptors (cones and rods) across the human retina. The area with the highest amount of photoreceptors is located in a depression at the centre of the retina and it is called the *fovea centralis*. The fovea is therefore the area responsible for high acuity vision. The acuity radially decreases from the fovea to the periphery of the eye.

2.1.2 Visual Attention

The HVS is in charge of performing several tasks related to the detection of objects of interest, motion and pattern recognition among others, but perhaps the most important task of the HVS is visual attention.

Visual attention is a set of cognitive operations that allow us to filter the relevant locations in our visual field [29]. This mechanism also guides the movement of our head and eyes to center the selected location in our fovea and therefore allows us to focus on the visual detail in the selected area [25].

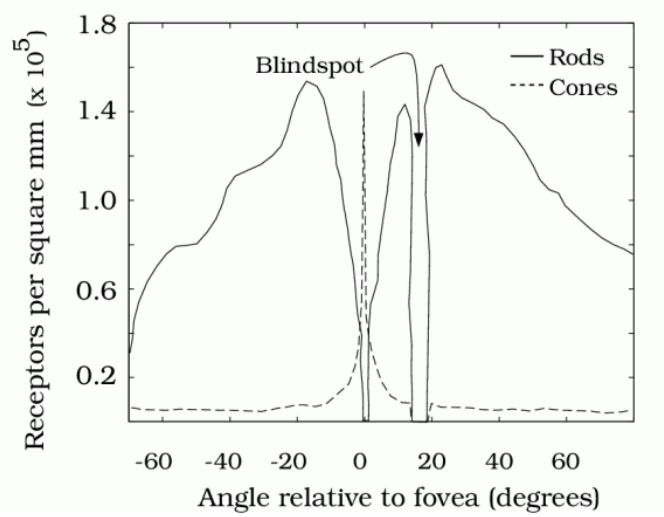

FIGURE 2.2: Distribution of rode and cone receptors across the human retina along a line passing through the fovea and the blind spot of a human eye vs the angle measured from the fovea. Image from [7].

2.1.3 Fixations and eye movements

Eye movements are an essential mechanism of visual attention which allows to bring the fovea to the region of the image to be fixated upon and processed with highest detail. There are mainly four types of eye movements: saccade, smooth pursuit, vergence and vestibulo-ocular movements [30].

Saccadic eye movements are fast, ballistic changes in the eye position that occur at a rate of about 3-4 per second. Saccadic movements can be voluntary or involuntary. Due to the fast motion of a saccade, the eye is blind during these movements. To be able to acquire information we have to maintain the visual gaze on a single location. *Fixations* are relatively long episodes (approximately 250 msec) [31] that occur during saccades on which the visual gaze is fixed on a single point. During this long interval, information is acquired and the target for the next saccade is calculated.

Smooth pursuits are voluntary movements slower than saccades that align a moving stimulus with the fovea.

Vergence is the name assigned to the involuntary movement performed to align the fovea with targets positioned at different focal distances. Unlike the previous movements, in this case the eyes do not move in the same direction to perform *vergence movements*.

Vestibulo-ocular movements are reflexive movements that occur to compensate the position of the eyes when the head is moving.

The *Vergence movements* and *vestibulo-ocular movements* drive the automatic occulomotor response. Retinal blur is a visual cue that indicates the HVS to perform the occulomotor response of *accomodation* to multiple depth stimuli, accomodation consists in the adjustment of the eye's lenses to minimize the blur. Similarly, retinal disparity is the visual cue that drives the

involuntary movement of *vergence*.

2.1.4 Saliency Maps

The fixations movements characterize the objects that a person details within a scene. The gaze points recorded by an eye-tracker across several users watching the same stimuli could be processed to generate so-called saliency maps. A saliency map is a fixation density heatmap that identifies what are the points in the scene that attract the attention of the viewers the most.

Several studies propose mechanisms based on exploiting features from the content to extract saliency maps from 2D images and videos [32, 33]. With the arrival of HMDs with an embedded eye-tracker, different works provided the extension of algorithms to compute saliency maps from 2D content to Virtual Reality content [34, 3, 35, 36].

Saliency maps are of capital importance to study the Visual Attention mechanism. Almquist et al. [8] studied several saliency maps on different 360° video stimuli and identified (See Fig. 2.3) the following main video categories for which they could discriminate significantly different users' behaviors: *Exploration, Static focus, Moving focus* and *Rides*. In *Exploration* videos, the spatial distribution of the users' head positions tends to be more widespread, making harder to predict where the users will watch and possibly focus on. *Static focus* videos are made of a single salient object (e.g., a standing-still person). In *Moving focus* videos, contrary to *Static focus* videos, the Regions of Interest (RoIs) move over the sphere and hence the angular sector where the FoV will be likely positioned changes over time. *Rides* videos are characterized by substantial camera motion, the attracting angular sector being likely that of the direction of the camera motion.

2.2 Virtual Reality Systems

The basic components to render a Virtual Reality scene are (i) the 3D scene where the entire virtual world is designed and (ii) a camera that captures and displays the virtual world to the viewer. The images captured by the cameras in the virtual world are then projected to the screen. To provide the perception of being physically present in the virtual world, the screen is positioned an inch away from the eyes through magnifying glasses. To give the stereoscopic effect, two cameras are mapped to the position of the head in the virtual world and separated at the same distance between the eyes of the viewer. The images captured by the cameras in the virtual world are then projected to the Head Mounted Display (HMD). This VR system would allow rotations and translations of the head that are then mapped to the virtual world, such system is referred to as six Degrees of Freedom (DoF) VR application.

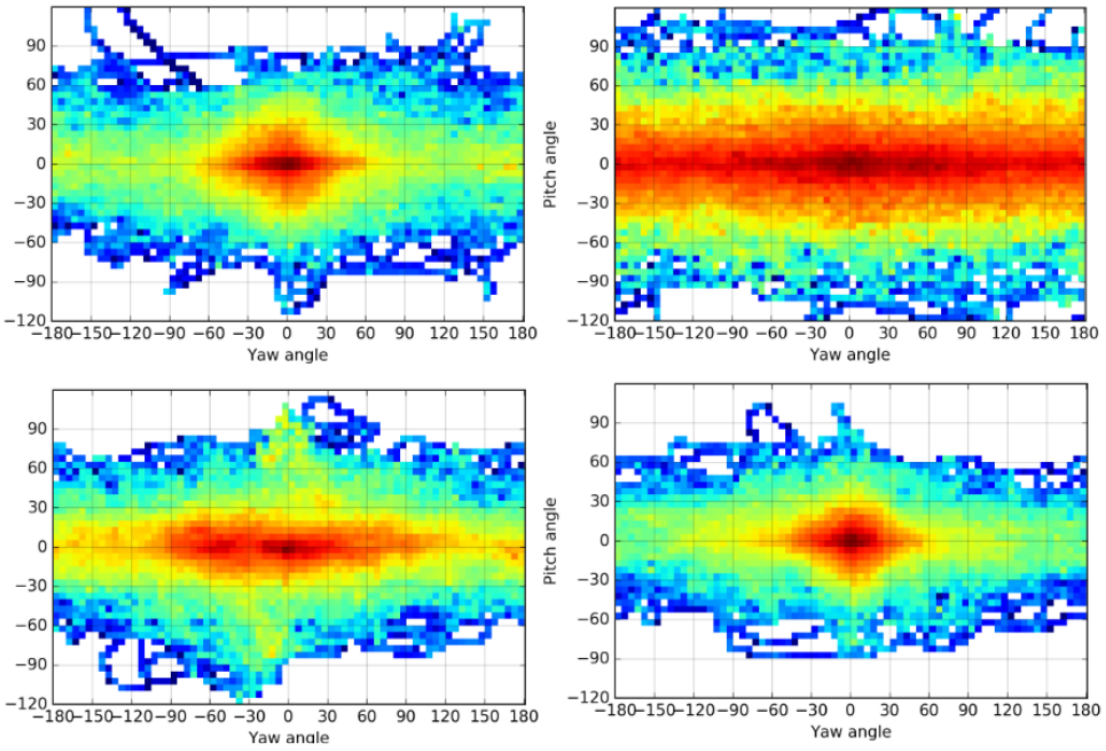

FIGURE 2.3: Saliency map of 360° videos categorized in four groups: Rides (top-left), Exploration (top-right), Moving focus (bottom-left), Static focus (bottom-right). Image from [8].

FIGURE 2.4: Layout of a Virtual Reality system with a wearable Head Mounted Display.

2.2.1 360° Videos

360° videos are an important modality of the Virtual Reality ecosystem, providing the users the ability to freely explore an omnidirectional pre-recorded scene and also providing a feeling of immersion when watched in a VR headset. The virtual reality scene in this case consists on a spherical video and the cameras that map the position of the head of the user are located at the center of the sphere. The VR experience in 360° videos is therefore limited to three DoF corresponding to the rotation (yaw, pitch and roll) of the head inside the content as depicted in Fig. 2.4.

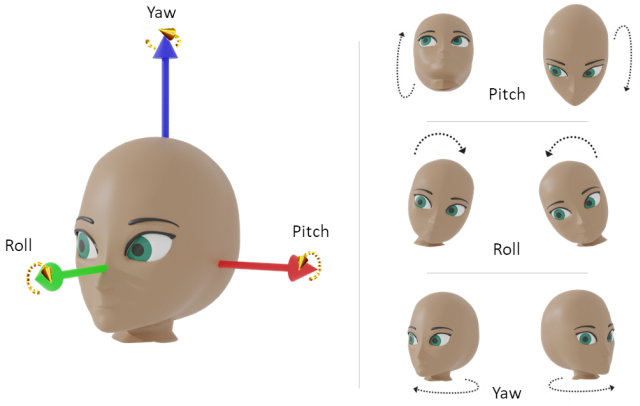

FIGURE 2.5: Three Degrees of Freedom: The viewers of 360° videos can rotate their heads around three axis (yaw, pitch and roll). Image based on [9].

2.2.2 Head position representation

2.2.2.1 3D Euclidean coordinates

A question that arises is how to represent the head orientation inside the video sphere. One option is to use the 3D vector representing the direction of the FoV projected towards the unit sphere and therefore 3D Euclidean coordinates $(x, y, z) \in \mathbb{R}^3$ are used to represent the head position. The series of head positions can also be represented as the rotation from a fixed coordinate frame.

2.2.2.2 Euler angles

Assuming a frame of reference with axis (**i**, **j**, **k**). Axis **i**, going through the viewer's viewport, axis **j** passing through the left ear and axis **k** going through the top of the head. The head orientation can be represented as the rotation around each of these axis (See Fig. 2.5). The rotation around **i** (also known as roll) is generally ignored for VR streaming, the head position is then represented by the rotation around **j** (also known as pitch or elevation) and **k** (also called yaw or azimuth).

2.2.2.3 Quaternions

Another option is to use quaternions to represent the series of head position in the unit sphere as the rotation from a fixed point (e.g. $(0, 0, 1)$) to the actual head orientation point (x, y, z). A rotation quaternion is a number generally represented as:

$$(A, B\hat{i}, B\hat{j}, B\hat{k}), \tag{2.1}$$

where $(\hat{i}, \hat{j}, \hat{k})$ represents the axis of spatial rotation and the angle of rotation ψ is given by the values of $A = \cos(\psi/2)$ and $B = \sin(\psi/2)$.

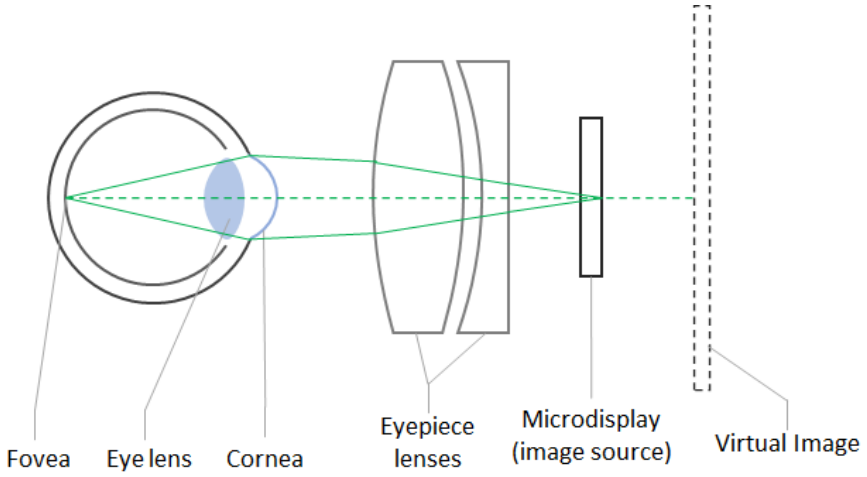

FIGURE 2.6: Schematic of the traditional VR HMD optical system. The HMD gives the sense of immersion by projecting images on a display unit. Image based on [10].

2.2.3 Head Mounted Displays

As already mentioned, the currently fast-developing products for the general public deal with 360° framed video content displayed on a virtual sphere, an inch away from the eyes through magnifying glasses as shown in Fig. 2.6.

The challenge in the design of HMDs comes mainly from the Induced Symptoms and Effects of Virtual Reality. If the feeling of immersion is not sufficient, VR users could experience discomfort to a distressing level, possibly yielding disorientation and nausea [20].

To ensure immersion, 360° videos can be stereoscopic to create a 3D effect. However, a major hurdle to the proper rendering of stereoscopic views in near-eye displays lies in the vergence/accommodation conflict [11].

2.2.4 Vergence-Accomodation Conflict

In Sec. 2.1.3 we introduced the visual cues of *retinal disparity* and *blur* that drive the oculomotor responses of *accomodation* and *vergence*. However, there is also a parallel feedback loop between the vergence and accomodation responses, and therefore one becomes a secondary cue influencing the other [37]. As illustrated in Fig. 2.6, in a Virtual Reality Head Mounted Display, the distance of the virtual image does not correspond to the distance of the image source.

In stereoscopic HMDs, the distance from the eyes to the screen remains constant, thus the accomodation distance remains constant, while the distance of the virtual image varies depending on the content (projected in each display) which results in conflicting information within the vergence-accomodation feedback cues as shown in Fig. 2.7.

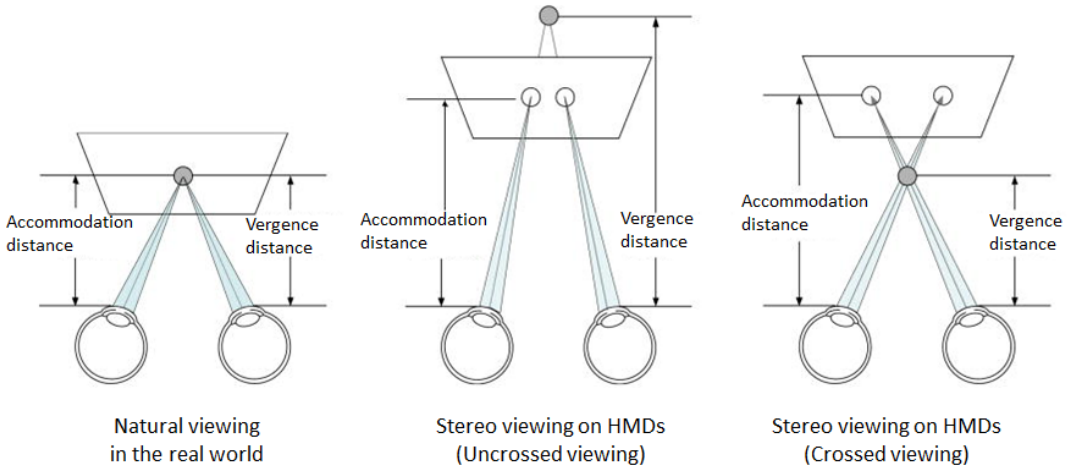

FIGURE 2.7: Diagram of stereo viewing in natural scenes and the vergence accomodation conflict on conventional stereo HMDs. Stereo viewing in VR HMDs creates inconsistencies between Vergence and accomodation (focal) distances. Image from [11].

2.2.5 Foveated Rendering

Main distribution platforms (YouTube VR[1], Facebook 360[2], etc.) are mostly monoscopic to date. While the absence of a 3D effect limits the sense of immersion, it prevents the effects of the vergence-accomodation conflict. A main set of solutions to contribute to the feeling of immersion relies on so-called foveated rendering, where clear content is rendered in a restricted radius around the fovea, while the rest is blurred away to reproduce the natural focusing process in a real scene, thereby lowering the visual discomfort and cognitive load [23]. This requires to constantly locate the gaze direction with an eye-tracker integrated within the HMD and render the content with radially-decreasing quality from the fovea to the eye's periphery.

2.2.6 Quality of Experience

In Virtual Reality systems it is important to assess the level of discomfort (dizziness, sickness, etc.) of a user and to design strategies that improve their Quality of Experience. The Quality of Experience (QoE) is defined as the degree of delight or annoyance that the user of an application experiences [38]. Hence, QoE is difficult to define and needs to be studied for each particular application. In the case of video streaming, the multimedia community has devised various metrics to measure the sensitivity of the user to certain aspects of the video [39]. For instance, to measure the visual quality, metrics based on Peak Signal-to-Noise Ratio (PSNR) exist such as Structural Similarity Index Measure (SSIM) or Video Quality Metric (VQM) [40], other metrics that have been found to impact the QoE include the video startup delay and the amplitude and frequency of quality variations [41].

[1] https://vr.youtube.com/
[2] https://facebook360.fb.com/

In regular videos, a manifold of policies aiming to provide the client with the best QoE while absorbing the network variations have been proposed, these techniques have been proven to improve the QoE and have been extended to the streaming of Virtual Reality.

2.3 Streaming of Virtual Reality

To improve the experience of users exploring virtual environments, the VR system has to satisfy human eye fidelity. Therefore, for streamed VR content, the quality of experience is hindered by the difficulty to access immersive content through Internet. In this section we first introduce the streaming mechanisms used to improve QoE in traditional 2D videos, we then present the main challenges of using such traditional techniques for the streaming of 360° videos, finally we present the protocols and current solutions for Virtual Reality streaming.

2.3.1 HTTP Adaptive Streaming (HAS)

Modern (regular non-360°) video streaming relies on the concept of HTTP Adaptive Streaming, whose most wide spread version is the MPEG-DASH standard [42]. A schematic of the operation in MPEG-DASH is shown in Fig. 2.8. The video file being chunked into temporal segments of fixed duration (often 2 sec. or 5 sec.), each encoded into several quality levels, that is at different bitrates (often corresponding to resolutions). A Media Presentation Description (MPD) file describing the available qualities for each video segment is stored in the server and send to the client at the beginning of video reproduction. The client strives to (i) prevent playback interruptions by maintaining a non-empty playback buffer where a certain number of segments (or seconds of video) are stored in advance of playback, while (ii) fetching and displaying qualities as high as possible. To do so, the client runs a so-called adaptive streaming logic (or algorithm) which chooses which quality to request for every segment to the remote server, based on the network bandwidth varying over time.

The challenge of streaming 360° videos using traditional Adaptive Streaming mechanisms (e.g. HAS) becomes evident when we analyze the required data rates. Given the closer proximity of the screen to the eye and the width of the content (2π steradians in azimuth and π in elevation angles), the required data rate is two orders of magnitude that of a regular video [21]. Traditional techniques are no longer feasible to stream VR videos.

2.3.2 Viewport Adaptive Streaming

A key aspect to ensure a high level of immersion is the video resolution which must be at least 12K [14]. Given the human eye acuity, fooling our visual perception to give a feeling of immersion would require a data rate of 5.2 Gbps considering the latest compression standards [22]. These data rates cannot be supported by the current Internet accesses, when the content is streamed from remote servers.

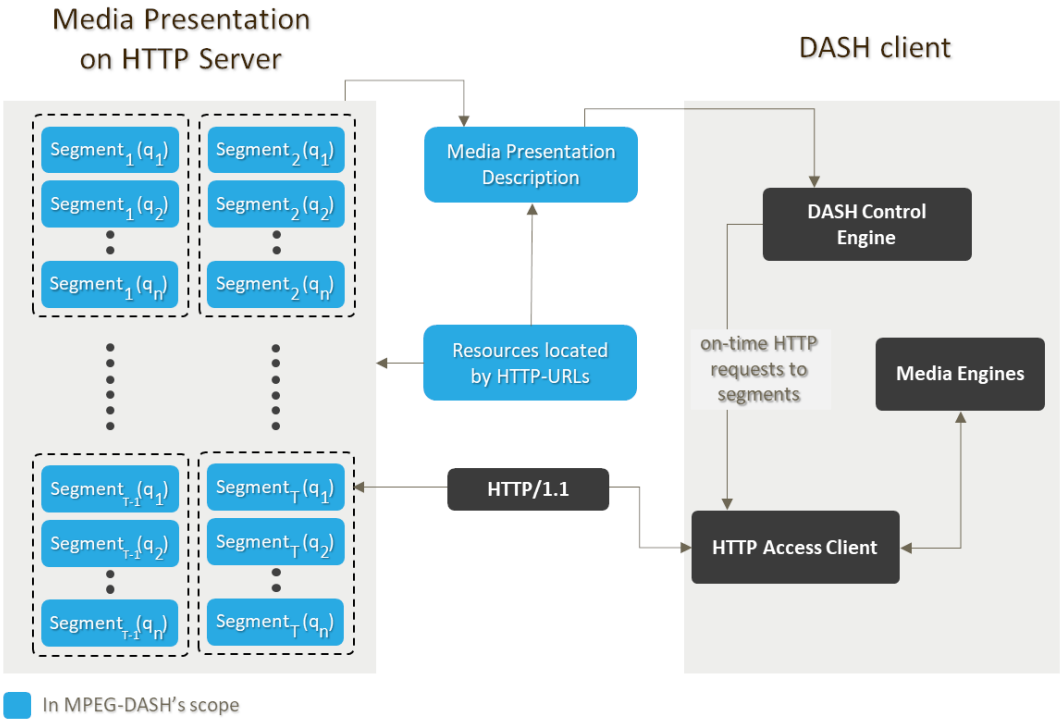

FIGURE 2.8: MPEG-DASH system overview. Image based on [12].

To cope with the discrepancy between the required video rate for best quality and the available network bandwidth, a simple principle is to send the non-visible part of the video sphere with lower quality. To do so, recent works have proposed to either segment the video spatially into tiles and set the quality of the tiles according to their proximity to the FoV, or use projections enabling high resolutions of regions close to the FoV.

2.3.2.1 Tiling

In the case of 360° video streaming, a single segment does not correspond anymore to a single entity (as is the case of 2D videos using HAS), but possibly to several tiles. Spatial Relationship Description (SRD) is an approach that extends the MPD file in the MPEG-DASH standard to describe spatial relationships between associated pieces of video content. SRD allows to request and fetch only sub-parts of a video not only in time but also in space. The goal is to reduce the required bandwidth to stream 360° videos by requesting high quality segments for the tiles that will intersect the FoV of the user and low quality elsewhere. The qualities to request for every tile of every segment must therefore adapt both to the network and the user dynamics, as represented in Fig. 2.9.

2.3.2.2 Encoding

There are various competing video encoding standards for 360° videos [43]. The most popular are standard 2D encoding techniques as High Efficiency Video Coding (HEVC) also known

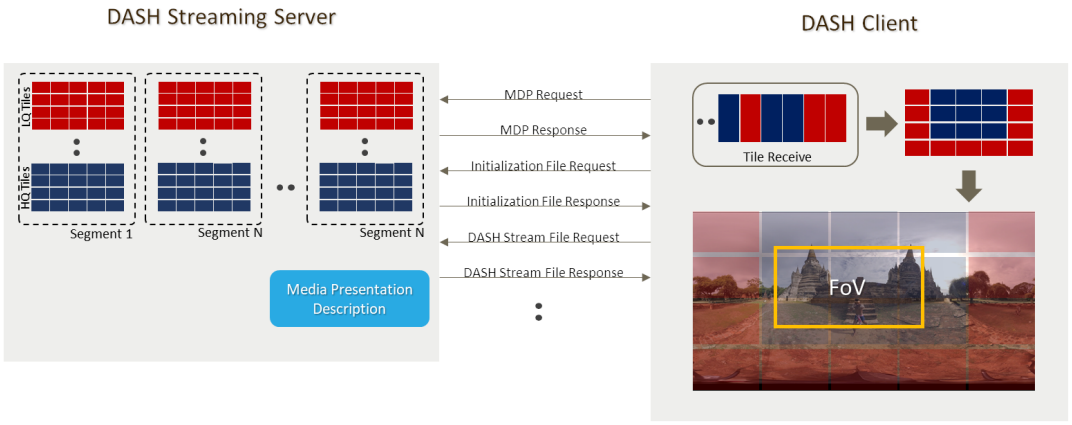

FIGURE 2.9: Tile-based Adaptive Streaming for 360° Videos using MPEG-DASH. Image based on [13].

as H.265 [44] and AOMedia Video 1 (AV1) [45]. These standards are highly optimized for 2D videos but are also used to encode 360° videos. Even the earlier Advanced Video Coding (AVC) also known as H.264 [46] is still used for this purpose. Additionally, Versatile Video Coding (VVC), also known as H.266, promises to add new capabilities to the existing standards [47].

360° videos are by nature more challenging to process, store and transmit than their traditional 2D counterparts. Current codecs cannot handle spherical formats, therefore to be able to use state-of-the-art codecs the spherical video is first transformed in a 2D representation.

2.3.2.3 Projections

Currently, 360° videos need to be projected in two-dimensional frames to be able to be encoded and transferred. Instead of tiling the video, one could take advantage of such projections or use heterogeneous spatial quality encoding to ensure that important parts of the video are encoded in higher quality than less important ones.

Fig. 2.10 illustrates different projections that have been proposed to map the video sphere [14]. These projections map the points on the unit sphere to pixel positions in a 2D map, for example, the azimuth and elevation angles in the unit sphere correspond to the horizontal and vertical positions on the *equirectangular* map. The different layouts can over-sample pixels from the sphere to certain regions of the planar shape, as is the case of *equirectangular* panoramic images that over-sample pixels in the poles. On the contrary, other projection layouts under-sample pixels from the video sphere, as is the case of *pyramid* layouts where some points in the sphere (corresponding to the top of the pyramid) become under-represented in the planar shape. Different versions of the video projected at each possible FoV position could be stored and then streamed to reduce the amount of bandwidth waste by sending the version with a higher-represented number of pixels in the area that covers the current FoV of the user. However,

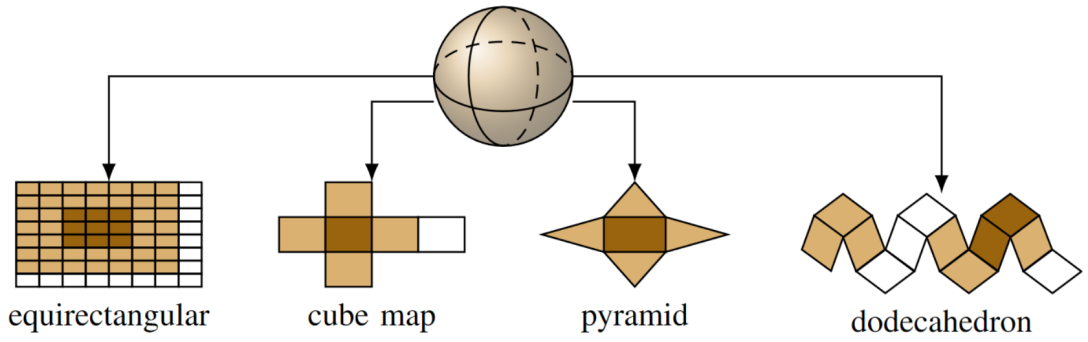

FIGURE 2.10: Projection of the video sphere into four geometric layouts. Image from [14].

the over- and under-sampling of these projections still cause distortion in the planar image and therefore degrade the performance of traditional video encoders [48].

2.4 Viewport Orientation Prediction

Different approaches have been proposed to send in low resolution the portions of the sphere outside of the FoV to reduce bandwidth waste. These approaches however require to know the user's head position in advance, that is at the time of sending the content from the server. This can go from a few tens of milliseconds (low network delay) to a few seconds (extreme network delay or presence of a video playback buffer at the client to absorb network rate variations). It is therefore crucial for an efficient 360° video streaming system to embed an accurate head motion predictor which can periodically inform where the user will be likely looking at over a future time horizon, based on the past head trajectory and on the video content.

Current methods for viewport orientation prediction exploit Deep Learning techniques including Recurrent Neural Networks (RNNs) and Reinforcement Learning paradigms.

2.4.1 Recurrent Neural Networks

A Recurrent Neural Network (RNNs) is a type of Artificial Neural Networks (ANN) suited for learning operations with time sequences. The time-series can be decomposed in a set of inputs for each time-step in the sequence. The architecture of a RNN contains feedback connections allowing outputs at previous time-steps to be used as inputs for predictions in future time-steps [15]. Several applications are derived from RNNs according to the way the architecture is used. If we denote the length (in time) of the input by T_x and the length (in time) of the output by T_y, the different RNN architectures illustrated in Fig. 2.11 are described as follows.
One-to-many: $T_x = 1$ and $T_y > 1$. From a single input a whole sequence is generated. This architecture could be used for music generation or to provide image descriptions.
Many-to-one: $T_x > 1$ and $T_y = 1$. From a time-series input obtain a single output. This architecture is used for instance to perform sentiment classification.

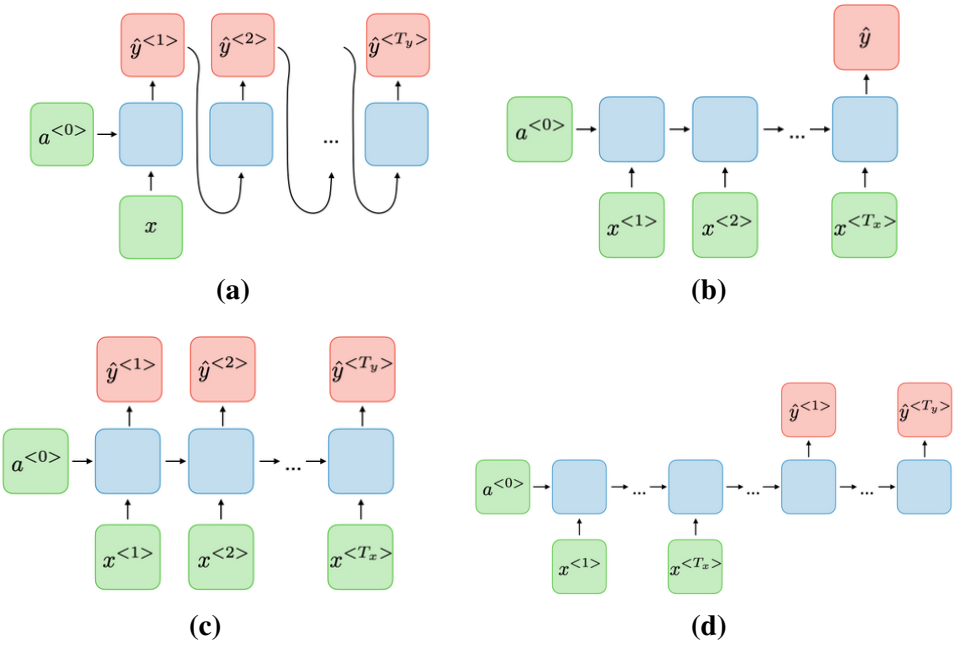

FIGURE 2.11: Type of RNNs for different time-series applications. **(a)** One-to-many. **(b)** Many-to-one. **(c)** Many-to-many. **(d)** Seq2Seq. A one-to-one architecture corresponds to a traditional neural network. Image from [15].

Many-to-many: $T_x = T_y$. From each input in the time-series obtain an output. This architecture could be used to classify words in a text.

Seq2Seq: $T_x \neq T_y$. From a time-series input produce another time-series (with possibly different length). An application of this architecture is for Machine translation and it is also important in the head motion prediction methods that are proposed in this dissertation.

A RNN is a block (Recurrent Unit) conformed by a Fully-Connected layer with feedback connections allowing to inform about the state at previous time-steps in the input series.

2.4.1.1 Gated Recurrent Neural Networks

Instead of using a Fully-Connected ANN in the recurrent unit, a gating mechanism (e.g. $W_i \odot x_i$, where W_i are the weights of an ANN) could be used to perform specific tasks (e.g. forget) inside the Recurrent Unit. An LSTM is a widely used gated RNN architecture that uses gates to control the data flow and in theory avoids forgetting long-term information.

LSTM

A common LSTM unit is composed of a **state gate** (g), **input gate** (i), **output gate** (o) and a **forget gate** (f). These gates regulate the flow of information that enters and leaves the cell state. The specific LSTM unit is shown in Fig. 2.12, the equations for the LSTM are given in Eq. 2.2:

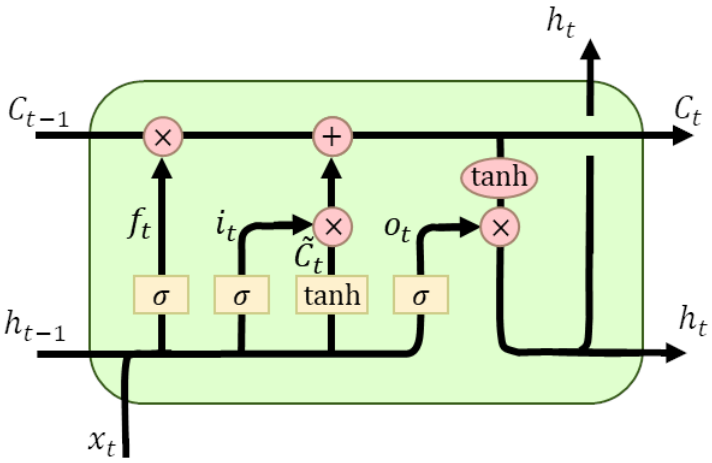

FIGURE 2.12: Diagram of an LSTM cell and the equations that describe its gates. Image from [16].

$$
\begin{aligned}
i_t &= \sigma(x_t U^i + h_{t-1} W^i) \\
f_t &= \sigma(x_t U^f + h_{t-1} W^f) \\
o_t &= \sigma(x_t U^o + h_{t-1} W^o) \\
\tilde{C}_t &= tanh(x_t U^g + h_{t-1} W^g) \\
C_t &= \sigma(f_t \times C_{t-1} + i_t \times \tilde{C}_t) \\
h_t &= tanh(C_t \times o_t),
\end{aligned}
\tag{2.2}
$$

where (U^i, W^i), (U^f, W^f), (U^o, W^o), (U^g, W^g) are the set of weights for the **input**, **forget**, **output** and **state** gates. C_t is the cell state, and $\tilde{C}_t$ is the candidate cell state, h_t is the hidden state of the LSTM.

2.4.2 Reinforcement Learning

Reinforcement Learning (RL) is a branch of Machine Learning aimed at teaching an agent (or several) to react to a dynamic environment to maximize some return [49]. As shown in Fig. 2.13 the *agent* can stay in one of many *states* ($s \in S$) of the *environment*, and choose to take one of many *actions* ($a \in A$) to switch from one *state* to another. Which *state* the agent will arrive is decided by transition probabilities between *states* (P). Once an *action* is taken following the *policy function* $\pi(s)$, the *environment* delivers a *reward* ($r \in R$) as feedback. The formal objective of RL is finding a policy function $\pi^*(.)$ such that:

$$
\pi^*(.) = \arg\max_{\pi} \mathbb{E}_{s \in \mathcal{S}, a \sim \pi(.)} \Big[\sum_{t=0}^{\infty} \gamma^t r_t \Big] \tag{2.3}
$$

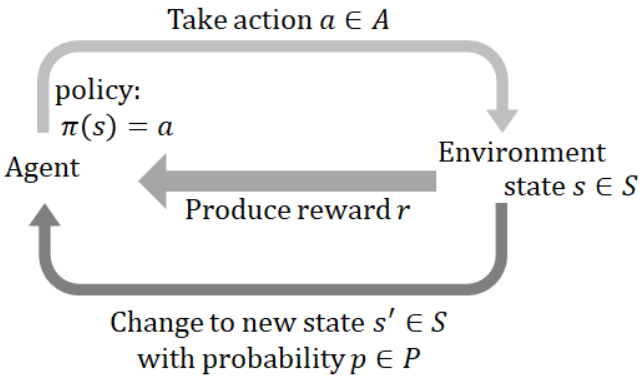

FIGURE 2.13: Formulation of a problem in the RL framework an *agent* re*acts* in an *environment* to maximize some *reward*.

Where $\gamma \in [0, 1]$ is a *discounting factor* that favours immediate rewards. If the transition probabilities between *states* of the *environment* is known, the planning is done with perfect information and methods like Dynamic Programming can be used to find the optimal solution. If the model of the environment is not known, Reinforcement Learning methods are used to learn the value of cummulative discounted rewards with incomplete information about the model (**model-free RL**) or to learn the model explicitly (**model-based RL**). When Deep Learning is used as function approximation methods in a Reinforcement Learning context, it is called *Deep Reinforcement Learning*.

2.4.2.1 Imitation Learning

Imitation Learning consists in initializing the Deep Neural Network used to predict the cummulative discounted rewards (called the *Value Network*) by supervised training on a set of trajectories generated by an expert or a baseline policy.

2.4.3 Visual Guidance Methods

Predicting the user's head motion is difficult and can be done accurately only over short horizons (less than 2s). The prediction error might be corrected when time progresses, by downloading again the same segments in higher quality to replace their low quality version close to the playout deadline. This however yields redundant transmissions and hence a higher consumed network rate. It implies a dependency between the consumed data rate and the prediction error (user's motion), which in turn depends on the user's attentional process.

Instead of adapting *reactively* by predicting the user's attention, another solution is to *proactively* motivate the user to change the viewing direction towards the areas the director wants them to explore. Driving the user's attention is critical for a director to ensure the story plot is understood, however, attention driving techniques are also of interest from the perspective of the multimedia network community. Film editing can be helpful for streaming 360° videos

by directing the user's attention to specific pre-defined Regions of Interest (RoI). The a-priori knowledge of such RoIs could be exploited during the streaming decision.

Several methods have been proposed to drive the user attention in VR environments:

Different cues can be used to engage the user towards desired locations in a Virtual Reality scene. Popular techniques include flickering effects in the user's periphery, arrows pointing towards the Regions of Interest (RoI) or saliency adjustments to the RoIs (i.e. modulations of contrast, saturation and color variations) [50]. In [51] a character is inserted in the scene and reflects an emotion associated with the region of interest to naturally incite the user to look at the desired location.

In [52], a vibrotactile HMD is introduced. Electromecanical tractors on the fronthead are instrumented to allow a natural, precise and rapid localization of the target in an immersive VR setup.

The autopilot feature of the 360fly 4K 360° camera allows to automatically pan to the area of footage that has the highest degree of motion [53], but is hence destined to viewing outside a headset.

In [54] two methods are mentioned in future work to shift the user's gaze to the required region, for collaborative narrative tasks in VR. The first idea envisioned is the introduction of a firefly in the FoV flying in the direction of the pre-set target region, until the users moves their heads. The second idea is the rotation of the sphere to reposition the user, inspiring from film techniques and implemented in [26] to improve streaming decisions.

Chapter 3

Foveated Streaming of Virtual Reality Videos

A main challenge to the massive adoption of Virtual Reality (VR) is the delivery through streaming over the Internet. Several works have proposed to provision better qualities in the restricted area the user can watch from the sphere, called the "viewport", lowering the quality of areas outside it [14].

Current VR systems are flawed on different aspects. First, it is hard for the Human Visual System (HVS) to focus naturally in current headsets, in particular owing to the vergence-accomodation conflict [55], incurring visual discomfort and cognitive overload. One of the major solutions envisioned to address this problem is foveated rendering. It exploits the radially-decreasing human visual acuity between the fovea and the eye's periphery [56]. Instead of adapting to the wider viewport, foveated rendering adapts to the narrower user's gaze position by blurring away the regions not in the gaze's target so as to reproduce and help the natural focusing process. Second, high-end Head Mounted Displays (HMDs) (e.g., HTC Vive and Oculus Rift) currently require powerful hardware tethered to the headset for scene synthesis. These hardware requirements can be reduced by employing foveated rendering [57].

There was no affordable (less than $1000) VR foveated rendering system until the second-half of 2017, mainly because of the high costs of integrating an eye-tracker into the VR hardware. This changed with the release of FOVE[1]. A number of works have looked at foveated streaming to couple the visual and computational gains with bandwidth gains, yet not for in-headset VR (e.g., see [58] and references therein).

In this Chapter, we consider the problem of streaming stored 360° videos to a VR headset equipped with eye-tracking and foveated rendering capabilities (the FOVE headset). We present our gaze-adaptive streaming prototype built on the FOVE's Unity Application Programming Interface (API). In one end, the client is designed to inform the server of the current gaze

[1] http://getfove.com

position, receives the video sphere in low-resolution and additionally the foveal region in high-resolution, and is responsible for the merging of textures. On the other end, the server prepares the content upon reception of a request. It computes the equirectangularly projected mask, crops the frame of the segment and formats the resulting piece for transmission without overhead. To enable full freedom in future design, we provide the ability to apply different masks over each frame of a segment, and verify that the whole system can work online.

3.1 Related Work

Traditional Two Dimensional (2D) video streaming is still challenging due to the increase of video demand. Despite the efforts made to enhance the performance of the networks, users are still unsatisfied by the received video quality [59].

A solution envisioned to reduce the bandwidth usage while keeping a good quality of experience is to use HTTP Adaptive Streaming (HAS). HAS is a technique that consists in detecting the network throughput in real time and adjust accordingly the version of the media file that is sent from the server to the client [60]. In HAS-based video streaming, the original video is partitioned into segments of the same temporal length. Each of these segments is encoded in different versions that vary in quality or resolution. A manifest file, containing information about the available representations of each video chunk is generated at the server and sent to the client at the beginning of each streaming session. During the streaming of the video, the client continuously checks its current network status and requests the next video segment(s) to fill the playback buffer and prevent video stalls with the goal of optimizing the Quality of Experience (QoE) [61].

The streaming of Virtual Reality videos is even more challenging than traditional 2D video streaming. The data rates needed to provide good immersion are two orders of magnitude higher than that of a regular video [21]. Furthermore, while such data rates are employed to send the video, most of the delivered video signal is not displayed in the Head-Mounted Display (HMD).

Viewport Adaptive Streaming (VAS) is a solution to reduce the bandwidth waste by making decisions not only in time but also in space to stream the 360° videos with heterogeneous quality levels. Portions of the video closer to the viewport are sent in high quality, while regions far from the viewers' Field of View (FoV) are sent in lower quality.

The most popular approach to perform viewport adaptive streaming consists in splitting the video spatially into tiles and send in high-quality tiles corresponding to the users' FoV [62].

Instead of adapting to the wider viewport as in legacy Viewport Adaptive Streaming techniques, our approach consists in adapting to the narrower user's gaze by blurring away the regions not in the gaze's target so as to reproduce and help the natural focusing process while further reducing the bandwidth waste.

Our work is mainly related to [58] and [63] addressing foveated streaming for mobile cloud gaming (not VR) and in-headset VR without foveation, respectively.

In [58], Illahi et al. live-encode frames by setting the Quantization Parameter (QP) of each macroblock depending on the gaze location, consider a Gaussian-smoothed circular foveal region and assert the processing latency to be order of 20 ms. To prevent changing the encoder and keep the complexity very low for the larger frames to be processed in 360°, we use the MPEG-Dynamic Adaptive Streaming over HTTP (DASH) principle and make the video available in 2 resolutions, cropping the foveal region from the high resolution for streaming. This thresholding is chosen for simplicity in our prototype owing to the non-circularity of the foveal region in the equirectangular projection. Generating one second-long segment made of 30 frames requires about 700 ms in our CPU implementation (FFmpeg cannot access the GPU through Virtualbox), amounting to about 23 ms per frame, which the same order as in [58].

In [63] (akin to [64]), VR videos are streamed with the viewport selected from high-resolution tiles, and the client reassembles the different regions at the destination. We leverage the same idea (with the same high-speed H.264 encoding flags) but develop the whole system for Unity and the FOVE, and specifically design the cropping filters to allow dynamic foveation over one-second segments to preserve the feeling of immersion.

3.2 Architecture of the Foveated Streaming System

In this section we introduce our working material: the FOVE headset and its Unity API with the components employed, then we define the eye-tracking data and how they are used with our FFmpeg-based cropping module.

3.2.1 FOVE Headset and Unity API

FOVE is a VR headset including an eye-tracker that allows to follow the user's gaze. It provides two programming interfaces, one is the Unity Plugin and the other is the C++ Software Development Kit (SDK). These APIs allow, among other tasks, to connect to the FOVE compositor, to capture the HMD orientation, to get the direction where the user is looking at, and to know if the user is blinking. We decided to work with the Unity API, since the Unity engine is a widely used industry standard that offers different resources built from a large community.

Unity[2] is a game engine used to develop three-dimensional simulations across several platforms. The basic components of a Unity simulation are a scene, where the entire virtual world is designed, and a camera that captures and displays the virtual world to the viewer. To give the stereoscopic effect, our Unity scene contains two cameras, mapped to the movements of the user's head through the FOVE SDK. To give the immersion illusion, the cameras are fixed in the center of a sphere, where the 360° video is projected.

VR videos, which are spherical in nature, are mapped onto a planar texture, one of these mappings is the commonly used equirectangular projection. With this panoramic projection we

[2]http://unity3d.com

can consider that the 360° video has the same rectangular shape as a regular video. In Unity, a video can be considered as a 2D-texture that changes in time, to play the 360° video onto a texture, we used the `VideoPlayer` component, since it supports the `H.264` video codec when playing a video from a Uniform Resource Locator (URL). The `VideoPlayer` component can be tuned to playback videos streamed from a server, using the following event-handlers:

• `prepareCompleted`. Invoked when the `VideoPlayer` has downloaded some frames, and reserved resources so that the video can be played.

• `loopPointReached`. Invoked after the `VideoPlayer` has finished the playback of the video.

To provide adaptive streaming capabilities, the video needs to be segmented in time: we chop the high-resolution video into segments with constant duration of 1 second. The `VideoPlayer` component can be tuned to request each segment of the video from the server by manipulating the requested URL, simply adding the id of the segment, and in our case, the user's gaze parameters.

3.2.2 User's Gaze Parameters and Foveal Cropping

The fovea of the viewer is modeled as a circle in the spherical coordinates system by the parameters described in Table 3.1. We can communicate the current user's gaze position to the server by sending the tuple (θ, φ), and set the size of the fovea with the parameter α, thereby controlling the 'feeling' of natural vision of the user and the bandwidth needed.

TABLE 3.1: Parameters of the user's gaze in the spherical coordinate system

Param.	Range	Description
r	$\in \mathbb{R}_+$	Radius of the sphere. In our experiments this is 1.
θ	$\in [-\pi, \pi]$	Azimuth, also known as yaw axis.
φ	$\in [-\frac{\pi}{2}, \frac{\pi}{2}]$	Elevation, also known as pitch axis.
α	$\in \mathbb{R}_+$	Controls the radius of the foveal area.

Since the video is projected with the equirectangular projection, even though the fovea has a circular shape, it gets deformed depending on its location, and the size of the rectangular bounding box enclosing it varies as shown in Figure 3.1.

Each segment request includes the timestamp t, the spherical angles (θ_t, φ_t) and the size of the fovea α_t. With this information, the server can crop each of the high-resolution segments to fit only the bounding box of the foveal area. As segments are 1 second-long, we need to crop and prepare the frames of each segment as low under a second as possible, for this purpose we used Fast Forward Motion Picture Experts Group (FFmpeg) [3].

[3] https://ffmpeg.org/

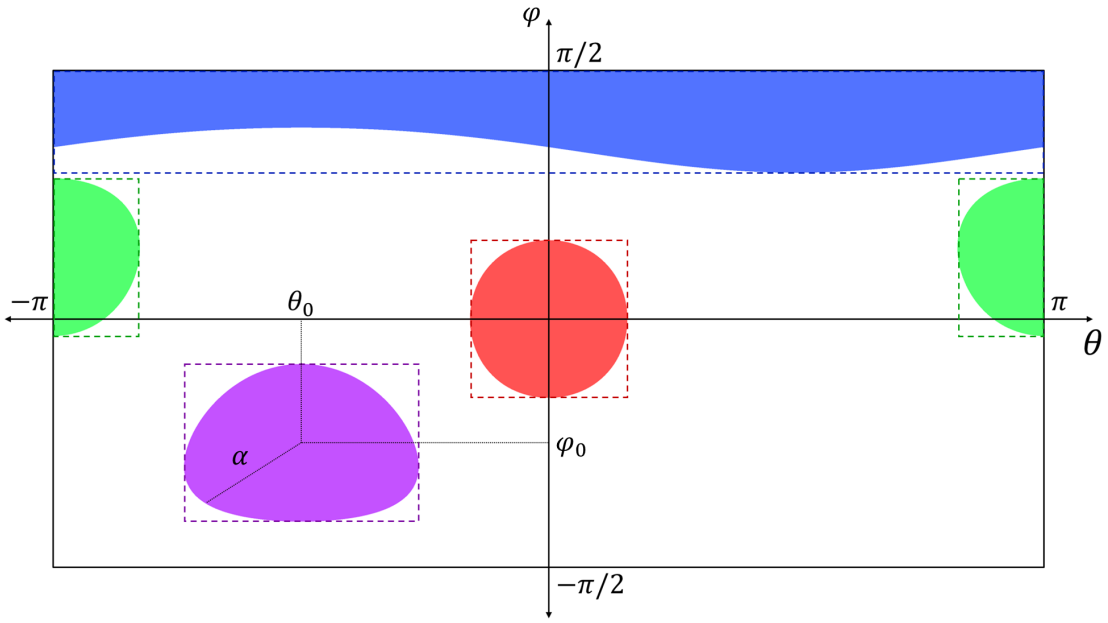

FIGURE 3.1: Deformation of the circular foveal area (and its respective bounding box) when the video-sphere is mapped to a plane using the equirectangular projection.

3.3 Design and Implementation of the Foveated Streaming System

In this section we present how all the building blocks are composed to make the proposed foveated streaming system. The full design of the system is shown in Figure 3.2. The client runs under Windows 10, where the Unity engine is in charge of the following tasks:

- Read user's gaze position from the FOVE HMD.
- Control the buffer to know when to request a new segment.
- Receive, decode and merge the high- and low-resolution frames.
- Project the result in the sphere.
- Use the Unity cameras to capture the viewport of the user in the sphere and render it in the HMD.

The server side is simulated using a Virtual Machine (VM) with Ubuntu 16.04 where the videos are stored in two resolutions: low-resolution (1024x512) and high-resolution (4096x2048). A regular system would stream both the high-resolution and low-resolution segments over time, but for the sake of simplicity, we have chosen to have the client fetching the complete low-resolution video at the beginning, and then stream only the cropped high-resolution segments.

3.3.1 Unity VideoPlayer Module for Streaming

Using Unity in the client side, we assign one distinct `VideoPlayer` to each requested segment to be able to load, prepare and play the segments independently. As described in Algorithm 1, the data structure that holds the `VideoPlayers` also acts as the buffer of the system. The event-handler `Prepared` is used to start the playback of the video and to play possible

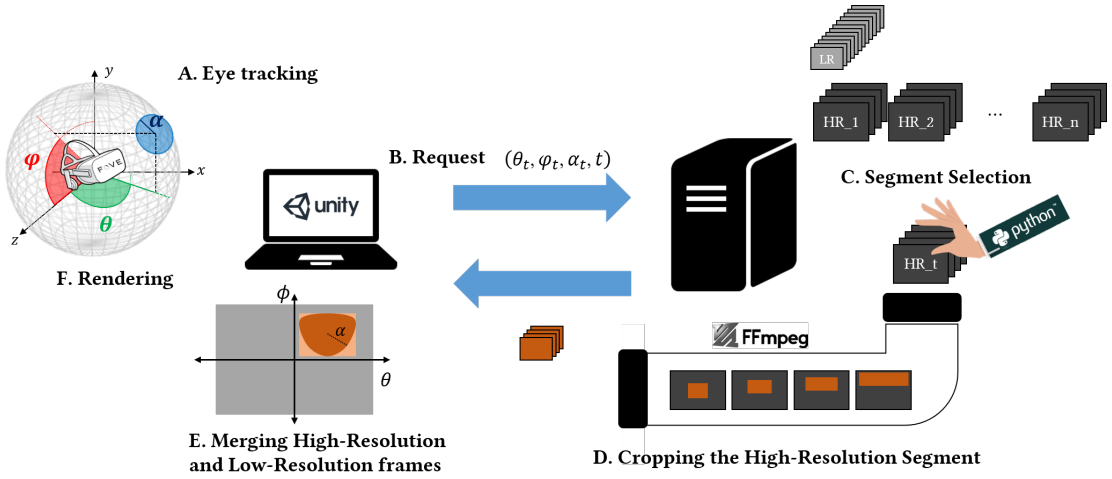

FIGURE 3.2: Workflow of the Foveated Streaming System. The steps are in the following order: **A**. Determine the gaze position with the FOVE headset. **B**. Request a new segment with the parameters of the gaze (Section 3.3.1). **C**. Select the segment according to the request. **D**. Crop the high-resolution segment (Section 3.3.2). **E**. Merge the high- and low-resolution frames (Section 3.3.3). **F**. Render the resulting frame.

subsequent unprepared segments, it also synchronizes the high-resolution and low-resolution frames. Once the playback of the current segment is finished, the event-handler `EndReached` allows to play the next segment if it is already prepared in the buffer, otherwise it pauses the playback of the low-resolution video, that would be played again in the `Prepared` event-handler. The function `RequestNextSegments()` requests the next video segments, passing the parameters $(\theta_t, \varphi_t, \alpha_t, t)$ to the request url, starting from segment t until filling the buffer.

3.3.2 Cropping the High-Resolution Segment

The server side is implemented in `Python`. If the user requests the low-resolution video, then it simply returns it. For the case when the user requests a high-resolution segment we devised a smooth transcoder using `FFmpeg` which cuts on the fly the frames to contain only the fovea of the user, the bounding box of the fovea is a rectangle (x, y, w, h) with origin (top-left vertex) in the point (x, y), width w and height h. Since segment duration is 1 second-long, we need to crop and prepare each segment as low under a second as possible. Importantly, we design the FFmpeg filter not to simply crop a whole segment at once using the same mask, but instead we want to provide the ability to apply different masks over each frame of a segment. Indeed, we want to guarantee such full freedom to enable in our future work attention driving with refined foveal region manipulations. For this purpose we implemented our own custom `FFmpeg` filter called "gazecrop", and it is executed using the following command:

`ffmpeg -i input_`t`.mp4 -vf gazecrop="bbox_expr='` $\theta_0, \varphi_0, \alpha_0, \theta_1, \varphi_1, \alpha_1, \ldots, \theta_{n-1}, \varphi_{n-1}, \alpha_{n-1}$ `'" -vcodec 'libx264' -preset veryfast -tune zerolatency -movflags 'frag_keyframe + empty_moov' -an -f mp4 pipe:1`

Algorithm 1: Basic Foveated Streaming Client

Data: *minBuffSize*, *maxBuffSize*, *serverUrl*, θ_t, φ_t, α_t
t = 0; idxCurrSeg = 0; currBuffSize = 0;
buffHighRes = new Array(*maxBuffSize*);
RequestNextSegments();
lowResVP = new VideoPlayer();
lowResVP.url = *serverUrl* + 'lr';

Function *RequestNextSegments()* **do**
  while *minBuffSize* $<$ *currBuffSize* $<$ *maxBuffSize* **do**
    i = t $\mod$ *maxBuffSize*;
    buffHighRes[i] = new VideoPlayer();
    buffHighRes[i].loopPointReached = **EndReached**;
    buffHighRes[i].prepareCompleted = **Prepared**;
    buffHighRes[i].url = *serverUrl* + $(\theta_t, \varphi_t, \alpha_t, t)$;
    t = t + 1;
    currBuffSize = currBuffSize + 1;
  end
end

Function *Prepared(VideoPlayer highResVP)* **do**
  if *highResVP.id == buffHighRes[idxCurrSeg].id* **then**
    highResVP.play(); lowResVP.play();
  end
end

Function *EndReached(VideoPlayer highResVP)* **do**
  idxCurrSeg = idxCurrSeg + 1;
  currBuffSize = currBuffSize - 1;
  RequestNextSegments();
  nextHighResVP = buffHighRes[t $\mod$ *maxBuffSize*];
  if *nextHighResVP.isPrepared()* **then**
    nextHighResVP.play();
  else
    lowResVP.pause();
  end
end

In the `gazecrop` filter, the string after `bbox_expr` expresses the triplets $(\theta_i, \varphi_i, \alpha_i)$ of the user's gaze for each frame i, and n is the number of frames in each video segment. This filter crops each frame i, after computing the foveal bounding box (x, y, w, h) using equations (3.1-3.4) from [63]. This command is executed in Python, the output video is piped out to a Python variable and then it can be simply written out as the response of the HTTP request.

The total server delay is about 700 ms per segment, that is ca. 23 ms per frame (with the filters running on the CPU only, owing to the virtualized server implementation in the prototype).

Algorithm 2: Merge high- and low-resolution frames

Data: *LowResTex*, *HighResTex*, *MergedTex*, θ_i, φ_i, α_i
foreach *pixel* $p \in$ *MergedTex* **do**
  p.color = *LowResTex*[p.texcoord];
  θ_p = $2\pi(p.\text{texcoord.x}) - \pi$;
  φ_p = $\pi(p.\text{texcoord.y}) - \frac{\pi}{2}$;
  if $\cos\alpha_i \leq \cos(\theta_p - \theta_i)\cos(\varphi_i)\cos(\varphi_p) + \sin(\varphi_i)\sin(\varphi_p)$ **then**
    p.color = *HighResTex*[p.texcoord];
  end
end

Pipelining the emission of frames before the completion of the segment is part of future work.

$$x = \begin{cases} \theta_i - \cos^{-1}\sqrt{\frac{\cos^2\alpha_i - \sin^2\varphi_i}{\cos\varphi_i}} & \text{if } \cos^2\alpha_i \geq \sin^2\varphi_i \\ 0 & \text{otherwise} \end{cases} \tag{3.1}$$

$$w = \begin{cases} 2\theta_i - \cos^{-1}\sqrt{\frac{\cos^2\alpha_i - \sin^2\varphi_i}{\cos\varphi_i}} & \text{if } \cos^2\alpha_i \geq \sin^2\varphi_i \\ 2\pi & \text{otherwise} \end{cases} \tag{3.2}$$

$$y = \varphi_i - \alpha_i \tag{3.3}$$

$$h = 2\alpha_i \tag{3.4}$$

3.3.3 Merging High-Resolution and Low-Resolution Frames

When the client receives back the response from the server with the high-resolution and low-resolution frames, before projecting it onto the sphere, it fuses both frames using a fragment shader that follows the behavior of Algorithm 2. This algorithm assigns the value of the pixel in the high-resolution texture if the condition is met, otherwise it sets the value of the pixel in the low-resolution texture. An illustration of the result is shown in Figure 3.3.

3.4 Demonstration of the Foveated Streaming Prototype

In this section we present the details of the demo that was shown to the MMSys'18 conference attendees. We ran the client and the server in the same laptop using a virtual machine to simulate the server, and to setup and control the network. The host machine was a laptop with Intel Core i7 processor, 64 GB of Random Access Memory (RAM) powered by a Geforce GTX 1070 GPU and running Windows 10 Operating System (OS). The server (guest machine) used the operating system Ubuntu 16.04, and contained the videos to be streamed, the high-resolution video was divided into segments of 1 second. The users could select the video they wanted to try from a list containing the description, the duration and a thumbnail of the 360° video. Then

FIGURE 3.3: On the left: Resulting foveated streaming effect. On the right: Comparison between total size of the frame against viewport size in red, and size of the cropped section of the foveated streaming system in blue.

the user could wear the FOVE HMD. The first step before starting the playback of the video was to calibrate the eye-tracker. To do this we ran the calibration process provided with the FOVE SDK that consists in following, with the gaze, a green dot in a gray background. The calibration of the headset takes around 20 seconds. Once the calibration was finished, the video started, the user could interact with the HMD by moving her head and eyes in the desired direction to explore the 360° video with the foveated streaming system working.

3.5 Conclusions

In this Chapter, we introduced our foveated streaming system, this system was presented in the Demo Track of MMSys'18. The foveated streaming system registers constantly the viewer's gaze to request from a server two different streams of the same video, one version in low-resolution of the entire 360° video and another version in high-resolution, cropped to fit only the gaze within segments of 1 second-long. The frames are then merged at the client and rendered in the HMD to emulate the naturalistic focusing process of the Human Visual System. To our best knowledge, at the time of publication, there was no similar system in the literature. This Chapter introduced our first step to make high-performing foveated streaming systems. Such system raises several research questions in terms of proper prediction of the future gaze and head position trajectories and foveal manipulation to anticipate and drive the user's gaze with foveated tunnels. Approaches to these questions will be studied in the following Chapters of this dissertation.

Chapter 4

A Unified Evaluation Framework for Head Motion Prediction Methods in 360° Videos

360° videos are an important part of the Virtual Reality (VR) ecosystem, providing the users the ability to freely explore an omnidirectional scene and a feeling of immersion when watched in a VR headset. Given the closer proximity of the screen to the eye and the width of the content, the required data rate is two orders of magnitude that of a regular video [21]. To decrease the amount of data to stream, a solution is to send in high resolution only the portion of the sphere the user has access to at each point in time, either the Field of View (FoV) or the Foveal Area (as introduced in Chapter 3). These approaches however require to know the user's head position in advance, that is at the time of sending the content from the server.

Owing to this acute need for head motion prediction in 360° video streaming, a number of approaches have proposed deep neural networks meant to exploit the knowledge of the past positions and of the content to periodically predict the next positions over a given horizon (e.g., [2, 1, 5, 3]). Some of these works have similar evaluation metrics or even use the same dataset, none of them however compares with their counterparts aiming the exact same prediction problem.

Our goal is to address the strong need for a comparison of existing approaches on common ground. For this reason, we present in this Chapter a framework that allows researchers to study the performance of their new head motion prediction methods when compared with existing approaches on the same evaluation settings (dataset, prediction horizon, and test metrics). This software framework therefore contributes to progress towards efficient 360° systems. The entire material (code, datasets, neural network weights and documentation) is available at [18].

The Chapter is organized as follows. Section 4.1 introduces the definition of the problem of head motion prediction and each of the methods considered for reproduction and comparison. Section 4.2 describes the datasets used in these approaches and suggests an algorithm to create

a uniform data structure from the heterogeneous dataset formats. Section 4.3 details the algorithms used to compute the saliency maps estimated from the raw video content or from the users' statistics. Section 4.4 details how to run existing approaches on customizable settings, and introduce two reference baselines. Section 4.5 presents how to prepare a testbed to assess comprehensively a new prediction method (on various datasets against several competitors). Finally, Section 4.6 concludes the Chapter.

4.1 Existing Methods for Head Motion Prediction

We first rigorously formulate the prediction problem which consists, at each video playback time t, in predicting the future user's head positions between t and $t + H$, as represented in Fig. 4.1, with the only knowledge of this user's past positions and the (entire) video content. We then provide a description and classification of each of the existing methods we compare with.

4.1.1 Problem Formulation

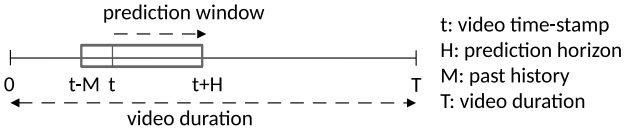

FIGURE 4.1: Head motion prediction: For each time-stamp t, the next positions until $t + H$ are predicted.

Let us first define some notation. Let $\mathbf{P}_t = [\theta_t, \varphi_t]$ denote the vector coordinates of the FoV at time t. Let $\mathbf{V}_t$ denote the considered visual information at time t: depending on the models' assumptions, it can either be the raw frame with each RGB channel, or a 2D saliency map resulting from a pre-computed saliency extractor (embedding the motion information). Let T be the video duration. We now refer to Fig. 4.1. Let H be the *prediction horizon* and M be the *history window*. We define the terms *prediction step* and video *time-stamp* as predicting for all *prediction steps* $s \in [0, H]$ from video *time-stamp* t. For every *time-stamp* $t \in [T_{start}, T]$, we run predictions $\hat{\mathbf{P}}_{t+s}$, for all *prediction steps* $s \in [0, H]$.
We formulate the problem of trajectory prediction as finding the best model $\mathbf{F}_H^*$ verifying:

$$\mathbf{F}_H^* = \arg\min \mathbb{E}_t \Big[D\Big(\big[\mathbf{P}_{t+1}, \ldots, \mathbf{P}_{t+H}\big], \mathbf{F}_H\big([\mathbf{P}_t, \mathbf{P}_{t-1}, \ldots, \mathbf{P}_{t-M}, \mathbf{V}_{t+H}, \mathbf{V}_{t+H-1}, \ldots, \mathbf{V}_{t-M}] \big)\Big)\Big]$$

where $D(\cdot)$ is the chosen distance between the ground truth series of the future positions and the series of predicted positions. For each s, we average the errors $D(\hat{\mathbf{P}}_{t+s}, \mathbf{P}_{t+s})$ over all $t \in [T_{start}, T]$.

4.1.2 Methods for Head Motion Prediction

Prior to the publication of our results in 2020, various approaches to predict user motion in 360° video environments were published. Here we consider that the users' statistics for the specific video are *not* known at test time, hence we do not consider methods relying on these per-video statistics, such as [65, 66]. Each considered method from the literature is named according to the name of the conference or journal it was published in, appended with the year of publication.

PAMI18: Xu et al. in [1] design a Deep Reinforcement Learning model to predict head motion. Their deep neural network only receives the viewer's FoV as a 42×42 input image, and must decide to which direction and with which magnitude the viewer's head will move. Features obtained from convolutional layers processing each 360° frame cropped to the FoV are then fed into an LSTM to extract direction and magnitude. The training is done end-to-end. The prediction horizon is only one frame, i.e., 30ms. By only injecting the FoV, the authors make the choice not to consider the positional information explicitly as input.

IC3D17: The strategy presented by Aladagli et al. in [67] simply extracts saliency from the current frame with an off-the-shelf method, identifies the most salient point, and predicts the next FoV to be centered on this most salient point. It then builds recursively. We therefore consider that this method to be a sub-case of PAMI18, and that the comparison with PAMI18 is thus more relevant.

ICME18: Ban et al. in [68] assume the knowledge of the users' statistics, and hence assume more information than our problem definition, which is to predict the user motion only based on the user's position history and the video content. We therefore do not consider this architecture for comparison. A linear regressor is first learned to get a first prediction of the displacement, which it then adjusts by computing the centroid of the k nearest neighbors corresponding to other users' positions at the next time-step.

CVPR18: In [5], Xu et al. predict the gaze positions over the next second in 360° videos based on the gaze coordinates in the past second and the video content. The time series of past head coordinates is processed by a doubly-stacked LSTMs. For the video information, spatial and temporal saliency maps are first concatenated with the RGB image, then fed to Inception-ResNet-V2 to obtain the "saliency features" denoted as $Vt + 1$. The gaze prediction problem is formulated using the same notation as the head position prediction problem.

MM18: Nguyen et al. in [3] first construct a saliency model based on a deep convolutional network and named PanoSalNet. The so-extracted saliency map is then fed, along with the position encoded as a mask, into a doubly-stacked LSTM, to finally predict the tiles that pertain to the FoV.

ChinaCom18: Li et al. in [4] present a similar approach as MM18, adding a correction module to compensate for the fact that tiles predicted to be in the FoV with highest probability may not correspond to the actual FoV shape (having even disconnected regions).

NOSSDAV17: Fan et al. in [2] propose two LSTM-based networks, predicting the likelihood that tiles pertain to future FoV. Visual features extracted from a pre-trained VGG-16 network are concatenated with positional information, then fed into LSTM cells for the past M time-steps, to predict the head orientations in the future H time-steps. The building block of NOSSDAV17 first concatenates flattened saliency map and position, and feeds it to a doubly-stacked LSTM whose output is post-processed to produce the position estimate. An extended version of this work has been published in [69].

Selected methods analyzed. From Sec. 4.2 we present the analysis of the following methods: PAMI18, NOSSDAV17, MM18 and CVPR18, the remaining methods are either considered subcases of the selected methods or assume there is more information available such as the viewers' position statistics.

4.2 Uniform Data Formats

One of the challenges when evaluating a head motion prediction method across multiple datasets is to adapt it to the specific attributes of each dataset. Consider the case of a model trained with a specific sampling rate that is evaluated on a dataset with a different sampling rate, or where the size or the format of the visual input is different. It is important to have a convention on the structure of the datasets, as it becomes easier to read, sort, understand and compare homogeneous data. In this section, we first describe how to use our framework to post-process the datasets and get a uniform structure shared among all datasets considered in this work. We then provide a way to analyze the datasets.

4.2.1 Make the Dataset Structure Uniform

The datasets used to evaluate the methods discussed in Chapter 5 contain visual and head motion data for 360° videos, stored in different formats. The description of each of the datasets analyzed in our repository is summarized in Table 4.1, and detailed here:

PAMI18: This dataset contains both head movement and eye movement data of 58 subjects on 76 360° videos of variable duration, from 10 to 80 seconds (25 seconds in average).

CVPR18: This dataset is made of 208 360° videos between 15 and 80 seconds (36s in average), each video is viewed by at least 31 participants.

NOSSDAV17: This dataset consists of 10 360° videos with a duration of 60 seconds, along with the identification number of the tiles that overlap with the FoV of the viewer according to the head orientation data (the tile size considered is 192×192). This dataset contains the traces of 50 participants, however, for the experiment performed in [2], the traces of only 25 participants were used.

MM18: The dataset used in MM18 consists on the post-processing of two publicly available datasets [72, 73]. The first dataset [73] includes 18 videos viewed by 48 users, from which 9

Reference	Head Pos. Log Format	Saliency Maps	Raw Videos	Storage of Head Pos. Traces	Code and Neural Network
NOSSDAV17 [2]	Yaw, Pitch and Roll in range [-180, 180].	A MP4 file per video of size 1920×3840.	No.	A CSV file per trace.	No.
PAMI18 [1]	Longitude and latitude in range [-180, 180] and [-180, 180] respectively.	Not provided.	MP4 format.	MATLAB file with an entry per video, each with a matrix with a column per user and alternating longitude and latitudes in the rows.	Found in [70].
CVPR18 [5]	Longitude and latitude in range [-0, 1], origin in bottom-left corner.	Not provided.	MP4 format.	A folder per user with a text file per trace.	No.
MM18 [3]	3D position in the unit sphere, (x, y, z) in range [-0, 1].	A Python array per video of size 9×16.	No.	Python dictionary with an entry per video, each with a list with an entry per user.	Found in [71].
MMSys18 [17]	longitude and latitude in range [-0, 1], origin in top-left corner.	A binary file per video of size 1024×2048.	MP4 format.	A CSV file with the traces of all users per video.	N/A.

TABLE 4.1: Features of the file structure and format of the datasets used in each referenced method.

videos are selected. The second dataset [72] has five videos viewed by 59 users, from which 2 videos are used. From the chosen videos, a segment is selected such that there are one or more events that introduce a new salient region (e.g. a scene change).

MMSys18: We also considered the dataset presented by David et al. in [17] and referred to as MMSys18. It is made of 19, 360° videos of 20 seconds, along with the head positions of 57 participants starting their exploration at a random angular position.

Each dataset has a particular format and schema, some of them store the head position data in language-specific formats (e.g. PAMI18 stores the data in a Matlab-file and MM18 stores the data in a Python dictionary), others store the head position data in text files (e.g. CVPR18 groups the files in a folder per user, MMSys18 uses a Comma-Separated Values (CSV) file per video, while NOSSDAV17 uses a CSV file per user and video). Some datasets contain the saliency maps and the raw videos (MMSys18), others store only the saliency maps (NOSSDAV17, MM18) while others contain only the raw videos in MPEG-4 (MP4) file (PAMI18, CVPR18).

We propose an algorithm that allows to read each of the datasets, with methods to cleanse the data and produce traces in a uniform format, common for all the datasets. The uniform dataset structure is shown in Fig. 4.2. The following command is used to run the analysis on each dataset:

```
python {Fan_NOSSDAV_17, Nguyen_MM_18, Xu_PAMI_18}/Read_Dataset.py -analyze_data
```

Thanks to the analysis on the original datasets, we found that: (i) there are a few missing entries in the PAMI18 dataset, (ii) when re-implementing the tile mapping algorithm from NOSSDAV17, we found that there is a discrepancy in the tiles generated and the tile numbers provided in the dataset, and (iii) when observing the time-stamps in MM18's dataset, most of the traces are splitted and concatenated, and there are intersections between the time-stamps.
By creating this dataset structure, we not only provide ways to read, parse and analyze the different datasets, we also allow to sample the datasets with a common sampling rate (by default 0.2 seconds).
To subsample the datasets, we first transform the head position format from the original dataset to the quaternion representation. Then, we perform the Spherical Linear Interpolation (SLERP) of the rotations (represented as quaternions) with a constant angular velocity, the rotations are interpolated at the rate of 0.2 seconds. Finally we transform the sampled quaternions into Three Dimensional (3D) coordinates. We provide a method on each dataset to visualize the exploration of the user in the unit sphere. For example, to obtain a plot similar to that of Fig. 4.3, the following command can be used:

```
python Fan_NOSSDAV_17/Read_Dataset.py -plot_3d_traces
```

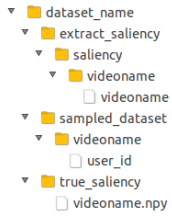

FIGURE 4.2: Uniform dataset file structure

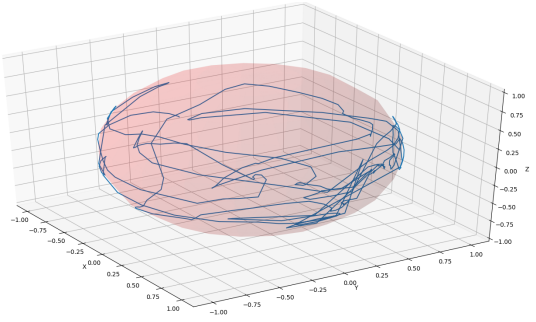

FIGURE 4.3: Exploration of user "45", in video "drive" from NOSSDAV17, represented in the unit sphere.

In our repository [18] we provide a folder "sampled_dataset" for each of the original datasets (NOSSDAV17, CVPR18, PAMI18, MM18 and MMSys18), with a sub-folder per video. Inside, a text file per user stores the head motion trace indicating the time-stamp, followed by the 3D coordinates of the unit vector (x, y, z).
For example, to create the sampled dataset from the original dataset of PAMI18, the command to use is:

```
python Xu_PAMI_18/Read_Dataset.py -creat_samp_dat
```

We also provide functions to plot and verify that the sampling is correctly done. For example, the following command is used to compare the sampled trace against the original trace to get plots similar to Fig. 4.4:

```
python Xu_PAMI_18/Read_Dataset.py -compare_traces
```

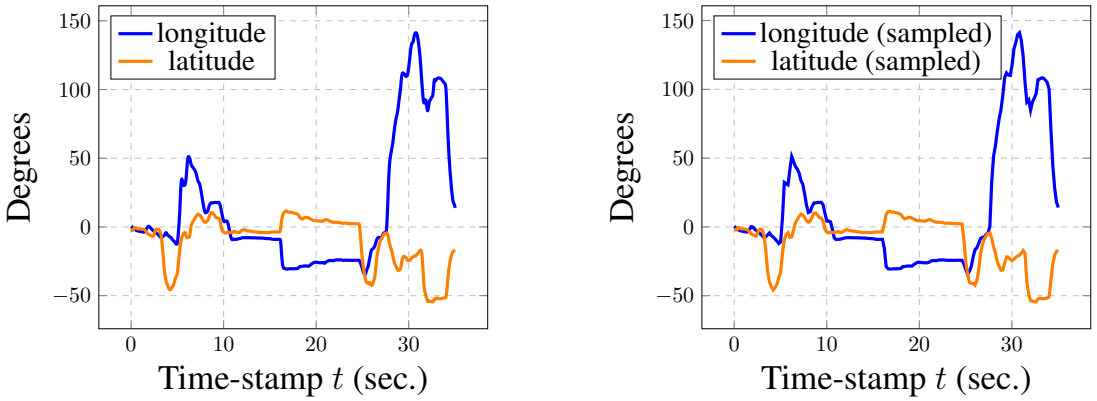

FIGURE 4.4: Comparison between the original trace (left) and the sampled trace (right) for user "m1_21" video "Terminator" in PAMI18 dataset.

4.2.2 Analysis of Head Motion in each Dataset

We provide the code to compute the Cumulative Distribution Function (CDF) of the maximum angular distance from the head position at the start of the prediction window t for different prediction window lengths $H \in 0.2, 0.5, 1, 2, 5, 15$ seconds. The following command can be used to get these plots for each dataset:

```
python DatasetAnalysis/DatasetAnalysis_{CVPR18, MM18, MMSys18, NOSSDAV17, PAMI18}.py
```

The analysis of the plots for each dataset is shown in the next Chapter, Fig. 5.11. This figure shows that in the MMSys18 dataset [17], 50% of the users have shifted their FoV by more than its width (100°) after 5 sec., while in the datasets of CVPR18, NOSSDAV17, MM18 and PAMI18, the percentage is 30%, 20%, 20% and 15%.

4.3 Saliency Extraction

The saliency map is a heatmap (2D distribution) that identifies what are the points in the 360° scene that attract the attention of the viewers the most. Besides the time series of past positions, the saliency map is one of the considered input modalities of the existing head motion prediction methods. Each of these methods extract the visual features in a different way. If we want to fairly compare different methods for head motion prediction, we would need to use the same post-processing to obtain the salient visual features. In our framework, we propose an algorithm to create saliency maps estimated from the video content using the same saliency detection model for all the datasets considered for reproduction and comparison. In a second case, if we want our evaluation to be independent from the imperfection of any saliency prediction model, we use a method based on users' statistics, namely *Ground-Truth (GT) saliency map*. It is the heatmap of the viewing patterns, obtained at each point in time from the users' traces. In this section, we describe how to compute each of these saliency maps using our code.

4.3.1 Ground-Truth Saliency Map

To be independent from the imperfection of any saliency predictor fed with the visual content, we consider here the ground-truth saliency: it is the heat map (2D distribution) of the viewing patterns, obtained at each point in time from the users' traces. To compute the ground-truth saliency maps, we consider the point at the center of the viewport $P^t_{u,v}$ for user $u \in U$ and video $v \in V$ at time-stamp $t \in [0, T]$, where T is the length of the trace.

We can compute the orthodromic distance between the point at the center of the viewport P and each pixel in the equirectangular frame Q using Eq. 4.1.

$$D(P, Q) = \arccos(\vec{P} \bullet \vec{Q}), \tag{4.1}$$

where $\bullet$ is the dot product operation, and $\vec{P}$ are the coordinates in the unit sphere of point P. For a point $P = (x, y)$, where x is the longitude and y is the latitude, the coordinates in the unit sphere are $\vec{P} = (\cos x \cos y, \sin x \cos y, \sin y)$.

For each head position $P^t_{u,v}$, we compute the orthodromic distance $D(\cdot)$ from $P^t_{u,v}$ to each point $Q_{x,y}$ at longitude x and latitude y in the equirectangular frame. Then, we use a modification of the radial basis function (RBF) kernel shown in Eq. 4.2 to convolve the points in the equirectangular frame and obtain the Ground-Truth Saliency (GT_Sal) for user u on video v at time t in image location (x, y):

$$GT\_Sal^t_{u,v,x,y} = \exp\left(-\frac{D(P^t_{u,v}, Q_{x,y})^2}{2\sigma^2}\right), \tag{4.2}$$

where $D(P^t_{u,v}, Q_{x,y})$ is the orthodromic distance, computed using Eq. 4.1. A value of $\sigma = 6°$ is chosen so that the ground-truth saliency maps look qualitatively similar to those of PanoSalNet [3] used in Sec. 5.5.2.

We compute saliency maps $GT\_Sal^t_{u,v}$ per user $u \in U$, video $v \in V$ and time-stamp t by convolving each head position $P^t_{u,v}$ with the modified RBF function in Eq. 4.2. The saliency map at time t of video v is calculated as $GT\_Sal^t_v = \frac{1}{U} \sum_{u \in U} GT\_Sal^t_{u,v}$, where U is the total number of users watching this video.

An example of the ground-truth saliency map is shown in Fig. 4.5. The file Read_Dataset.py under the folder of each dataset contains all the methods to create the ground-truth saliency maps, for example, the command to compute and store the ground-truth saliency maps for David_MMSys_18 dataset is:

```
python David_MMSys_18/Read_Dataset.py -creat_true_sal
```

4.3.2 Content-Based Saliency Maps

To extract saliency maps from the content, we provide the workflow that uses PanoSalNet [71, 3], also considered in MM18. The neural network of PanoSalNet is composed by nine

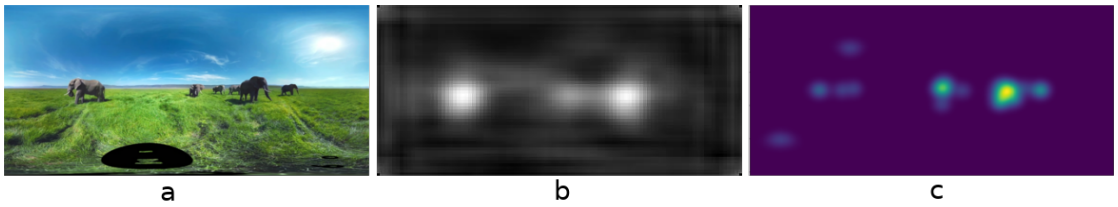

FIGURE 4.5: Saliency maps computed for frame "98" in video "160" from CVPR18 dataset. **a)** Original frame. **b)** Content-based saliency. **c)** Ground-truth saliency.

convolution layers, the first three layers are initialized with the parameters of VGG16 [74], the following layers are first trained on the images of the SALICON dataset [75], and finally the entire model is re-trained on 400 pairs of video frames and saliency maps in equirectangular projection.

To create the Content-Based (CB) saliency maps we first need to transform the videos into scaled images. We provide a executable file to create images from each video with a rate of 5 samples per second (the same sampling rate used to create our "sampled_dataset" from Sec. 4.2). The file for each dataset is:

```
{Xu_CVPR_18, Xu_PAMI_18, David_MMSys_18}/dataset/ creation_of_scaled_images.sh
```

The file panosalnet.py under the folder Extract_Saliency contains the methods to create the content-based saliency maps. As an example, we provide the command to create the saliency map for each frame in each video in CVPR18's dataset:

```
python Extract_Saliency/panosalnet.py -gpu_id 0 -dataset_name CVPR_18
```

However, for the datasets that do not provide the 360° videos, but directly the saliency maps (NOSSDAV17 and MM18), we can create the content-based saliency maps using their provided information. For example, this command can be used for MM18:

```
python Nguyen_MM_18/Read_Dataset.py -creat_cb_sal
```

An example of content-based saliency map is shown in Fig. 4.5.

4.4 Evaluation of Original Methods

We provide the algorithms to run the experiments of PAMI18, CVPR18, MM18, ChinaCom18 and NOSSDAV17 with their original settings, evaluation metrics and datasets. To have a common reference point on each evaluation experiment, we also present how to run two different baselines:

• *trivial-static baseline*: Simple baseline that assumes that the head of the user stays still during the whole prediction horizon, no learning involved.

• *deep-position-only baseline*: Sequence-to-sequence LSTM-based architecture that exploits the time series of past positions only (disregarding the video content), described in detail in Sec. 5.2.

The file *Baselines.py* under the folder of each dataset contains all the methods to run the experimental setup of each of the works for a given method. Depending on the type of result

either a plot or a table is shown at the end of the execution, the results obtained by executing this file are discussed in Chapter 5. The following command can be used to get the results for the *trivial-static baseline* in the experimental setup of MM18:

```
python Nguyen_MM_18/Baselines.py -gpu_id "" -model_name no_motion
```

4.5 Typical Usage of the Head Motion Prediction Framework

Importantly, the software framework we propose enables to prepare a testbed and compare different methods on the same head motion prediction experiment. It therefore eases the assessment of new prediction techniques, and compare them with other existing prediction methods and baselines. Our framework allows to train and evaluate a given prediction model on a chosen dataset, specifying the prediction horizon and history window, among other parameters described below. We first detail the metrics used by each considered method before explaining the formatting of the commands and the available options, and finally developing some examples.

4.5.1 Metrics Used in Each Method

We define below the metrics used for every considered predictor:

• **NOSSDAV17** [2] considers the following metrics:

− *Accuracy*: ratio of correctly classified tiles to the union of predicted and viewed tiles.

− *Ranking Loss*: number of tile pairs that are incorrectly ordered by probability normalized to the number of tiles.

− *F-Score*: harmonic mean of *precision* and *recall*, where *precision* is the ratio of correctly predicted tiles by the total number of predicted tiles, and *recall* is the ratio of correctly predicted tiles by the number of viewed tiles.

Let us point out here that the tile data is not balanced, as more tiles pertain to class 0 (tile $\notin$ FoV) than to class 1 (tile $\in$ FoV) owing to the restricted size of the FoV compared to the complete panoramic size. If we predict all the tiles systematically in class 0, the accuracy already gets to 83.86%. The accuracy is indeed known to be a weak metric to measure the performance of such unbalanced datasets.

• **PAMI18** [1] uses as metric the Mean Overlap (MO) defined as:

$$MO = \frac{A(FoV_p \cap FoV_g)}{A(FoV_p \cup FoV_g)}$$

Where FoV_p is the predicted FoV, FoV_g is the ground-truth FoV, and $A(\cdot)$ is the area of a panoramic region.

• **CVPR18** [5] uses the Intersection Angle Error IAE for each gaze point (θ, φ) and its prediction $(\hat{\theta}, \hat{\varphi})$, defined as $IAE = arccos(\langle P, \hat{P} \rangle)$, where P is the 3D coordinate in the unit sphere:

$P = (x, y, z) = (cos(\theta)cos(\varphi), cos(\theta)sin(\varphi), sin(\theta))$. Let us mention that CVPR18 also considers a deep-position-only baseline. However, ours appears stronger, likely due to the seq2seq architecture. We readily apply our different predictors on the gaze data available in the CVPR18-dataset.

• **MM18** [3] takes the tile with the highest viewing probability as the center of the predicted viewport, and assigns it and all the neighboring tiles that cover the viewport, with label 1. Tiles outside the viewport are assigned 0. Then, the score is computed on these labels as $IoU = TP/TT$ (True Positive TP, True Total TT). The Intersection over Union (IoU): the intersection between prediction and ground-truth of tiles with label 1 (TP) over the union of all tiles with label 1 in the prediction and in the ground-truth (TT).

• **ChinaCom18** [4] uses the Accuracy and F-Score on the labels assigned to each predicted tile.

4.5.2 Training and Evaluation

To train or evaluate a given neural network in a specific dataset and configure some basic settings, the following command can be used:

```
python training_procedure.py -{evaluate, train} -gpu_id GPU_ID -dataset_name
    DATASET_NAME -model_name MODEL_NAME -init_window T_START -m_window M_WINDOW
    -h_window H_WINDOW [-end_window T_END] -exp_folder FOLDER_NAME [-provided_videos]
    -use_true_saliency -metric {orthodromic, mse}
```

Here is the detail of each option:

• **-evaluate/-train:** This option allows to decide if we want to train or evaluate the neural network defined in MODEL_NAME.

• **-gpu_id:** Specify the ID of the Graphics Processing Unit (GPU) to load the neural network, if the parameter is left empty, the neural network will be loaded on the Central Processing Unit (CPU).

• **-dataset_name:** Select the dataset to use with the parameter DATASET_NAME, the options are:
Xu_PAMI_18, Xu_CVPR_18, Fan_NOSSDAV_17, Nguyen_MM_18, Li_ChinaCom_18 and David_MMSys_18.

• **-model_name:** Select the model to train or evaluate, the options are: no_motion, pos_only, CVPR18, MM18, TRACK, among others.

• **-init_window:** In the experiment, the prediction will not be assessed over the first T_START time-stamps of the videos.

• **-m_window:** The neural network takes into account the last M_WINDOW time-stamps from time t, also named history window in Fig. 4.1.

• **-h_window:** The prediction horizon, we try to predict over the following H_WINDOW time-stamps from time t.

• **-end_window:** The prediction is not assessed over the last T_END time-stamps of the videos, by default T_END is equal to H_WINDOW.

• **-exp_folder:** The folder to read the traces. The default value is "sampled_dataset", the folder created when uniformly sampling all datasets in Sec. 4.2.
• **-provided_videos:** Flag to use in case the partition into train and test videos are provided in the original dataset.
• **-use_true_saliency:** Flag that tells whether to use true saliency, if not set, then content-based saliency is used.
• **-metric:** Metric used for the evaluation, by default *orthodromic distance* (orthodromic), but *mean squared error* (mse) can be used too. More metrics can be easily added by filling up the Python dictionary "all_metrics" in the script "Utils.py".

4.5.3 Examples of Usage

We now present a few examples on how to use our framework to get the results for the methods of CVPR18 and MM18 in an experimental setup where the prediction horizon is $H = 5$ seconds, the evaluation metric is the orthodromic distance, using the the ground-truth saliency in the dataset of MMSys18 [17]. In this dataset we have a set of users U and a set of videos V. In the validation stage, there is no intersection between the subsets $U_{train} \times V_{train}$ and $U_{test} \times V_{test}$. This way we make sure that the network does not exploit any information about the behavior of each user, or particular features of a video. All the plots and the analysis of the results are discussed in more detail in Sec. 5.

CVPR18

Since the code of CVPR18 is not publicly available, the neural network of CVPR18 used here is a replica from the description in [5]. In our replica of CVPR18, we decided to prune the Saliency Encoder Module and replace it directly with the ground-truth to be independent from the imperfection of the saliency encoder module fed with the visual content, more details about the replica is given in the Appendix A.5.4. The following command is used to get the results for the replica of the neural network of CVPR18 on our experimental setup, trained and tested with ground-truth saliency maps:

```
python training_procedure.py -evaluate -gpu_id 0 -dataset_name David_MMSys_18
    -model_name CVPR18 -init_window 30 -m_window 5 -h_window 25 -exp_folder
    original_dataset_xyz -provided_videos -use_true_saliency
```

MM18

For the case of MM18, the model and weights are publicly available in [71]. Since the model of MM18 predicts the head orientation at time $t + H$, we had to retrain the model for each prediction step in the prediction horizon, i.e., for each $s \in \{0.2s, 0.4s, \cdots, H = 5s\}$. To get the results for the neural network of MM18 on our experimental setup, using ground-truth saliency maps, use the following command:

```
python training_procedure.py -evaluate -gpu_id 0 -dataset_name David_MMSys_18
    -model_name MM18 -init_window 30 -m_window 15 -h_window 25 -exp_folder
    original_dataset_xyz -provided_videos -use_true_saliency
```

4.6 Conclusions

In this Chapter we presented a framework to evaluate and compare different methods to predict head position in 360° videos. In this framework, we propose an algorithm to create a uniform data structure from each of the heterogeneous datasets evaluated in our work. We described the algorithms used to compute the saliency maps either estimated from the raw video content or from the users' statistics, considering a kernel fitted for the equirectangular projection used to encode 360° videos. To compare each of the head motion prediction settings to a common reference, we detailed the commands to estimate the performance of different approaches in each original evaluation context (prediction horizon, metrics and datasets). Finally, we presented how to use our framework to prepare a testbed to assess comprehensively a new prediction method (on various datasets against several competitors). This software framework therefore contributes to progress towards efficient 360° streaming systems. The entire material (codes, datasets, neural network weights and documentation) is available at [18]. In the following Chapter we present the results of the plots and the analysis obtained by using this framework.

Chapter 5

A Critical Analysis of Deep Architectures for Head Motion Prediction in 360° Videos

In this Chapter, we consider the problem of predicting the user's head motion in 360° videos over a future horizon, based both and only on the past trajectory and on the video content. As introduced in Chapter 4, various methods tackling this problem with deep neural networks have been proposed (e.g., [1, 5, 3, 4, 2]). We show that the relevant existing methods have hidden flaws, that we thoroughly analyze to overcome with a new proposal establishing state-of-the-art performance.

This Chapter is organized as follows: Sec. 5.1 formulates the prediction problem considered, and presents a taxonomy of the studied methods. Sec. 5.2 evaluates these methods against two baselines, the *trivial-static baseline* and the *deep-position-only baseline*. Sec. 5.4 presents the first part of the root-cause analysis by analyzing the data, introducing the *saliency-only baseline*. Sec. 5.5 completes the root-cause analysis by analyzing the architectural choices. Sec. 5.6 presents our reasoning to obtain our new prediction method, TRACK, which establishes state-of-the-art performance. Sec. 5.7 gives perspective and connects our work to most recent critical re-examinations of deep learning-based approaches for other application domains. Sec. 5.8 concludes the Chapter.

5.1 Taxonomy of Existing Head Prediction Methods

This section reviews the existing methods relevant for the problem we consider. We start by formulating the exact problem: it consists, at each video playback time t, in predicting the future user's head positions between t and $t + H$, as illustrated in Fig. 5.1 (also represented in Chapter 4 Fig. 4.1), with the only knowledge of this user's past positions and the (entire) video content. We therefore do not consider methods aiming to predict the entire user trajectory

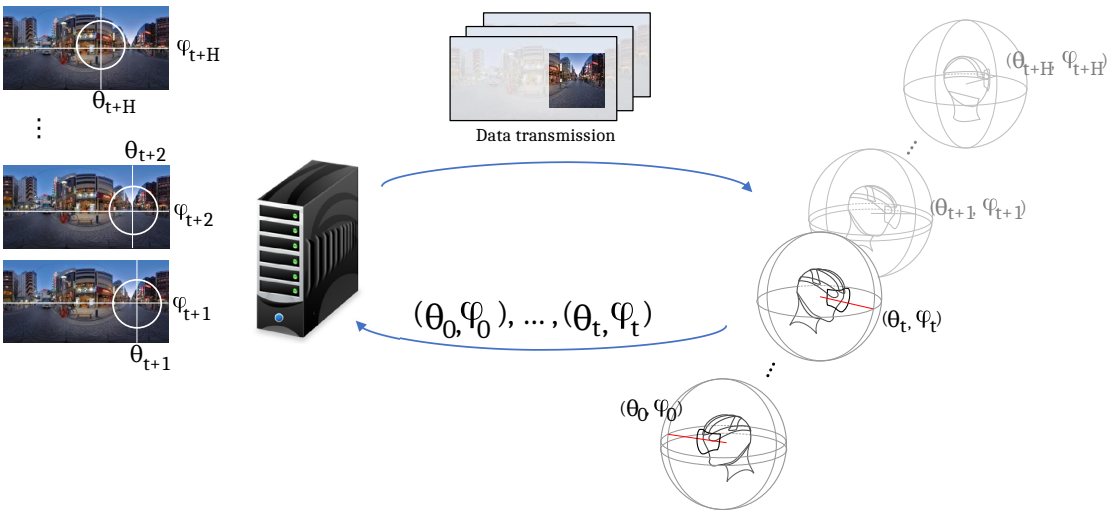

FIGURE 5.1: **360° video streaming principle**. The user requests the next video segment at time t, if the future orientations of the user $(\theta_{t+1}, \varphi_{t+1}), ..., (\theta_{t+H}, \varphi_{t+H})$ were known, the bandwidth consumption could be reduced by sending in higher quality only the areas corresponding to the future FoV.

from the start based on the content and on the starting point as, e.g., targeted by the challenge in [76] or summarizing a 360° video into 2D [77, 78]. As well, and importantly, we consider that the users' statistics for the video are *not* known at test time, hence we do not consider methods relying on these per-video statistics, such as [65, 66]. Also, the domain of egocentric videos is related to that of 360° video. However, the assumptions are not exactly the same: only part of the scene and some regions likely to attract the users are available (video shot from a mobile phone), contrary to a 360° video. We therefore do not compare with such works.

5.1.1 Problem Formulation

In this Chapter we keep the same notation defined in Chapter 4.1.1. Let $\mathbf{P}_t = [\theta_t, \varphi_t]$ denote the vector coordinates of the FoV at time t. Let $\mathbf{V}_t$ denote the considered visual information at time t: depending on the models' assumptions, it can either be the raw frame with each RGB channel, or a 2D saliency map resulting from a pre-computed saliency extractor. Let T be the video duration. The prediction is not assessed over the first T_{start} seconds of video. To match the settings of the works we compare with, T_{start} is set to 0 sec. for all the curves generated in Sec. 5.2. In order to skip the exploration phase, as explained in Sec. 5.4.4, and be more favorable to all methods as they are not able to consider non-stationarity of the motion process, we set $T_{start} = 6$ sec. from Sec. 5.4 onward. Let H be the *prediction horizon* and M be the *history window*. We define the terms *prediction step* s, and video *time-stamp* t, such that: at every *time-stamp* $t \in [T_{start}, T]$, we run predictions $\hat{\mathbf{P}}_{t+s}$, for all *prediction steps* $s \in [0, H]$.

Except for the results in Fig. 5.7, for each s, we average the errors $D(\hat{\mathbf{P}}_{t+s}, \mathbf{P}_{t+s})$ over all $t \in [T_{start}, T]$. As considered in the existing methods we compare with, we make H vary between 0.2 sec. and 2.5 sec., then extend H to 5 sec. as detailed from the analysis in Sec. 5.4.

5.1.2 Taxonomy

As presented in Chapter 4, various approaches to predict user motion in 360° video environments have been published. These methods are organized in Table 5.1. They consider different objectives (col. 2 starting from the left), such as predicting the future head position, gaze position or tiles in the FoV. The prediction horizons (col. 3) also span a wide range, from 30ms to 2.5 seconds. Some articles share common datasets for experiments (col. 4), while generally not comparing with each other. Different types of input and output formats are considered (col. 5): some consider the positional information implicitly by only processing the content in the FoV (PAMI18), other consider the position separately, represented as a series of coordinates (e.g., CVPR18) or as a mask (e.g., MM18), with the last sample only (IC3D17) or various length of history, some extract features from the visual content by employing some pre-trained saliency extractors (e.g. NOSSDAV17, MM18) or training end-to-end representation layers made of convolutional and max-pooling layers (e.g., PAMI18). Finally, most of the methods but the first two in Table 5.1 rely on deep-learning approaches. A key aspect is the way they handle the combination of the positional information (if they consider it individually) with the video content information. As these two types of information are time series, those works all consider the use of deep Recurrent Neural Networks (RNN), and all use Long Short Term Memory (LSTM). However, whether the features are first extracted from each time series independently, or whether the time series samples are first concatenated then fed to a common LSTM, depends on each method. The positioning of the recurrent network in the whole architecture is the multimodality fusion criterion we have selected (col. 6) to order the rows in Table 5.1 (within each group, methods are ordered from the most recently published), thereby extracting 3 groups of methods:

- if the positional information is not explicitly considered, then no combination is made and a single LSTM processes the content of the FoV: PAMI18;
- combination is made after the single LSTM module in CVPR18: the LSTM processes past positions, and its output gets fused with the video features through a fully connected layer (see Fig. 5.2-Right);
- if the current saliency map extracted from the content is first concatenated with the current position information, then the LSTM module handles both pieces of information modalities simultaneously: NOSSDAV17, ChinaCom18, MM18 (see Fig. 5.2-Left).

The architectures tackling this dynamic head motion prediction problem have hence three main objectives: (O1) extracting attention-driving features from the video content, (O2) processing the time series of position, and (O3) combining (fusing) both information modalities to produce the final position estimate. We depict the modules in charge of (O2) and (O3) of methods MM18 and CVPR18 in Fig. 5.2.

Reference	Objective	Prediction horizon	Dataset	Inputs	RNN before/after concatenation of modalities
PAMI18 [1]	head coordinates	30ms	76 videos, 58 users	frame cropped to FoV	N/A (no fusion)
IC3D17 [67]	head coordinates	2s	16 videos, 61 users	Pre-trained sal. in FoV	N/A (no fusion, no LSTM)
ICME18 [68]	tiles in FoV	6s	18 videos, 48 users	Position history, users' distribution	N/A (no LSTM)
CVPR18 [5]	gaze coordinates	1s	208 videos, 30+ users	Video frame, position history as coordinates	before
MM18 [3]	tiles in FoV	2.5s	11 videos, 48+ users from [72, 73] with custom pre-processing	Pre-trained saliency, mask of positions	after
ChinaCom18 [4]	tiles in FoV	1s	NOSSDAV17's dataset	Pre-trained saliency, FoV tile history	after
NOSSDAV17 [2]	tiles in FoV	1s	10 videos, 25 users	Pre-trained saliency, FoV position or tile history	after

TABLE 5.1: Taxonomy of existing dynamic head-prediction methods. References in bold are considered for comparison in Sec. 5.2.

These methods make for a wide range of deep network architectural choices. In particular the fusion problem (O3) may be handled differently. MM18 and CVPR18 are selected as representatives: combining both modalities before or after the recurrent (LSTM) unit, respectively. There is no pairwise comparison between any of the above works. From the articles in Table 5.1, the only works which provided their code and their deep neural networks for reproducibility are PAMI18 and MM18. However, we could obtain all the datasets to compare with all (the datasets not publicly available were kindly shared by the authors whom we have contacted).

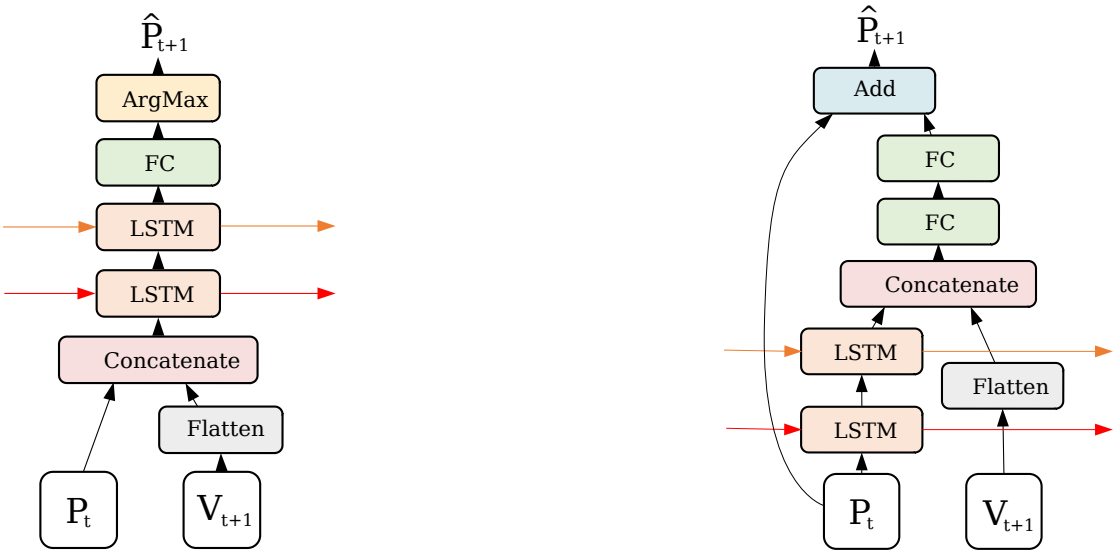

FIGURE 5.2: The building blocks in charge, at each time step, of processing positional information P_t and content information V_t, that are visual features learned end-to-end or obtained from a saliency extractor module (omitted in this scheme). Left: MM18 [3]. Right: CVPR18. [5]

5.2 Comparison of State of the Art Methods Against Two Baselines: Trivial-Static and Deep-Position-Only

To compare the above recent proposals (PAMI18, CVPR18, MM18, ChinaCom18, NOSSDAV17) to a common reference, we first introduce the *trivial-static baseline*. First, we show that all these methods on their original settings, metrics and datasets, are outperformed by this trivial baseline. This is surprising and raises the question of whether it is actually possible to learn anything meaningful with these settings (datasets and prediction horizons). To answer this question, we then introduce the *deep-position-only baseline*, that we design as a sequence-to-sequence LSTM-based architecture exploiting the time series of past positions only (disregarding the video content). We show this new baseline is indeed able to outperform the *trivial-static baseline* (establishing state-of-the-art performance). Later, Sec. 5.4 introduces a *saliency-only baseline*.

5.2.1 Definition of the Trivial-Static Baseline

Different linear predictors can be considered as baselines. We consider here the simplest one which predicts no motion: $\left[\hat{\mathbf{P}}_{t+1}, \ldots, \hat{\mathbf{P}}_{t+H}\right] = \left[\mathbf{P}_t, \ldots, \mathbf{P}_t\right]$.

More complex baselines exist. For example in [79], a Linear Regressor and a Neural Network perform better than the *trivial-static baseline*. However, as we will see in Chapter 5, all existing methods trying to leverage both the video content and the position to predict future positions perform worse than the *trivial-static baseline*, without exception.

5.2.2 Details of the Deep-Position-Only Baseline

We now present an LSTM-based predictor which considers positional information only. An LSTM enables non-linear shape of the motion and the memory effect due to inertia, as discussed in [5] and shown by the generated trajectories in Fig. 5.4. The *deep-position-only baseline* consists of a sequence-to-sequence LSTM-based architecture, with an encoder that processes the history of head positions and a decoder that produces the outputs for the prediction horizon. We select a Sequence-to-Sequence (Seq2Seq) architecture because it has proven powerful at capturing complex dependencies and generating realistic sequences, as shown in text translation for which it has been introduced [80].

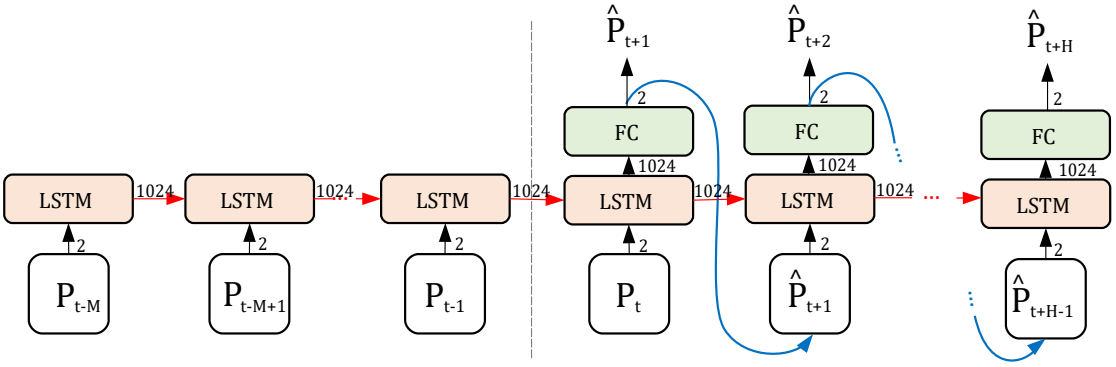

FIGURE 5.3: The *deep-position-only baseline* based on an encoder-decoder (seq2seq) architecture.

As depicted in Fig. 5.3, a seq2seq framework consists of an encoder and a decoder. The encoder receives the *historic window* input (samples from $t-M$ to $t-1$ shown in Fig. 4.1) and generates an internal representation. The decoder receives the output of the encoder and progressively produces predictions over the target horizon, by re-injecting the previous prediction as input for the new prediction time-steps.

The encoder can be represented as:

$$l_t = L(P_t, L(P_{t-1}, L(P_{t-2}, ...L(P_{t-M+1}, L(P_{t-M}, 0))))), \tag{5.1}$$

where l_t is the state of the LSTM at time t.

The decoder can be represented as:

$$\begin{aligned} h_{t+1}, l_{t+1} &= L(\hat{P}_t, l_t)) \\ \Delta\hat{P}_{t+1} &= D_m(h_{t+1}) \times D_d(h_{t+1}) \\ \hat{P}_{t+1} &= \hat{P}_t \bigoplus \Delta\hat{P}_{t+1} \end{aligned} \tag{5.2}$$

A single LSTM $L(\cdot)$ with 1024 units is used for both the encoder and the decoder. At the

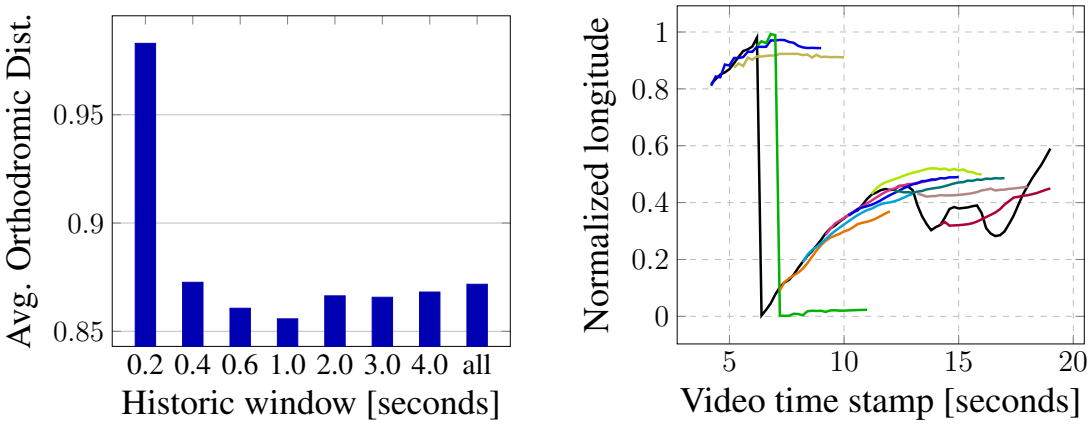

FIGURE 5.4: Left: Impact of the historic-window size. Right: Ground truth longitudinal trajectory (for video "Diner", user 4) is shown in black, colors are the non-linear trajectories predicted by the position-only baseline from each time-stamp t.

decoder, two fully connected layers D_1, D_2 with 2 neurons each are used to predict the magnitude and the direction of the displacement, to compute the new longitude and latitude given the previous position P_t and the displacement $\Delta\hat{P}_{t+1}$, we add the angles with the function $\bigoplus$ that is able to handle the periodicity of the longitude and the latitude, as discussed in Sec. 5.3.1.

How Much Historic Information to Use?: Fig. 5.4-Left shows that the error progressively reduces when increasing the historic window up to 1 sec. Beyond this value, no further improvement is obtained.

Training Settings: During both training and testing, the decoder unit is executed H times in a loop to obtain all the predictions for the time-steps in the prediction horizon. The deep-position-only baseline was developed using Keras and Scikit-Learn. We used Adam optimization algorithm with a learning rate of 0.0005, and we select the best performing model after training for 500 epochs to produce each of the results in this work. The batch size was set to 128.

Generated Trajectories: We finally illustrate the type of head trajectories generated with our baseline. As shown in Fig. 5.4-Right, the network is able to learn non-linear realistic trajectories ($[-180°, 180°]$ is projected onto $[0, 1]$, note that the jump from 1 to 0 only reflects the crossing from $180°$ to $-180°$). We also mention here that we observe the predicted motion tends to vanish over time. This is a well-known drawback of the $l1$-type losses, where the network copes with uncertainty increasing over time by averaging over possible modes, generating vanishing motion or blur, as exhibited for segmentation prediction in [81] and 3D-skeleton pose prediction in [82] (possibly remedied with adversarial losses, out of the scope of this work).

5.2.3 Results of Comparison Against State of the Art

We now present the comparisons of the state of the art methods presented in Sec. 5.1.2 with the *trivial-static baseline* and *deep-position-only baseline* defined above.

We report the exact results of the original articles, along with the results of our baselines, the *deep-position-only baseline* being trained and tested on the exact same train and test subsets of

Method	KingKong	SpaceWar2	StarryPolar	Dancing	Guitar	BTSRun	InsideCar	RioOlympics	Average
PAMI18 [1]	0.809	0.763	0.549	0.859	0.785	0.878	0.847	0.820	0.753
trivial-static baseline	0.974	0.963	0.906	0.979	0.970	0.983	0.976	0.966	0.968
deep-position-only baseline	**0.983**	**0.977**	**0.930**	**0.984**	**0.977**	**0.987**	**0.982**	**0.976**	**0.977**
TRACK	0.974	0.964	0.912	0.978	0.968	0.982	0.974	0.965	0.968
Method	SpaceWar	CMLauncher2	Waterfall	Sunset	BlueWorld	Symphony	WaitingForLove		Average
PAMI18 [1]	0.626	0.763	0.667	0.659	0.693	0.747	0.863		0.753
trivial-static baseline	0.965	0.981	0.973	0.964	0.970	0.968	0.978		0.968
deep-position-only baseline	**0.976**	**0.989**	**0.984**	**0.973**	**0.979**	**0.976**	**0.982**		**0.977**
TRACK	0.965	0.981	0.972	0.964	0.970	0.969	0.977		0.968

TABLE 5.2: Comparison with PAMI18 [1]: Mean Overlap scores of FoV prediction, prediction horizon $H \approx 30ms$ (1 frame). The model TRACK is introduced in Sec. 5.5.2.

	trivial-static baseline		*deep-position-only baseline*		ChinaCom18	
	Accuracy	F-score	Accuracy	F-score	Accuracy	F-score
Hog Rider	96.29%	0.8858	**96.97%**	**0.9066**	77.09%	0.2742
Driving with	95.96%	0.8750	**96.59%**	**0.9843**	77.34%	0.2821
Shark Shipwreck	95.23%	0.8727	**96.12%**	**0.8965**	83.26%	0.5259
Mega Coaster	97.20%	0.9144	**97.71%**	**0.9299**	88.90%	0.7011
Roller Coaster	96.99%	0.9104	**97.50%**	**0.9256**	88.28%	0.6693
Chariot-Race	97.07%	0.8802	**96.91%**	**0.9056**	87.79%	0.6040
SFR Sport	96.00%	0.8772	**96.91%**	**0.9054**	89.29%	0.7282
Pac-Man	96.83%	0.8985	**97.16%**	**0.9089**	87.45%	0.6826
Peris Panel	95.60%	0.8661	**96.54%**	**0.8947**	89.12%	0.7246
Kangaroo Island	95.35%	0.8593	**96.54%**	**0.8954**	82.62%	0.5308
Average	96.15%	0.8840	**96.90%**	**0.9063**	72.54%	0.5155

TABLE 5.3: Comparison with ChinaCom18 [4], prediction horizon $H = 1$ second.

Method	Accuracy	F-Score	Rank Loss
NOSSDAV17-Tile [2]	84.22%	0.53	0.19
NOSSDAV17-Orient. [2]	86.35%	0.62	0.14
trivial-static baseline	95.79%	0.87	0.10
deep-position-only baseline	**96.30%**	**0.89**	**0.09**
TRACK	95.48%	0.85	0.15

TABLE 5.4: Comparison with NOSSDAV17: Performance of Tile- and Orientation-based networks of [2] compared against our *deep-position-only baseline*, prediction horizon $H = 1$ second. The model TRACK is introduced in Sec. 5.5.2.

the original dataset as the original method (there is no training for the *trivial-static baseline*). The benchmark metrics (discussed in Sec. 4.5.1 and related to predicting head or gaze positions, or FoV tiles) are those from the original articles, so are the considered prediction horizons H.

Results for PAMI18 are shown in Table 5.2, for CVPR18 in Fig. 5.5-Bottom, for MM18 in Fig. 5.5-Top, for ChinaCom18 in Table 5.3 and for NOSSDAV17 in Table 5.4. Let us mention that none of these methods considered baselines identical to the *trivial-static baseline* and *deep-position-only baseline* defined above. All perform worse than both our *trivial-static* and *deep-position-only baselines*. Specifically, all but one (CVPR18) perform significantly worse.

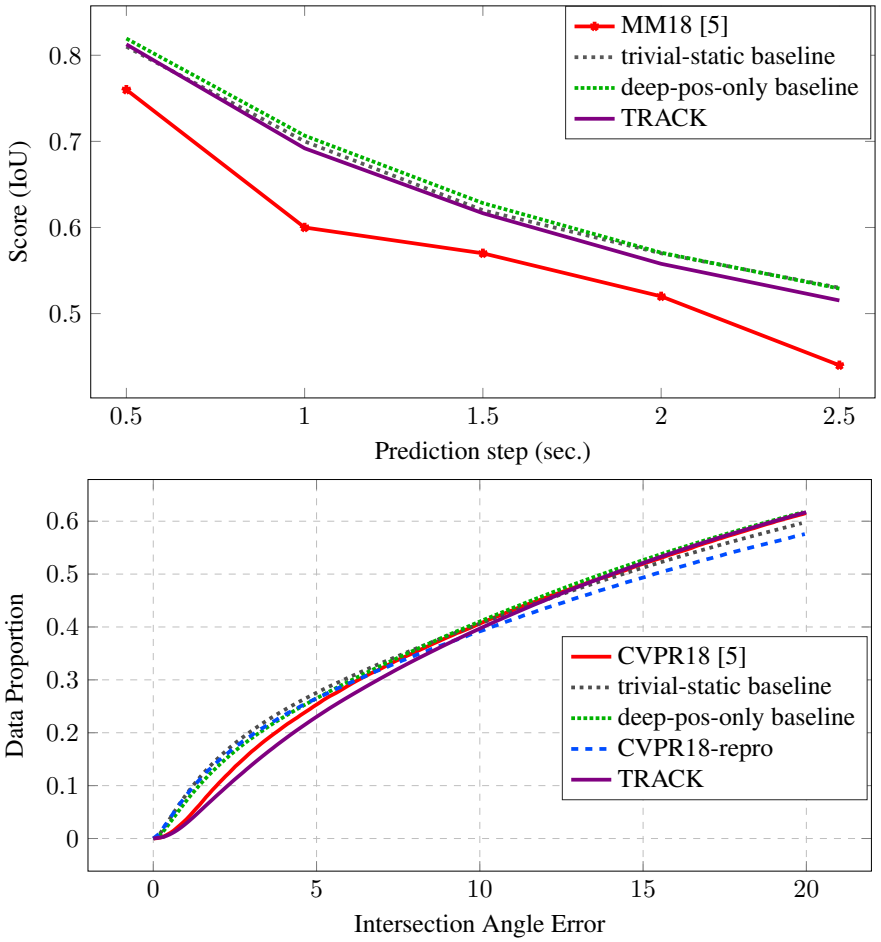

FIGURE 5.5: **Top**: Comparison with MM18 [3], H =2.5 seconds. **Bottom**: Comparison with CVPR18 [5], prediction horizon $H = 1$ sec. CVPR18-repro is introduced in Sec. 5.3.1, the model TRACK in Sec. 5.5.2.

5.3 Root Cause Analysis: the Metrics in Question

We have shown that the existing methods assessed above, which try to leverage both positional information and video content to predict future positions, perform worse than a simple baseline assuming no motion, which in turn can be outperformed by the *deep-position-only baseline* (considering only positional information). This section and the next two (Sec. 5.4 & Sec. 5.5) aim to identify the reasons why the existing approaches perform worse than the baselines. In this part, we focus on the possible causes due to the evaluation, specifically asking:

Q1 Metrics: Can the methods perform better than the baselines for some specific videos or pieces of trajectories?

5.3.1 Evaluation Metrics $D(\cdot)$

Let us first describe the losses and evaluation metrics considered from now on. The prediction of the FoV motion can be cast as a classification problem, where pixels or tiles are classified

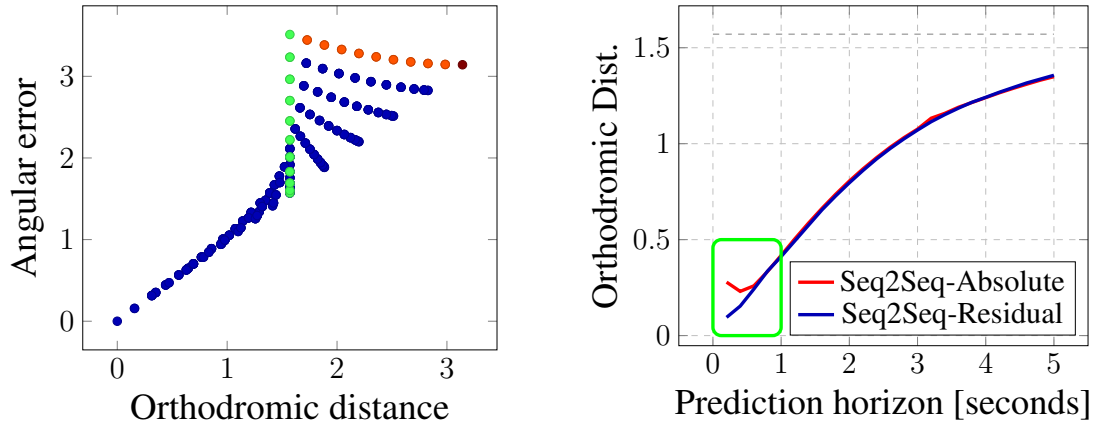

FIGURE 5.6: Left: Relationship between orthodromic distance and angular error. Right: Performance of the network on the MMSys18 dataset when predicting absolute fixation position P_t and when predicting fixation displacement ΔP_t using a residual network, the performance gain when predicting fixation displacement ΔP_t is in the short-term prediction.

in or out of future FoV (as done in NOSSDAV17, MM18, ChinaCom18). However, this problem is inherently imbalanced. Therefore, for the analysis, we choose to keep the original formulation as a regression problem. The tracking problem on a sphere can be assessed by different distances. Given two points on the surface of the unit sphere $P_1 = (\theta_1, \varphi_1)$ and $P_2 = (\theta_2, \varphi_2)$, where θ is the longitude and φ is the latitude of the point, possible distances are:

- Mean squared error $= ((\theta_1 - \theta_2)^2 + (\varphi_1 - \varphi_2)^2)/2$
- Angular error $= \sqrt{\arctan(\sin(\Delta\theta)/\cos(\Delta\theta))^2 + (\varphi_1 - \varphi_2)^2}$, where $\Delta\theta = \theta_1 - \theta_2$
- Orthodromic distance

$= \arccos(\cos(\varphi_1)\cos(\varphi_2)\cos(\Delta\theta) + \sin(\varphi_1)\sin(\varphi_2))$ which is a reformulation of Eq. 4.1.

The latter two metrics are able to handle the periodicity of the latitude, which the first one cannot. The difference between *angular error* and *orthodromic distance* is that the latter computes the distance on the surface of the sphere, while the *angular error* computes the error of each angle independently.

Fig. 5.6-Left shows that the relationship between the *angular error* and the *orthodromic distance* is not bijective, and importantly that the *orthodromic distance* varies rather logarithmically with the *angular error*. The green dots are the points at the pole $P_{pole} = (\theta, \frac{\pi}{2})$ with $\theta \in [-\pi, \pi]$. We observe how the *angular error* as loss function penalizes points that are in the same spot in the surface of the sphere but with different angles (the pole's latitude described a unique point for any longitude). The largest difference in *orthodromic distance* is the antipodal point $P_{antipode} = (\pi, 0)$, while for the *angular error* the largest distance occurs at the poles $P_{pole} = (\pi, \frac{\pi}{2})$. This is shown by the red dots which are all the points $P = (\pi, \varphi)$ with $\varphi \in [0, \frac{\pi}{2}]$. Let us note how the *angular error* increases when the *orthodromic distance* decreases for these points. In general, for a point $P = (\theta, \varphi)$ the *orthodromic distance* decreases and the *angular error* increases when we set θ fixed and move to either of the poles by varying φ from 0 to π (or $-\pi$). Finally, owing to its fitness to the tracking problem on the unit sphere

with latitude and longitude as inputs, we choose the *orthodromic distance* as the train and test metric with the input formatted with longitude and latitude (θ, φ) of the FoV's center.

5.3.2 Q1: Can the Methods Perform Better than the Baselines for Some Specific Pieces of Trajectories or Videos?

The metrics used in Sec. 3 are averages over time trajectories and videos. The question we ask is whether the methods can perform better than the baselines for some specific pieces of trajectories or videos.

5.3.2.1 Specific Pieces of Trajectory

To evaluate whether the existing methods perform better than the baselines in some specific pieces of the trajectory, we adopt the same approach as in [83, Sec. 4], introducing the *Average non-linear displacement error* as a metric to evaluate the error around the non-linear regions of the trajectory where most errors occur owing to human-content interactions. We therefore quantify the *difficulty of prediction* with the second derivative of the trajectory, i.e., the radius of curvature. To obtain detailed results (for each instant of time of each user and video pair), we re-implement CVPR18 with the exact same architectural and training parameters as those described in the article [5].[1]

The curve CVPR18-repro in Fig. 5.5-Bottom shows that we obtain similar results on the original dataset (higher on the first half of the truncated CDF, then slightly lower on the second half of the truncated CDF). This confirms the validity of our re-implementation. Fig. 5.7-Left depicts the distribution of the prediction difficulty. Fig. 5.7-Right shows that for every difficulty range, CVPR18-repro is not able to improve the prediction over the baselines.

We obtained similar qualitative results with MM18, Fig. 5.8-Left depicts the distribution of the prediction difficulty, and Fig.5.8-Right shows that for every difficulty range, MM18 is not able to improve the prediction over the baselines.

Considering CVPR18 and MM18 the two representative and best performing methods in Sec. 3 (apart from the baselines).

We conclude that for more difficult parts of the trajectory, the CVPR18-repro or MM18 methods are not able to improve over the baselines.

5.3.2.2 Specific Videos

Fig. 5.7-Left shows that the majority of the data is in the 0-1 difficulty range, therefore, we can think the models have difficulty to pay attention to the rarer cases of trajectory pieces where the prediction difficulty is higher. To evaluate whether the existing methods perform better than the baselines when the dataset (train and test sets) is properly balanced with videos where the

[1] We had to replicate the architecture of CVPR18 because we could not find any official code and the authors did not reply to our emails. Our reproduced code is available online at [18] and detailed in Appendix A.5.4.

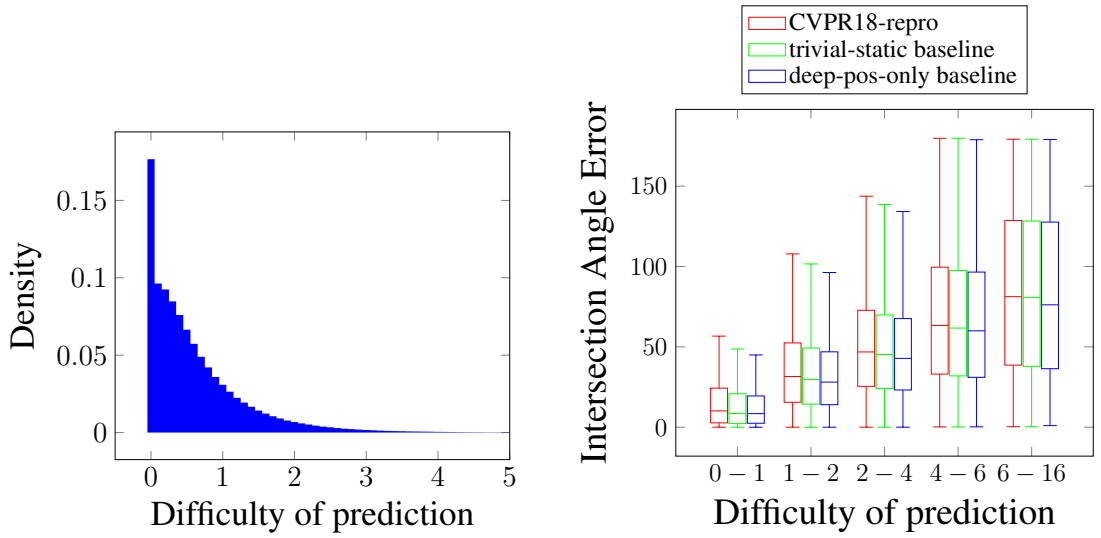

FIGURE 5.7: Left: Distribution of difficulty in the CVPR18 dataset. Right: Error as a function of the difficulty for the CVPR18-repro model.

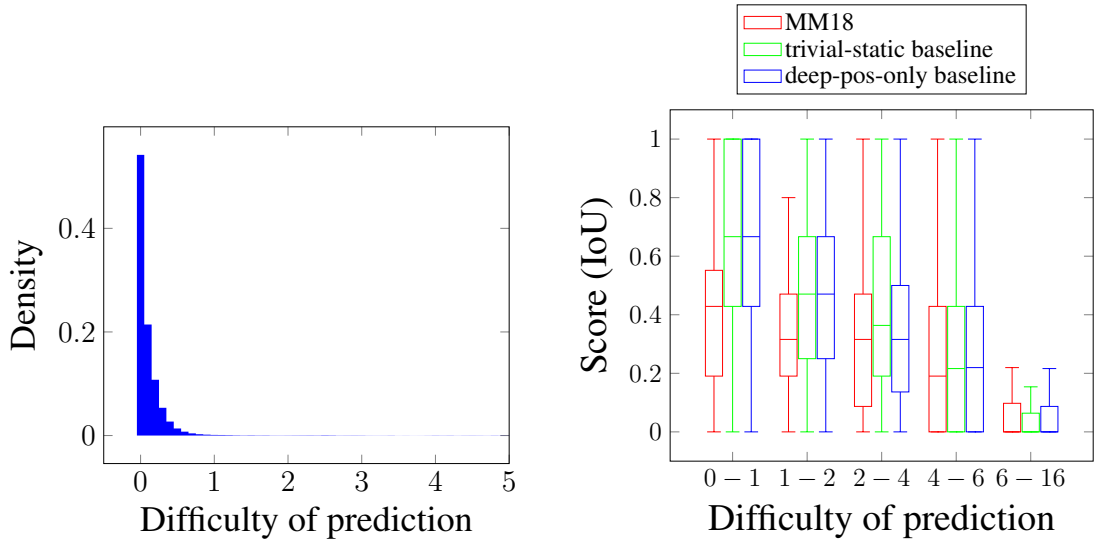

FIGURE 5.8: On the MM18 dataset: (Left) Distribution of difficulty in the dataset. (Right) Score of the MM18 method as a function of the difficulty.

content is proved to help, we consider the dataset prepared in Sec. 5.5.1. The details on the usefulness of the content are given in Sec. 5.4.

The average performance of CVPR18-repro and MM18-repro on this dataset can be seen in Fig. 5.17: they are never able to take advantage of the content as they are systematically outperformed by the *deep-position-only baseline*.

Fig. 5.9 shows the performance of CVPR18-repro and MM18-repro on the MMSys18 dataset per test video. It is important to mention that both models are fed with Ground Truth (GT) saliency. The results show that these methods are not able to take advantage of the content as they are outperformed, over the entire prediction horizon 0s-5s, by the *deep-position-only baseline* even for the videos where the saliency is proved useful (Sec. 5.4.2).

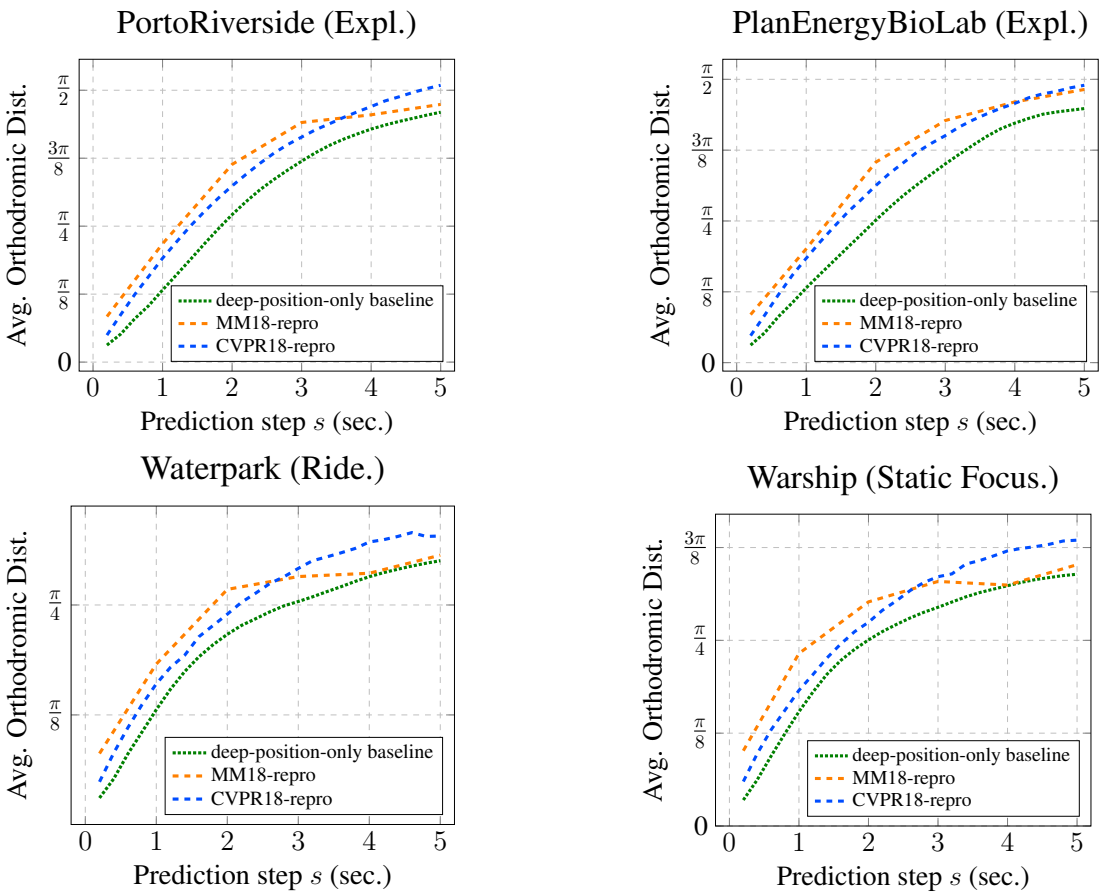

FIGURE 5.9: Prediction error results for MM18-repro, CVPR18-repro and *deep-position-only baseline*, detailed for each test video of the MMSys18 dataset. The results of MM18-repro and CVPR18-repro obtained with Ground Truth (GT) saliency.

Answer to Q1: No, the methods considering the video content do not perform better than the *deep-position-only baseline* for specific pieces of trajectories or videos where the knowledge of the content should improve the prediction.

5.4 Root Cause Analysis: the Data in Question

In this section, we focus on the possible causes due to the data. In Sec. 5.5, we analyze the possible architectural causes. This section therefore aim to answer question Q2, whose answer is provided at the end of the section:

Q2 Data: Do the datasets (made of videos and motion traces) match the design assumptions the methods build on?

To answer Q2, we consider the assumptions at the core of the existing architectures attempting to leverage the knowledge of position history and video content, and break them down into :

- Assumption (A1): the position history can inform the prediction of future positions

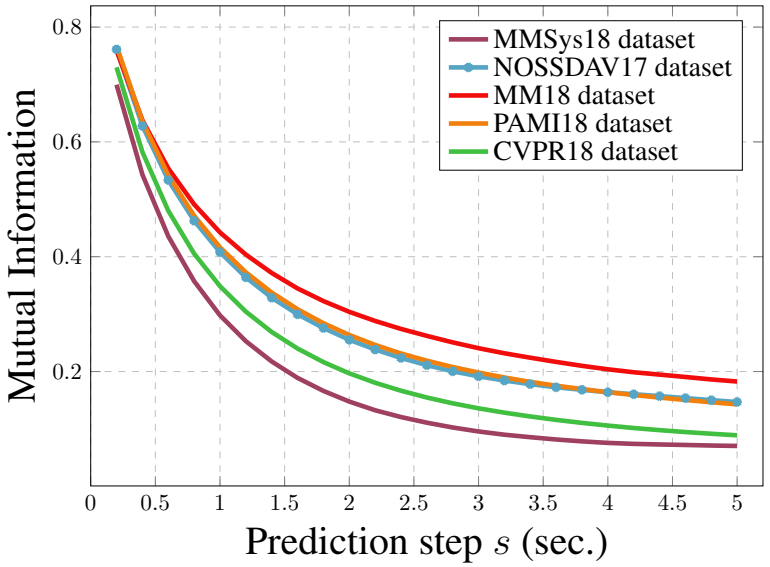

FIGURE 5.10: Mutual information $MI(P_t; P_{t+s})$ between P_t and P_{t+s} (averaged over t and videos) for all the datasets used in NOSSDAV17, PAMI18, CVPR18 and MM18, with the addition of MMSys18.

- Assumption (A2): the visual content can inform the prediction of future positions

We identify whether these assumptions hold in the datasets and settings considered by the existing methods (Sec. 5.4.1 and 5.4.4), and introduce a new *saliency-only baseline* to do so (Sec. 5.4.2).

5.4.1 Assumption (A1): the Position History is Informative of Future Positions

The amount of information held by a process about another one can be quantified by the Mutual Information (MI). This in turns informs on the degree of predictability of the target process using the first process. MI has been used in [84] for inter-user analysis. Here, we define the MI between head positions of a given user at time t and $t+s$ by $MI(P_t; P_{t+s}) = D_{KL}(Pr[P_t, P_{t+s}]||Pr[P_t] \bigotimes Pr[P_{t+s}])$, where $D_{KL}(\cdot)$ and $\bigotimes$ stand for the Kullback–Leibler divergence and convolutional product, respectively. For each of the datasets considered in PAMI18, CVPR18, MM18, NOSSDAV17, and MMSys18, Fig. 5.10 represents MI normalized and averaged over all videos and time stamp t, as a function of $s \in [0, H = 5sec.]$. The 2D-coordinates have been discretized in 128 bins. This figure shows that position at time $t+s$ can be predicted to a significant degree by P_t when s is low (e.g., lower than 2 sec.). As expected, the further away the prediction step, the lowest the predictability of P_{t+s} from P_t.

To relate Mutual Information with a more intuitive characterization of the datasets, we consider the motion continuity (inertia). Fig. 5.11 represents the Cumulative Distribution Function (CDF) of the displacement within each prediction horizon $H = 0.2s, \ldots, 15s$ for the datasets considered in PAMI18, CVPR18, MM18, NOSSDAV17, and MMSys18. Each point (x, y) on a curve represents the fraction y of samples (among users' traces) for which the displacement

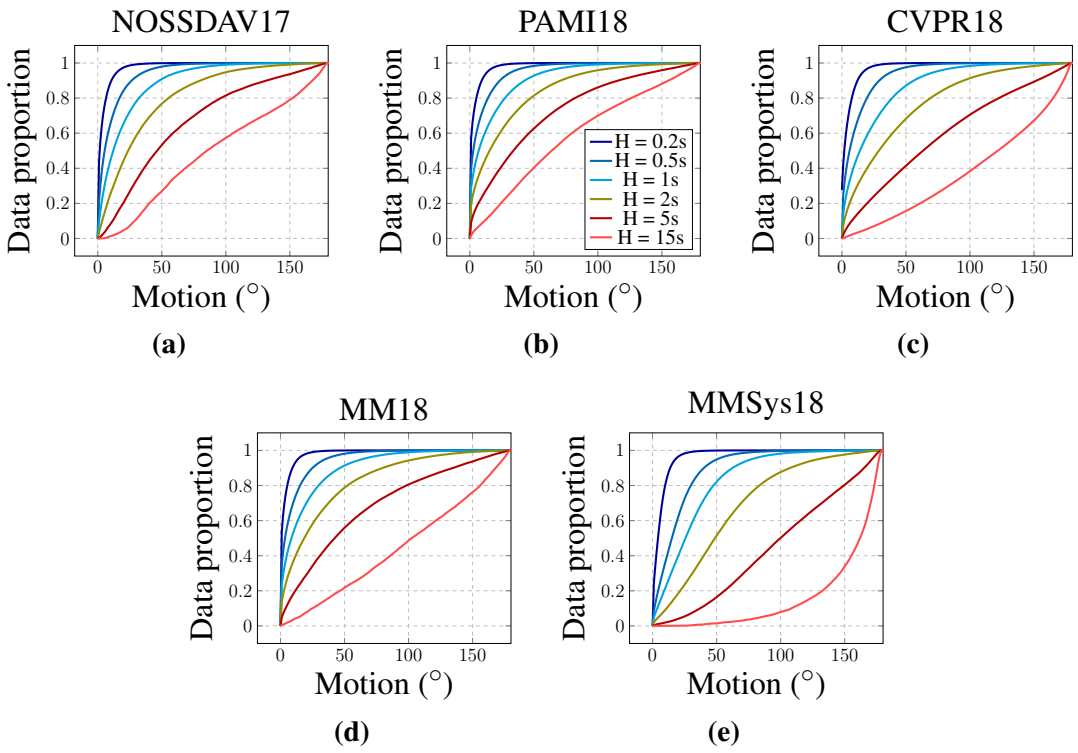

FIGURE 5.11: Motion distribution of the 4 datasets used in **(a)** NOSSDAV17, **(b)** PAMI18, **(c)** CVPR18 and **(d)** MM18, respectively. In **(d)** we show the distribution of the MMSys18 dataset from [17] and considered in the sequel. The x-axis corresponds to the motion from position at t to $t + H$ in degrees. Legend is identical in all sub-figures.

within H seconds has been less than x degrees. If we consider a FoV to be about 100° wide [2], Fig. 5.11 informs on how many seconds it takes for the FoV to shift by at least half of its width for half of the samples. It takes respectively at least 5 seconds for all but CVPR18 (the data of CVPR18 is the eye gaze positions), and for the MMSys18 dataset from [17] for which it takes about 2s. Over the considered forecast window in each of the experiments of PAMI18, CVPR18, MM18 and NOSSDAV17, the FoV has shifted by half of its width for less than 0.5%, 5%, 5% and 7% of the samples, respectively. These last datasets have therefore a low amount of motion.

Does Assumption (A1) hold?: On the datasets and prediction horizons considered in the literature ($H \leq 2$ sec.), the position history is therefore strongly informative of the next positions. Another element supporting this observation is the best performance obtained by our baseline exploiting position only (see Sec. 5.2 above). A similar study was conducted in [79] showing that the viewer motion has a strong temporal auto-correlation.

5.4.2 Definition of the Saliency-Only Baseline

To analyze Assumption A2 in Sec. 5.4.4 and assess how much gain can the consideration of the content bring to the prediction, we first define a so-called *saliency-only baseline*. This baseline is defined from an attentional heat map, either extracted from the visual content (heat

map then named Content-Based saliency) or directly from the position data of all the users (heat map then named Ground-Truth saliency). For either type of heat map, the *saliency-only baseline* provides an upper-bound on the prediction error that a more refined processing of the heat map, in combination with the past positions, would make. In this section, we only consider heat maps obtained from the users data, we therefore start by defining such heat maps. Only in Sec. 5.5.2 do we use the heat maps estimated from the video content.

5.4.2.1 Definition of the K-Saliency-Only Baseline

We extract the K highest peaks of the heat map for every prediction step $t+s$ (for all t, for all $s \in [0, H]$). At every $t+s$, the *K-saliency-only baseline* predicts $\hat{\mathbf{P}}_{t+s}$ as the position of the peak, amongst the K peaks, which is closest to the last known user's position $\mathbf{P}_t$.

Fig. 5.12 and 5.13 show the prediction error of the *K-saliency-only baseline* for $K = 1$, 2, 5. For low s, we verify that the higher K, the lower the error close to time t, because the more the number of points of interest possibly considered. However, as the prediction step s increases and $t+s$ gets away from t, the error is lower for lower K. Indeed, if the user moves, then she is more likely to get closer to a more popular point of interest, that is to a higher-ranked peak.

Each ***K-saliency-only baseline*** can be considered as an upper-bound on the error that the best predictor optimally combining position and content modality could get. Therefore, for a given κ, we define the *saliency-only baseline* as the minimum of these *K-saliency-only baseline*, for $K \in [1, \kappa]$ and for every s in $[0, H]$. In this Chapter, we set $\kappa = 5$. The *saliency-only baseline* is shown in red in Fig. 5.16. From Fig. 5.16, we do not represent the *K-saliency-only baselines* anymore, but only the *saliency-only baseline*.

5.4.3 Background on Human Attention in VR

Before analyzing Assumption (A2), let us first provide some characteristics of the human attention in VR identified recently. It has been recently shown in [35] and [8] that, when presented with a new VR scene (the term "scene" is defined by Magliano and Zacks in [85] as a period of the video between two edits with space discontinuity), a human first goes through an exploratory phase that lasts for about 10 to 15 sec. ([8, Fig. 18], [35, Fig. 2]), before settling down on so-called Regions of Interest (RoIs), that are salient areas of the content. The duration and amplitude of exploration, as well as the intensity of RoI fixation, depend on the video content itself. Almquist et al. [8] have identified the following main video categories for which they could discriminate significantly different users' behaviors: *Exploration, Static focus, Moving focus* and *Rides*. In *Exploration* videos, the spatial distribution of the users' head positions tends to be more widespread, making harder to predict where the users will watch and possibly focus on. *Static focus* videos are made of a single salient object (e.g., a standing-still person), making the task of predicting where the user will watch easier in the focus phase. In *Moving focus* videos, contrary to *Static focus* videos, the RoIs move over the sphere and hence

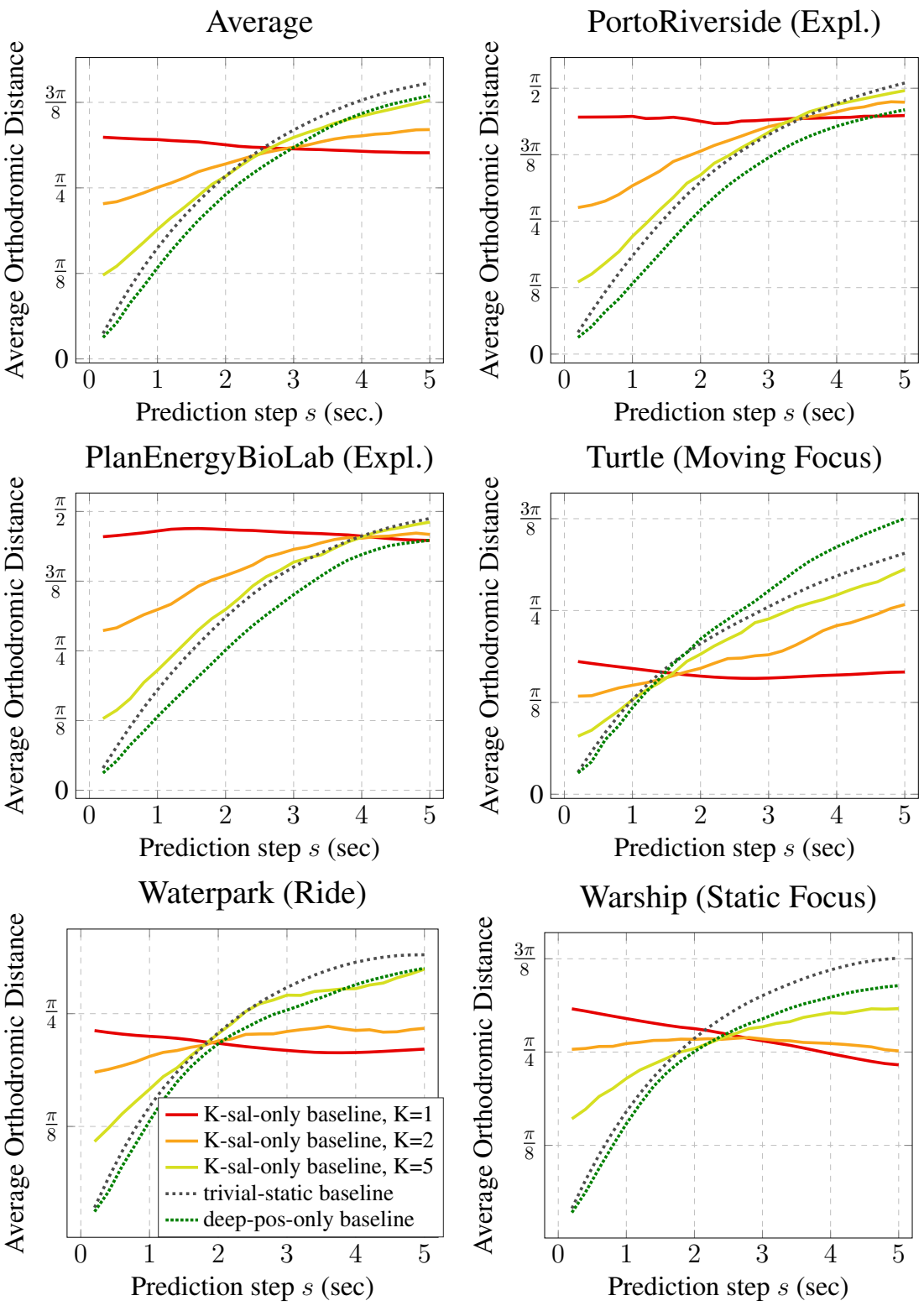

FIGURE 5.12: Prediction error on the MMSys18 dataset. The *deep-position-only baseline* is tested on the 5 videos above, and trained on the others (see Sec. 4.5.3 or [18]). Top left: Average results on all 5 test videos. Rest: Detailed result per video category (Exploration, Moving Focus, Ride, Static Focus). Legend is identical in all sub-figures.

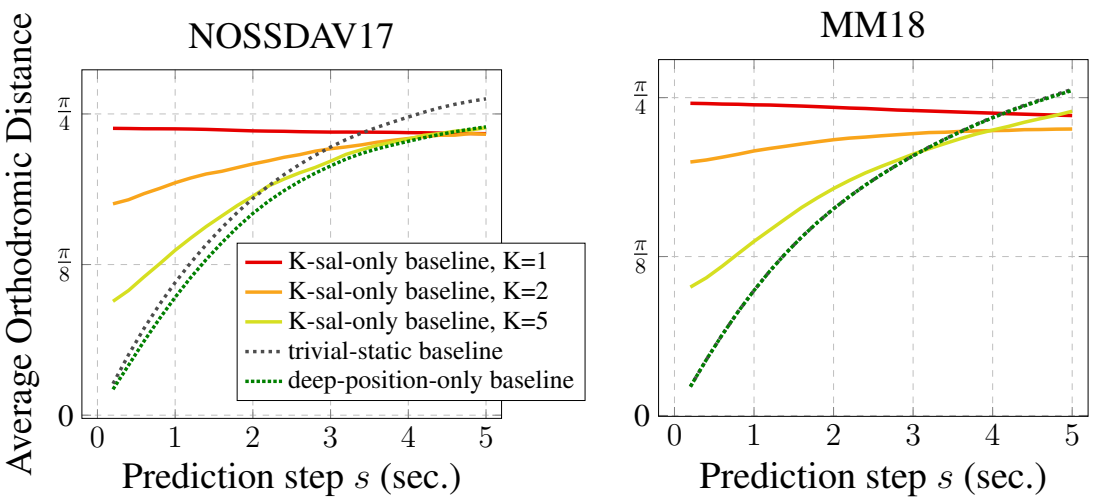

FIGURE 5.13: Prediction error averaged on test videos of the datasets of NOSSDAV17 (left) and MM18 (right). We refer to the description in Appendix A or [18] for the train-test video split used for the *deep-position-only baseline* (identical to original methods). Legend is identical in both sub-figures.

the angular sector where the FoV will be likely positioned changes over time. *Rides* videos are characterized by substantial camera motion, the attracting angular sector being likely that of the direction of the camera motion.

5.4.4 Assumption (A2): the Visual Content is Informative of Future Positions

We now analyze whether this assumption (A2) holds, and for which settings (datasets, prediction horizons). As for (A1), we first quantify how much additional information can be gained on P_{t+s} by knowing the visual content V_{t+s} at time $t+s$, given we already know the past positions. This corresponds to the conditional MI $MI(P_{t+s}; V_{t+s}|P_t)$, also named Transfer Entropy (TE) and satisfying for every video: $TE_{V\to P}(t,s) = MI(P_{t+s}; V_{t+s}|P_t) = H(P_{t+s}|P_t) - H(P_{t+s}|P_t, V_{t+s})$, where $H(\cdot)$ denotes the entropy. TE has been used in [84] but not with saliency data. Fig. 5.14 represents $TE_{V\to P}(t,s)$ averaged over all time stamps t and videos of every dataset. The 2D-coordinates have been discretized in 128 bins and V_{t+s} is taken as the Content-Based saliency defined in Sec. 5.5.2, the probability values being discretized into 256 bins. The TE values cannot be compared across the datasets, but the important observation is that the TE value triples from $s = 0$ to $s = 5$ sec. It shows that the predictability of future positions from the content, conditioned on the position history, is initially low then increases with s. The results of MI in Fig. 5.10 and TE in Fig. 5.14 therefore show that short-term motion is mostly driven by inertia from t, while the content saliency may impact the trajectory in the longer-term. To cover both short-term and long-term, we set the prediction horizon $H = 5$ sec.. We confirm this and better quantify the durations of both phases for the different video categories in the next results. We analyze A2 on the datasets used in NOSSDAV17, MM18, CVPR18 and PAMI18. We also consider an additional dataset, referred to as MMsys18-dataset

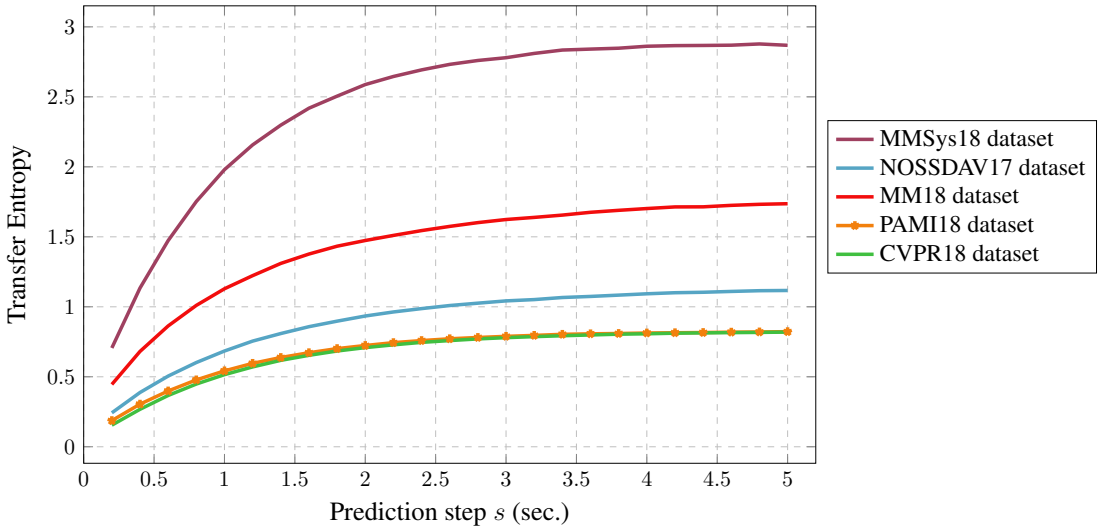

FIGURE 5.14: Transfer Entropy (TE) $TE_{V \to P}(t, s)$ between V_{t+s} and P_{t+s} (averaged over t and videos) for all the datasets used in NOSSDAV17, PAMI18, CVPR18 and MM18, with the addition of MMSys18.

[17]. All these datasets are detailed in Sec. 4.2.1. In MMsys18-dataset, the authors show that the exploration phase in their videos lasts between 5 and 10s, and show that after this initial period, the different users' positions have a correlation coefficient reaching 0.4 [17, Fig. 4]. This dataset is made of 12 Exploration videos, 4 Static focus videos (Gazafisherman, Sofa, Mattswift, Warship), 1 Moving focus video (Turtle) and 2 Ride videos (Waterpark and Cockpit). Fig. 5.12, 5.13, 5.16 and 5.15 depict the prediction error for prediction steps $s \in [0, H = 5 \text{ sec.}]$, obtained with the *deep-position-only baseline* and *saliency-only baseline* on the 4 previous datasets. We remind that each point for every given step s, is an average over all the users and all time-stamp $t \in [T_{start}, T]$, with T the video duration and $T_{start} = 6$ sec. from now on to skip the initial exploration phase (presented right above in the beginning of this Sec. 5.4.4) and ensure that the content can be useful for all time-stamps t. By analyzing the *saliency-only baseline* for every prediction step s (saliency baseline in red in Fig. 5.16), the same phenomenon can be observed on all the datasets: the *saliency-only baseline* has a higher error than the *deep-position-only baseline* for prediction steps s lower than 2 to 3 seconds. This means that there is no guarantee that the prediction error over the first 2 to 3 seconds can be lowered by considering the content. After 2 to 3 sec., on non-Exploration videos, we can see that relevant information can be exploited from the heat maps to lower the prediction error compared to the *deep-position-only baseline*. When we isolate the results per video type, e.g., in Fig. 5.12, for Exploration (PortoRiverside, PlanEnergyBioLab), a Ride (WaterPark) a Static focus (Warship) and a Moving focus (Turtle) videos, we observe that the saliency information can significantly help predict the position for prediction steps beyond 2 to 3 seconds.

We therefore conclude by answering

Q2 Data: Do the datasets (made of videos and motion traces) match the design assumptions

the methods build on?

5.4.5 Q2: Do the Datasets (Made of Videos and Motion Traces) Match the Design Assumptions the Methods Built on?

Answer to Q2:
• Study of MI for assumption A1 confirms that the level of predictability of short-term position from past position is significant, corresponding to the inertia effect and frequent low velocity in some datasets.
• Considering the ground-truth saliency (attentional heat maps), we conclude on A2 by stating that considering the content in the prediction can significantly help for non-Exploration videos if the prediction horizon is longer that 2 to 3 sec.. There is no guarantee it can significantly or easily help for shorter horizons. All the selected existing works considered prediction horizons lower than 2.5 sec., making it very unlikely to outperform the *deep-position-only baseline*.

Having shown it is difficult to outperform the *deep-position-only baseline* on these short horizons, next we investigate why most existing methods are however not able to match its performance.

5.5 Root Cause Analysis: the Architectures in Question

In Sec. 5.4, we have analyzed the possible causes for the weakness of the existing predictors, related to the metrics and the assumptions on the dataset. As they do not suffice to explain the counter-performance of the existing methods compared with single-modality baselines, in this section, we state and analyze the possible architectural causes. Let us recall the three main objectives a prediction architecture must meet, as stated in Sec. 5.1.2: (O1) extracting attention-driving features from the video content, (O2) processing the time series of position, and (O3) fusing both information modalities to produce the final series of position estimates. Note that this is a conceptual description, and does not necessarily correspond to a processing sequence: fusion (O3) can be performed from the start and O1 and O2 may not be performed in distinguishable steps or elements, as it is the case in NOSSDAV17 or MM18.

The main interrogation is: Why does the performance (of existing predictors compared with baselines) degrade when both modalities are considered? To explore this question from the architectural point of view, we divide this in two intermediate questions *Q3* and *Q4*.

Q3 on ground-truth saliency: If O1 is solved perfectly by providing the ground-truth saliency, what are good choices for O2 and O3?
That is, in comparison with the baselines considering each modality individually, choices whose

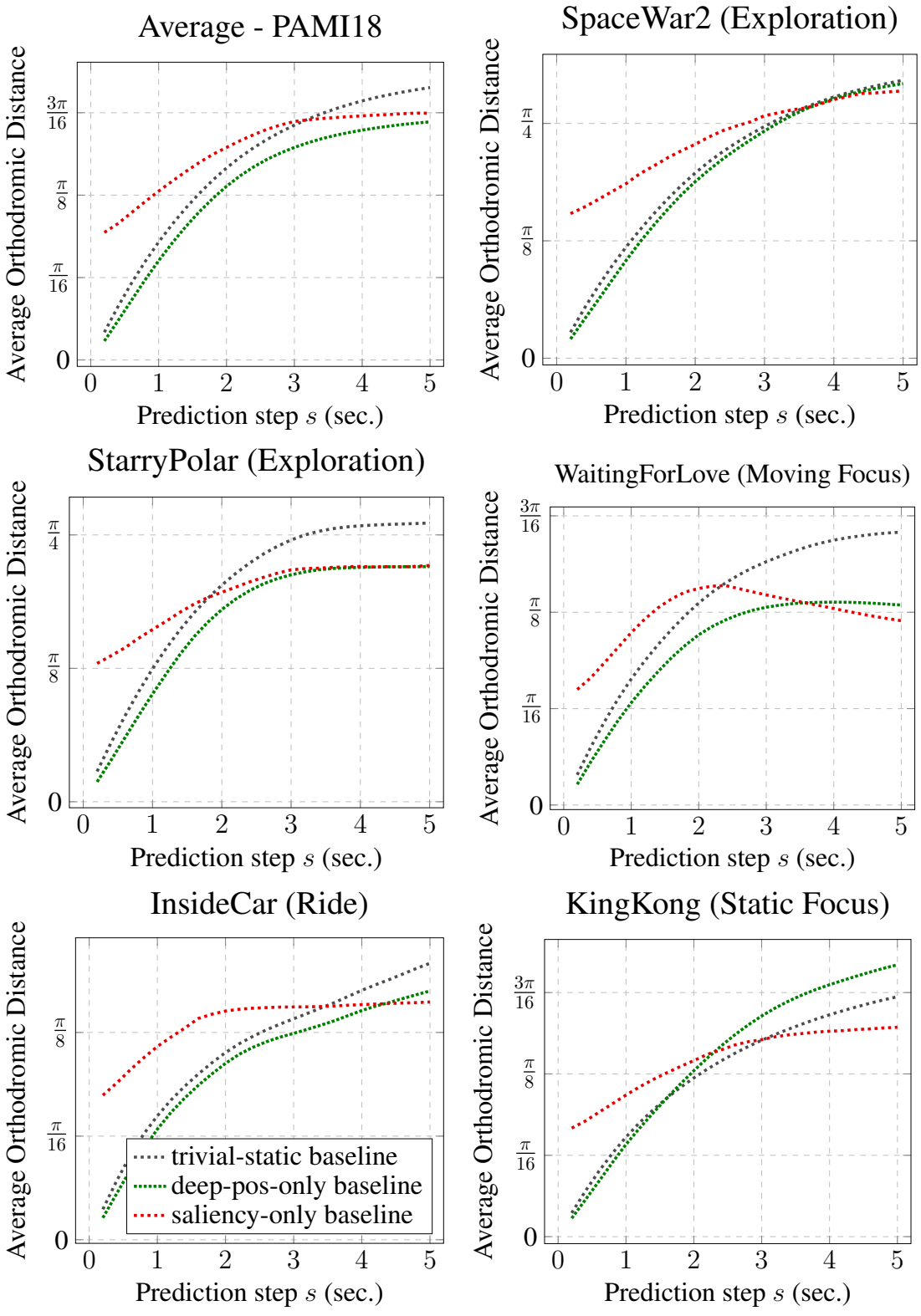

FIGURE 5.15: Prediction error on the dataset of PAMI18. We refer to the description in Appendix A.1 or [18] for the train-test video split used for the *deep-position-only baseline* (identical to original method). Top left: Average on test videos. Rest: Results per video category (Exploration, Moving Focus, Ride, Static Focus). Legend is identical in all sub-figures.

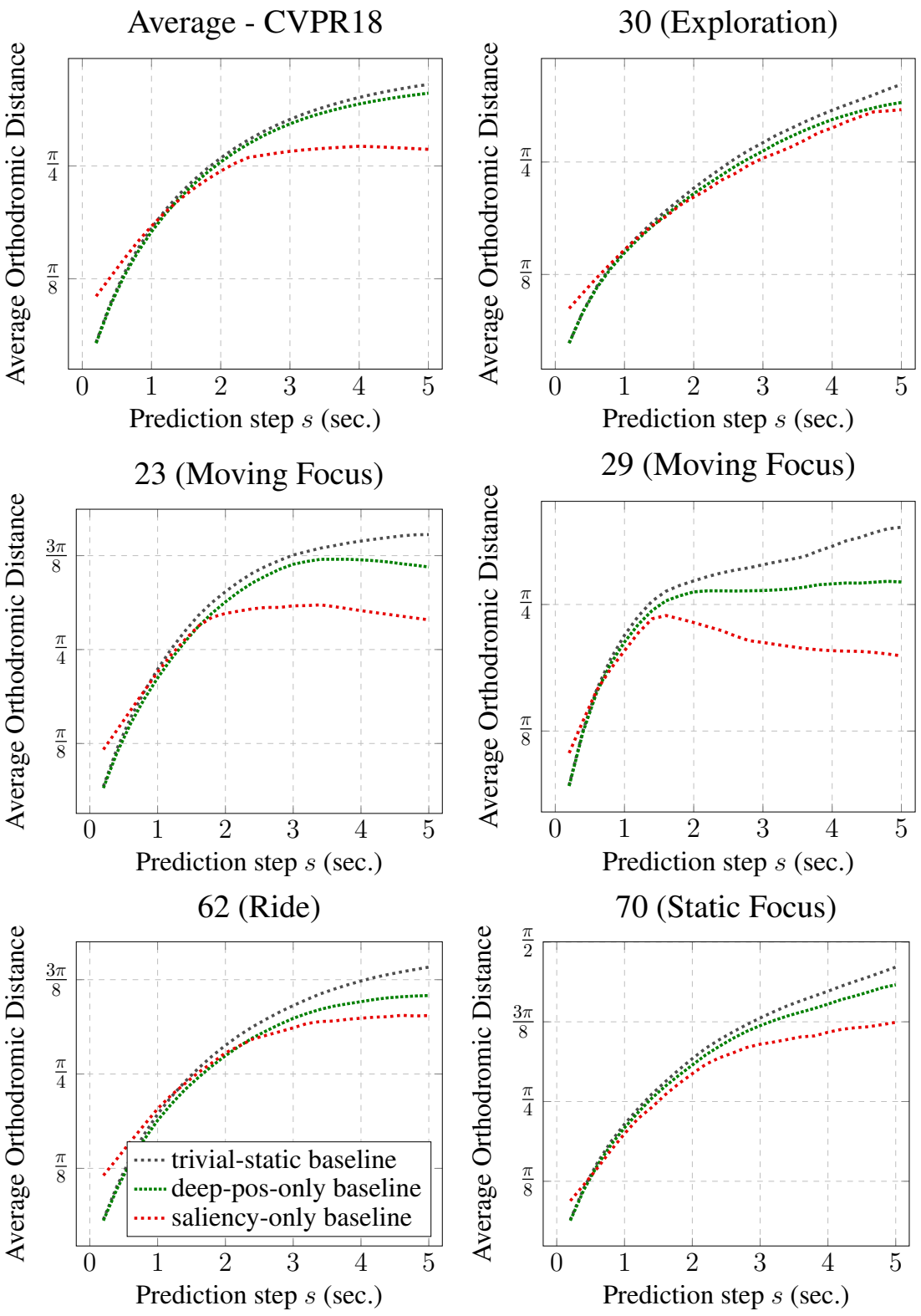

FIGURE 5.16: Prediction error on the dataset of CVPR18. We refer to the description in Appendix A.5 or [18] for the train-test video split used for the *deep-position-only baseline* (identical to original method). Top left: Average on test videos. Rest: Results per video category (Exploration, Moving Focus, Ride, Static Focus). Legend is identical in all sub-figures.

performance improves, or at least does not degrade, when considering both information modalities.

5.5.1 Answer to Q3 - Analysis with Ground-Truth Saliency

In our taxonomy in Sec. 5.1.2, we have distinguished the prediction methods that consider both input modalities, based on the way they handle the fusion: either both position and visual information are fed to a single RNN, in charge of at least O3 and O2 at the same time (case of MM18, ChinaCom18, NOSSDAV17), or the time series of positions are first processed with a dedicated RNN, the output of which then gets fused with visual features (case of CVPR18). To answer Q3, we consider their most recent representatives: the building blocks of MM18 and CVPR18 (see Fig. 5.2). We still consider that O1 is solved perfectly by considering the ground-truth saliency introduced in Sec. 5.4.4.

Prediction horizon: From the answer to Q2, we consider the problem of predicting head positions over a prediction horizon longer than the existing methods (see Table 5.1), namely 0 to $H = 5$ seconds. This way, both short-term where the motion is mostly driven by inertia at t, and long-term where the content saliency impacts the trajectory, are covered.

Dataset: Given the properties of MMSys18-dataset, where users move significantly more (see Sec. 5.4.1) and which comprises different video categories (introduced in Sec. 5.4.4), we select this dataset for the next experiments investigating the architectures. In particular, we draw a new dataset out of MMSys18-dataset, selecting 10 train and 4 test videos by making sure that the sets are balanced between videos where the content is helpful (Static focus, Moving focus and Rides) and those where it is not (Exploration). Specifically, the train set is made with 7 Exploration videos, 2 Static Focus and 1 Ride, while the test set has 2 Exploration, 1 Static focus and 1 Ride videos. This number of videos is equivalent to the dataset considered in MM18, ChinaCom18 and NOSSDAV17 (10). This dataset is therefore challenging but also well fitted to assess prediction methods aiming to get the best out of positional and content information.

Auto-regressive framework: Our re-implementation of CVPR18, named CVPR18-repro, has been introduced in Sec. 5.3.1. For MM18, we use the code provided by the authors in [71]. The evaluation metric is still the orthodromic distance as exposed in Sec. 5.4.4. We make three modifications to CVPR18 and MM18 (shown in Fig. 5.2), which we refer to as CVPR18-improved and MM18-improved, respectively. **First**, as for our *deep-position-only baseline*, we add a sequence-to-sequence auto-regressive framework to predict over longer prediction windows. We therefore embed each MM18 and CVPR18 building blocks into the sequence-to-sequence framework. It corresponds to replacing every LSTM cell in Fig. 5.3 with the building blocks represented in Fig. 5.2. **Second**, we train them with the mean squared error based on 3D Euclidean coordinates $(x, y, z) \in \mathbb{R}^3$. This helps the convergence with a seq2seq framework handling content, which is likely due to the removal of the discontinuity of having to use a modulo after each output in the training stage when Euler angles are considered. With 3D Euclidean

coordinates, the projection back onto the unit sphere is made only at test time. We however retain the orthodromic distance as the benchmark metric. **Third**, instead of predicting the absolute position as done by MM18, we predict the displacement (motion). This corresponds to having a residual connection, which helps to reduce the error in the short-term, as also identified by [82]. Specifically for the MM18 block, we also change (1) the saliency map that we grow from 16×9 to 256×256, and (2) the output, i.e. the center of the FoV, which is defined by its (x, y, z) Euclidean coordinates.

Training: We train each model for 500 epochs, with a batch size of 128, with Adam optimization algorithm with a learning rate of 0.0005 and the mean squared error based on 3D Euclidean coordinates $(x, y, z) \in \mathbb{R}^3$ as loss function.

Results: Fig. 5.17 shows the improved models of MM18 and CVPR18 perform better than the original models. It also shows that MM18-improved is still not able to perform at least as well as the *deep-position-only baseline*. However, it is noticeable that CVPR18-improved is able to outperform the *deep-position-only baseline* for long-term prediction, approaching the *saliency-only baseline*. CVPR18-improved is also able to stick to the same performance as the *deep-position-only baseline* for short-term prediction. Fig. 5.18 provides the detailed results of CVPR18-improved over the different videos in the test set, associated with their respective category identified in [8]. While the average results show reasonable improvement towards the *saliency-only baseline*, we observe that CVPR18-improved significantly improves over the *deep-position-only baseline* for non-exploratory videos. Finally, we recall that the visual features provided to CVPR18-improved are the ground-truth saliency (i.e., the heat maps obtained from the users traces).

Answer to Q3: If O1 is solved perfectly by providing the ground-truth saliency, then O2 and O3 are best achieved separately by having a dedicated recurrent unit to extract features from the positional information only, before merging them in subsequent layers with visual features, as CVPR18 does. If the same recurrent unit is both in charge of O2 and O3, as in MM18, it appears to prevent from reaching the performance of the *deep-position-only baseline*.

Therefore, we next analyze:

Q4 on content-based saliency: If O1 is solved approximately by providing a saliency estimate obtained from the video content only, do the good choices for Q3 still hold, or does the performance degrade away from the baselines again? If so, how to correct?

5.5.2 Answer to Q4 - Analysis with Content-Based Saliency

We first summarize the findings of the root-cause analysis so far. In Q1, we found that even though averaging the prediction error over the trajectory might benefit the baselines, it does not and it is not a cause for the worse performance. In Q2, we have shown that the design assumption of the predictors are met if the dataset is made of non-exploratory videos with sufficient motion,

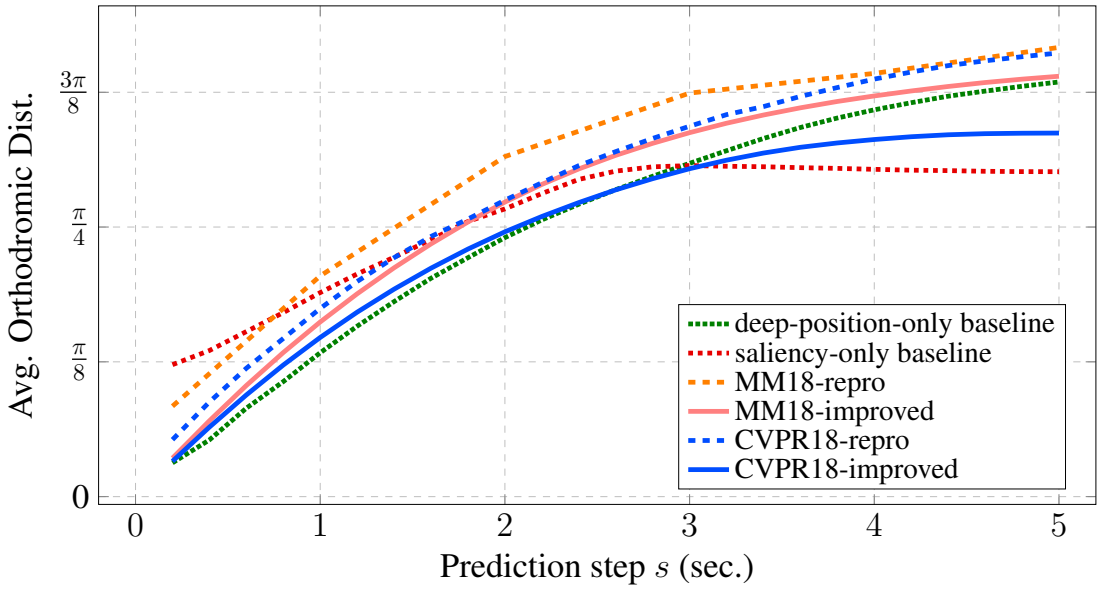

FIGURE 5.17: Average prediction error of the original and improved models of MM18 and CVPR18, all fed with GT-sal, compared with baselines.

and the prediction horizon is greater than 2 to 3 sec.. In Q3, on horizons and datasets verifying the latter conditions, we have found that when the visual information is represented by ground-truth saliency (O1 is perfectly solved), only the architecture of CVPR18 is able to exploit this modality without degrading compared with the baselines.

In this section, we do not consider O1 perfectly solved anymore. We consider the saliency information (i.e., heat map) is estimated from the video content only, not obtained from the users' statistics anymore. Our goal is not to find the best saliency extractor for O1, but instead to uncover the impact of less accurate saliency information onto the architecture's performance, to then overcome this impact if necessary.

In the remainder of the Chapter, when the heat map fed to a method is obtained from the video content (not from the users traces), the name of the method is prefixed with CB-sal (for Content-Based saliency). Also, CB *saliency-only baseline* denotes the *saliency-only baseline* defined in Sec. 5.4.2 when the heat map is obtained from the content, and not from the users traces. Conversely, when the heat map fed to a method is obtained from the users traces (and not estimated from the video content), the name of the method is prefixed with GT-sal (for Ground-Truth saliency, defined in Sec. 4.3.1). The GT *saliency-only baseline* denotes the *saliency-only baseline* defined in Sec. 5.4.2 when the heat map is obtained from the users traces.

Saliency extractor: We consider PanoSalNet [71, 3], also considered in MM18. The architecture of PanoSalNet is composed by nine convolution layers, the first three layers are initialized with the parameters of VGG16 [74], the following layers are first trained on SALICON[75], and finally the entire model is re-trained on 400 pairs of video frames and saliency maps in equirectangular projection. We exemplify the resulting saliency on a frame in Fig. 4.5.

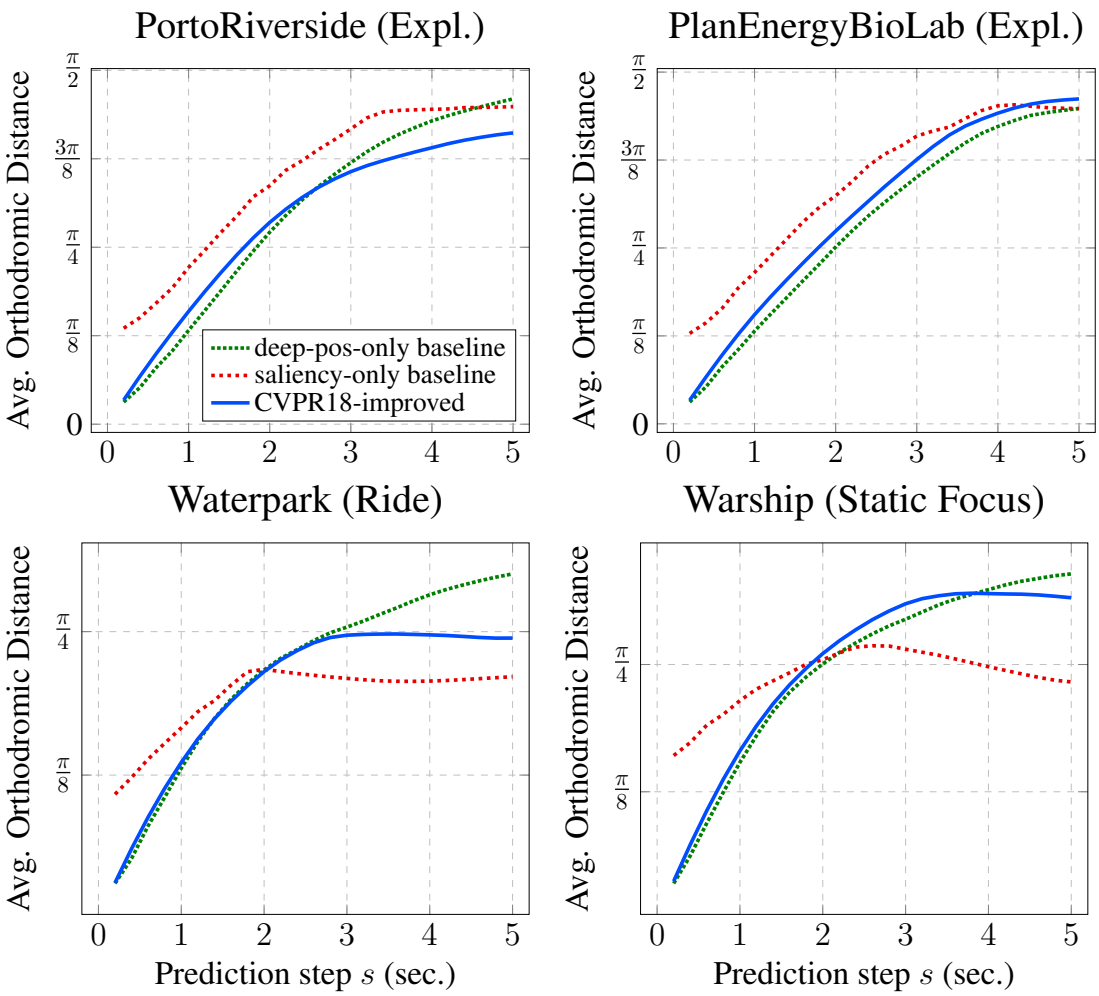

FIGURE 5.18: Prediction error for CVPR18-improved. Detailed result for each type of test video. Legend is identical in all sub-figures.

Results of CVPR18-improved: First, Fig. 5.19 shows the expected degradation using the content-based saliency (obtained from PanoSalNet) compared with the ground-truth saliency: the CB *saliency-only baseline* (dashed red line) is much less accurate than the GT *saliency-only baseline* (solid red line).

Second, we observe that, despite performing well with ground-truth saliency, CVPR18-improved fed with content-based saliency degrades again away from the *deep-position-only baseline*. Specifically, two questions arise:

- Why does CB-sal CVPR18-improved degrades from Ground-Truth Saliency (GT-Sal) CVPR18-improved for horizons $H \leq 2$ sec., where the best to achieve is the *deep-position-only baseline* according to Fig. 5.17?

  The training losses are the same. The only difference is in the input values representing the saliency. We can show that the saliency CB-sal is less sparse than GT-sal, hence there are more non-zero inputs, which are also less accurate (obviously, compared to the GT). Therefore, the contribution of the CB-sal inputs should be nullified by the weights

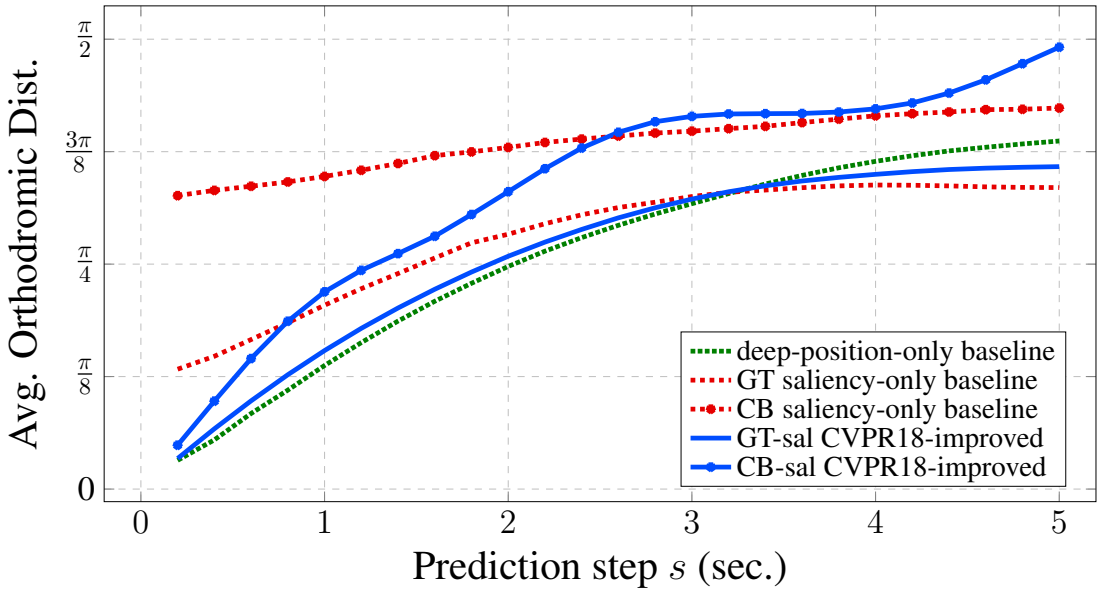

FIGURE 5.19: Prediction error of CB-sal CVPR18-improved (with Content-Based saliency) against GT-sal CVPR18-improved (with Ground-Truth saliency) and baselines.

of the fully-connected layer in charge of the fusion. It is simple to verify that when fully connected layers have to cancel out part of their inputs acting as noise for the classification task, the convergence of the training error degrades with the number of such inputs. Such wrong performance in training indicates a sub-optimal architecture for the problem at hand.

- Why does CB-sal CVPR18-improved degrade from original CVPR18 for $H \in [0s, 1sec.]$? The first difference is the training loss, defined over a longer horizon for CB-sal CVPR18-improved ($H \in [0$ sec.,5 sec.$]$), while it is only for $H = 1$ sec. in original CVPR18. The former loss is therefore likely more difficult to explore and minimize. The second difference is the presence, in original CPVR18, of convolutional and pooling layers processing various visual inputs including saliency before the fusion. Such layers can help decrease the input level into the fusion layer. However, they are not sufficient to enable a fully-connected layers to predict over $[0s, Hs]$ for $H \geq 3$ sec., as discussed in the next section.

Partial answer to Q4: If O1 is solved approximately by providing a saliency estimate obtained from the video content only, the good choice for Q3 (CVPR18-improved) is not sufficient anymore.

5.6 TRACK: A new Architecture for Content-Based Saliency

We now first complete the root-cause analysis by examining more detailedly the architectural reasons for CVPR18-improved to degrade away again from the baselines with CB-sal. We

then propose our new deep architecture, TRACK, stemming from this analysis. Its evaluation shows superior (once equal) performance on all the datasets of considered competitors and wider prediction horizons.

5.6.1 Analysis of the Problem with CVPR18-Improved and Content-Based Saliency (CB-sal)

The fundamental characteristic of the problem at hand is: over the prediction horizon, the relative importance of both modalities (past positions and content) varies. Indeed, we expect the motion inertia to be more prominent first, and only then the content to possibly attract attention and change the course of the motion. It is therefore crucial to have a way of combining both modality features in a time-dependent manner to produce the final prediction. However, in the best-performing architecture so far, CVPR18-improved, we notice that the single RNN component enables this time-dependent modulation only for the positional features, while the importance of the content cannot be modulated over time. Replacing the ground-truth saliency with content-based saliency, the saliency map becomes much less correlated with the positions to predict. It is therefore important to be able to attenuate its effect in the first prediction steps, and give it more importance in the later prediction step.

5.6.2 Designing TRACK

From the latter analysis, **a key architectural element to add is a RNN processing the visual features (such as CB-sal), before combining it with the positional features.** Furthermore, this analysis connects with the seminal work of Jain et al., introducing Structural-RNN in [86]. It consists in casting a spatio-temporal graph describing a problem's structure into a rich RNN mixture following well-defined steps. Though the connection with head motion prediction is not direct, we can formulate our problem structure in the same terms. First, two contributing factor components are involved: the user's FoV and the video content. We can therefore express the spatio-temporal graph of a human watching a 360° video in a headset as shown in Fig. 5.20. Second, these two components are semantically different, and are therefore associated with: (i) an edgeRNN and a nodeRNN for the FoV, (ii) an edgeRNN for the video (only one input to the node), resulting in the architectural block shown in purple in Fig. 5.21. Embedded into a sequence-to-sequence framework, we name this architecture **TRACK**.

Components of TRACK: The modules of TRACK are represented by (i) a doubly-stacked LSTM with 256 units each, processing the flattened CB-saliency map pre-generated for each time-stamp; (ii) another set of doubly-stacked LSTM with 256 units to process the head orientation input; (iii) a third set of doubly-stacked LSTM with 256 units to handle the multimodal fusion; and finally (iv) a Fully Connected (FC) layer with 256 and a FC layer with 3 neurons is used to predict the (x,y,z) coordinates, as described in Sec. 5.5.

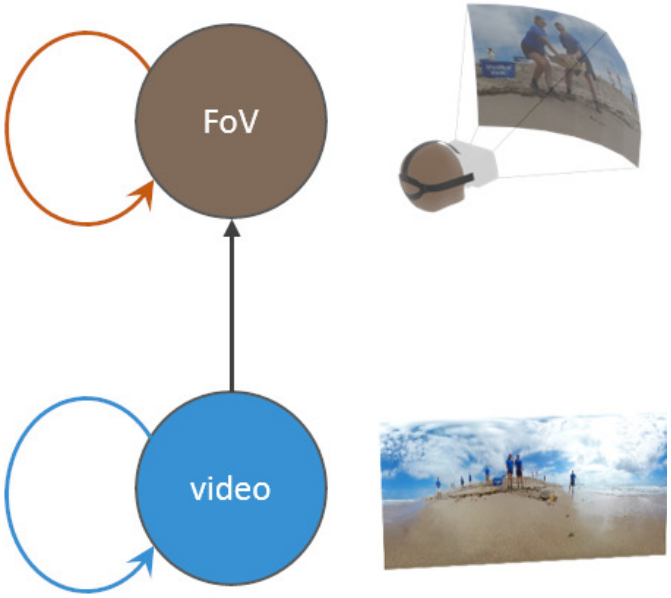

FIGURE 5.20: The dynamic head motion prediction problem cast as a spatio-temporal graph. Two specific edgeRNN corresponds to the brown (inertia) and blue (content) loops, a nodeRNN for the FoV encodes the fusion of both to result into the FoV position.

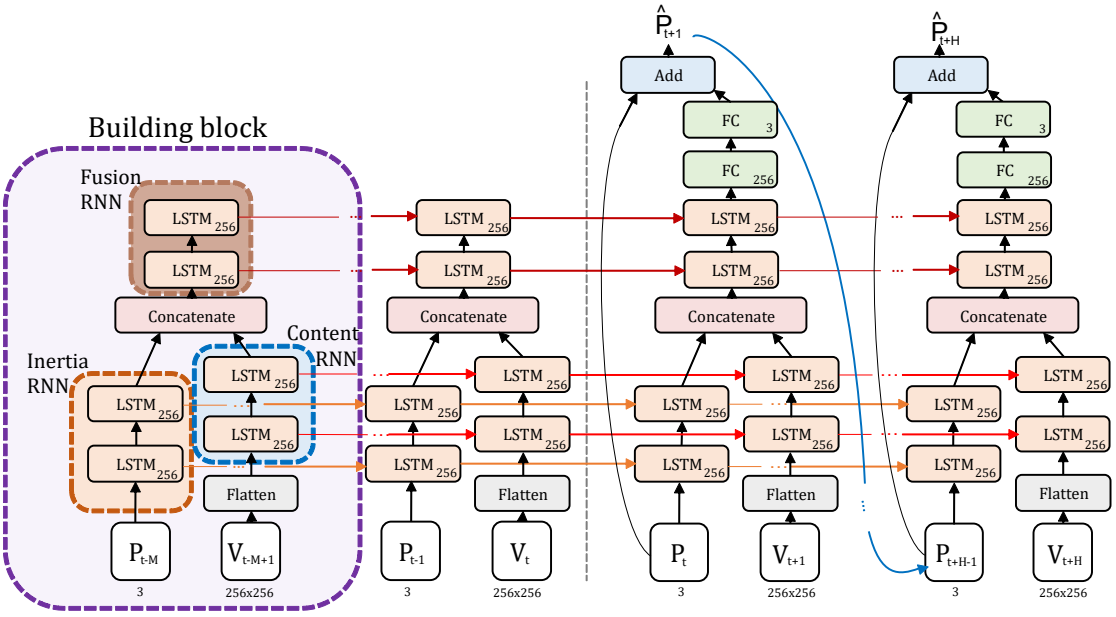

FIGURE 5.21: The proposed TRACK architecture. The colors refer to the components in Fig. 5.20: the building block (in purple) is made of a an Inertia RNN processing the previous position (light brown), a Content RNN processing the content-based saliency (blue) and a Fusion RNN merging both modalities (dark brown).

5.6.3 Evaluation of TRACK

5.6.3.1 Comparison with GT-sal CVPR18-Improved

On the MMSys18 dataset introduced in Sec. 5.5.1 (with higher user motion, and balanced video categories) and for prediction horizons up to 5 sec., Fig. 5.22 compares the results of

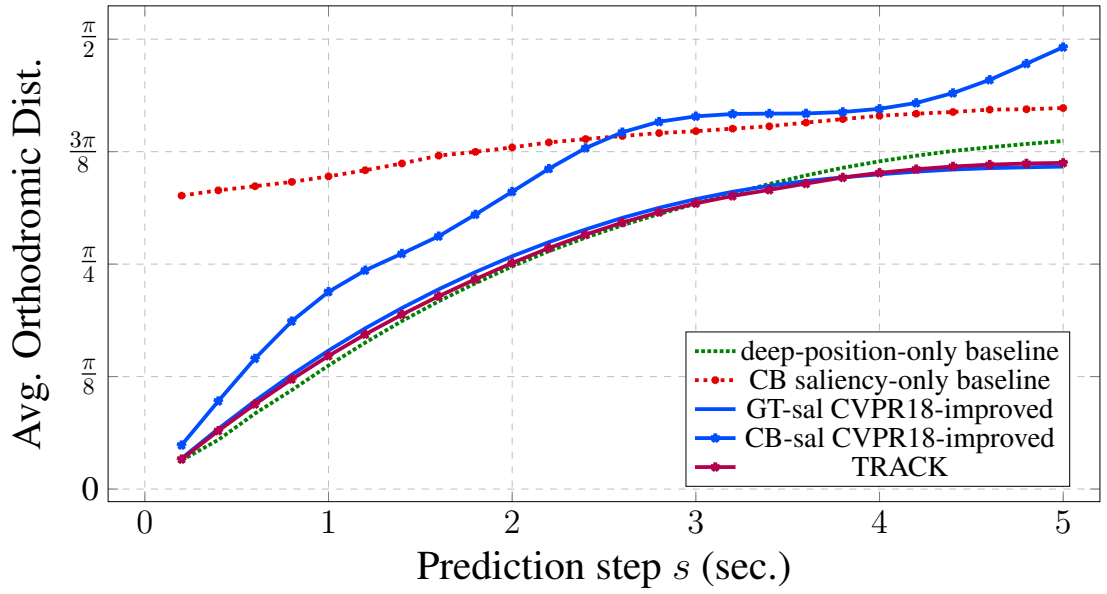

FIGURE 5.22: Comparison, on the MMSys18 dataset, of TRACK with baselines and both CB-sal CVPR18-improved and GT-sal CVPR18-improved.

TRACK with both CB-sal CVPR18-improved and GT-sal CVPR18-improved. Indeed, GT-sal CVPR18-improved is considered as a lower-bound on the error of CVPR18, which does not use PanoSalNet (and whose implementation is not available online nor was communicated on request). We observe that TRACK outperforms CB-sal CVPR18-improved (as expected), and equates to GT-sal CVPR18-improved, which is remarkable. This confirms the importance of the additional architectural elements of TRACK, able to exploit the (approximated) CB-saliency.

5.6.3.2 Comparison with all Methods on their Original Metrics and $H \leq 2.5$ sec.

The results of TRACK against all the considered existing methods, on their original metrics and prediction horizons, were presented in Sec. 5.2. It can be seen that on every dataset, TRACK (always with CB-saliency) establishes state-of-the-art performance: Fig. 5.5-Top shows that it outperforms MM18 (which also uses PanoSalNet), Table 5.2 shows that it significantly outperforms PAMI18, as does Table 5.4 for NOSSDAV17. ChinaCom18 is trained with the leave-one-out strategy, and the dataset is the same as NOSSDAV17. The results of TRACK listed against NOSSDAV17 in Table 5.4 are thus a lower-bound to TRACK's performance if it were trained with the leave-one-out strategy, already outperforming ChinaCom18 by more than 30%. As expected from the answer to Q2 in Sec. 5.4.5, for such short prediction horizons ($H \leq 2.5$ sec.), TRACK does not outperform the *deep-position-only baseline*. Its slightly inferior performance is due to the fact that we did not do any hyperparameter tuning for TRACK, while we did for the *deep-position-only baseline* which is smaller (tuning the number of layers and neurons). When training for $H = 5$ sec., the next results in Fig. 5.23 show that, for $s \leq 3$ sec., TRACK is similar to or even outperforms the *deep-position-only baseline* for 4 datasets in 5.

5.6.3.3 Exhaustive Cross-Comparison with all Methods on all Datasets with the Orthodromic Distance and $H = 5$ sec.

Average results: Fig. 5.23 presents the performance, on all 5 datasets (CVPR18, PAMI18, MMSys18, MM18, NOSSDAV17) of every (re-)implemented method, all with CB-sal: TRACK, CVPR18-improved, MM18-improved, *deep-position-only baseline*, *trivial-static baseline*. The results are averaged over the videos in the respective test sets made of 42 videos for CVPR18, 16 for PAMI18, 4 for MMSys18, 2 for MM18 and 2 for NOSSDAV17.

• For prediction steps $s \geq 3$ sec., TRACK outperforms all methods on all five datasets, except for the NOSSDAV17 dataset where it equates to the best (likely because the *saliency-only baseline* does not outperform the *deep-position-only baseline* on the NOSSDAV17 dataset, as shown in Fig. 5.13).

• For $s \leq 3$ sec., TRACK equates to the best method which is the *deep-position-only baseline*, except on the CVPR18 dataset where it has a slightly inferior performance but equates to the other methods.

Gains on video categories: The results in Sec. 5.4.4 have shown that the gains that can be expected from a multimodal architecture over the *deep-position-only baseline* are different depending on the video category: whether it is a *focus-type* or an *exploratory* video. The results in Fig. 5.23, averaged over all the videos of a test set, are therefore not entirely representative of the gains. To analyze the gains of TRACK over different video categories, we proceed as follows. First, we only focus on the CVPR18, PAMI18 and MMSys18 datasets to have a sufficient number of videos in the test set. Then, for MMsys18, we group the test videos into a Focus category (with Waterpark and Warship) and an Exploration category (with Portoriverside and Energybiolab), as done in Sec. 5.4.4. Finally for CVPR18 and PAMI18, in order to apply this binary categorization Focus vs Exploratory, we rely on the users behavior. Indeed, the more the users tend to have a focusing behavior, the lower the entropy of the GT saliency map[2]. Thus we consider the entropy of the GT saliency map of each video to assign the video to one category or the other. We sort the videos of the test set in increasing entropy, and we represent in Fig. 5.24 the results averaged over the bottom 10% (focus-type videos) and top 10% (exploratory videos).

• On the low-entropy/focus-type videos and for $s \geq 3$ sec., TRACK significantly outperforms the second-best method: by 16% for PAMI18 to 20% for both CVPR18 and MMSys18 at $s = H = 5$ sec.. TRACK performs similarly or better for $s < 3$ sec..

• On the high-entropy/exploratory videos, the gains of TRACK are much less significant: TRACK often performs similarly or slightly worse than the *deep-position-only baseline*, yet never degrading significantly away from this baseline, as the other methods do. Such results are expected from the observations drawn in Sec. 5.4.4 (Fig. 5.12,5.15,5.16) showing that the *saliency-only baseline* does not outperform the *deep-position-only baseline* on exploratory videos.

[2]The entropy of the 2D map is computed per frame, then averaged over all the frames for $t \geq 6$ sec. to skip the exploratory phase.

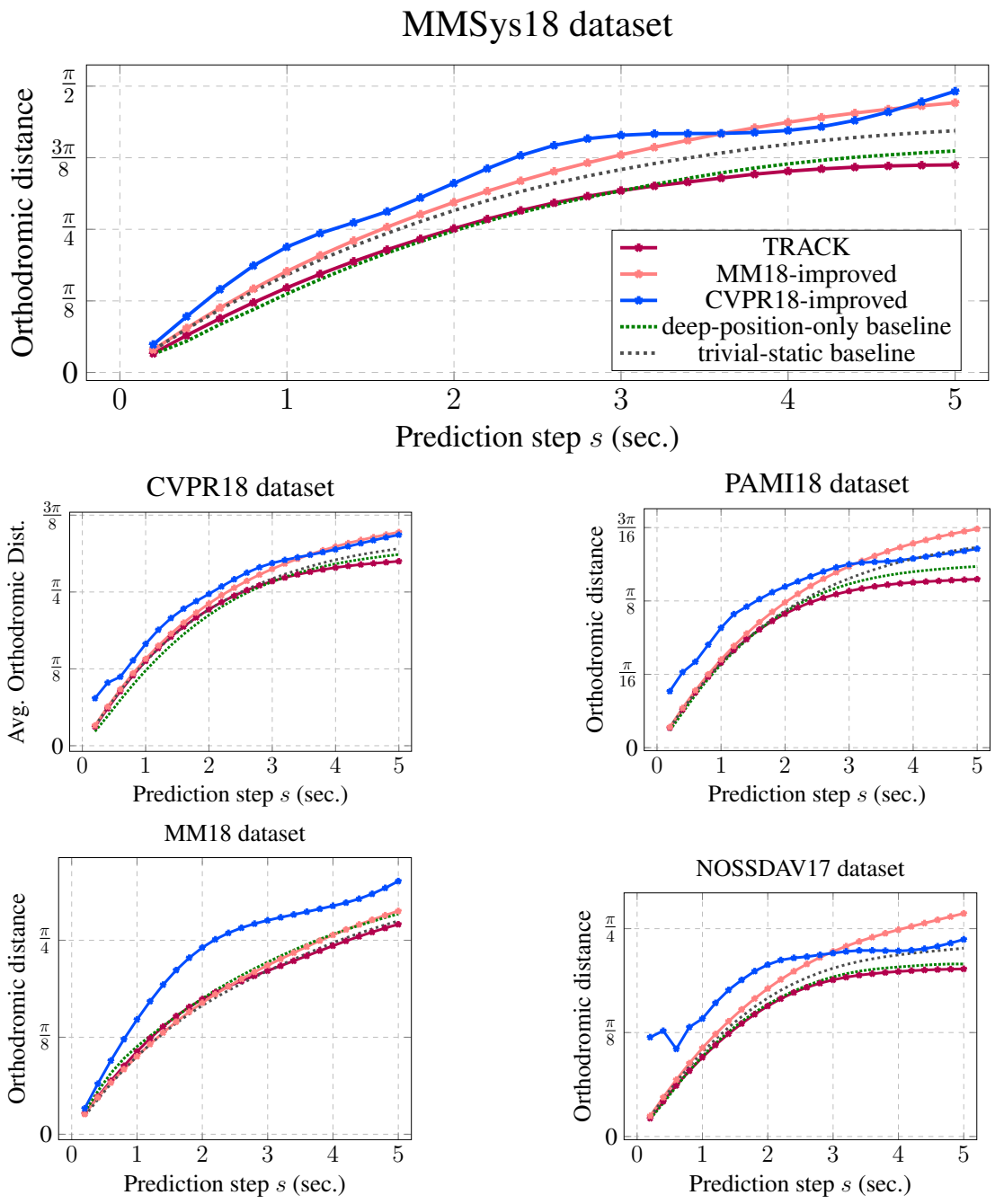

FIGURE 5.23: Evaluation results of the methods TRACK, MM18-improved, CVPR18-improved and baselines, averaged over all test videos for the datasets of CVPR18, PAMI18 MMSys18, NOSSDAV17 and MM18. Legend are the same in all figures.

Qualitative examples: In Figs. 5.25, 5.26 and 5.27, we exemplify the results on two low-entropy videos per dataset, CVPR18, PAMI18 and MMSys18 respectively, also showing a representative frame with a user's future trajectory and the prediction of TRACK. On focus-type videos, TRACK outperforms significantly the second-best method: by up to 25% in the examples.

5.6.4 Ablation Study of TRACK

To confirm the analysis that led us to introduce this new architecture TRACK for dynamic head motion prediction, we perform an ablation study of the additional elements we brought compared to CVPR18-improved: we either replace the RNN processing the CB-saliency with two FC layers (line named AblatSal in Fig. 5.28), or replace the fusion RNN with two FC layers (line named AblatFuse).

Fig. 5.22 and 5.28 confirm the analysis in Sec. 5.6.1: the removal of the first extra RNN (not present in CVPR18) processing the saliency input has more impact: AblatSal degrades away from the *deep-position-only baseline* in the first time-steps. The degradation is not as acute as in CVPR18-improved as the fusion RNN can still modulate over time the importance of CB-saliency. However, it seems this fusion RNN cancels most of its input (position and saliency features), as the performance of AblatSal is consistently similar to that of the *trivial-static baseline* (not plotted for clarity). The AblatFuse line shows that the impact of removing the fusion RNN is less important.

Answer to Q4: If O1 is solved approximately by providing a saliency estimate obtained from the video content only, the good choice (CVPR18-improved) for Q3 is not sufficient anymore. A RNN dedicated to processing the saliency must be added to prevent the prediction in the first time-steps from degrading away from the *deep-position-only baseline*. Our new deep architecture, named TRACK, achieves state-of-the-art performance on all considered datasets and prediction horizons.

5.7 Discussion

It is interesting to note that only a few architectures have been designed in the same way as TRACK, and none for head motion prediction. Indeed, following up on [86], Sadeghian et al. in [87] proposed a similar architecture to predict a pedestrian's trajectory based on the image of the environment, the past ego trajectory and the trajectories of others. Let us also mention that the CVPR18 block is similar to an early architecture proposed for visual question answering in 2015 [88], and PAMI18 is similar to Komanda proposed in 2016 for autonomous driving [89].

This Chapter brings a critical analysis to existing deep architectures aimed to predict the user's head motion in 360° videos from past positions and video content. As we exhibit the weaknesses of the evaluation scenarios considered by previous works (dataset and competitor

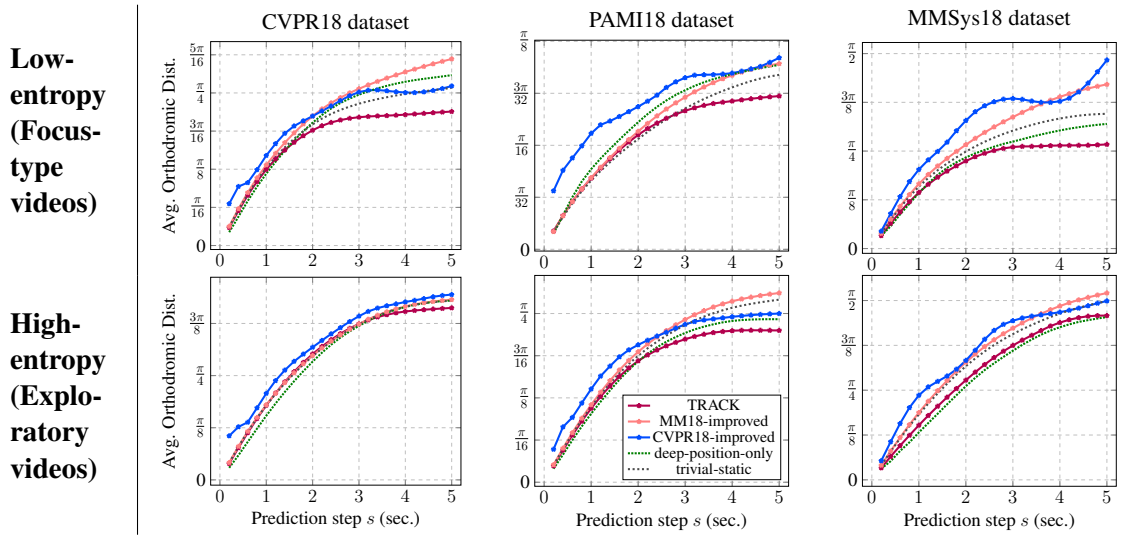

FIGURE 5.24: Top row (resp. bottom row): results averaged over the 10% test videos having lowest entropy (resp. highest entropy) of the GT saliency map. For the MMSys dataset, the sorting has been made using the Exploration/Focus categories presented in Sec. 5.4.4. Legend and axis labels are the same in all figures.

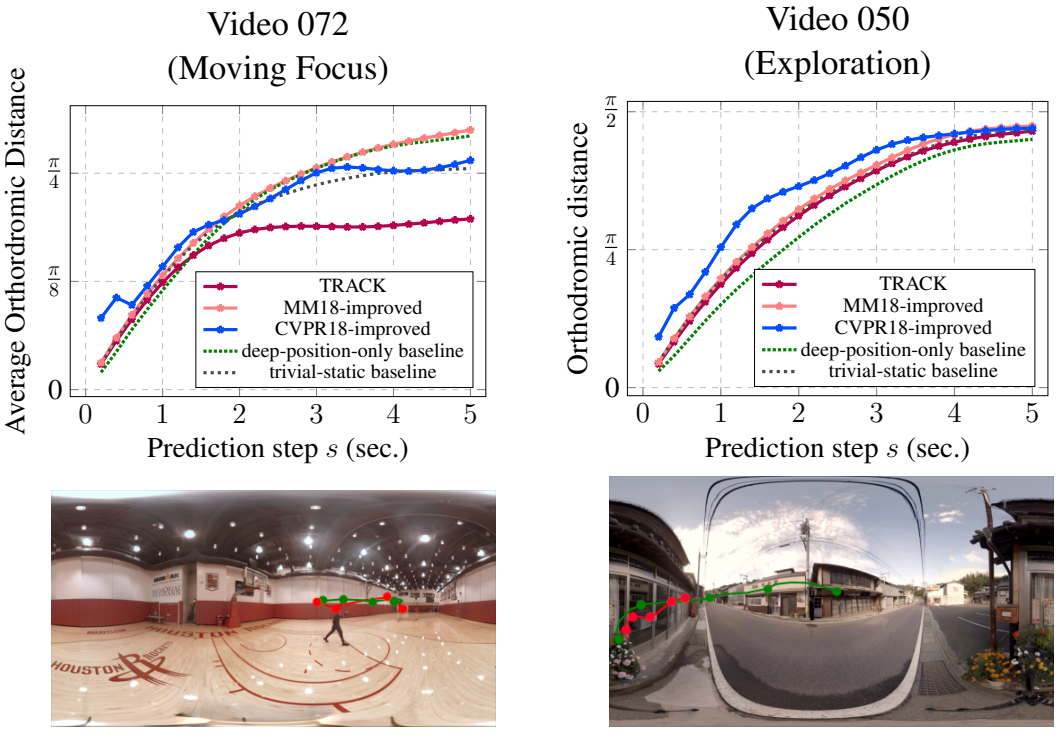

FIGURE 5.25: Example of performance on two individual test videos of type Focus and Exploration for CVPR18 dataset [5]. On the frame, the green line represents the ground truth trajectory, and the corresponding prediction by TRACK is shown in red

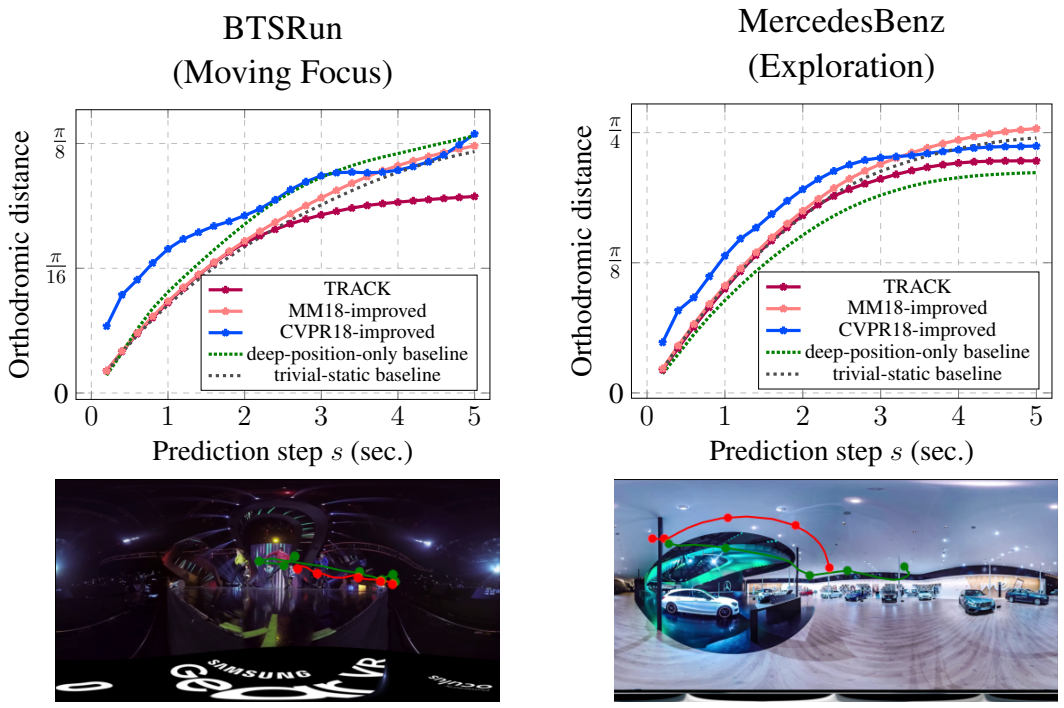

FIGURE 5.26: Example of performance on two individual test videos of type Focus and Exploration for PAMI dataset [1]. On the frame, the green line represents the ground truth trajectory, and the corresponding prediction by TRACK is shown in red

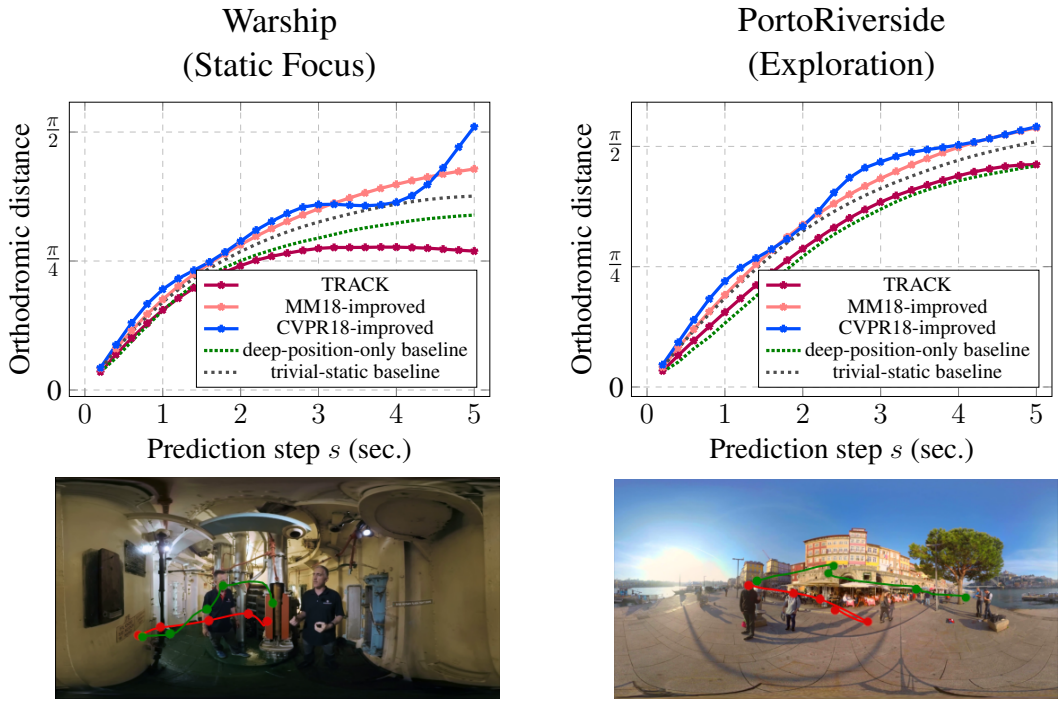

FIGURE 5.27: Example of performance on two individual test videos of type Focus and Exploration for MMSys18 dataset [17]. On the frame, the green line represents the ground truth trajectory, and the corresponding prediction by TRACK is shown in red

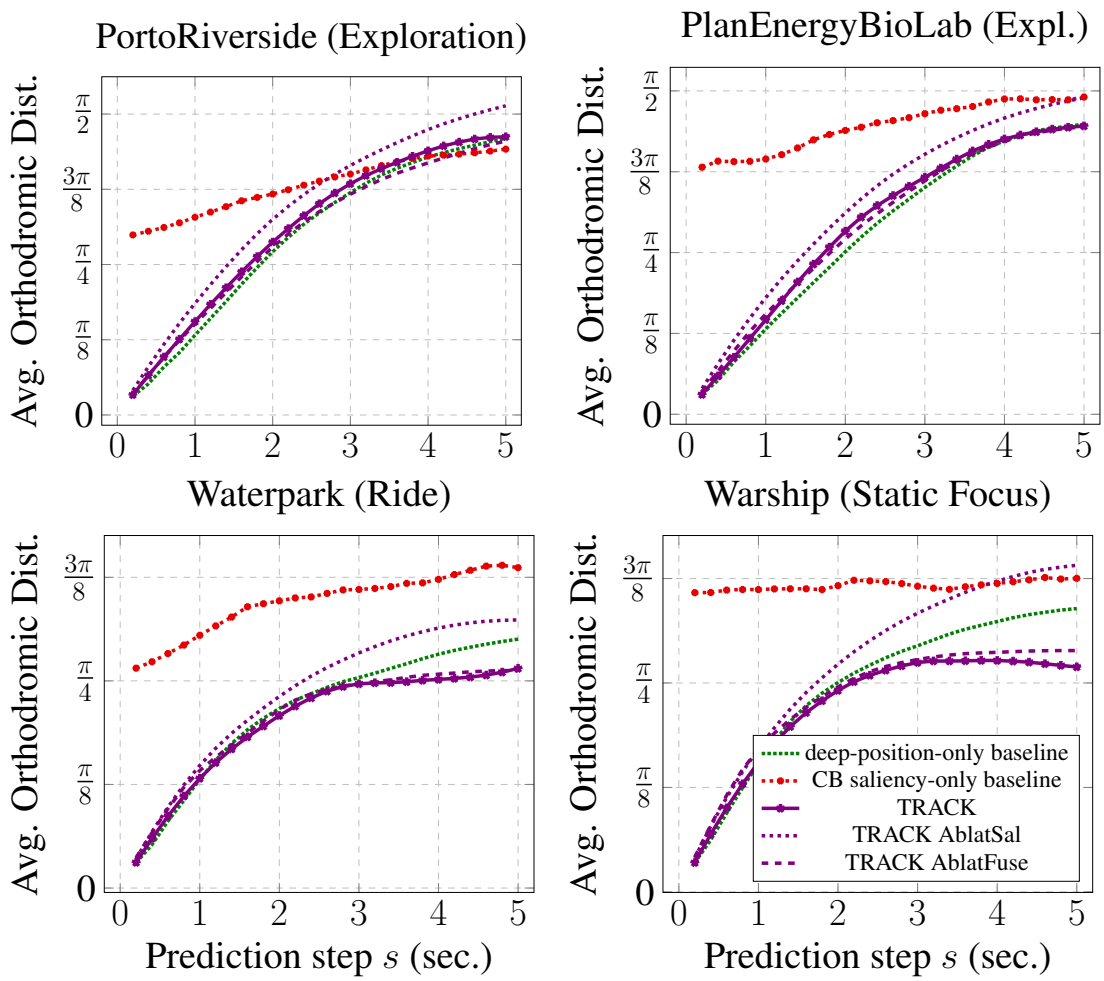

FIGURE 5.28: Per-video results of TRACK and ablation study. The legend is identical for all sub-figures.

baselines), it is important to mention that other such critical analyses have been made for other application domains of deep learning very recently. Indeed, besides Martinez et al. mentioned earlier who showed in [82] the weakness of existing architectures for 3D-skeleton pose prediction, Ferrari Dacrema et. al. performed an analysis of recommendation systems in [90]. Not only did they show the difficulty to reproduce the evaluated algorithms, but also that the state-of-the-art methods could not outperform simple baselines. Similarly, the meta-analysis of Yang et. al. [91] for information retrieval, and Musgrave et. al. [92] for loss functions, show that, contrary to the claims of the authors of multiple recent papers, there has been no actual improvement in several years of proposed neural networks to solve the problem in each of these fields.

In [93], Blalock et. al. show that the difficulty to reproduce, measure and compare the performances of different algorithms makes it difficult to determine how much progress has been made in a field, and this difficulty grows when each work uses different datasets, different performance metrics and different baselines. In the this Chapter, we have faced the same difficulties. From

the entire reproducible framework introduced in Sec. 4 we have made to enable replication and comparison, we could perform a critical and constructive analysis.

Our approach and findings are therefore aligned with other critical re-examinations of existing works in other application domains of deep learning.

5.8 Conclusion

This Chapter has brought two main contributions. First, we carried out a critical and principled re-examination of the existing deep learning-based methods to predict head motion in 360° videos, with the knowledge of the past user's position and the video content. We have shown that all the considered existing methods are outperformed, on their datasets and with their test metrics, by baselines exploiting only the positional modality. To understand why, we have analyzed the datasets to identify how and when should the prediction benefit from the knowledge of the content. We have analyzed the neural architectures and shown there is only one whose performance does not degrade compared with the baselines, provided that ground-truth saliency information is provided, and none of the existing architectures can be trained to compete with the baselines over the 0-5 sec. horizon when the saliency features are extracted from the content. Second, decomposing the structure of the problem and supporting our analysis with the concept of Structural-RNN, we have designed a new deep neural architecture, named TRACK. TRACK establishes state-of-the-art performance on all the prediction horizons $H \in [0 \text{ sec.}, 5 \text{ sec.}]$ and all the datasets of the existing competitors. In the 2-5 sec. horizon, TRACK outperforms the second-best method by up to 20% on focus-type videos, i.e., videos with low-entropy saliency maps.

The Deep Learning models studied in this Chapter are often referred to as "black-boxes" since they do not provide any insight on the dependence and interplay between head motion and the visual content. In the next Chapter we investigate the human head motion process by means of a "white-box" model that allows us to get knowledge regarding the connection between visual saliency information and head motion.

Chapter 6

HeMoG: A White-Box Model to Unveil the Connection Between Saliency Information and Human Head Motion in Virtual Reality

Immersive environments for entertainment or training are gaining traction, in particular Virtual Reality (VR) for applications related to, e.g., gaming, museums, journalism, or rehabilitation. Designing VR experiences that are both interactive, comfortable and engaging is key to create immersive personalized environments. The challenge is to identify, adapt to and guide the attentional and emotional trajectory of the user. Visual attention is already considered in a number of such systems, be it for cinematic VR with 360° videos [26] or 3D-interactive environments [94], or to enable efficient VR streaming by predicting where the user is going to look at and send in high-quality only the attended Field of View (FoV) to save data rate (See Chapter 5).

Understanding the connection between the audio-visual content and the human attentional process is therefore key for the design of immersive and personalized environments. Focusing only on the visual aspect, visual attention is a set of cognitive operations that allow us to filter the relevant locations in our visual field [29]. This mechanism also guides the movement of our head and eyes to center the selected location in our fovea, that is the area of the retina with the highest amount of photoreceptors and therefore allows sharp central vision [25].

Recently, VR in the form of 360° videos has been considered to study how people explore 360° environments with 3 DoF. The work of [35] collects user data to analyze and identify first properties (e.g., user congruence, the existence of an initial exploratory phase for ca. 18 sec. before a user focuses). Other works such as [3] aim at extracting the saliency maps, i.e., 2D-distributions of head positions, from the content. To dynamically predict the head motion over a certain time *prediction horizon*, several Deep Learning (DL) models have been proposed,

such as [5], [1] or TRACK (See Chapter 5).

These models, often referred to as "black-boxes", however do not provide any insight on the dependence of the head motion on the visual content. In this Chapter, we address **2 research questions**:

Q1: To which extent can we investigate the inner workings of these Deep Learning (DL) models with a white-box model?

Q2: What knowledge can we obtain from a white-box model regarding the connection between saliency information and head motion?

6.1 Related Work

Several DL models have been proposed to predict head or gaze motion in 360° videos [2, 1, 4, 5]. In Chapter 5, we made a critical study of existing DL models, showing systematic weaknesses by comparing their performance with simple yet stronger baselines. We also proposed a new DL model, named TRACK, that establishes state-of-the-art performance on several datasets. We therefore consider TRACK as the DL model our proposed HeMoG model must be compared with.

All these DL models are black-box models whose, to the best of our knowledge, explanability has not been studied. Explainability and interpretability of DL models decisions and predictions is a wide and highly active research area (see, e.g., [95]). In this work, our goal is not only to understand what type of inductive bias is exploited by existing DL models, but rather to design a white-box model that we can leverage both to gain insight on what the DL model learns, and unveil the connection between visual content and head motion.

Finally, for regular 2D videos, [96] recently proposed a gravitational model to generate human-plausible visual scanpaths. We take inspiration from this model to design HeMoG, which, contrary to [96], is built on a 3D-rotational motion description with specific terms related to head/neck fatigue.

6.2 HeMoG: A Model of Head Motion in 360° videos

In this section we present a new model of head motion in 360° videos named Head Motion with Gravitational laws of attention (HeMoG). We formulate the shift in human attention as the analogous mechanics of a ball rotating around a fixed origin. As shown in Fig. 6.1, the red ball represents the center of the FoV of a user exploring a virtual environment. All elements in a visual scene compete as attractors for the human attention process. This concept of attraction can be effectively described by means of gravitational models, where each location in the scene is associated with a virtual mass that is capable of attracting attention.

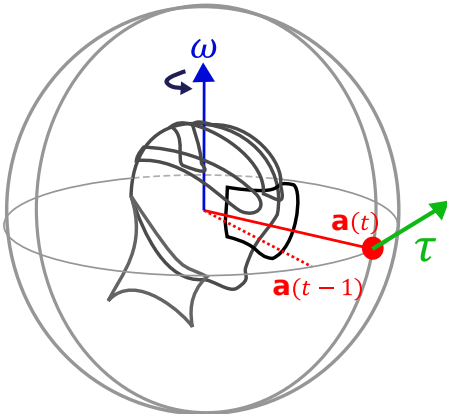

FIGURE 6.1: Gravitational model of the head position of a person exploring a VR scene. The center of the FoV $\mathbf{a}(t)$ is modeled as a ball attached to a stick of fixed length that rotates with an angular velocity ω and with torque τ.

The fundamental equation of rotational motion is:

$$\dot{\mathbf{L}} = \tau \ , \tag{6.1}$$

where:

• $\mathbf{L}$ is the angular momentum, expressed as $\mathbf{L} = I\omega$, with ω the angular velocity and I the moment of inertia. For a ball attached to a fixed point (red dot in Fig. 6.1), I can be expressed as the product of the ball's mass with $|\mathbf{a}(t)|$. There is not such a valid analogy in our modeling of the center of focus, and we shall keep I as a parameter in what follows.

• τ represents the torque applied to the system. This torque results from various forces, as described below.

We therefore have $\tau = \frac{d(I\omega)}{dt} = \dot{I}\omega + I\dot{\omega}$. Having constrained the attention on the unit sphere, the norm of $\mathbf{a}(t)$ does not change over time, resulting in $\dot{I} = 0$. Therefore we obtain

$$I\dot{\omega} = \tau \ . \tag{6.2}$$

Modeling of τ: The torque is the turning effectiveness of a force. To model head rotation, we assume that two types of forces are at play:

• forces that drive the head focus to salient areas of the 360° content. Every 360° frame therefore generates a field of force

$$\mathbf{E}(\mathbf{a}) = \int_{\mathbf{r}\in\Upsilon} \mathbf{F}_{\mathbf{E}}(\mathbf{r},\mathbf{a})d\mathbf{r}, \tag{6.3}$$

where Υ is the set of points in the sphere. Given the virtual mass $\mu(\mathbf{r},t)$ of every point $\mathbf{r}$ at time t, the force exerted at the current focus point $\mathbf{a}(t)$ is assumed to decrease radially as:

$$\mathbf{F}_{\mathbf{E}}(\mathbf{r},\mathbf{a}) = \gamma(t)\frac{1}{||\mathbf{r}-\mathbf{a}||^2}\mu(\mathbf{r},t)(\mathbf{r}-\mathbf{a}) \ . \tag{6.4}$$

The parameter $\gamma(t)$ weights the importance of the attraction force over time. We set

$$\gamma(t) = 1 - e^{(-\beta t)},$$

with parameter β to be a model parameter. This models the growing importance of the content over the *prediction horizon*: the motion continuity should be most important for short-term prediction, while the content diverts attention after a few seconds. The model input $\mu(\mathbf{r}, t)$ for every pair $(\mathbf{r}, t)$ can be set in different ways. Three cases are considered in this Chapter. In Sec. 6.3.2, $\mu(\mathbf{r}, t)$ is set to 0. In Sec. 6.3.3, $\mu(\mathbf{r}, t)$ is set to the so called *ground-truth saliency map* $sal_{gt}(\mathbf{r}, t)$. In Sec. 6.3.4, $\mu(\mathbf{r}, t)$ is set to the element-wise product $so(\mathbf{r}, t) \bigodot of(\mathbf{r}, t)$, with $so(\mathbf{r}, t)$ being a 0-1 pixel map of bounding boxes (1 inside, 0 outside) of detected objects, and $of(\mathbf{r}, t)$ the optical flow at this pixel.

• a torque modeled as $-\lambda\omega$, corresponding to a force of friction modeling the energy dissipation when a user continues on their momentum, equivalently the fatigue or the principle of least effort in which humans tend to return static.

Computation of $\mathbf{a}(t)$: The final motion equation is therefore:

$$I\dot{\omega} = \left(\int_{\mathbf{r} \in \Upsilon} \mathbf{a} \times \mathbf{F}_{\mathbf{E}}(\mathbf{r}, \mathbf{a}) d\mathbf{r} \right) - \lambda\omega \ , \tag{6.5}$$

where the first term in the right-hand-side is the torque associated with the field of force, $\times$ denoting the vector product. In the implementation, we drop I as parameters $\gamma(t)$ and λ in the right-hand-side can compensate for it. The evolution of $\mathbf{a}(t)$ is computed with quaternion rotations at each time instant:

$$\mathbf{a} = q \otimes \mathbf{a}_x \otimes q^{-1}, \tag{6.6}$$

where $\mathbf{a}_x$ is a constant unit vector, and $\otimes$ is the quaternion multiplication. As a consequence, considering the second order derivatives of the quaternion q:

$$\ddot{q} = \dot{q} \otimes q^{-1} \otimes \dot{q} + \frac{1}{2}\dot{\omega} \otimes q. \tag{6.7}$$

The relation between quaternions and angular velocity and angular acceleration is derived and studied in depth in Appendix B. We can now describe the dynamics of the system, by introducing the auxiliary variable $z(t) = \frac{d}{dt}(\mathbf{a}_x)$, with the system of first order differential equations:

$$\begin{cases} \mathbf{a}(t) = q(t) \otimes \mathbf{a}_x \otimes q^{-1}(t) \\ \dot{q}(t) = z(t) \\ \dot{z}(t) = \dot{q}(t) \otimes q^{-1}(t) \otimes \dot{q}(t) + \frac{1}{2}\dot{\omega} \otimes q(t), \end{cases} \tag{6.8}$$

subject to the boundary conditions $\mathbf{a}(t_0) = \mathbf{a}_0$, $\mathbf{a}_x = (1, 0, 0)$ and $z(t_0) = z_0$. If we pose $y = (q, z)$, then system (6.8) can be compactly re-written in the canonical form:

$$\dot{y} = \Phi(y, \mu, \gamma, \lambda), \tag{6.9}$$

that can be solved numerically by classic methods like Euler's and Runge-Kutta's. In this system of equations there are three parameters that are key in defining the head motion process:

- λ : models the fatigue of the user or the tendency to return to rest.
- $\gamma(t, \beta)$: models the strength of the forces from the visual input at each time-step.
- μ : the virtual masses generated from the visual input.

We vary these parameters throughout the Chapter to explain the usage of HeMoG to properly model the dynamics of head motion.

6.3 Comparing Deep Models with HeMoG

In this section, we address Q1: To which extent can we investigate the inner workings of these DL models with a white-box model? To do so, we compare the performance of HeMoG with the reference DL models of TRACK (introduced in Chapter 5).

6.3.1 Experimental Setup

6.3.1.1 Dataset

We selected the publicly available dataset of [5] to perform our experiments. This dataset consists of 208 omnidirectional videos. The duration of each video ranges between 15 and 80 seconds long (36s in average), each video is viewed by at least 31 participants. To perform the parameter estimation, we randomly selected a subportion of the traces of 166 videos (80%) and 15 users (50%) from the dataset, and exploited them to estimate the model parameters. Then the model with the parameters found is tested in the remaining traces (42 videos and 16 users), there is no overlap between videos or users in the train and test set. We subsampled all the videos in the dataset to 5 frames per second. The frames are resized to a resolution of 952×476.

Instead of using the equirectangular frame as visual input where the pixels in the poles are oversampled, the Vogel method [97] is employed to generate approximately uniformly distributed points on the sphere, as proposed in [98]. As illustration of the uniform sampling of the equirectangular frame using the Vogel method, the sampling of 200 points is shown in Fig. 6.2. In our experiments we used a sampling of 10000 points. Fig. 6.2 also shows the interaction between the field of forces $\mu(r, t)$, the position of the head $\mathbf{a}(t)$, the angular velocity ω and the torque τ.

The integration of Eq. 6.9 that drives the focus of attention trajectory is based on the `odeint` function of Python SciPy library. The function is based on LSODA, which is a general purpose

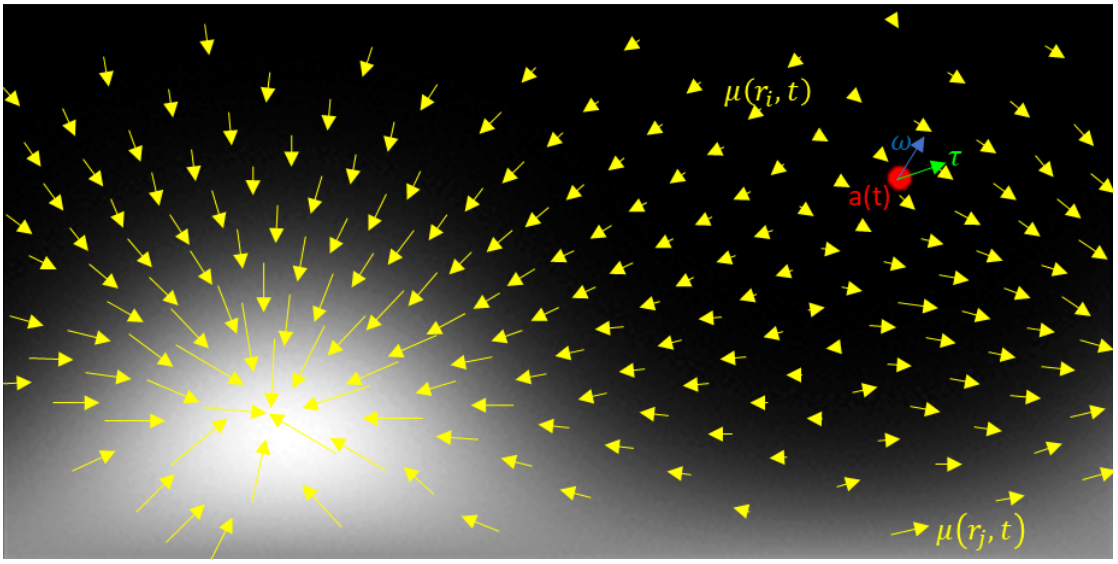

FIGURE 6.2: Interaction between the Field of forces of a synthetic image and the position of the head $\mathbf{a}(t)$.

software that dynamically determines where the problem is stiff and chooses the appropriate solution method.

6.3.1.2 Problem Definition and Metric

We focus on the **dynamic prediction problem** that consists, at each video playback time t, in predicting the future user's head positions between t and $t + H$, with H being the *prediction horizon*. We set $H = 5$ sec. to match the settings defined in Chapter 5. Let T be the video duration. We define the terms *prediction step* s, and video *time-stamp* t, such that: at every *time-stamp* $t \in [0, T]$, we run predictions $\hat{\mathbf{a}}(t+s)$, for all *prediction steps* $s \in [0, H]$. In what follows, t therefore identifies with t_0 and s with t in Sec. 6.2, with initial conditions being position $\mathbf{a}(t)$ ($\mathbf{a}_0$) and current rotational velocity $\dot{q}(t)$ (z_0). We evaluate the predictions at every step s with the orthodromic distance between the ground-truth of the future position and the predicted positions. The orthodromic distance is the shortest distance of two points measured along the surface of the sphere, and is calculated as $D(\mathbf{a}(t+s), \hat{\mathbf{a}}(t+s)) = \arccos\left(\mathbf{a}(\mathbf{t}+\mathbf{s}) \cdot \hat{\mathbf{a}}(\mathbf{t}+\mathbf{s})\right)$, where $\cdot$ is the dot product operation.

6.3.2 HeMoG Models well Head Motion Continuity and Attenuation

We first investigate the impact of parameter λ of HeMoG, which is meant to represent the attenuation of energy when the user continues on their momentum (modeled as a force of friction in Sec. 6.2). To do so, we set the visual content weight $\gamma(s)$ to 0 by setting $\beta = 0$. We compare HeMoG against the DL model named *deep-position-only*, introduced in Chapter 5.2.2, because it uses only the history of past positions to make the predictions and it has been shown

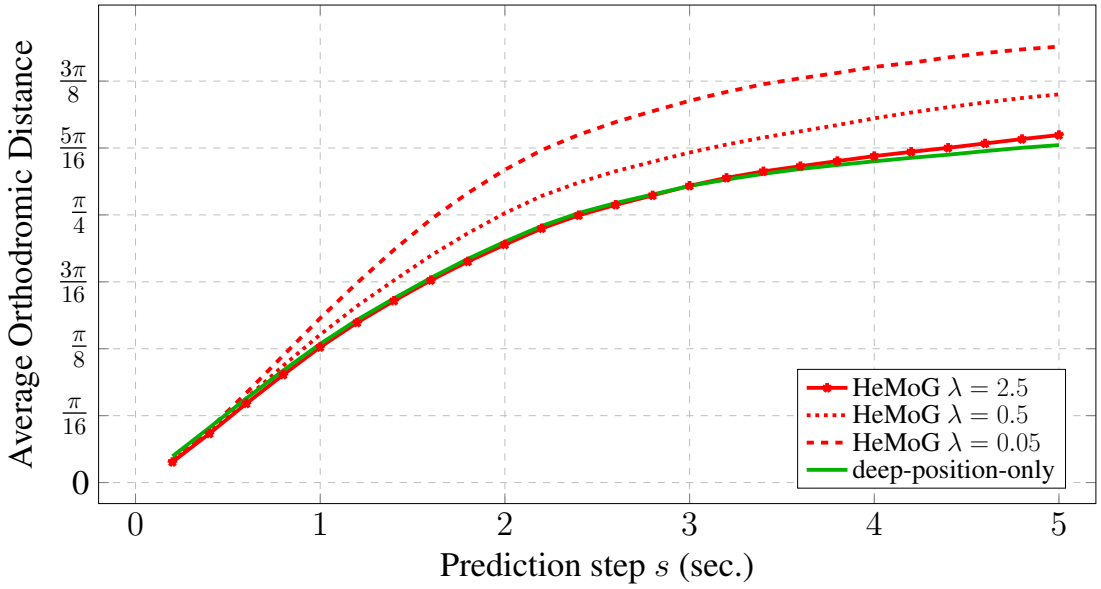

FIGURE 6.3: Prediction error of HeMoG with $\lambda = 2.5$ (and $\beta = 0$) compared with the *deep-position-only* baseline. The performance of HeMoG with other values of $\lambda = 0.5$ and 0.05 are shown to illustrate the impact of the parameter.

to outperform all previously existing DL models over all *prediction steps*. It is a Sequence-to-Sequence LSTM framework consisting in an encoder and a decoder that does not consider any visual input. The encoder receives the *historic window* input of past head positions and generates an internal representation that initializes the decoder producing the series of predictions.

6.3.2.1 Results

Fig. 6.3 depicts the results of HeMoG in the test set with the parameter $\lambda = 2.5$ tuned in the train set. We observe that $\lambda = 2.5$ yields performance of HeMoG close to that of the *deep-position-only* baseline. Fig. 6.3 also presents the results of HeMoG with other values of λ, a lower value of λ represents lower fatigue (more volatility), while a higher value of λ represents higher fatigue (motion reduced more quickly).

First, it is remarkable that such a white-box model predicts head motion as well as a DL model. Second, **we interpret this as the DL model *deep-position-only* learning the curvature and friction dynamics of head motion that HeMoG is explicitly built on**. This is the first element of answer to question **Q1**.

6.3.3 HeMoG Combines well Past Motion and Accurate Content Information

We study whether HeMoG correctly models the fusion between visual information and history of head positions. To do so, we keep λ set to 2.5 following the previous results. To be independent from the imperfection of any saliency predictor fed with the visual content, we

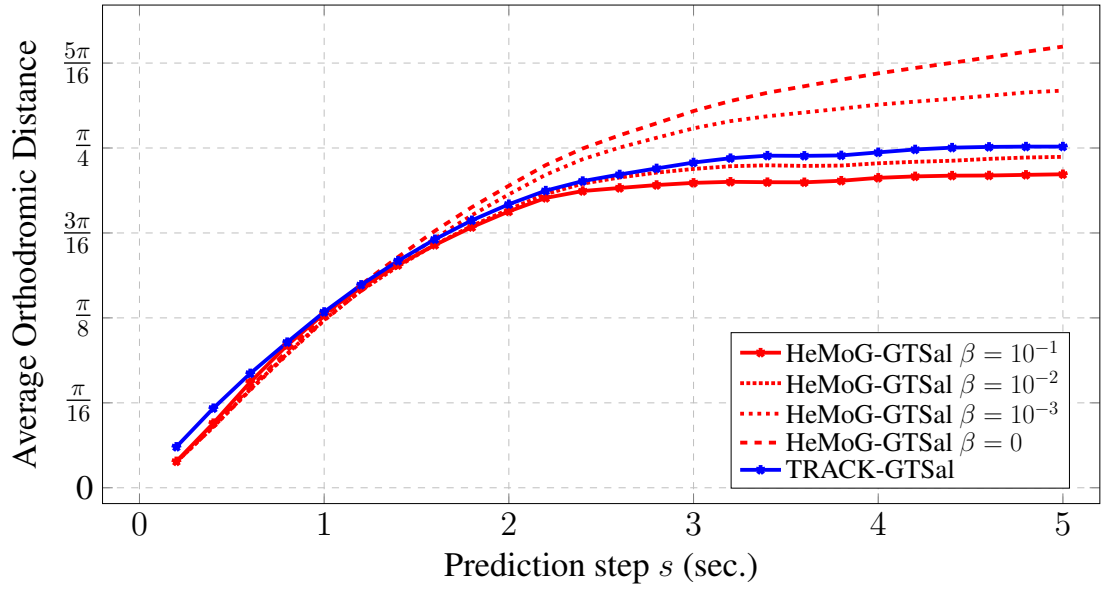

FIGURE 6.4: Prediction error of HeMoG with $\lambda = 2.5$, $\beta = 10^{-1}$ and *ground-truth saliency* (GT-Sal) input, compared with TRACK. Other values of $\beta = 10^{-2}$ and 10^{-3} are shown to illustrate the impact of the parameter.

consider here the *ground-truth saliency*: it is the heat map (2D-distribution) of the viewing patterns, obtained at each point in time from the users' traces. Here we compare HeMoG with the complete DL model TRACK. To compare HeMoG and TRACK fairly, we specify that TRACK is fed with the same type of visual content information as HeMoG.

6.3.3.1 Results

Fig. 6.4 presents the results of HeMoG fed with *ground-truth saliency* (named GTSal) with the value of $\beta = 0.1$ found in the train set. With $\beta = 0.1$, HeMoG performs similarly or slightly better than the DL model TRACK, which was shown to efficiently fuse the multi-modal inputs (See Chapter 5.6.3.3). Fig. 6.4 also presents the results of HeMoG for lower values of β. The value of β affects the coefficient of the attraction force $\gamma(s)$ (the coefficient of the visual input) through $\gamma(s) = 1 - e^{(-\beta s)}$. The higher the value of β the faster the growth of importance of the visual coefficient.

Given that TRACK features a dedicated recurrent neural unit for each of both input modalities (past position and frame saliency) and a recurrent neural unit for the fusion of the so-obtained embeddings, TRACK has the flexibility to learn various ways of combining both modalities. The fact that **HeMoG, with its fixed fusion scheme shown in Eq. 6.5 performs as well or better can be interpreted as TRACK performing a similar type of fusion as HeMoG**, which enables to benefit from both types of information (the lowest curves in Fig. 6.4 are lower than those with the positional modality only in Fig. 6.3). This is the second element of answer to **Q1**.

6.3.4 HeMoG Behaves as the DL Model and Lowers the Impact of a Noisy Saliency Estimate

In a non-ideal case where the saliency is not obtained from the viewing patterns but rather estimated from the content, we analyze the performance of HeMoG in comparison with TRACK. The extraction of visual saliency in 360° videos has been studied as an extension of image saliency [3]. However, additionally to the salient objects that can be found in images and videos, the motion of objects in the scene becomes an important cue specifically for videos [99]. For this reason we considered the *moving objects* as important cues to extract saliency from the 360° video content. The objects in each FoV of the scene are detected using YOLOv4 [100], the aggregation of all detected objects in all FoVs provides a binary map, shown in Fig. 6.5(c). To obtain the *moving objects* map shown in Fig. 6.5(d), we perform the element-wise product of the binary map and the norm of the pixel velocities computed in the 360° scene. This *moving objects* map obtained from the visual content is named the *content-based saliency* (CBSal).

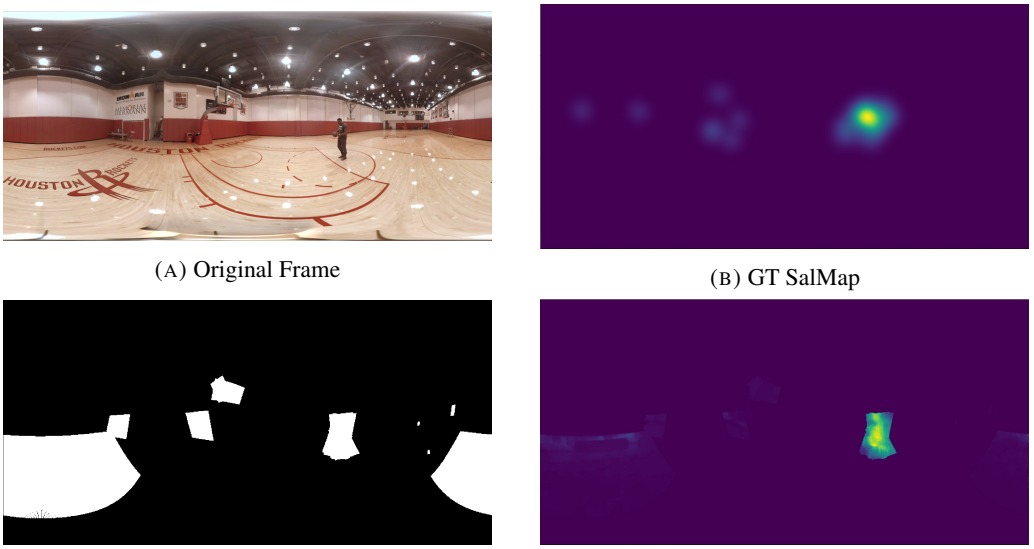

(A) Original Frame

(B) GT SalMap

(C) Detected Objects

(D) CB SalMap

FIGURE 6.5: Saliency map extraction from a frame of video '072'. **(a)** Original frame. **(b)** *Ground-truth saliency* map. **(c)** Detected objects map. **(d)** *Content-based saliency* map: *moving objects* map.

6.3.4.1 Results

In Fig. 6.6, we present the results of our model HeMoG against the DL model TRACK using the same visual information CBSal as input. First, we observe that both models increase their error significantly when they use a noisy input for the visual saliency. Second, contrary to what occurred with *ground-truth saliency*, HeMoG performance improves by reducing the value of β, in other words, by minimizing the impact of the CBSal input. Using a value of $\beta = 10^{-5}$, HeMoG approaches the performance of TRACK. **This reinforces the hypothesis that TRACK and HeMoG perform the same type of fusion**.

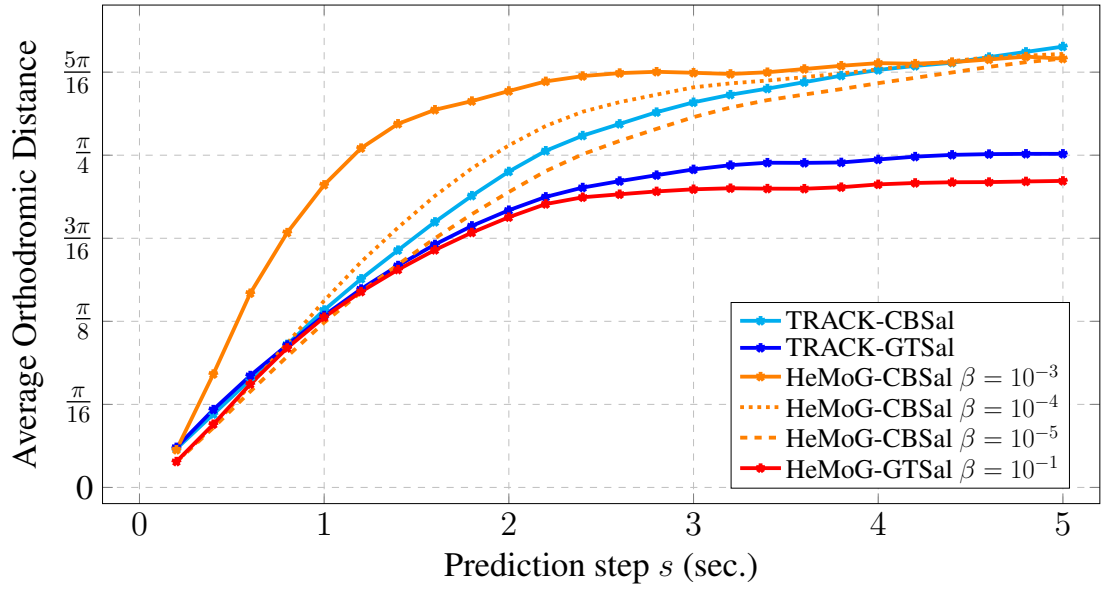

FIGURE 6.6: Prediction error of HeMoG with $\lambda = 2.5$, $\beta = 10^{-5}$ and *content-based saliency* (CBSal), compared with TRACK using CBSal. The curves of HeMoG and TRACK with GTSal are shown for reference. Other values of $\beta = 10^{-3}, 10^{-4}$ are shown to illustrate the impact of the parameter.

6.4 Impact of the Visual Saliency on Head Motion

In this section, we address Q2 by analyzing the impact of the visual saliency on head motion, in terms of the video category and the time-step in the *prediction horizon*.

6.4.1 Visual Saliency Impacts Head Motion Only for Certain Video Categories

The videos from the dataset of [5], contain heterogeneous scenes including music shows, documentaries, sports, movies, etc. More generally, [8] have identified the following main video categories for which they could discriminate significantly different users' behaviors: *Exploration, Static Focus, Moving Focus* and *Rides*. In *Exploration* videos, there is no specific attraction point and the spatial distribution tends to be more widespread and hence individual trajectories more difficult to predict. *Static Focus* videos are made of a single or few attraction areas (e.g., a standing person in an empty room). In *Moving Focus* videos, the attraction points move over the sphere. *Rides* videos are shot with the 360° camera moving. In this case, the attraction point for the user is usually the camera moving direction to minimize motion sickness.

We categorized each of the videos in the dataset of [5] into one of the four groups: *Exploration, Static Focus, Moving Focus* or *Rides*. The number of videos belonging to each of the classes is: 16 videos of *Rides*, 100 *Exploratory* videos, 74 *Moving Focus* and 18 *Static Focus* videos. In Fig. 6.7, we show some of the videos from the dataset with their respective category.

In Fig. 6.8, we present the results of HeMoG per video category, with CBSal and for different values of β. We expect that there is no much information for CBSal to capture from *Exploration*

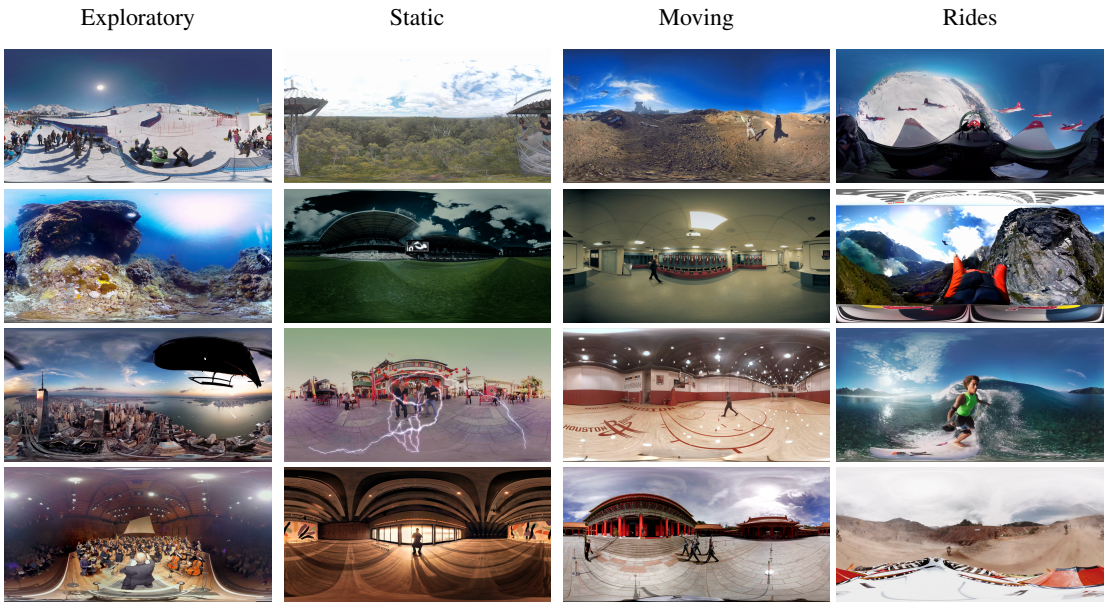

FIGURE 6.7: Some videos from [5], categorized into *Exploratory, Static (focus), Moving (focus)* and *Rides*

videos, and that CBSal cannot capture the relevant information from *Rides* videos. Indeed, CBSal is the product of the optical flow with the objects bounding boxes, and hence the camera direction where the optical flow is minimum cannot be highlighted as salient this way. Fig. 6.8 confirms that the lowest values of β are those providing best results for *Exploration* and *Rides* videos. HeMoG therefore reduces the weight of the saliency information in these cases (as it is also possibly the behavior of the DL model TRACK given its curve).

For the *Moving Focus* and *Static Focus* categories, we observe that when we increase the value of β, the error in the long-term decreases, showing the relevance of the saliency information for longer-term prediction. However, the error in the short-term increases, which we discuss in the next section. **These results with different optimal values of β per video category show that the impact of saliency on head motion is stronger for *Static Focus* and *Moving Focus* (and likely for *Rides* too) than for the *Exploration* category**.

6.4.2 Visual Saliency Impacts Head Motion Only After 3 Seconds

As discussed above, increasing β in *Static Focus* and *Moving Focus* videos lowers the error in the long-term *prediction steps* but degrades it in the short-term. This reveals a possibly not optimal choice of the $\gamma(s)$ function that controls the rapidity of importance growth of the saliency information over s. For now we have set, from Sec. 6.2, $\gamma(s) = 1 - e^{(-\beta s)}$. We ran numerical searches and identified that the values of $\gamma(s)$ that give the best performance of the

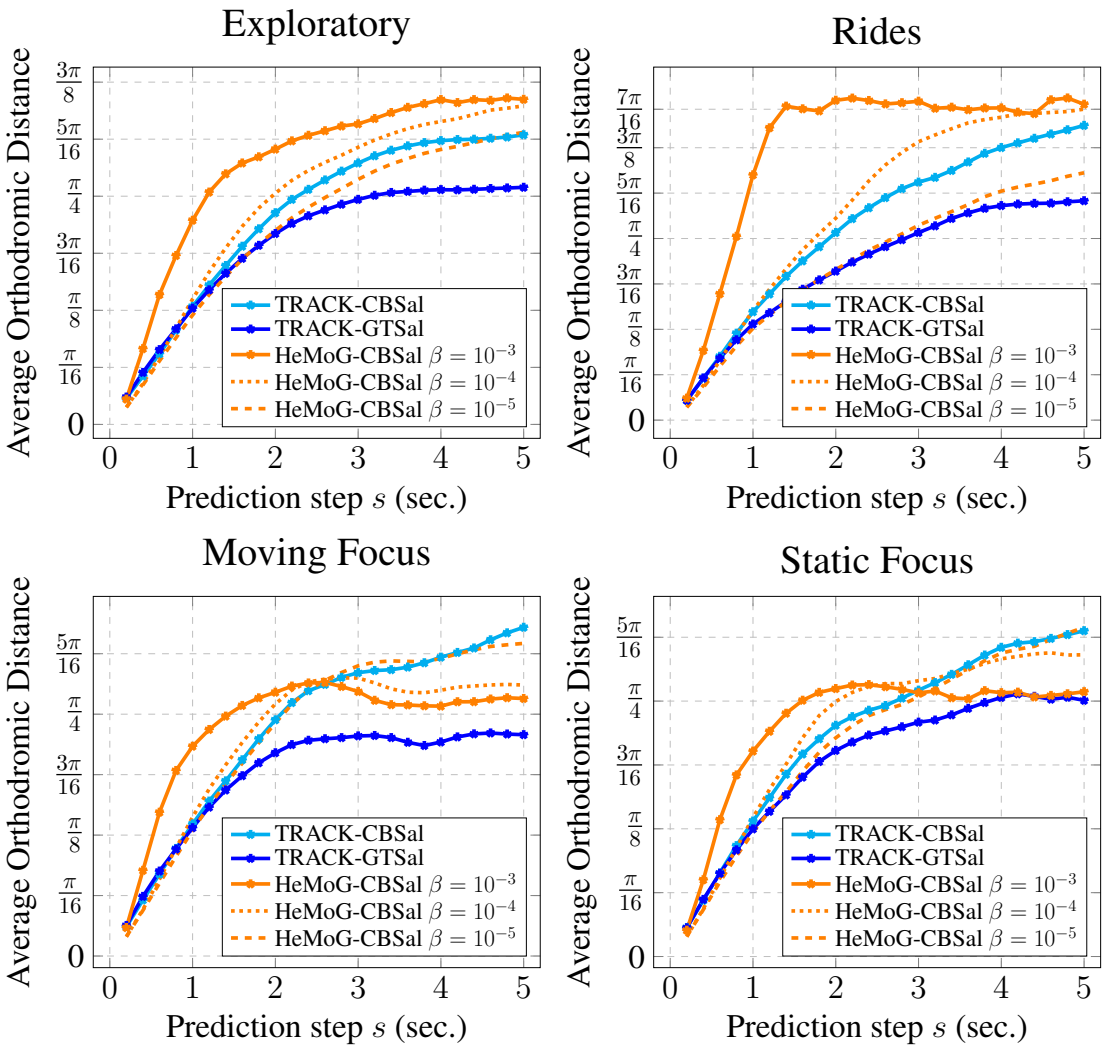

FIGURE 6.8: Prediction error of HeMoG compared with TRACK grouped per category. **Top-left**: *Exploratory*. **Top-right**: *Rides*. **Bottom-left**: *Moving Focus*. **Bottom-right**: *Static Focus*.

gravitational model per time-step are:

$$\gamma(s) = \begin{cases} 10^{-}5 & \text{if } 0 < s <= 3 \\ 10^{-}1 & \text{if } 3 < s <= 5, \end{cases} \tag{6.10}$$

from which we draw two conclusions. First, **the motion momentum is more important than the visual content in the first 2.5 seconds of the *prediction horizon*, and the visual content can inform the head motion prediction model only for horizons longer than 3 seconds**. Second, that a sigmoid-like function $\gamma(s) = \frac{C}{1+\exp(-\beta(s-S))}$ with additional parameters C for the scaling and S to center the transition from 0 to 1, would be a better fit. This is confirmed in Fig. 6.9 with the comparison of HeMoG when the parameters are set properly for the different categories and for each prediction step s. Let us note that this also shows that the DL model

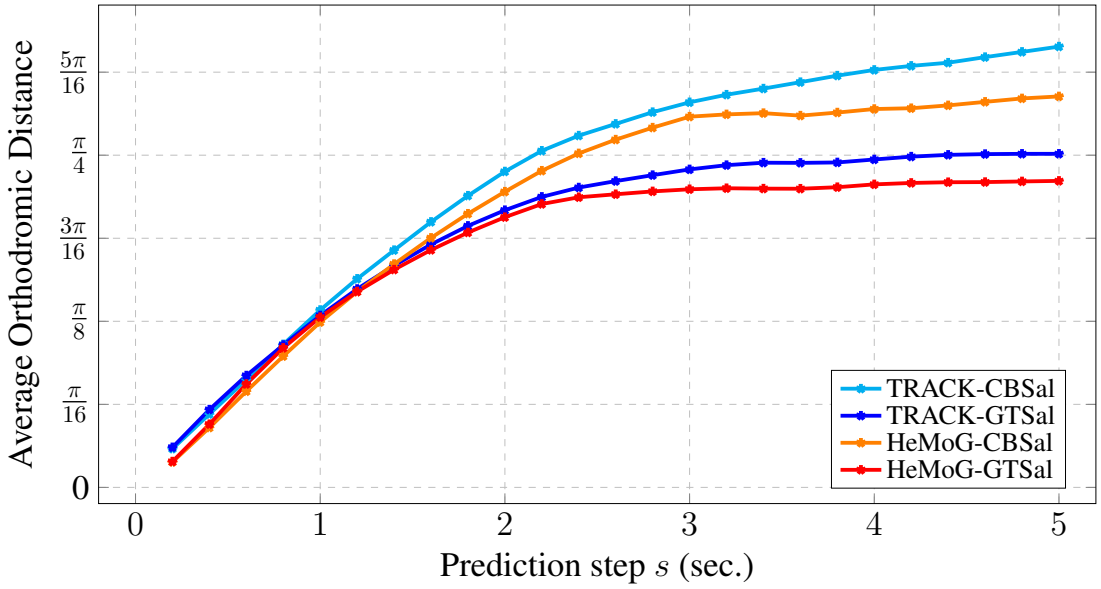

FIGURE 6.9: Results averaged over all video categories. HeMoG is set with $\gamma(s) = 1 - e^{(-\beta s)}$ and $\beta = 10^{-}5$ for *Exploratory* and *Rides* videos, and $\gamma(s)$ from Eq. 6.10 for *Moving Focus* and *Static Focus* videos, compared with TRACK. The curves of HeMoG and TRACK with GTSal are shown for reference.

TRACK is capable to learn and adapt to the different video categories, while the white-box approach is limited by the right choices of parameters. However, we show here that the differential equation model of HeMoG captures the main dynamics and yields performance similar to the DL models in average.

6.5 Discussion

Comparison of HeMoG with Deep Learning models: The main difference between both types of models is as follows. The latter are equipped with representation learning capability (learning how to extract relevant features from the saliency map they are fed) and able to modulate the weights assigned to momentum and saliency features in the fusion depending on the saliency and motion information (capabilities detailed in [101]). In comparison, HeMoG is able to properly fuse both types of information for any video, provided that the saliency information is the ground-truth. When it is not the ground-truth anymore (when fed with CB-sal), then the saliency weight β in the HeMoG model must be adapted to the video category. Also, we mention that when using other types of saliency extracted from the content, for example the saliency maps obtained from PanoSalNet [3], the performance of HeMoG shown in Fig. 6.10 is slightly worse than that of TRACK, which we explained by the lower level of information present in the estimated saliency map in relation with the user motion. On focus-type videos, TRACK is able to extract some useful information (improvement compared with *deep-position-only*), while HeMoG is not.

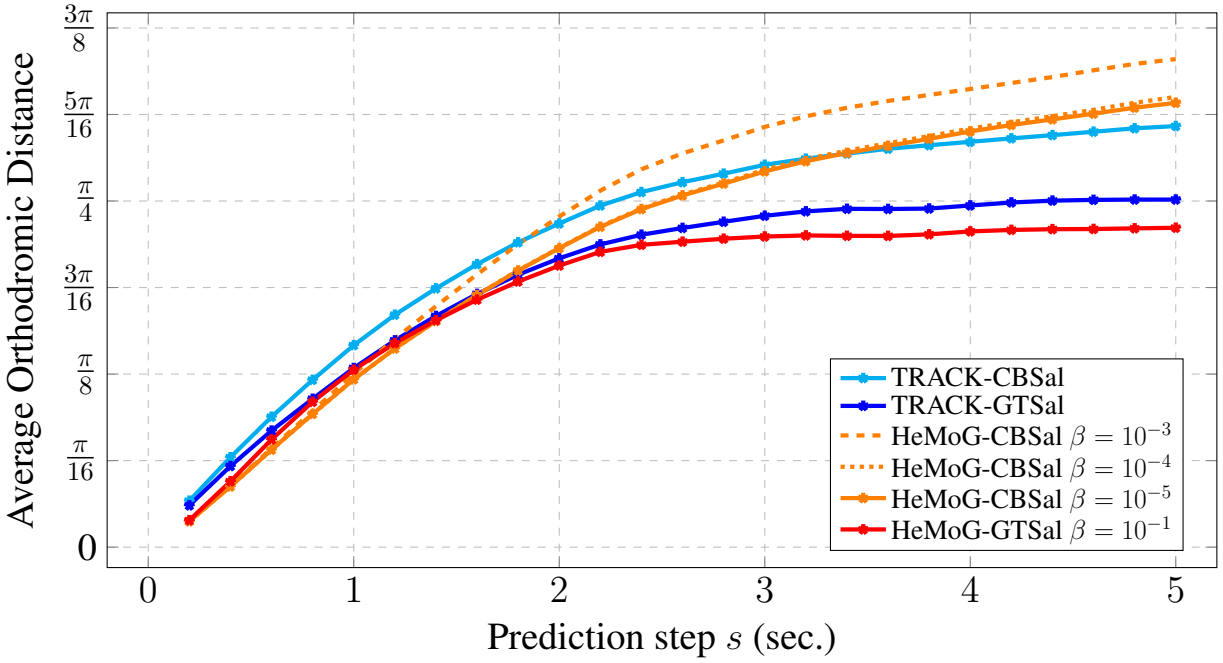

FIGURE 6.10: Prediction error of HeMoG with $\lambda = 2.5$, $\beta = 10^{-5}$, and *content-based saliency* (CBSal) computed from PanoSalNet [3], compared with TRACK using the same CBSal-PanoSalNet. The curves of HeMoG and TRACK with GTSal are shown for reference. Other values of $\beta = 10^{-3}, 10^{-4}$ are shown to illustrate the impact of the parameter.

Indeed, the Content-Based saliency obtained from PanoSalNet can be noisy, as we show in Fig. 6.11 with an original frame of video '072' and its extracted saliency with PanoSalNet, and the Ground-truth saliency from user statistics on this frame. While the salient object in the frame is the human, low-level features like the lights reflected in the floor and high-level features like the text written in the floor are taken into account by the saliency extractor, making the resulting saliency map noisy and more difficult to get motion-relevant information from.

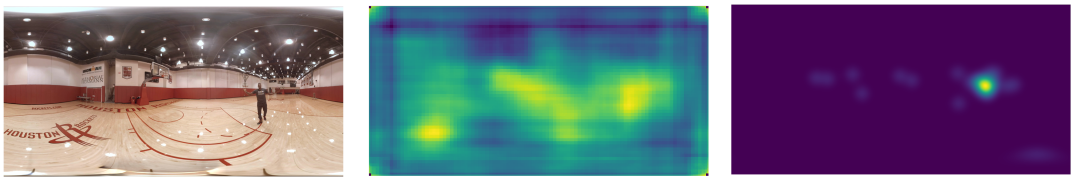

FIGURE 6.11: Saliency map extraction from a frame of video '072'. **(left)** Original frame. **(center)** *PanoSalNet saliency* map. **(c)** *Ground-truth saliency* map

Generalizing to more comprehensive saliency maps: While the study of this Chapter has been restricted to saliency attractors based on moving objects, we can consider extending to static objects whose importance can be ranked, meaning that the trajectory of focus of attention is also subjected to a gravitational field created by static objects [102, 103]. We can also study how to improve for the case of *Rides* scenes characterized by camera motion. To have more solid estimates of pixel velocities, methods for camera motion estimation [104] are already present in

the literature and can help in creating more suitable saliency estimates for the proposed model. The treatment of such complex scenes is left for future work.

6.6 Conclusions

In this Chapter we have investigated the human head motion process driven by attention when a user experiences an immersive 360° video. We have first introduced a new computational model named HeMoG, enabling to predict future head positions from the user's past positions and the visual content. HeMoG is built on differential equations obtained from the physics of rotational motion where the attractive salient areas in the 360° frames are represented as virtual masses. HeMoG is hence a white-box model and its (time-varying) parameters control the connection between visual content and head motion process. The performance of HeMoG are comparable with those of DL predictors, which we interpret as the DL models learning the same type of fusion as HeMoG: curvature continuity and momentum attenuation from friction in the short-term, diversion of motion with saliency attraction in the longer-term. The evolution of best parameter values in terms of video categories and horizon reveals that, on videos that are not exploratory, the initial motion momentum is most important until ca. 3s, after which the saliency weights more in the motion equation. Future works include refining the saliency extractor to feed the model with, and incorporating these findings into an attention-driven system to produce personalized immersive environments.

Chapter 7

Control Mechanism for User-Adaptive Rotational Snap-Cutting in Streamed 360° Videos

Predicting the user's head motion is difficult and can be done accurately only over short horizons (less that 2s, see [3] and Sec. 5). If the server makes an error in prediction and the level of bandwidth is sufficient to attempt sending again in High Quality (HQ) tiles previously sent in Low Quality (LQ), then the prediction error translates into a higher level of network bandwidth consumption. In 360° video streaming, the consumed data rate therefore depends on the prediction error, that is on the user's motion, which in turn depends on the user's attentional process and hence on attention driving techniques. Fig. 7.1 depicts this interplay, from which can arise interdisciplinary approaches to jointly design 360° video streaming algorithms and 360° film editing techniques.

If driving the user's attention is critical for a director to ensure the story plot is understood, in this Chapter we investigate attention driving techniques from a different perspective: that of the multimedia networking community. After presenting attention driving techniques based on user-adaptive rotational cuts in Sec. 7.1, related works are introduced in Sec. 7.2. Sec. 7.3 presents the problem formulation. The design of the learning approaches is presented in Sec. 7.4, and

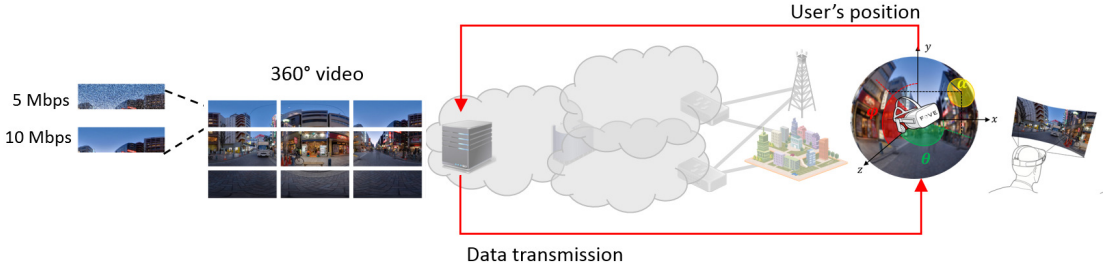

FIGURE 7.1: Streaming 360° videos: the sphere is tiled and each tile of the sphere is sent into low or high quality depending on the user's motion and network bandwidth.

Sec. 7.5 gathers the results and their analysis. Finally, the limitations of this preliminary work are discussed in Sec. 7.5.3, and conclusions are given in Sec. 7.6.

7.1 User-Adaptive Rotational Cutting for Streamed 360° Videos

The question of designing editing cuts to drive the user's attention in cinematic Virtual Reality (VR) has been under active investigation for the last 3 to 4 years.

In [26], for the first time, Dambra et al. have showed that film editing can be helpful for streaming 360° videos by directing the user's attention to specific pre-defined Regions of Interest (RoI), thereby lowering the randomness of the user's motion and using this a-priori knowledge in the streaming decisions (consisting, at each point in time, in deciding which area/tile of which video segment to send in which quality). This is done by periodically regaining control on the user's FoV using so-called snap-changes, which are a type of intra-scene rotational cuts. They are interchangeably called snap-cuts. The details of the method and its positioning with respect to the relevant literature are provided in Sec. 7.2. Dambra et al. showed that it is beneficial both for application-level metrics (level of quality in FoV, consumed bandwidth) and user-experience metrics (user's angular speed, story understanding). Their results are a proof-of-concept where the set of cuts is pre-defined in an Extensible Markup Language (XML) file by, e.g., the film director, and all cuts are executed at their corresponding time instants. However, snap-cuts are forced re-positioning corresponding to momentaneously taking some freedom off of the user. These intra-scene cuts can hence be envisioned as levers that the 360° video player can leverage to cope with an insufficient bandwidth and still succeeding in displaying HQ in the user's FoV (which gets re-positioned in front of the HQ area). Every cut may hence not always be necessary:

- if the user will be close enough to the FoV targeted by the cut: this is implemented by the 30°rule already implemented in the original method [26] (with a moderate impact on the quality downloading decision)
- if the network bandwidth is high enough so that replacements are possible and not costly, and/or
- if the user moves slowly enough that the spatial qualities fetched earlier for each area/tile overlap sufficiently the FoV at the time of playback (so the cut will not help increase the quality in the FoV).

Whether or not a cut will be beneficial therefore depends on the user's motion and on the network conditions. Specifically, the trade-off involves: (i) a snap-change guarantees that the user will see the FoV desired by the director, and that HQ is displayed in this FoV, while (ii) not having a snap-change may preserve the level of presence and keep low the probability of disorientation.

In this Chapter, we consider the network conditions being fixed and investigate how to optimize cut triggering to obtain best trade-off, by designing a user-adaptive editing policy for 360° video streaming.

7.2 Related works

This section reviews the main categories of existing works relevant to the problem at hand. We provide successfully an overview of techniques to partly control the user's FoV, introduce the concept of adaptive 360° video streaming and the required adaptation to the user, and finally review some ML-based approaches for various questions arising with 360° videos.

7.2.1 Directing Change of FoV

The works presented in [105, 106, 107] are aimed at assisting the user in moving in the virtual environment to increase comfort and/or lower sickness, while those presented in [108, 109, 110, 111, 26] consist in operating FoV changes independently from the user's motion or will. In [106], amplified and guided head rotation are introduced for seated use of VR in HMDs: physical head rotation angles are magnified in the Virtual Environment (VE) so that physically turning in a (limited) comfortable range can allow wider range. In [107], Farmani et al. show that it is possible to artificially reduce vection − the illusion of self-motion, which is connected to cybersickness − by snapping the viewpoint, reducing continuous viewpoint motion by skipping frames. They show that both rotational and translational snapping reduce cybersickness by 40% and 50 %, respectively. In [112], the authors compare an auto-pilot mode deciding which FoV is exposed to a seated user, independently of the user movements, with assisting the user by displaying an arrow of where to look. In [108] and [109], user-initiated (by pressing a button) and system-initiated rotational re-positioning of FoV are performed, independently of the user motion. The re-positioning is progressive and while participants could most easily track scene changes, they generally and unsurprisingly experienced sickness due to rotational vection. Much interestingly, it has been uncovered in [110] that participants can automatically update their sense of spatial orientation during rotation using only visual cues, and that the accompanying physical rotation may not be necessary for fast and reflexive updating. Also, how cut frequency influences viewers' sense of disorientation and their ability to follow the story has been studied in [113]. The results show that high editing cut frequency can be very well received, as long as the user's attention is appropriately guided at the point of cut. In [111, 26], the authors introduce so-called dynamic editing with (rotational) snap-changes, combining the positive aspects of the above methods: to periodically regain control over the user's FoV at the time of 360° video playback (these intra-scene cuts are hence not built into the video file), the FoV is repositioned, in a snap, that is from one frame (image) to the next, in front of a pre-determined FoV (possibly decided by the director). To do so, only an additional XML file has to be downloaded at the

begining of the video, and the custom player [114] implements the snap-changes at the indicated times in front of the indicated angular sectors. Fig. 7.2 depicts the effect of a snap-change on the FoV. It is shown in [26] that this strategy enables to reduce the average head motion speed by up to 30%, that these repositionings are mostly not noticed by the users when performed towards a meaningful RoI (possibly perceived as fast-cutting, which may sometimes feel like missing in cinematic VR), and when they notice it, no discomfort or sickness are yielded as no motion is sensed, and the vestibular system is not involved. It is also shown that incorporating the knowledge of the future snap-changes into the adaptive streaming algorithm enables bandwidth savings, as described below.

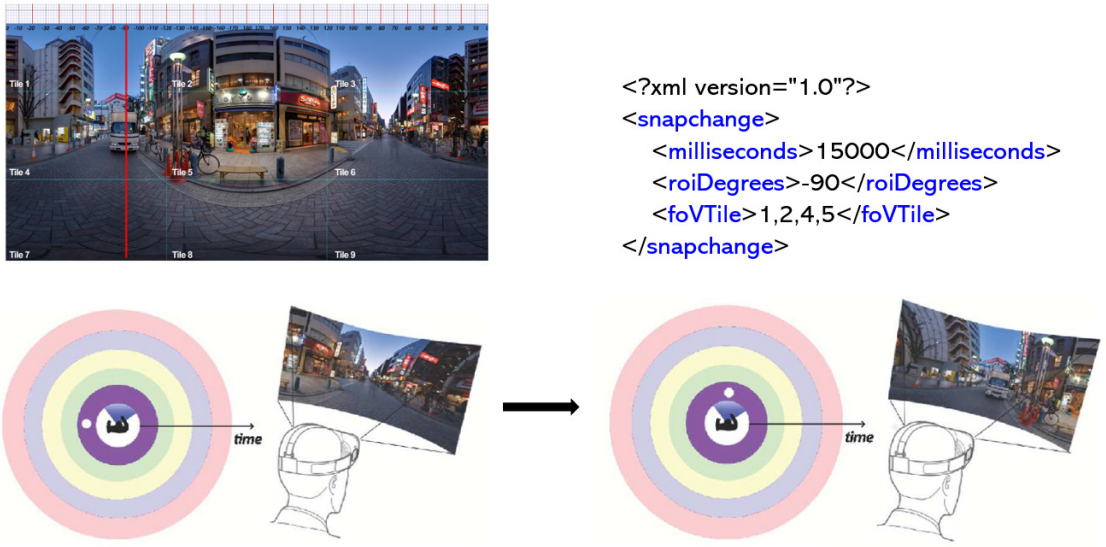

FIGURE 7.2: Top left: Identification of the RoI targeted by the snap-change. Top right: Description of the list of snap-changes over the video as an XML file.
Bottom: FoV re-positioning in front of the targeted RoI by the snap-change.

7.2.2 Adaptive Streaming for 360° Videos

Modern (regular non-360°) video streaming relies on the concept of HTTP Adaptive Streaming, whose most wide spread version is the MPEG-DASH standard [42]. It consists in the video file being chunked into temporal segments of fixed duration (often 2 sec. or 5 sec.), each encoded into several quality levels, that is at different bitrates (often corresponding to resolutions). The client strives to (i) prevent playback interruptions by maintaining a non-empty playback buffer where a certain number of segments (or seconds of video) are stored in advance of playback, while (ii) fetching and displaying qualities as high as possible. To do so, the client runs a so-called adaptive streaming logic (or algorithm) which chooses which quality to request for every segment to the remote server, based on the network bandwidth varying over time. In the case of 360° video streaming, a single segment does not correspond anymore to a single entity, but possibly to several tiles. The goal is to reduce the required bandwidth to stream 360° videos

by requesting high quality for the tiles that will intersect the FoV of the user. The qualities to request for every tile of every segment must therefore adapt both to the network and the user dynamics, as represented in Fig. 7.3. The challenge is that at the time of the decision, the future of the network bandwidth (which will support the currently decided object to download) and the user motion (which will determine where will the FoV be at the time this segment is played out) are unknown. Most recent examples of strategies addressing this difficult problem are [115, 116], which strive to predict network bandwidth and user's motion with recurrent deep neural networks. The innovative interdisciplinary approach presented in [26] consisted in not trying to predict the future user's motion (which is much difficult to do as presented in Sec. 5), but instead in designing a 360° adaptive streaming algorithm which benefits from the knowledge of the future rotational cuts to better target which tile must be fetched in HQ. The bandwidth savings yielded by such approach have been shown to be substantial (up to 25%). In [117], a first attempt of learning how to trigger snap-changes of [26] is demoed. It implements a deep Reinforcement Learning (RL) strategy to adapt to the user's motion, without proving that it can work better than a simple baseline, nor quantifying the gains. In the present Chapter, we present the design of a complete learning framework addressing the problem of FoV overlap (quality) prediction and snap-change triggering decision, to best trade between quality in FoV and user's freedom while streaming a 360° video over a bandwidth-limited network.

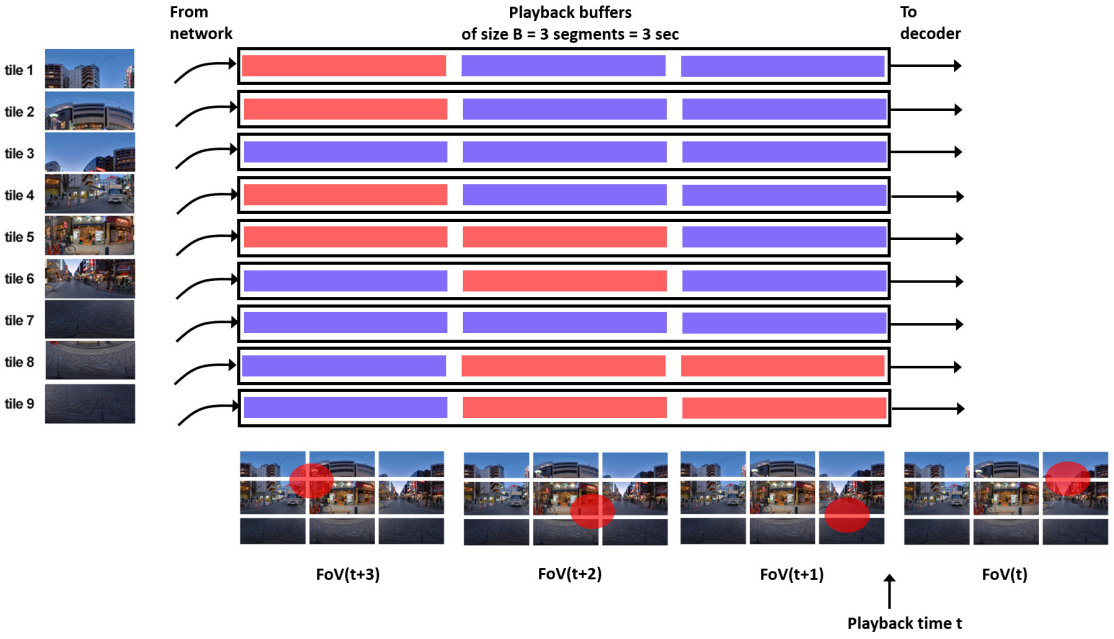

FIGURE 7.3: Buffering process for a tiled 360° video. While segment n is being decoded at time t, segment $n + B$ is being downloaded. Red (resp. blue) rectangles represent tiles' segments in HQ (resp. LQ). Idealistically, the tiles in HQ must match the user's FoV at their time of playback.

7.3 Problem Definition

In this section, we first expose, in Sec. 7.3.1 all the system and model assumption we make (that we implement in our simulator used for training and analysis in 7.4 and Sec. 7.5), before formally describing the optimization problem in Sec. 7.3.2. The notations are provided in Table 7.1.

7.3.1 System Assumptions

System assumptions: As aforementioned, a 360° streaming strategy has to be both network- and user-adaptive. In this work, we focus on how to adapt the frequency of the snap-changes to the user's motion and maximize their level of experience − a Quality of Experience (QoE) function defined in Sec. 7.3.2. Therefore, we set fix the underlying streaming strategy, detailed in Algo. 3, working as follows. We consider (wlog) that 2 quality levels are available. The qualities (HQ or LQ) for every tile of every segment are decided based on the current user's FoV at the time of downloading this tile (HQ for the tiles intersecting the FoV, LQ for the others). The tile's download can occur up to B seconds before its playback, where B is the size of the playback buffer. We consider the time to download a tile negligible. The downloading process pauses when the buffer is full, and resumes when at least one segment has been dequeued and fed to the video decoder. We consider that the list $\mathcal{C}$ of potential snap-changes is loaded with the video description file before the playback starts (each snap-change is described as depicted in Fig. 7.2-top right). We then augment the streaming strategy as described in Algo. 3: when the first tile of a new segment is about to be downloaded, if the list of possible snap-changes indicates that a snap-change may be trigger at this segment, then a decision function is called to decide whether this snap-change should be triggered to maximize the objective function described below. Designing such a snap-triggering decision function is the subject of this Chapter.

7.3.1.1 QoE Model Assumptions

We model the user's reaction to the triggering of a snap-change. It has been shown in [26, Fig. 11], with user experiments, that snap-changes decrease the head motion speed of users by up to 30%. In the simulations used in this Chapter (later used to train classifiers), we use the user motion dataset presented in [17], which contains the head tracking data of 57 users exploring 19 videos. In this dataset, considering a FoV to be about 100° wide [2], it takes about 5 sec. for 50% of the users to shift their FoV entirely. This can be seen in Sec. 5.4.1[Fig. 5.11]. In this Chapter, we adopt a preliminary simplistic user model: considering that a 30% decrease in angular speed would add 1.5 sec. to shift the field of view of half of these users, we consider in our simulator that right after each triggered snap-change, repositioning the user in front of a meaningful/interesting FoV, every user pauses for 2 sec. before resuming her motion.

System param.	Definition
N ($\mathcal{N}$), W ($\mathcal{W}$)	number (set) of segments, tiles
C ($\mathcal{C}$)	number (set) of possible snap-changes
B	playback buffer size (in sec.)
$q_m(n) \in \{0, 1\}$	quality level of tile w at segment n
$buf_m(t)$	num. of sec. stored in buffer of tile w at time t
$time(c)$	playback time of snap-change c
$FoV_{snap}(c)$	FoV targeted by snap-change c
$flag_{decided}(c)$	$= 1$ if the decision for c is made, $= 0$ ow.
$flag_{trigger}(c)$	$= 1$ if c has been decided to be triggered, $= 0$ ow.
$w_{past}(t)$	time interval $[0, t]$
$w_{fut1}(t)$	time interval $]t, t + B]$
$w_{fut2}(t)$	time interval $]t + B, t + B + G]$
Model param.	**Definition**
G	duration of snap-cut impact on user's motion
ϱ	penalty for triggering a snap-change

TABLE 7.1: Notation of the system and model parameters.

Algorithm 3: Downloading process: quality allocation and snap-change triggering decisions

Data: Current playback time t. Buffer states $buf_w(t)$, $\forall w \in \mathcal{W}$. List of possible snap-changes $c \in \mathcal{C}$. Initially $flag_{decided}(c) = 0$ and $flag_{trigger}(c) = 0$, $\forall s \in \mathcal{C}$.

Result: which segment n of which tile w to download next in which quality $q_w(n)$, whether to trigger a snap-change if n has one not decided yet, $\forall w \in \mathcal{W}$, $n \in \mathcal{N}$, $q_w(n) \in \{0, 1\}$

if *all W buffers are full* **then**
    stay idle;
else
    set w to the tile index with the least full buffer;
    set n to the lowest value not having entered buffer m yet;
    $q_w(n) = 0$ # initialize with LQ;
    if *there exists a snap-change c such that time(c)= n* ***and*** $flag_{decided}(c) = 0$ **then**
        # Whether this snap-change will be triggered at time $time(c)$ must be decided now;
        form environment state $state(t)$;
        $flag_{trigger}(c)$ =decision($state(t)$);
        $flag_{decided}(c) = 1$;
    identify the highest snap index c_{last} with $flag_{trigger}(s_{last}) = 1$;
    if *c_{last} not empty* ***and*** *$t \leq$time(c_{last})$\leq n$* **then**
        if *w intersects snap-change's $FoV_{snap}(c_{last})$* **then**
            $q_w(n) = 1$ # download in HQ;
    else
        if *w intersects current user's FoV(t)* **then**
            $q_w(n) = 1$ # download in HQ;

7.3.2 Formulation of the Optimization Problem

To formulate the decision problem, we adopt a model for the level of user's experience under adaptive 360° streaming and snap-changes. We define an instantaneous reward obtained after the playout of segment n (of duration 1s in the simulator):

$$r(n) = q_{FoV}(n) - \varrho^{t(n)-t_{last}(n)} \ . \tag{7.1}$$

The components are as follows. We define the average quality in the FoV over segment n's duration as $q_{FoV}(n) = \sum_{w=1}^{W} q_w(n) Fr(n,w)$, with $q_w(n)$ the quality level of tile w at segment n, and $Fr(n,w)$ the average fraction of FoV at segment n occupied by tile w. The second component represents the penalty incurred by triggering snap-changes: ϱ is a penalty parameter, $t(n)$ is the playback time of segment n (close to n depending on playback interruption), and $t_{last}(n)$ is the time of the last triggered snap-change.

Let us denote by S_u the state of the streaming process (tiles' qualities stored in the buffer) and user's state (past head coordinates but also fatigue, likeliness to move) at the time of deciding for snap-change c. Given that the decision of triggering each snap is taken at the time of downloading it, hence of it entering the playback buffer, S_{u+1} is independent of what happened before u conditionally on S_u, and hence the Markov property is verified. The snap triggering problem is therefore a Markov Decision Process defined by the tuple $(\mathcal{S}, \mathcal{A}, \mathcal{P}, \mathcal{R}, \gamma)$, where $P^a_{ss'} = Pr[S_{u+1} = s' | S_u = s, A_u = a]$, $R^a_s = \mathbb{E}[R_u | S_u = s, A_u = a]$. The time is paced with snap-triggering decisions, $a \in \{0,1\}$, and $R_u = \sum_{n \in N(u)} r(n)/|N(u)|$ where $N(u)$ is the segments played between both snaps decided at u and $u+1$. We define $\pi(a|s) = Pr[A_u = a | S_u = s]$ and formulate the snap-change triggering optimization problem as:

$$\pi^\star = \arg\max \mathbb{E}\big[\sum_{u=0}^{C-1} \gamma^u R_u \big] \ . \tag{7.2}$$

The optimal snap-triggering strategy must therefore trigger a snap-change when the contribution, to the cumulative reward, of the quality increase due to this snap exceeds the incurred penalty. It therefore must trigger depending on the user's motion. The transition probability distribution $P^a_{ss'}$ is unknown as, to take online decisions sequentially, we cannot know how the user is going to move and react, given a certain state. The decision-making problem is hence that of model-free RL.

Finally, it is interesting to notice that other forms of similar problems have appeared in much different application domains. In [118], Pineau et al. present how to automatically learn an optimal neurostimulation strategy for the treatment of epilepsy. The goal is to trigger the minimum amount of neurostimulation (electric discharge from intra-cerebral electrodes) as a function of the Electroencephalogram (EEG) signal, so as to minimize the number of seizures.

7.4 Learning How to Trigger a Snap-Cut

For the reasons exposed in Sec. 7.3.2, deciding dynamically during the video playback how to trigger a snap-change is a model-free RL problem. However, rather than designing an RL agent learning from its own observations, we instead leverage here the principle of learning from expert's demonstration, also known as Imitation Learning (IL) [119]. In our case, for the short videos considered, we indeed have access to an expert which is the *offline optimal* defined below in Sec. 7.4.1. We consider in this Chapter the simplest version of IL, known as Behavioral Cloning (BC) [119]. It consists in supervising the training of the action policy/decision classifier (deciding whether or not to trigger the next snap-change), with the trigger labels provided by the *offline optimal*. A major design difficulty is the possibly loose correlation between the past motion at time t, and the decision to trigger snap c decided at time t but impacting user's motion only from time $t + B$, as represented in Fig. 7.4. We therefore split the snap-triggering problem at time t into 2 sub-problems: (P1) predicting the FoV overlap over $w_{fut2}(t)$ from $w_{past}(t)$ (as defined in Table. 7.1 and shown in Fig. 7.4), and (P2) deciding whether to trigger based on the series of predicted overlaps.

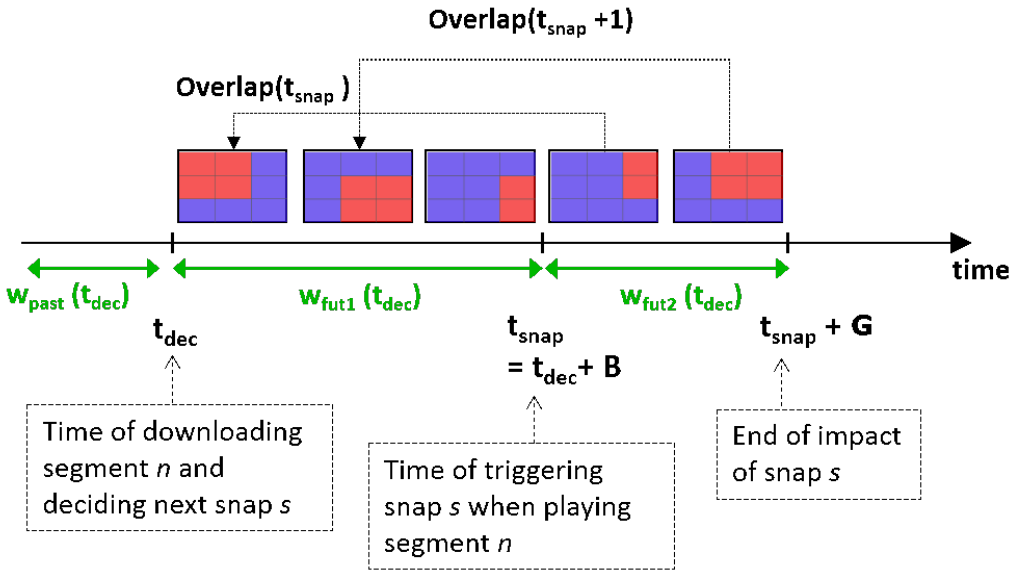

FIGURE 7.4: Timing of the process: the tiles' qualities displayed at time t have been downloaded at time $t - B$. If segment n to be downloaded at time t_{dec} and to be played at $t_{dec} + B$, contains a possible snap-change c, either (i) this snap is not triggered, then the quality in the user's FoV at any $t \in w_{fut2}(t_{dec})$ is given by $overlap(t) = FoV(t) \cap FoV(t - B)$, or (ii) it is triggered, then only HQ is displayed in the FoV as the qualities fetched at $t - B$ are based on the snap-change's FoV $FoV_{snap}(c)$.

7.4.1 Definition of Expert and Baseline

We consider supervised learning and the labels being the optimal decisions. With the perfect knowledge of the user's motion over the entire video, we are able to compute the set of optimal

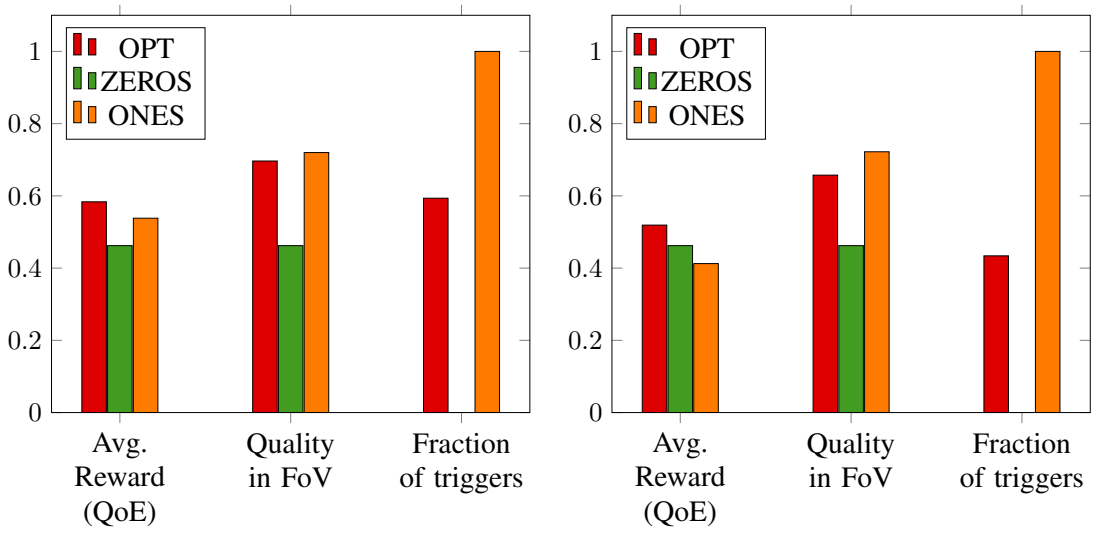

FIGURE 7.5: Reward, quality and snap frequency for the optimal prediction and for the control baselines: always trigger (ONES) and never trigger (ZEROS). The parameters are: FoV Area: 100°x50°, regular snap interval of 3 sec., $G = 2$, $B = 4$ (Left) $\varrho = 0.2$, (Right) $\varrho = 0.35$.

decisions for each trace, corresponding to a given user watching a given video. This *offline optimal* solution is computed with Dynamic Programming. This is feasible in reasonable time only if the number of decisions is not too high. In Sec. 7.5, we consider 20 sec-long videos with a possible snap-changes every 3 sec., hence a total of 7 snap-changes. Fig. 7.5 illustrates, for $B = 4$ and $\varrho = 0$ and 0.2, the gain of the *offline optimal* (*OPT* in legend) over two baselines: *ZEROS* where no snap-change is triggered, and *ONES* where every snap-change is triggered. Let us now present how to design online decision strategies able to outperform the baselines and approach the *offline optimal* as much as possible.

7.4.2 P1: Prediction of Future Overlap

As shown in Fig. 7.4 and defined in Sec. 7.3.2, the quality in the user's FoV at any time t is given by $overlap(t) = FoV(t) \cap FoV(t - B)$. One set of inputs we feed the decision classifier with at the decision time t_{dec}, is therefore the prediction of the D values of overlap over $w_{fut2}(t_{dec})$, i.e., $FoV(t_{dec} + B + w - B) \cap FoV(t_{dec} + B + w)$ for $w \in \{0, \ldots, G\}$. We consider two options to solve P1.

Past Overlap as estimate of future overlap: The D overlap values anterior to t_{dec} are considered as those over $w_{fut2}(t_{dec})$.

Future overlap estimation from FoV prediction: The deep neural network architecture named TRACK and introduced in Sec. 5 is used to predict the series of FoV positions between t_{dec} and $t_{dec} + B + G$, from (i) the series of FoV positions anterior to t_{dec} and (ii) the visual saliency extracted from the video content available for the entire video (streaming of pre-recorded content).

7.4.3 P2: Classification to Decide Whether to Trigger a Snap-Cut

The goal of the decision step is to classify whether the snap-cut should be triggered (1) or not (0). A Decision Tree (DT) is used to perform this classification, as it provides a simple yet informative structure that allows to investigate how the different configurations of the environment change the way the input features are used. The inputs are set to be as close as possible to the reward's components defined in Eq. 7.1: the overlap values predicted over $w_{fut2}(t_{dec})$ as described above, and input describing the relative snap position in time. The latter is made of the elapsed time since the last snap-cut triggered ($t(n) - t_{last}(n)$ in Eq. 7.1), and the remaining playback time after the playback time of the snap (to represent the likely impact of the snap, impacting less the cumulative reward as we reach the end of the video).

7.4.4 Training the Complete Framework

The training of the snap-cut decision framework is not in an end-to-end manner. TRACK is pre-trained to provide the overlap predictions, the DT decision classifier is trained on top. The dataset is split into 70% for training, 20% for testing and 10% for validation. The training, validation and test sets are the same for both overlap prediction and decision layers. We perform hyper-parameter tuning by varying the maximum tree depth in the range $[1, 10)$, and selecting the depth yielding the highest F1-Score (defined as the harmonic mean of precision and recall) on the validation set. During train, the $t(n) - t_{last}(n)$ input above is fed from the *offline optimal*. However at test time, the input is determined from the previous decisions already made. The test is therefore made in an iterative process, where the previous decision will affect the future ones.

7.5 Evaluation

We present here the performance in terms of reward, quality in FoV and fraction of snap-cut triggered, for the different baselines and proposed dynamic methods for different values of buffer size (B in sec.) and snap-cut penalty ϱ. We identify the difficulties and discuss the limitations in Sec. 7.5.3.

7.5.1 Simulator Settings

The results in this section are generated with an emulated streaming process developed in Python and serving as training and testing environment. Given the simple user's behavior model introduced in Sec. 7.3.1 where the user's reaction does not depend on the FoV targeted by the snap-cut, we consider equally spaced possible snap-changes to trigger, with the FoV for each picked uniformly at random in $[-180°, 180°[$. From Sec. 7.3.1, the snap-cut impact duration is $G = 2$s. One video segment corresponds to one second of playback. Playback starts at second 0, the first possible snap at second 1, and possible snap-changes are evenly spaced every 3s.

With the 20 sec-long videos in the dataset of David et al. [17] described in Sec. 7.3.1, there are 7 possible snaps, occurring at times $\{1, 4, 7, 10, 13, 16, 19\}$.

7.5.2 Results

7.5.2.1 Results on Overlap Prediction

As a preliminary result, Table 7.2 compares the error (overlap computed as orthodromic distance of the centers of the FoVs) of overlap prediction for both methods for P1 (PAST-Past overlap and TRACK), when varying the buffer size. We confirm the interest of employing a refined FoV predictor in lowering the overlap prediction error.

	B=2	B=3	B=4
PAST	40.79°	42.42°	45.54°
TRACK	36.07°	37.17°	36.74°

TABLE 7.2: Absolute error of (TRACK) future overlap prediction using TRACK or (PAST) estimating the future overlap from the past overlap, varying the buffer size $B \in \{2, 3, 4\}$.

7.5.2.2 Results on Reward, Quality and Snap Frequency

Fig. 7.6 depicts the results in terms of reward, quality in the FoV and percentage of triggered snap-cuts. The values for playback buffer size B (still in sec.) and snap penalty ϱ are the combination of $B \in \{2, 3, 4\}$ and $\varrho \in \{0.2, 0.3, 0.35\}$. One baseline is added: *GT*, standing for Ground Truth, when the DT is fed with the GT overlap over $w_{fut2}(t_{dec})$, for every decision time. It refines the upper-bound accessible by the online methods predicting the future overlap.

First, general and expected trends can be observed from *OPT*. The optimal reward decreases when B or ϱ increase. So does the quality. Indeed, the higher B, the lower the FoV overlap between t and $t - B$, for any time t, hence the lower the quality, hence the reward (we can trigger a snap only every 3 sec., i.e., every 3 segments, with these settings). The optimal fraction of triggers increases with B but decreases with ϱ. Indeed, the higher B, the lower the FoV overlap, the more snap-cuts needed to get back a high quality. However the higher the snap-cut penalty ϱ, the lower the amount of snap-cut allowed to not decrease the reward. Second, *GT* is relatively close to *OPT* when ϱ is small, but gets away from *OPT* when ϱ increases: this shows the need of not being myopic and considering a future horizon longer than $w_{fut2}(\dot{})$ to make decisions, when the snap penalty ϱ increases. Third, it is interesting to observe that the gap between *OPT* and the best of both *ZEROS* and *ONES*, where online methods can bring improvement, is greater for higher values of B and intermediate values of ϱ (for example, $B = 3$ and $\varrho = 0.2$, or $B = 4$ and $\varrho = 0.3$). In these cases, the online methods *PAST* and *TRACK* (not assuming any knowledge of the future) are able to slightly outperform (in reward) the *ZEROS* and *ONES* baselines. However, when observing their snap-cut triggering decisions, we observe that for $\varrho \geq 0.3$, they often are much more conservative than *GT*, triggering almost no snap-cut.

In such case of high ϱ, for high B (3 and even more so 4), the quality is much impacted by the lower accuracy of future prediction.

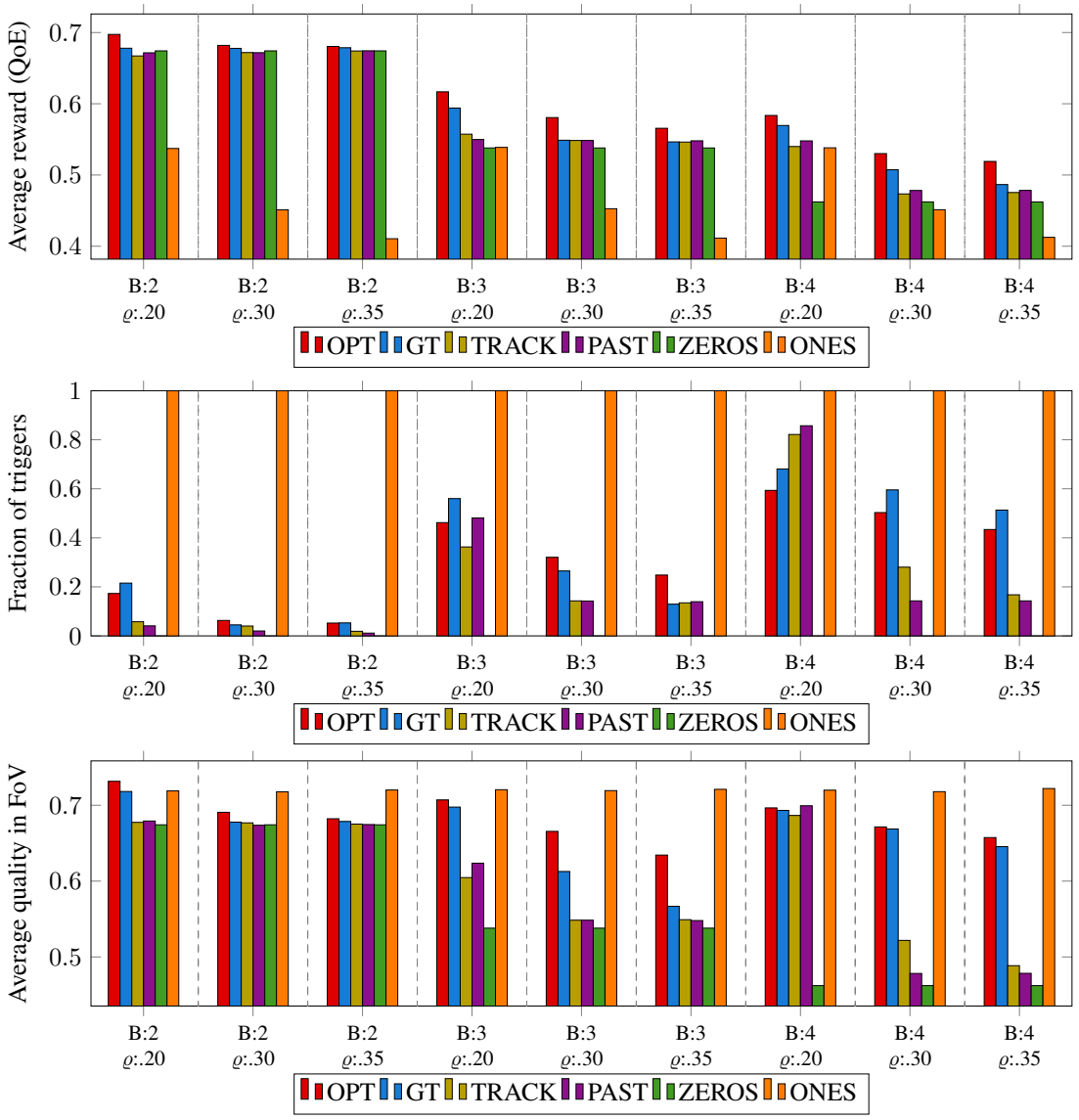

FIGURE 7.6: **(Top)** Average reward (QoE), **(Center)** fraction of triggered snap-changes and **(Bottom)** average quality in FoV, for each method in OPT: Optimal, GT: Using the groundtruth future overlap as features, TRACK: Using the overlap computed with the prediction from TRACK (Sec. 5), PAST: Using the overlaps before the decision, ZEROS: Never triggering a snap, ONES: Always triggering the snaps. The values are computed for each of the experiments, varying the buffer size B, and the penalty for triggering a snap-change ϱ.

7.5.3 Discussion

In this Chapter we define and investigate how to learn to trigger (rotational) snap-cuts meant to jointly benefit the user and the streaming algorithm to increase the user's QoE. It is however a preliminary work, suffering from several limitations. First, in comparison with *GT*, we can observe that the performance of the proposed method *TRACK* (even more so *PAST*) is limited

by the difficulty of predicting the overlap (the prediction horizon is $B + G$ sec., 4 to 6 sec. here). To overcome this difficulty, it will be important to extract less volatile features that can be exploited in deciding to trigger, particularly user or video profiles. Second, the considered model of user's reactions to a snap-cut (freezing for G sec.) and the QoE model (for the reward) are simplistic. Future work should carry out user experiments to determine accurate models, and considering complex or unknown reaction models will require to adopt other types of learning approaches (RL approaches where the test set is collected using a behavior policy different from the target policy). Finally, the snap-cuts are modulated here to help the streaming process (using a playback buffer). However, we have considered the network state fix and the streaming logic independent of the available bandwidth. Future work will design advanced network-adaptive strategies making use of user- and content-adaptive snap-cutting strategies.

7.6 Conclusions

In this Chapter, we have investigated user-centric film editing rotational snap-cut techniques to guide the user's attention. We have studied control mechanisms to learn how to dynamically trigger rotational snap-cuts that re-position a user in front of new FoV, when watching a VR content streamed over the Internet. These snap-cuts can benefit the user's experience both by helping stream and improve the quality in the FoV, and ensuring the user sees RoIs important for the story plot. However, snap-cuts should not be too frequent and may be avoided when not beneficial to the streamed quality. We have formulated the snap-cut triggering optimization problem and investigated possible gains in quality of experience. We have shown that learning approaches are relevant to design online snap-cut triggering strategies to outperform baselines. Finally, we have identified the limitations of this preliminary work and the future steps to take.

Chapter 8

Conclusions and Future Work

8.1 Conclusions

In this dissertation we present our comprehensive processing chain tailored to the streaming of Virtual Reality videos. We contributed to VR streaming systems with prediction and optimization of guidance techniques to maximize the streaming quality. We split this work into six main contributions.

The first contribution in this processing chain is the design of a reactive transcoder to structure the VR content and decide what to send and when driven by the user's gaze position.

Chapter 3 introduced our first step to make high-performing foveated streaming systems. Our streaming architecture adapts to the user's gaze position by focusing the quality in the gaze target and delivering low-quality blurred content outside, so as to reproduce and help the natural focusing process while reducing bandwidth waste. This prototype is based on the FOVE headset, one of the first commercially available headsets with an integrated eye-tracker. We build on the FOVE's Unity API to design a gaze-adaptive streaming system compatible with the MPEG-DASH principle. We propose to generate at the server side two video representations (low- and high-resolution segments) that can be transcoded using information about the gaze position of the viewer to crop the high-resolution segments around the fovea using per-frame filters. The cropped high-resolution segment and the entire low-resolution video sphere are then merged at the client and rendered in the HMD to emulate the naturalistic focusing process of the Human Visual System. The entire foveated streaming system runs in real-time and our prototype was presented in the Demo Track of MMSys'18.

A high-performing foveated streaming system requires to anticipate the future user's head positions at the time of sending the content from the server. Owing to this acute need for head motion prediction in 360°video streaming, a number of recent approaches have proposed deep neural networks meant to exploit the knowledge of the past positions and of the 360° video content to periodically predict the next positions over a given time horizon.

The second contribution is the development of a tool to obtain solid results for head motion estimation and progress towards efficient 360° streaming systems.

In Chapter 4, we proposed a framework to evaluate and compare different methods to predict head position in 360° videos. This framework is composed by an algorithm to create a uniform data structure from each of the current heterogeneous datasets of head and gaze traces. We describe the algorithms used to compute the saliency maps either estimated from the raw video content or from the users' statistics, considering a kernel fitted for the equirectangular projection used to encode 360° videos. To compare each of the head motion prediction settings to a common reference, we detail the commands to estimate the performance of different approaches in each original evaluation context (prediction horizon, metrics and datasets). This framework allows to prepare testbeds to assess comprehensively different prediction methods (on various datasets against several competitors).

This software framework led to uncover major flaws of existing prediction methods, we therefore examined these flaws to be able to propose Deep Learning architectures that are better suited for head motion estimation.

Chapter 5 brought two main contributions:
For our third contribution, we carried out a critical and principled re-examination of the existing deep learning-based methods to predict head motion in 360° videos. We showed that all the considered existing methods are outperformed, on their datasets and with their test metrics, by baselines not considering the visual input and exploiting only the past trajectory of head positions. To understand why, we analyzed the datasets to identify how and when should the prediction benefit from the knowledge of the content. We analyzed the neural architectures proposed in the state of the art and showed there is only one whose performance does not degrade compared with the baselines, given that ground-truth saliency information is provided, and none of the existing architectures can be trained to compete with the baselines over the 0-5 sec. horizon when the saliency features are extracted from the content.
The fourth contribution is the design of a deep neural architecture named TRACK, built by decomposing the structure of the problem and supporting our analysis with the concept of Structural-RNN. TRACK is proved to establish state-of-the-art performance on all the prediction horizons $H \in [0 \text{ sec.}, 5 \text{ sec.}]$ and all the datasets of the existing competitors.

The Deep Learning models studied in Chapter 5, often referred to as "black-boxes" do not provide any insight on the dependence and the interplay between head motion and the visual content.

The fifth contribution is the development of a white-box predictor model to investigate the connection between the visual content and the human attentional process.

In Chapter 6 we have investigated the human head motion process driven by attention when a user experiences an immersive 360° video. We have first introduced a new computational model named HeMoG, enabling to predict future head positions from the user's past positions and the visual content. HeMoG is built on differential equations obtained from the physics of

rotational motion where the attractive salient areas in the 360° frames are represented as virtual masses. HeMoG is hence a white-box model and its (time-varying) parameters control the connection between visual content and head motion process. The performance of HeMoG can be comparable with those of DL predictors, which we interpret as the DL models learning the same type of fusion as HeMoG: curvature continuity and momentum attenuation from friction in the short-term, diversion of motion with saliency attraction in the longer-term. The evolution of best parameter values in terms of video categories and horizon reveals that, on videos that are not exploratory, the initial motion momentum is most important until ca. 3s, after which the saliency weights more in the motion equation.

Another approach instead of adapting reactively to the estimation of the future attention trajectories is to exploit gaze guidance techniques, the goal is to change the users' viewing direction towards the areas the director wants them to explore. If driving the user's attention is critical for a director to ensure the story plot is understood, in this dissertation we investigated attention driving techniques from a different perspective: that of the multimedia network community.

The sixth contribution of the thesis is to design a user-adaptive control scheme to automatically trigger VR cuts, named snap-cuts.

In Chapter 7, we have studied control mechanisms for guidance techniques, specifically applied to learn how to dynamically trigger rotational snap-cuts that re-position a user in front of a new FoV, when watching a VR content streamed over the Internet. These snap-cuts can benefit the user's experience both by helping stream and improve the quality in the FoV, and ensuring the user sees RoIs important for the story plot. However, snap-cuts should not be too frequent and may be avoided when they are not beneficial to the streamed quality. We have formulated the snap-cut triggering optimization problem and investigated possible gains in quality of experience. We have shown that learning approaches are relevant to design online snap-cut triggering strategies to outperform different baselines.

8.2 Future Works

In this section we present the future steps that could be taken to continue towards the goal of optimizing the streaming of VR content. We will first discuss about new strategies to guide the user's attention and we thus present the work carried out to advance in this perspective, a guidance technique based on our foveated streaming system. We then present future research perspectives in the area of trajectory prediction with attention and uncertainty quantification. Then, we identify the limitations of the preliminary work on control mechanisms for gaze guidance techniques and the future works to overcome these limitations. Finally, we introduce possible research directions to refine the current saliency maps in VR videos with the creation of emotional maps to quantify the effect of emotions in the attention mechanism.

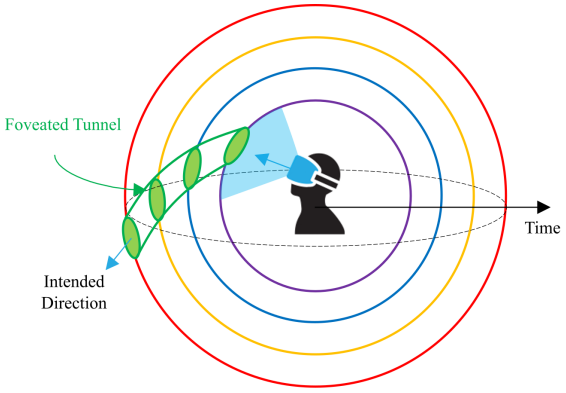

FIGURE 8.1: Foveated tunnel to attract the attention of the viewer towards the intended direction.

8.2.1 Foveated Tunnels: Future User Gaze Guidance Techniques

A direct usage of our foveated streaming system (introduced in Chapter 3) is to reactively send in high quality the areas that are close to the user's gaze to improve the QoE and bandwidth usage. However, we also considered another perspective, it is to investigate attention-driving techniques to attract proactively the user's gaze by using the foveated region.

Attention driving techniques can be helpful for the streaming of 360° videos by directing the user's attention to specific pre-defined Regions of Interest (RoI), thereby lowering the randomness of the user's motion. The user's attention in VR is however a complex process difficult to harness. We describe here the work already started to properly direct the user's attention by using some components involved into the user's experience (spatial qualities, depth and luminance) based on the works of [105, 106, 107, 108, 109, 110]. Future work should carry out user experiments to evaluate the performance of foveal tunnels as a novel gaze-driving technique.

We make the hypothesis that the eye will be attracted by a high resolution area that moves in an appropriate manner to redirect the attention. The foveal tunnel corresponds to the circular zone (a tunnel when we consider the time dimension) on the sphere on which the video is projected in high quality as shown in Fig. 8.1. This tunnel moves every frame to attract the viewer's gaze towards the desired position. The movement strategies of the foveal tunnel are inspired by real eye movements to resemble as much as possible a natural gaze movement. The possible voluntary motions of the eye are therefore *smooth pursuit* where the gaze follows smoothly the motion of an object of interest and keeps focusing on it, and *saccade* where there is a rapid gaze movement to focus on a new object (not in the fovea).

Other strategies allowing the responsiveness of the tunnel to the actual movement and position of the user's gaze are used in parallel. We adopted two strategies *Stay in FoV* and *Shift*. The former prevents the tunnel to go out of the user's FoV by blocking it at the edge. The latter corrects the path of the tunnel when the user ignores it, it is implemented by bringing the tunnel to the user's current gaze position if the gaze moves away x degrees or t seconds, thus too far or for too long time from the tunnel.

To create a system that allows us to use the foveated tunnel proactively, that is, not just reacting to the user's gaze but also anticipating it. We decided to use the clustering strategy proposed by Rossi et al. [66]. The trajectories of other users that have observed the video are grouped into clusters and then we obtain the average trajectory corresponding to each cluster to represent the trajectory of each group of users. During user experiments (planned for future work), the trajectory of the user will be categorized into one of the clusters and the foveated tunnel corresponding to the average trajectory will be used to drag the attention of the current user.

To implement these ideas, we have supervised a Master-2 project of four students that worked during five months on an initial implementation of the foveated tunnels. This work was then followed up by another Master-2 internship of six months. A Unity implementation of the proposed system has therefore already been made and its test with user experiments is planned for future work.

8.2.2 Future Head Motion Prediction Methods

Efforts could also be directed to improve the architecture of TRACK proposed in Chapter 5 and illustrated in Fig. 8.2. We started advancing in this regard with the supervision of an internship of a student that worked during three months on the investigation of deep attention mechanisms to refine the time- and space-varying fusion of modalities. We studied the incorporation into TRACK of an attention mechanism based on [120] and on the multi-headed attention mechanism proposed in [121]. Future works will also consider variational approaches with the use of Variational Recurrent Neural Networks [122] or Memory Networks [123, 124] to obtain confidence on the prediction of multiple trajectories, as has been proposed in the analogous task of trajectory prediction in autonomous driving [125]. Another important consideration in TRACK is the embedding of the visual input. As the shape of the video is spherical, regular convolutional layers need to be adapted to vary the filters to match the distorted shape of the 2D projections [126]. An important investigation is the use of Graph Neural Networks and its generalized version of Convolutional Neural Networks for non-Euclidean structured data called Graph Convolutional Networks [127] to create the embedding from the spherical visual input.

Given the performance of HeMoG, described in Chapter 6, we could build new Deep Learning Architectures based on the attributes of HeMoG to fuse the different input modalities. For instance, the operation to obtain the gravitational field of forces (Eq. 6.3) can be compactly re-written using the convolution operator $\mathbf{E}(\mathbf{a}) = -(e \bigotimes \mu)$. Let $r \in \Upsilon$ be any point in the sphere and $a(t)$ be the position of the head at time t. Indeed, to compute the overall field of forces, a convolution operator is applied between the distance matrix $e(r, a(t)) = \frac{1}{2\pi} \frac{r-a(t)}{||r-a(t)||^2}$ and the saliency map $\mu(r, t)$. This convolution could be directly replaced by a convolutional layer or, as described above, by a Graph Convolutional Network for which the parameters of the kernel will be learned. Another choice is to formalize the problem to be able to replace the

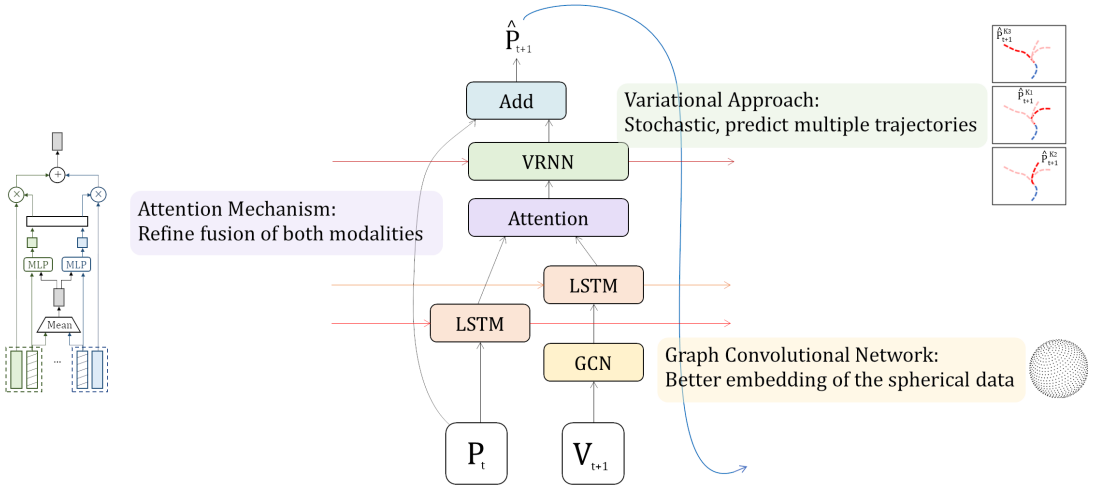

FIGURE 8.2: Illustration of future works to improve the building-block of TRACK's architecture. The Concatenation layer is replaced by an Attention Mechanism, the Flatten layer is replaced by a Graph Convolutional Network and the LSTMs are replaced by a Variational Approach.

ODE solver (LSODA) by a Neural-ODE model, a novel Deep Neural Network model to solve Ordinary Differential Equations [128].

To further improve the performance of HeMoG, in future works we can study better mechanisms to compute saliency maps from the content. While the study of Chapter 6 has been restricted to saliency attractors based on moving objects, we can consider extending to static objects whose importance can be ranked, meaning that the trajectory of focus of attention is also subjected to a gravitational field created by static objects [102, 103]. We can also study how to improve for the case of *Rides* scenes characterized by camera motion. To have more solid estimates of pixel velocities, methods for camera motion estimation [104] are already present in the literature and can help in creating more suitable saliency estimates for the proposed model.

8.2.3 Future Strategies on Control Mechanisms for Attention Guidance

A key aspect in VR streaming is that the consumed data rate depends on the motion of the user: the higher the motion, the more data needs to be sent from the server. Therefore, to lower the required data rate, new levers have been created to reduce the user's motion. In Chapter 7 we defined and investigated how to learn to trigger (rotational) snap-cuts meant to jointly benefit the user and the streaming algorithm to increase the user's QoE. It is however a preliminary work, suffering from several limitations.

First, in comparison with the upper-bound using *Ground-Truth* information, we observed that the performance of the proposed method is limited by the difficulty of predicting the overlap (the prediction horizon is 4 to 6 seconds). To overcome this difficulty, it will be important in future works to extract less volatile features that can be exploited in the decision to trigger the cuts. Particularly it is important to study ways to categorize the trajectories of users and to define new

video profiles to classify how the video content affects the user trajectories, and subsequently use these classifications as features for the snap-cut decision process.

Second, the considered model of user's reactions to a snap-cut (freezing for 2 seconds) and the QoE model (for the reward) are simplistic. Future work should carry out user experiments to determine more accurate models, and considering complex or unknown reaction models will require to adopt other types of learning approaches. An exciting prospect is to use Reinforcement Learning approaches where the test set is collected using a behavior policy different from the target policy. Another important idea is to simulate the reaction model based on an enhanced version of HeMoG (Head Motion with Gravitational laws, introduced in Chapter 6) and taking inspiration from [120] where the human behavior is controlled by a physics based simulator [129].

Third, the snap-cuts were modulated to help the streaming process (using a playback buffer). However, we have considered the network state fixed and the streaming logic independent of the available bandwidth. Future work will design advanced network-adaptive strategies based on network bandwidth traces making use of user- and content-adaptive snap-cutting strategies.

Finally, more levers should be considered to improve the attention-guidance toolbox such as dynamic foveated streaming (discussed in Sec. 8.2.1), slow-down the video [130] or prevent the user from seeing certain sectors of the sphere [131]. In a real-world environment, these levers must be smartly triggered so that they can optimize the complex user's experience models. For instance, we would trigger a rotational cut or restrict the field of view only when the network rate is not sufficient to grant the user full freedom and only if the current scene is suitable for such effect, or if the user's attentional or sickness level requires it. Therefore we need to choose, for each piece of content to send from the server to the client, which lever can be activated, and whether it needs to be activated, depending on the user's motion and sickness state, the available network rate, and the type of scene. This is a very difficult dynamic optimization problem where decisions must be taken based on random time series partly unknown (user's motion, available network rate, video frames). Machine learning, and deep neural networks specifically, are therefore key to design smart dynamic streaming strategies targeting a fluid experience of the VR content even in limited network conditions.

8.2.4 Emotional Maps and Future Perspective on Saliency Maps

In Virtual Reality, compared to traditional 2D videos, the user's senses are immersed in the experience and therefore elicits a more intense emotional response. The emotional response is defined in neuroscience as the combination of levels of valence and arousal, measured through biological responses such as pulse and skin conductance that can be obtained with physiological sensors [132].

To edit and deliver content tailored to VR, it is critical to understand the user experience and, in particular, to predict which parts of the 360° sphere will be attended by the user. Until

now, saliency maps are the main visual tool used to predict where the user is likely to look at. However, as shown in Chapter 6, these saliency maps are only partially informative and can be noisy and more difficult to get information from.

To address the strong need of more informative saliency maps, future work will have to include solid estimates of maps extracted from the content adding the emotional value of an object. Future works should be directed towards emotional maps to investigate (i) the spatial and temporal relationships between the physiological data (levels of arousal and valence) and head and gaze movements regardless of the content, extending the work in [133, 134], and (ii) the correlation between arousal and the characteristics of objects in 360° videos, applying the normalization used in [135] to obtain the actual interest in objects and study if arousal correlates with low-level or normalized-high-level saliency.

Another important modality, which highly impacts the direction of attention and has not been considered yet in any approach, is directional sound. Recent advances have been made to detect the source of the sound in a video [136, 137]. These works are useful to create sound maps of VR environments and refine the saliency maps obtained only from the visual content.

Appendix A

Experimental Settings of Existing Methods

Except for PAMI18 and MM18, none of the methods we studied came with publicly available code to reproduce the results, we had to reproduce each of the original experiments. In this section, we detail the specific configurations we used to replicate the original experiments of PAMI18, NOSSDAV17, CVPR18, MM18 and ChinaCom18 with the description given in the papers. In case further information is needed, we provide our code (with detailed explanations and reproducible figures) in a publicly available repository https://gitlab.com/miguelfromeror/head-motion-prediction.

To prove fairness in our comparison, we justify each of the decisions we made in our code by presenting some quotes written in the description of the original works. The only changes we made with respect to these citations are the notation and the reference number.

To describe each of the experiments we first detail the metrics used in each method, second we show the prediction horizon used in these works, and third we present the dataset used in each work and the split in train and test sets.

A.1 PAMI18 [1]

A.1.1 Metric

The authors of PAMI18 use the metric mean overlap, here is a description of this metric, given in [1]:

> The metric of mean overlap (MO), which measures how close the predicted HM position is to the ground-truth HM position. MO ranges from 0 to 1, and a larger MO indicates a more precise prediction. Specifically, MO is defined as,

$$MO = \frac{A(FoV_p \cap FoV_g)}{A(FoV_p \cup FoV_g)}, \tag{A.1}$$

where FoV_p and FoV_g represent the FoVs at the predicted and ground-truth HM positions, respectively.

A represents the area of a panoramic region, which accounts for number of pixels.

In this article the authors also express that they used this metric to measure the performance of their network:

> For evaluating the performance of online-Deep Head Prediction (DHP), we compared our approach with [138] and two baseline approaches. The same as [138], MO of (A.1) is measured as the metric to evaluate the accuracy of online prediction in HM positions. Note that a larger value of MO means a more accurate online prediction in HM positions. Since the Deep Reinforcement Learning (DRL) network of offline-DHP was learned over 61 training sequences and used as the initial model of online-DHP, our comparison was conducted on all 15 test sequences of our PVS-HM database.

We used the metric MO from the code of PAMI18 authors, provided in their repository[1].
The file was copied to our repository and used to measure the performance of our baselines.

A.1.2 Prediction horizon H

From [1]:

> The online-DHP approach refers to predicting a specific subject's HM position $(\hat{\theta}_{t+1}, \hat{\varphi}_{t+1})$ at frame $t+1$, given his/her HM positions $(theta_1, \varphi_1), ..., (\theta_t, \varphi_t)$ till frame t. [...] the output is the predicted HM position $(\hat{\theta}_{t+1}, \hat{\varphi}_{t+1})$ at the next frame for the viewer. Stage II: Prediction: [...] When entering the prediction stage, the DRL model trained in the first stage is used to produce the HM position as follows. [...] the HM position $(\hat{\theta}_{t+1}, \hat{\varphi}_{t+1})$ can be predicted, given the ground-truth HM position (θ_t, φ_t) and the estimated HM scanpath $(\Delta(\theta, \hat{\varphi}), \hat{v}_t)$ at frame t.

Meaning that the ground-truth of the previous HM position is used to predict each HM position frame by frame.

This is clear in Table 5 of [1]. The authors explicitly say:

> Both the online-DHP approach and baseline make predictions based on the ground-truth previous frames.

A.1.3 Train and Test Split

From [1]:

[1] https://github.com/YuhangSong/DHP/blob/master

> Since the DRL network of offline-DHP was learned over 61 training sequences and used as the initial model of online-DHP, our comparison was conducted on all 15 test sequences of our PVS-HM database.

We can find in Table 5 of [1], the 15 videos that were used to test:

BlueWorld, BTSRun, CMLauncher2, Dancing, Guitar, InsideCar, KingKong, RioOlympics, SpaceWar, SpaceWar2, StarryPolar, Sunset, Symphony, WaitingForLove and Waterfall

Therefore, we can deduce that the *61 training sequences* that correspond to the 61 videos in the train set are:

A380, AcerEngine, AcerPredator, AirShow, BFG, Bicycle, Camping, CandyCarnival, Castle, Catwalks, CMLauncher, CS, DanceInTurn, DrivingInAlps, Egypt, F5Fighter, Flight, GalaxyOnFire, Graffiti, GTA, HondaF1, IRobot, KasabianLive, Lion, LoopUniverse, Manhattan, MC, MercedesBenz, Motorbike, Murder, NotBeAloneTonight, Orion, Parachuting, Parasailing, Pearl, Predator, ProjectSoul, Rally, RingMan, Roma, Shark, Skiing, Snowfield, SnowRopeway, Square, StarWars, StarWars2, Stratosphere, StreetFighter, Supercar, SuperMario64, Surfing, SurfingArctic, TalkingInCar, Terminator, TheInvisible, Village, VRBasketball, Waterskiing, WesternSichuan and Yacht.

We made this partition of the dataset in our repository [18], the traces appear in the folder *Song_PAMI_18/orig_dataset_partition*.

A.2 NOSSDAV17 [2]

A.2.1 Metric

Our experiment follows the specifications in NOSSDAV17's paper [2], where we find a description of the formatting of the output:

> The ground-truth of the fixation prediction networks are the tiles viewed by the viewers at each frame. Using the dataset collected [139], we sample the points within the FoV by mapping the orientation on the sphere to the equirectangular model. Then, the viewed tiles are the tiles that are overlapped with the mapped points. For a single video frame, each tile is either watched or not, i.e., it has a boolean viewing probability.
>
> We fix the Quantization Parameter (QP) and resolution of all tiles at 28 and 192×192 respectively.

In the file *Fan_NOSSDAV_17/TileMappingReplica.py* of our repository [18], we have implemented the tile mapping algorithm.

We also provide the file *Fan_NOSSDAV_17/CompareTileInfoWithReplica.py*, to evaluate how good is our replica of the tile mapping algorithm, since the original is not provided. We used a

FoV of size 120° , to better match the original tiles, however, using a FoV of size 100° does not vary the results.

The authors also introduce the metrics used:

> To select the optimal parameters of the two models, we consider three metrics:
> (i) **accuracy**, which is the ratio of correctly classified tiles to the union of predicted and viewed tiles,
> (ii) **F-score**, which is the harmonic mean of prediction and recall, where the precision and recall are the ratios of correctly predicted tiles to the predicted and viewed tiles, respectively, and,
> (iii) **ranking-loss**, which is the number of tile pairs that are incorrectly ordered by probability normalized to the number of tiles.

The metrics we used correspond to the implementation of the Scikit-Learn package:

```
sklearn.metrics: accuracy_score, f1_score, label_ranking_loss
```

And according to the authors:

> We consider the fixation prediction on tiles as a multi-label classification problem and have implemented the neural networks using **Scikit-Learn** and Keras.

A.2.2 Prediction Horizon H

From [2]:

> Both networks take features of M past video frames in a sliding window as inputs, and predict the viewing probability of tiles with H future video frames in a prediction window as outputs.
>
> We let both the sliding window size M and prediction window size H to be 30 [frames].

The prediction horizon H is therefore 1 second.

A.2.3 Train and Test Split

From [2], the composition of the dataset is:

> We download **ten 360° videos** from YouTube, which are in 4096×2048 pixels (4K) resolution with a frame rate of 30 Hz. [...] Each video lasts for one minute. We recruit **25 viewers** for dataset collections.

> We use the traces from 12 viewers (training set) to train the two proposed fixation prediction networks. Among the traces, we randomly divide them into 80% and 20% for training and validation, respectively.

Therefore, the training set is composed by the 120 traces of 12 viewers watching 10 videos, and is further subdivided in train and validation, with 80% of the 120 traces (96 traces) used to train the networks and 20% of the traces (24 traces) are used to validate.

The remaining 13 traces, from the dataset with traces of 25 users, are used for another experiment, this is clear in the paper:

> Some pilot simulation runs with $|U| = 13$ viewers (testing set), $B = 150$ Mbps, $D_l = 2$ secs, and $M = 30$.

In summary, we have to select 12 viewers from the dataset, and randomly select from their traces 96 traces to train and 24 traces to validate.

We made this partition of the dataset in the folder *Fan_NOSSDAV_17/orig_dataset_partition* in our repository [18].

A.3 MM18 [3]

A.3.1 Metric

Our experiment follows the specifications in MM18's paper [3], the recommendations of the authors in the public repository [71] and some extra clarifications made by the authors when contacted by mail:

In [3]:

> The evaluation metric is the accuracy of head movement prediction. Accuracy is calculated based on the ratio of the number of overlapping tiles between predicted and ground-truth head orientation map over the total number of predicted and viewed tiles.

According to the authors:

> The accuracy defined in this paper is neither a traditional sense of accuracy nor precision. We followed the definition in reference [2]. For example, if we predict two tiles, but only one of them matches with the two viewed tiles, the accuracy will be the number of intersected tiles (between the two predicted and two viewed tiles) over the number of unioned tiles, i.e., 1/3.

The metrics we used in this case do not correspond to the implementation of the Scikit-Learn package: *sklearn.metrics: accuracy_score*, we implemented the metric given the specifications of the authors, in our repository we provide the file *Nguyen_MM_18/AccuracyMetricIoU.py*.

For the computation of the output head position probability map, the authors provide insights on how it is computed in their source code [71]. In our code is implemented in *Nguyen_MM_18/ TileMappingReplica.py* following the specification from the paper that "the equirectangular frame is spatially configured into 16×9 tiles."

A.3.2 Prediction Horizon H

From [3]:

> We use the input feature from the past one second to predict the head orientation in the future.
>
> The default prediction window H is set to be 0.5 seconds.
>
> To explore the effect of prediction window H on the accuracy of the proposed model and other three benchmarks, we vary H from 0.5 seconds to 2.5 seconds.

A.3.3 Train and Test Split

From [3], about the compositon of the dataset

> For each video, we select one segment with a length of 20-45 seconds. The video segment is selected such that there are one or more events in the video that introduce new salient regions (usually when new video scene is shown and lead to fast head movement of users. We extract the timestamped saliency maps and head orientation maps from these videos, generating a total of 300,000 data samples from 432 time series using viewing logs of 48 users.
>
> We use 5 videos from our dataset for model training and another 4 videos for model validation.

We made this partition of the dataset in the folder *Nguyen_MM_18/orig_dataset_partition*.

A.4 ChinaCom18 [4]

A.4.1 Metric

Our experiment follows the specifications in ChinaCom18's paper [4], where we find a description of the formatting of the metrics used:

> Table 1 provides the specific measurement of accuracy and F-score of the prediction on each video. Accuracy presents the primary performance of the prediction model by calculating the ratio of tiles correctly classified to all tiles. F-score is the

> weighted mean of the precision and recall (precision is the ratio of tiles classified to be positive correctly to all positive classified tiles, and recall is the ratio of tiles classified to be positive to all viewed tiles)

The metrics we used correspond to the implementation of the Scikit-Learn package:

`sklearn.metrics: accuracy_score, f1_score.`

A.4.2 Prediction Horizon H

From [4]:

> When omnidirectional videos are partitioned into N tiles, our model provides short-term prediction results $Pred_{short} = p_1^N$ and additional long-term prediction results $Pred_{long} = p_1^N$ to adapt to the variation of user's FoV in the prediction window.
>
> The sliding window is set to be 1 second, as well as the size of short-term and long-term prediction window.

Meaning that the prediction horizon is 1 second in the long-term and 0.03 seconds (1 frame) in the short-term. In the paper there is no description of a longer-term prediction horizon than 1 second.

A.4.3 Train and Test Split

From [4], the composition of the dataset is:

> The LSTM network of the prediction model has to be trained by the omnidirectional video dataset [139]. The dataset has ten omnidirectional videos all lasting one minute. All videos are of 4K resolution with 30 fps. The videos are projected with equirectangular projection. Each video is viewed by 30 viewers wearing HMD and the orientation of each frame has been collected by Open Track and presented in both Cartesian coordinates and Euler angles. The omnidirectional video is partitioned into 10×20 tiles, which are labeled whether is viewed by the user.

So, we need to select the traces of 30 viewers from the dataset of [2] as stated in [4]:

> We divide the dataset into 80% and 20% for training and validation respectively. Different videos are trained and validated separately, so that a unique prediction network is trained for each video

This means that there should be 10 partitions of the dataset, in each partition we consider the data for a single video, the traces of all 30 viewers on each video are splitted into 80% and 20% for training and validation respectively.

In summary, we have to select 30 viewers from the dataset, then, we iterate per video and partition the 30 traces (of each video) into 24 traces to train and 6 traces to validate.

We made these partitions of the dataset in the folders:

- *orig_dataset_partition_coaster*
- *orig_dataset_partition_coaster2*
- *orig_dataset_partition_diving*
- *orig_dataset_partition_drive*
- *orig_dataset_partition_game*
- *orig_dataset_partition_landscape*
- *orig_dataset_partition_pacman*
- *orig_dataset_partition_panel*
- *orig_dataset_partition_ride*
- *orig_dataset_partition_sport*

A.5 CVPR18 [5]

A.5.1 Metric

Our experiment follows the specifications in CVPR18's paper [5], where we find a description of the metric:

> Since our goal aims at predicting a sequential gaze points in a video for each user, so we use the **Mean Intersection Angle Error (MA)** over all videos and all users to measure the performance. For the gaze point in the i^{th} frame ($i = 1, ..., T$) with ground-truth (x_i^p, y_i^p) and prediction ($\hat{\theta}_i^p$, $\hat{\varphi}_i^p$), the viewing angle between them can be represented as d_i (the way to compute d i will be provided in supplementary material), then MIAE can be calculated as follows $MIAE = \frac{1}{TP}\sum_{i,p} d_i$. Here P is the total number of users watching this video. We then average MAE over all videos. Following the work of face alignment, we also use cumulative distribution function (CDF) of all gaze points for performance evaluation. A higher CDF curve corresponds to a method with smaller MAE.

According to the supplementary material of [5]:

> For a given gaze point (θ, φ), where θ is latitude and φ is longitude, its coordinate in the unit sphere is $P = (\cos x \cos y, \cos x \sin y, \sin x)$, then for a ground-truth gazepoint (θ, φ) and its predicted gaze point $(\hat{\theta}, \hat{\varphi})$, we can get corresponding coordinates in unit sphere as P and $\hat{P}$, the intersection angle error between them can be computed as $d = arccos(< P, \hat{P} >)$ where $<, >$ is inner product.

The file to compute the Intersection angle error according to this definition is given in *Xu_CVPR_18/ IntersectionAngleError.py*.

A.5.2 Prediction Horizon H

From [5]:

> We propose to use the history gaze path in the first five frames to predict the gaze points in next five frames ($M = 5$ and $H = 5$). We use the observation (the results of gaze tracking) in the first 1 second to predict the gaze points in the frames of upcoming 1 second.

However, according to the problem formulation:

> We formulate gaze prediction as a task of learning nonlinear mapping function F which maps the history gaze and image contents to the coordinates.

F is the deep neural network of CVPR18, therefore, from the problem formulation the neural network consider a prediction horizon of 1 frame, since in the same problem formulation the authors propose to use "the current frame and next frame and the history gaze path as input when we predict the gaze point in the next frame".

> Following the common setting in trajectory prediction for crowd, we downsample one frame from every five frames for model training and performance evaluation. In this way, the interval between two neighboring frames in our experiments corresponds to $\frac{5}{25}$ seconds, and such setting makes our gaze prediction task more challenging than that for the neighboring frames in original videos.

Finally, to avoid the confusion about the actual prediction horizon, we consider the larger prediction horizons of 5 frames, that corresponds to 1s.

A.5.3 Train and Test Split

From [5], the partition of the dataset is:

> In our experiments, we randomly select 134 videos as training data, and use the remaining 74 videos as testing. Some participants are shared in training and testing, but the videos in training/testing have no overlap.

In the dataset [140] we can find the partition of the data in the file *dataset/train_test_set.xlsx*.
So, the 134 videos for the train set are:
1, 2, 3, 4, 5, 6, 7, 8, 9, 10, 11, 12, 13, 14, 15, 16, 17, 18, 19, 20, 21, 22, 35, 37, 38, 39, 40, 41, 42, 43, 44, 45, 46, 47, 48, 49, 50, 51, 52, 53, 54, 55, 56, 57, 72, 73, 74, 75, 76, 77, 78, 79,

80, 81, 82, 83, 85, 87, 88, 89, 90, 91, 92, 93, 94, 95, 109, 110, 111, 112, 113, 114, 115, 116, 117, 118, 119, 120, 121, 122, 123, 124, 125, 126, 127, 128, 129, 130, 144, 145, 146, 147, 148, 149, 150, 151, 152, 153, 154, 155, 156, 157, 158, 159, 160, 161, 162, 163, 164, 165, 179, 180, 181, 182, 183, 184, 185, 186, 187, 188, 189, 190, 191, 192, 193, 194, 195, 196, 197, 198, 199, 200, 201, 202

While the 74 videos in the test set are:

23, 24, 25, 26, 27, 28, 29, 30, 31, 32, 33, 34, 58, 59, 60, 62, 63, 64, 65, 66, 67, 68, 69, 70, 71, 96, 97, 98, 99, 100, 101, 102, 103, 104, 105, 106, 131, 132, 133, 134, 135, 136, 137, 138, 139, 140, 141, 142, 143, 166, 167, 168, 169, 170, 171, 172, 173, 174, 175, 176, 177, 178, 203, 204, 205, 206, 208, 209, 210, 211, 212, 213, 214, 215

We made this partition of the dataset in the folder *Xu_CVPR_18/orig_dataset_partition* in our repository [18].

A.5.4 Replica of CVPR18's Architecture

Here we describe our re-implementation of CVPR18, we kept the exact same architectural and training parameters as those described in [5]. Citing the authors of CVPR18:

> The network consists of a Trajectory Encoder module, a Saliency Encoder module and a Displacement Prediction module.

A.5.4.1 Trajectory Encoder Module

From the manuscript [5]:

> Trajectory encoder module is designed to encode the history gaze path of a user. [...] We employ an LSTM network to encode the gaze pattern along the time. For each video clip, we sequentially feed the gaze points (P_t^u) corresponding to history frames in this video sequence into a stacked LSTM, and denote the output of stacked LSTM f_{t+1}^u at $(t+1)^{th}$ frames,
>
> $$f_{t+1}^u = h(P_1^u, P_2^u, ..., P_t^u) \tag{A.2}$$
>
> Here the function $h(\cdot)$ represents the input-output function of stacked LSTM. In addition, the function h is stacked LSTMs with 2 LSTM layers, both with 128 neurons.

Therefore our Trajectory Encoder Module consists of a doubly-stacked LSTM with 128 neurons each.

A.5.4.2 Saliency Encoder Module

For the Saliency Encoder Module, to be independent from the imperfection of any saliency predictor fed with the visual content, we consider the ground-truth saliency as output of the Saliency Encoder module. When we compare the architectural choices of the different methods, to be independent of the particular saliency extraction choice we used the saliency map extracted from PanoSalNet [3] directly as output of the Saliency Encoder module.

$$g_{t+1}^u = z(V_1^u, V_2^u, ..., V_t^u, ..., V_{t+1}), \tag{A.3}$$

where $z(\cdot)$ represents the saliency extractor (either ground-truth or PanoSalNet).

A.5.4.3 Displacement Prediction Module

Citing [5]:

> The displacement prediction module takes the output of saliency encoder module and trajectory encoder module, use another two fully connected layer to estimate the displacement between the gaze point at time $t+1$ and gaze point at time t:
>
> $$\Delta\hat{P}_{t+1}^u = r([f_{t+1}^u; g_{t+1}^u]), \tag{A.4}$$
>
> where $r(\cdot)$ represents two connected layers. The function r contains two fully connected layers with 1000, 2 neurons, respectively.

Therefore to replicate the Displacement Prediction Module, we used 2 fully connected layers with 1000 neurons for the hidden layer and 2 neurons in the output layer.

A.5.4.4 Loss function

Citing [5]:

> Once we get the location displacement, we can compute the gaze coordinate P_{t+1}^u at time $t+1$

We used a residual link from the input position P_t^u to the output of the Displacement Prediction Module $\Delta\hat{P}_{t+1}^u$, and compute $\hat{P}_{t+1}^u = P_t^u + \Delta\hat{P}_{t+1}^u$. Citing [5]: "We train the model by minimizing this loss across all the persons and all video clips in the training-set."

Citing [5]:

> Mathematically, we formulate the objective of gaze tracking as follows:
>
> $$F^* = \arg\min_F \sum_{t=M}^{M+H-1} ||P_{t+1} - (P_t + F(V_{t:t+1}, P_{1:t}))|| \tag{A.5}$$

Given this, we set the loss function as the mean squared error between P_{t+1} and $\hat{P}_{t+1}$.

We train our network with the following hyper-parameters setting: mini-batch size (128), learning rate (0.1), momentum (0.9), weight decay (0.0005), and the number of epochs (5000). The only setting we changed with respect to the original experiment was the mini-batch size, it is set to 8 in the original experiment.

Appendix B

Derivative of the Quaternion, Angular Acceleration and Velocity

B.1 Angular Velocity and Quaternion

We define a differential equation that relates the time derivative of the quaternion $\dot{q}$ and the angular velocity vector ω [141].

Tangential velocity $\mathbf{v}_\perp$ is defined as:

$$\mathbf{v}_\perp = \frac{d}{dt}\mathbf{a} = \omega \times \mathbf{a}, \tag{B.1}$$

where ω is the orbital angular velocity. We can consider the quaternions ω_q and a_q, where the scalar part of ω_q is equal to zero (since ω and $\mathbf{a}$ are perpendicular, their dot product is zero), and the vector part of ω_q corresponds to ω; similarly for $a_q = [0, a_x, a_y, a_z]$, where the position vector $\mathbf{a} = [a_x, a_y, a_z]$ is represented in 3d coordinates in the unit sphere.

We can then write Eq. (B.1) in quaternion form:

$$\dot{\mathbf{a}} = \omega \otimes \mathbf{a}, \tag{B.2}$$

where $\otimes$ is the quaternion multiplication.

We can also represent the position at each time instant as a quaternion rotation from a constant vector $\mathbf{a_0}$ (set to an arbitrary axis, for example $a_0 = [x = 1, y = 0, z = 0]$).

$$\mathbf{a} = \mathbf{q} \otimes \mathbf{a_0} \otimes \mathbf{q^{-1}}, \tag{B.3}$$

And therefore,

$$\frac{d}{dt}\mathbf{a} = \frac{d}{dt}[\mathbf{q} \otimes \mathbf{a_0} \otimes \mathbf{q^{-1}}] \tag{B.4}$$

$$\frac{d}{dt}[\mathbf{q}\otimes\mathbf{a_0}\otimes\mathbf{q^{-1}}]=\frac{\mathbf{d}}{\mathbf{dt}}[\mathbf{q}]\otimes\mathbf{a_0}\otimes\mathbf{q^{-1}}+\mathbf{q}\otimes\mathbf{a_0}\otimes\frac{\mathbf{d}}{\mathbf{dt}}[\mathbf{q^{-1}}] \tag{B.5}$$

Given that $\mathbf{q}\otimes\mathbf{q^{-1}}=1$, then $\frac{d}{dt}(\mathbf{q}\otimes\mathbf{q^{-1}})=0$:

$$\frac{d}{dt}[q]\otimes q^{-1}+q\otimes\frac{d}{dt}[q^{-1}]=0 \tag{B.6}$$

$$\frac{d}{dt}[q^{-1}]=-q^{-1}\otimes\frac{d}{dt}[q]\otimes q^{-1} \tag{B.7}$$

From Eq. (B.3), we can get a_0 in terms of a:

$$\mathbf{a_0}=\mathbf{q^{-1}}\otimes\mathbf{a}\otimes\mathbf{q} \tag{B.8}$$

Replacing Eq. (B.8) in Eq. (B.5):

$$\frac{d}{dt}[\mathbf{q}\otimes\mathbf{a_0}\otimes\mathbf{q^{-1}}]=\frac{\mathbf{d}}{\mathbf{dt}}[\mathbf{q}]\otimes\mathbf{q^{-1}}\otimes\mathbf{a}\otimes\mathbf{q}\otimes\mathbf{q^{-1}}+\mathbf{q}\otimes\mathbf{q^{-1}}\otimes\mathbf{a}\otimes\mathbf{q}\otimes\frac{\mathbf{d}}{\mathbf{dt}}[\mathbf{q^{-1}}] \tag{B.9}$$

Substituting Eq. (B.7) in Eq. (B.9):

$$\frac{d}{dt}[\mathbf{q}\otimes\mathbf{a_0}\otimes\mathbf{q^{-1}}]=\dot{\mathbf{q}}\otimes\mathbf{q^{-1}}\otimes\mathbf{a}\otimes\mathbf{q}\otimes\mathbf{q^{-1}}+\mathbf{q}\otimes\mathbf{q^{-1}}\otimes\mathbf{a}\otimes\mathbf{q}\otimes-\mathbf{q^{-1}}\otimes\dot{\mathbf{q}}\otimes\mathbf{q^{-1}} \tag{B.10}$$

Simplifying $q\otimes q^{-1}$ and using Eq. B.2:

$$\frac{d}{dt}\mathbf{a}=\frac{d}{dt}[\mathbf{q}\otimes\mathbf{a_0}\otimes\mathbf{q^{-1}}]=\dot{\mathbf{q}}\otimes\mathbf{q^{-1}}\otimes\mathbf{a}-\otimes\mathbf{a}\otimes\dot{\mathbf{q}}\otimes\mathbf{q^{-1}}=\omega\otimes\mathbf{a} \tag{B.11}$$

Using the quaternion commutator operation: $[p,q]=p\otimes q-q\otimes p=[0,2(\mathbf{p_1}\times\mathbf{p_2})]$, when both q and p are quaternions without scalar part, $[\mathbf{p},\mathbf{q}]=2(q_1\times q_2)=2(q_1\otimes q_2)$.

$$\dot{\mathbf{q}}\otimes\mathbf{q^{-1}}\otimes\mathbf{a}-\otimes\mathbf{a}\otimes\dot{\mathbf{q}}\otimes\mathbf{q^{-1}}=\omega\otimes\mathbf{a} \tag{B.12}$$

$$[\dot{\mathbf{q}}\otimes\mathbf{q^{-1}},\mathbf{a}]=\omega\otimes\mathbf{a} \tag{B.13}$$

$$2\dot{\mathbf{q}}\otimes\mathbf{q^{-1}}\otimes\mathbf{a}=\omega\otimes\mathbf{a} \tag{B.14}$$

$$\dot{\mathbf{q}}=\frac{1}{2}\omega\otimes\mathbf{q} \tag{B.15}$$

B.2 Angular Acceleration and Quaternion

Now we need to define a differential equation that relates the second time derivative of the quaternion $\ddot{q}$ and the angular acceleration vector $\frac{d\mathbf{w}}{dt}$.

Using Eq. (B.15):

$$\omega = 2\dot{\mathbf{q}} \otimes \mathbf{q}^{-\mathbf{1}} \tag{B.16}$$

The second derivative of the quaternion (from Eq. (B.15)) is:

$$\ddot{\mathbf{q}} = \frac{1}{2}(\omega \otimes \dot{\mathbf{q}} + \dot{\omega} \otimes \mathbf{q}) \tag{B.17}$$

Replacing Eq. (B.16) in Eq. (B.17):

$$\ddot{\mathbf{q}} = \frac{1}{2}(2\dot{\mathbf{q}} \otimes \mathbf{q}^{-\mathbf{1}} \otimes \dot{\mathbf{q}} + \dot{\omega} \otimes \mathbf{q}) \tag{B.18}$$

$$\ddot{\mathbf{q}} = \dot{\mathbf{q}} \otimes \mathbf{q}^{-\mathbf{1}} \otimes \dot{\mathbf{q}} + \frac{1}{2}\dot{\omega} \otimes \mathbf{q} \tag{B.19}$$

Appendix C

Publications and Complementary Activities

C.1 Publications

The subject of this thesis is multi-disciplinary (involving concepts from Multimedia Communication and Networking, Machine Learning and Deep Learning, Attentional Models and Perception). Our work has been proven to be relevant in the context of international research. We have published our research in the following journals, international conferences and workshops.

C.1.1 Journal Paper

Romero Rondón, M. F., Sassatelli, L., Aparicio-Pardo, R., & Precioso, F. (2021). TRACK: A New Method from a Re-examination of Deep Architectures for Head Motion Prediction in 360° Videos. IEEE Transactions on Pattern Analysis and Machine Intelligence (TPAMI).

C.1.2 International Conferences

Romero Rondón, M. F., Zanca, D., Melacci, S., Gori, M. & Sassatelli, L. (2021, November). HeMoG: A White Box Model to Unveil the Connection Between Saliency Information and Human Head Motion in Virtual Reality. In IEEE International Conference on Artificial Intelligence and Virtual Reality (AIVR).

Romero Rondón, M. F., Sassatelli, L., Precioso, F., & Aparicio-Pardo, R. (2018, June). Foveated Streaming of Virtual Reality Videos. In Proceedings of the 9th ACM Multimedia Systems Conference, (MMSys) Demo track (pp. 494-497).

Romero Rondón, M. F., Sassatelli, L., Aparicio-Pardo, R., & Precioso, F. (2020, May). A Unified Evaluation Framework for Head Motion Prediction Methods in 360° Videos. In Proceedings of

the 11th ACM Multimedia Systems Conference, (MMSys) ODS track (pp. 279-284).

Romero Rondón, M. F., Sassatelli, L., Aparicio-Pardo, R., & Precioso, F. (2020, May). User-Adaptive Rotational Snap-Cutting for Streamed 360° Videos. In EUROGRAPHICS Workshop on Intelligent Cinematography and Editing (WICED).

Romero Rondón, M. F., Sassatelli, L., Aparicio-Pardo, R., & Precioso, F. (2020, October). TRACK: A Multi-Modal Deep Architecture for Head Motion Prediction in 360° Videos. In 2020 IEEE International Conference on Image Processing (ICIP) (pp. 2586-2590). IEEE.

C.1.3 National Conferences

Romero Rondón M. F., Sassatelli L., Aparicio-Pardo R., & Precioso F. (2021, November). Une approche multi-modale à la prédiction des mouvements de tête en réalité virtuelle. In 21e édition du colloque COmpression et REprésentation des Signaux Audiovisuels (CORESA).

C.1.4 Oral Presentations

The work "Head Motion Prediction in 360 Virtual Reality Videos" was presented at the GdR ISIS meeting on "Compression and quality of 360 content, light field and point cloud (3D)" at INSA Rennes in March 2019. The different works in Sec. C.1.2 have been presented in the respective conferences and the work in Sec. C.1.3 will be presented in November 2021.

Bibliography

[1] M. Xu, Y. Song, J. Wang, M. Qiao, L. Huo, and Z. Wang, "Predicting head movement in panoramic video: A deep reinforcement learning approach," *IEEE Trans. on PAMI*, 2018.

[2] C.-L. Fan, J. Lee, W.-C. Lo, C.-Y. Huang, K.-T. Chen, and C.-H. Hsu, "Fixation prediction for 360 video streaming in head-mounted virtual reality," in *ACM NOSSDAV*, 2017, pp. 67–72.

[3] A. Nguyen, Z. Yan, and K. Nahrstedt, "Your attention is unique: Detecting 360° video saliency in head-mounted display for head movement prediction," in *ACM Int. Conf. on Multimedia*, 2018, pp. 1190–1198.

[4] Y. Li, Y. Xu, S. Xie, L. Ma, and J. Sun, "Two-layer FoV prediction model for viewport dependent streaming of 360° videos," in *EAI Int. Conf. on Communications and Networking (ChinaCom)*, Chengdu, China, Oct. 2018.

[5] Y. Xu, Y. Dong, J. Wu, Z. Sun, Z. Shi, J. Yu, and S. Gao, "Gaze prediction in dynamic 360° immersive videos," in *IEEE CVPR*, 2018, pp. 5333–5342.

[6] C. E. Willoughby, D. Ponzin, S. Ferrari, A. Lobo, K. Landau, and Y. Omidi, "Anatomy and physiology of the human eye: effects of mucopolysaccharidoses disease on structure and function–a review," *Clinical & Experimental Ophthalmology*, vol. 38, pp. 2–11, 2010.

[7] B. Wandell and S. Thomas, "Foundations of vision," *Psyccritiques*, vol. 42, no. 7, 1997.

[8] M. Almquist, V. Almquist, V. Krishnamoorthi, N. Carlsson, and D. Eager, "The prefetch aggressiveness tradeof in 360 video streaming," in *ACM Int. Conf. on Multimedia Systems (MMSys)*, 2018.

[9] E. N. A. Neto, R. M. Barreto, R. M. Duarte, J. P. Magalhaes, C. A. Bastos, T. I. Ren, and G. D. Cavalcanti, "Real-time head pose estimation for mobile devices," in *International Conference on Intelligent Data Engineering and Automated Learning*. Springer, 2012, pp. 467–474.

[10] K. Yin, Z. He, J. Xiong, J. Zou, K. Li, and S.-T. Wu, "Virtual reality and augmented reality displays: advances and future perspectives," *Journal of Physics: Photonics*, 2021.

[11] T. Shibata, J. Kim, D. M. Hoffman, and M. S. Banks, "Visual discomfort with stereo displays: effects of viewing distance and direction of vergence-accommodation conflict," in *Stereoscopic Displays and Applications XXII*, vol. 7863. International Society for Optics and Photonics, 2011, p. 78630P.

[12] S. Zhao and D. Medhi, "Sdn-assisted adaptive streaming framework for tile-based immersive content using mpeg-dash," in *2017 IEEE Conference on Network Function Virtualization and Software Defined Networks (NFV-SDN)*. IEEE, 2017, pp. 1–6.

[13] H.-W. Kim and S.-H. Yang, "Region of interest–based segmented tiled adaptive streaming using head-mounted display tracking sensing data," *International Journal of Distributed Sensor Networks*, vol. 15, no. 12, p. 1550147719894533, 2019.

[14] X. Corbillon, G. Simon, A. Devlic, and J. Chakareski, "Viewport-adaptive navigable 360-degree video delivery," in *2017 IEEE international conference on communications (ICC)*. IEEE, 2017, pp. 1–7.

[15] A. Amidi and S. Amidi, "Vip cheatsheet: Recurrent neural networks," 2018.

[16] S. Varsamopoulos, K. Bertels, and C. G. Almudever, "Comparing neural network based decoders for the surface code," *IEEE Transactions on Computers*, vol. 69, no. 2, pp. 300–311, 2019.

[17] E. J. David, J. Gutiérrez, A. Coutrot, M. P. Da Silva, and P. L. Callet, "A dataset of head and eye movements for 360° videos," in *ACM Int. Conf. on Multimedia Systems (MMSys)*, 2018, pp. 432–437.

[18] M. F. Romero-Rondon, L. Sassatelli, R. Aparicio-Pardo, and F. Precioso, "head-motion-prediction," https://gitlab.com/miguelfromeror/head-motion-prediction/tree/master, 2020.

[19] Grand View Research, Inc., "Virtual Reality Market Share & Trends Report, 2021-2028," Industry report, 2021.

[20] S. Sharples, S. Cobb, A. Moody, and J. R. Wilson, "Virtual reality induced symptoms and effects (vrise): Comparison of head mounted display (hmd), desktop and projection display systems," *Displays*, vol. 29, no. 2, pp. 58–69, 2008.

[21] J. Park, P. A. Chou, and J.-N. Hwang, "Rate-utility optimized streaming of volumetric media for augmented reality," *IEEE Journal on Emerging and Selected Topics in Circuits and Systems*, vol. 9, no. 1, pp. 149–162, 2019.

[22] E. Bastug, M. Bennis, M. Médard, and M. Debbah, "Toward interconnected virtual reality: Opportunities, challenges, and enablers," *IEEE Communications Magazine*, vol. 55, no. 6, pp. 110–117, 2017.

[23] A. Caputo, A. Giachetti, S. Abkal, C. Marchesini, and M. Zancanaro, "Real vs simulated foveated rendering to reduce visual discomfort in virtual reality," in *Proceedings of the 18th International Conference promoted by the IFIP Technical Committee 13 on Human-Computer Interation - INTERACT 2021*. INTERACT 2021, 2021.

[24] S. Mangiante, G. Klas, A. Navon, Z. GuanHua, J. Ran, and M. D. Silva, "Vr is on the edge: How to deliver 360 videos in mobile networks," in *Proceedings of the Workshop on Virtual Reality and Augmented Reality Network*, 2017, pp. 30–35.

[25] O. Le Meur, P. Le Callet, and D. Barba, "Predicting visual fixations on video based on low-level visual features," *Vision research*, vol. 47, no. 19, pp. 2483–2498, 2007.

[26] S. Dambra, G. Samela, L. Sassatelli, R. Pighetti, R. Aparicio-Pardo, and A.-M. Pinna-Déry, "Film editing: New levers to improve vr streaming," in *Proceedings of the 9th ACM Multimedia Systems Conference*, 2018, pp. 27–39.

[27] M. Lambooij, M. Fortuin, I. Heynderickx, and W. IJsselsteijn, "Visual discomfort and visual fatigue of stereoscopic displays: A review," *Journal of imaging science and technology*, vol. 53, no. 3, pp. 30 201–1, 2009.

[28] M. F. Land, "The human eye: Structure and function," *Nature Medicine*, vol. 5, no. 11, pp. 1229–1229, 1999.

[29] S. A. McMains and S. Kastner, *Visual Attention*. Berlin, Heidelberg: Springer Berlin Heidelberg, 2009, pp. 4296–4302. [Online]. Available: https://doi.org/10.1007/978-3-540-29678-2_6344

[30] E. Kowler, "Attention and eye movements," in *Encyclopedia of neuroscience*. Elsevier Ltd, 2009, pp. 605–616.

[31] J. E. Hoffman, "Visual attention and eye movements," *Attention*, vol. 31, no. 2, pp. 119–153, 1998.

[32] M. Cornia, L. Baraldi, G. Serra, and R. Cucchiara, "A deep multi-level network for saliency prediction," in *2016 23rd International Conference on Pattern Recognition (ICPR)*. IEEE, 2016, pp. 3488–3493.

[33] J. Pan, C. C. Ferrer, K. McGuinness, N. E. O'Connor, J. Torres, E. Sayrol, and X. Giro-i Nieto, "Salgan: Visual saliency prediction with generative adversarial networks," *arXiv preprint arXiv:1701.01081*, 2017.

[34] Y. Fang, J. Wang, M. Narwaria, P. Le Callet, and W. Lin, "Saliency detection for stereoscopic images," *IEEE Transactions on Image Processing*, vol. 23, no. 6, pp. 2625–2636, 2014.

[35] V. Sitzmann, A. Serrano, A. Pavel, M. Agrawala, D. Gutierrez, B. Masia, and G. Wetzstein, "Saliency in VR: How do people explore virtual environments?" *IEEE Trans. on Visualization and Computer Graphics*, vol. 24, no. 4, pp. 1633–1642, 2018.

[36] M. Assens Reina, X. Giro-i Nieto, K. McGuinness, and N. E. O'Connor, "Saltinet: Scan-path prediction on 360 degree images using saliency volumes," in *Proceedings of the IEEE International Conference on Computer Vision Workshops*, 2017, pp. 2331–2338.

[37] G. Kramida, "Resolving the vergence-accommodation conflict in head-mounted displays," *IEEE transactions on visualization and computer graphics*, vol. 22, no. 7, pp. 1912–1931, 2015.

[38] M. S. Anwar, J. Wang, A. Ullah, W. Khan, Z. Li, and S. Ahmad, "User profile analysis for enhancing qoe of 360 panoramic video in virtual reality environment," in *2018 International Conference on Virtual Reality and Visualization (ICVRV)*. IEEE, 2018, pp. 106–111.

[39] X. Yin, A. Jindal, V. Sekar, and B. Sinopoli, "A control-theoretic approach for dynamic adaptive video streaming over http," in *Proceedings of the 2015 ACM Conference on Special Interest Group on Data Communication*, 2015, pp. 325–338.

[40] M. H. Pinson and S. Wolf, "A new standardized method for objectively measuring video quality," *IEEE Transactions on broadcasting*, vol. 50, no. 3, pp. 312–322, 2004.

[41] G. Calvigioni, R. Aparicio-Pardo, L. Sassatelli, J. Leguay, P. Medagliani, and S. Paris, "Quality of experience-based routing of video traffic for overlay and isp networks," in *IEEE INFOCOM 2018-IEEE Conference on Computer Communications*. IEEE, 2018, pp. 935–943.

[42] MPEG Dynamic adaptive streaming over HTTP (DASH), "Iso/iec 23009-1:2014," 2014. [Online]. Available: https://www.iso.org/standard/65274.html

[43] F. Chiariotti, "A survey on 360-degree video: Coding, quality of experience and streaming," *arXiv preprint arXiv:2102.08192*, 2021.

[44] V. Sze, M. Budagavi, and G. J. Sullivan, "High efficiency video coding (hevc)," in *Integrated circuit and systems, algorithms and architectures*. Springer, 2014, vol. 39, p. 40.

[45] Y. Chen, D. Murherjee, J. Han, A. Grange, Y. Xu, Z. Liu, S. Parker, C. Chen, H. Su, U. Joshi *et al.*, "An overview of core coding tools in the av1 video codec," in *2018 Picture Coding Symposium (PCS)*. IEEE, 2018, pp. 41–45.

[46] I. Bauermann, M. Mielke, and E. Steinbach, "H. 264 based coding of omnidirectional video," in *Computer vision and graphics*. Springer, 2006, pp. 209–215.

[47] Y. Ye, J. M. Boyce, and P. Hanhart, "Omnidirectional 360° video coding technology in responses to the joint call for proposals on video compression with capability beyond hevc," *IEEE Transactions on Circuits and Systems for Video Technology*, vol. 30, no. 5, pp. 1241–1252, 2019.

[48] M. Yu, H. Lakshman, and B. Girod, "A framework to evaluate omnidirectional video coding schemes," in *2015 IEEE International Symposium on Mixed and Augmented Reality*. IEEE, 2015, pp. 31–36.

[49] R. S. Sutton and A. G. Barto, *Reinforcement learning: An introduction*. MIT press, 2018.

[50] A. Schmitz, A. MacQuarrie, S. Julier, N. Binetti, and A. Steed, "Directing versus attracting attention: Exploring the effectiveness of central and peripheral cues in panoramic videos," in *2020 IEEE Conference on Virtual Reality and 3D User Interfaces (VR)*. IEEE, 2020, pp. 63–72.

[51] N. Q. K. Duong, J. Sirot, G. Marquant, and C.-H. Demarty, "Method and apparatus for inciting a viewer to rotate toward a reference direction when consuming an immersive content item," Aug. 18 2020, uS Patent 10,748,321.

[52] V. A. de Jesus Oliveira, L. Brayda, L. Nedel, and A. Maciel, "Designing a vibrotactile head-mounted display for spatial awareness in 3d spaces," *IEEE transactions on visualization and computer graphics*, vol. 23, no. 4, pp. 1409–1417, 2017.

[53] 360fly, "360fly - 4k user guide," 2016. [Online]. Available: https://www.360fly.com

[54] C. Brown, G. Bhutra, M. Suhail, Q. Xu, and E. D. Ragan, "Coordinating attention and cooperation in multi-user virtual reality narratives," in *2017 IEEE Virtual Reality (VR)*. IEEE, 2017, pp. 377–378.

[55] K. Carnegie and T. Rhee, "Reducing visual discomfort with hmds using dynamic depth of field," *IEEE computer graphics and applications*, vol. 35, no. 5, pp. 34–41, 2015.

[56] A. Patney, M. Salvi, J. Kim, A. Kaplanyan, C. Wyman, N. Benty, D. Luebke, and A. Lefohn, "Towards foveated rendering for gaze-tracked virtual reality," *ACM Transactions on Graphics (TOG)*, vol. 35, no. 6, pp. 1–12, 2016.

[57] A. Patney, J. Kim, M. Salvi, A. Kaplanyan, C. Wyman, N. Benty, A. Lefohn, and D. Luebke, "Perceptually-based foveated virtual reality," in *ACM SIGGRAPH 2016 Emerging Technologies*, 2016, pp. 1–2.

[58] G. Illahi, M. Siekkinen, and E. Masala, "Foveated video streaming for cloud gaming," in *2017 IEEE 19th international workshop on multimedia signal processing (MMSP)*. IEEE, 2017, pp. 1–6.

[59] Z. Ye, "Performance analysis of http adaptive video streaming services in mobile networks," Ph.D. dissertation, Université d'Avignon, 2017.

[60] A. Bentaleb, B. Taani, A. C. Begen, C. Timmerer, and R. Zimmermann, "A survey on bitrate adaptation schemes for streaming media over http," *IEEE Communications Surveys Tutorials*, vol. 21, no. 1, pp. 562–585, 2019.

[61] A. Yaqoob, T. Bi, and G.-M. Muntean, "A dash-based efficient throughput and buffer occupancy-based adaptation algorithm for smooth multimedia streaming," in *2019 15th International Wireless Communications Mobile Computing Conference (IWCMC)*, 2019, pp. 643–649.

[62] X. Corbillon, A. Devlic, G. Simon, and J. Chakareski, "Optimal set of 360-degree videos for viewport-adaptive streaming," in *Proceedings of the 25th ACM international conference on Multimedia*, 2017, pp. 943–951.

[63] P. Rondao Alface, M. Aerts, D. Tytgat, S. Lievens, C. Stevens, N. Verzijp, and J. F. Macq, "16k cinematic vr streaming," in *ACM Multimedia Conf. (MM)*, 2017.

[64] J. Ryoo, K. Yun, D. Samaras, S. R. Das, and G. Zelinsky, "Design and evaluation of a foveated video streaming service for commodity client devices," in *ACM Int. Conf. on Multimedia Sys. (MMSys)*, 2016.

[65] S. Petrangeli, G. Simon, and V. Swaminathan, "Trajectory-based viewport prediction for 360° virtual reality videos," in *IEEE Int. Conf. on Artificial Intelligence and Virtual Reality (AIVR)*, Dec 2018, pp. 157–160.

[66] S. Rossi, F. De Simone, P. Frossard, and L. Toni, "Spherical clustering of users navigating 360 content," in *ICASSP 2019-2019 IEEE International Conference on Acoustics, Speech and Signal Processing (ICASSP)*. IEEE, 2019, pp. 4020–4024.

[67] A. D. Aladagli, E. Ekmekcioglu, D. Jarnikov, and A. Kondoz, "Predicting head trajectories in 360° virtual reality videos," in *IEEE Int. Conf. on 3D Immersion (IC3D)*, 2017.

[68] Y. Ban, L. Xie, Z. Xu, X. Zhang, Z. Guo, and Y. Wang, "Cub360: Exploiting cross-users behaviors for viewport prediction in 360 video adaptive streaming," in *IEEE Int. Conf. on Multimedia and Expo (ICME)*, 2018.

[69] C.-L. Fan, S.-C. Yen, C.-Y. Huang, and C.-H. Hsu, "Optimizing fixation prediction using recurrent neural networks for 360° video streaming in head-mounted virtual reality," *IEEE Transactions on Multimedia*, 2019.

[70] M. Xu, Y. Song, J. Wang, M. Qiao, L. Huo, and Z. Wang, "Dataset for predicting head movement in panoramic video: A deep reinforcement learning approach (pami 2018)," https://github.com/YuhangSong/DHP, 2018.

[71] A. Nguyen, Z. Yan, and K. Nahrstedt, "PanoSalNet - source code for Your Attention is Unique: Detecting 360° video saliency in head-mounted display for head movement prediction," https://github.com/phananh1010/PanoSalNet, 2019.

[72] X. Corbillon, F. De Simone, and G. Simon, "360° video head movement dataset," in *ACM Int. Conf. on Multimedia Systems (MMSys)*, 2017, pp. 199–204.

[73] C. Wu, Z. Tan, Z. Wang, and S. Yang, "A dataset for exploring user behaviors in VR spherical video streaming," in *ACM Int. Conf. on Multimedia Systems (MMSys)*, 2017, pp. 193–198.

[74] K. Simonyan and A. Zisserman, "Very deep convolutional networks for large-scale image recognition," *arXiv preprint arXiv:1409.1556*, 2014.

[75] X. Huang, C. Shen, X. Boix, and Q. Zhao, "Salicon: Reducing the semantic gap in saliency prediction by adapting deep neural networks," in *IEEE Int. Conf. on Computer Vision (ICCV)*, 2015, pp. 262–270.

[76] J. Gutiérrez, E. J. David, A. Coutrot, M. P. Da Silva, and P. Le Callet, "Introducing un salient360! benchmark: A platform for evaluating visual attention models for 360° contents," in *IEEE Int. Conf. on Quality of Multimedia Exp. (QoMEX)*, 2018.

[77] Y. Su and K. Grauman, "Making 360 video watchable in 2d: Learning videography for click free viewing," in *IEEE CVPR*, July 2017, pp. 1368–1376.

[78] Y. Yu, S. Lee, J. Na, J. Kang, and G. Kim, "A deep ranking model for spatio-temporal highlight detection from a 360 video," in *AAAI*, 2018.

[79] Y. Bao, H. Wu, T. Zhang, A. A. Ramli, and X. Liu, "Shooting a moving target: Motion-prediction-based transmission for 360° videos," in *IEEE Int. Conf. on Big Data (Big Data)*. IEEE, 2016, pp. 1161–1170.

[80] I. Sutskever, O. Vinyals, and Q. V. Le, "Sequence to sequence learning with neural networks," in *Adv. in Neural Info Proc. Sys. (NEURIPS)*, 2014, pp. 3104–3112.

[81] P. Luc, N. Neverova, C. Couprie, J. Verbeek, and Y. LeCun, "Predicting deeper into the future of semantic segmentation," in *IEEE ICCV*, 2017.

[82] J. Martinez, M. J. Black, and J. Romero, "On human motion prediction using recurrent neural networks," in *IEEE CVPR*, 2017, pp. 4674–4683.

[83] A. Alahi, K. Goel, V. Ramanathan, A. Robicquet, L. Fei-Fei, and S. Savarese, "Social LSTM: Human trajectory prediction in crowded spaces," in *IEEE CVPR*, 2016.

[84] S. Rossi and L. Toni, "Understanding user navigation in immersive experience: An information-theoretic analysis," in *ACM Int. Workshop on Immersive Mixed and Virtual Environment Systems*, ser. MMVE '20, 2020, p. 19–24.

[85] J. P. Magliano and J. M. Zacks, "The impact of continuity editing in narrative film on event segmentation," *Cognitive Science*, vol. 35, no. 8, pp. 1489–1517, 2011.

[86] A. Jain, A. R. Zamir, S. Savarese, and A. Saxena, "Structural-RNN: Deep learning on spatio-temporal graphs," in *Proceedings of the ieee conference on computer vision and pattern recognition*, 2016, pp. 5308–5317.

[87] A. Sadeghian, A. Alahi, and S. Savarese, "Tracking the untrackable: Learning to track multiple cues with long-term dependencies," in *IEEE ICCV*, 2017, pp. 300–311.

[88] A. Agrawal, J. Lu, S. Antol, M. Mitchell, C. L. Zitnick, D. Batra, and D. Parikh, "VQA: Visual Question Answering," in *IEEE ICCV*, 2015.

[89] 1st Rank in Udacity Challenge, "Team komanda," https://github.com/udacity/self-driving-car/tree/master/steering-models/community-models/komanda, 2016.

[90] M. F. Dacrema, P. Cremonesi, and D. Jannach, "Are we really making much progress? A worrying analysis of recent neural recommendation approaches," in *ACM Conf. on Recommender Systems*, 2019, pp. 101–109.

[91] W. Yang, K. Lu, P. Yang, and J. Lin, "Critically examining the "neural hype" weak baselines and the additivity of effectiveness gains from neural ranking models," in *ACM SIGIR Conf. on Research and Development in Information Retrieval*, 2019, pp. 1129–1132.

[92] K. Musgrave, S. Belongie, and S.-N. Lim, "A metric learning reality check," *arXiv preprint arXiv:2003.08505*, 2020.

[93] D. Blalock, J. J. G. Ortiz, J. Frankle, and J. Guttag, "What is the state of neural network pruning?" *arXiv preprint arXiv:2003.03033*, 2020.

[94] H.-Y. Wu, T.-Y. Li, and M. Christie, "Logic control for story graphs in 3d game narratives," in *Smart Graphics*, Y. Chen, M. Christie, and W. Tan, Eds. Cham: Springer International Publishing, 2017, pp. 111–123.

[95] N. Xie, G. Ras, M. van Gerven, and D. Doran, "Explainable deep learning: A field guide for the uninitiated," *CoRR*, vol. abs/2004.14545, 2020. [Online]. Available: https://arxiv.org/abs/2004.14545

[96] D. Zanca, M. Gori, S. Melacci, and A. Rufa, "Gravitational models explain shifts on human visual attention," *Scientific Reports*, vol. 10, no. 1, pp. 1–9, 2020.

[97] R. Swinbank and R. J. Purser, "Fibonacci grids," in *AMS 13th Conference on Numerical Weather Prediction*, vol. 13, 1999, p. 125.

[98] H. Fassold, "Adapting computer vision algorithms for omnidirectional video," in *Proceedings of the 27th ACM International Conference on Multimedia*, 2019, pp. 1026–1028.

[99] L. Maczyta, P. Bouthemy, and O. Le Meur, "Unsupervised motion saliency map estimation based on optical flow inpainting," in *2019 IEEE International Conference on Image Processing (ICIP)*. IEEE, 2019, pp. 4469–4473.

[100] A. Bochkovskiy, C.-Y. Wang, and H.-Y. M. Liao, "Yolov4: Optimal speed and accuracy of object detection," *arXiv preprint arXiv:2004.10934*, 2020.

[101] D. Alvarez-Melis and T. S. Jaakkola, "Towards robust interpretability with self-explaining neural networks," in *Proceedings of the 32nd International Conference on Neural Information Processing Systems*, ser. NIPS'18. Red Hook, NY, USA: Curran Associates Inc., 2018, p. 7786–7795.

[102] G. Ma, S. Li, C. Chen, A. Hao, and H. Qin, "Stage-wise salient object detection in 360° omnidirectional image via object-level semantical saliency ranking," *IEEE Transactions on Visualization and Computer Graphics*, vol. 26, no. 12, pp. 3535–3545, 2020.

[103] J. Li, J. Su, C. Xia, and Y. Tian, "Distortion-adaptive salient object detection in 360° omnidirectional images," *IEEE Journal of Selected Topics in Signal Processing*, vol. 14, no. 1, pp. 38–48, 2019.

[104] D. Kim, S. Pathak, A. Moro, A. Yamashita, and H. Asama, "Selfsphnet: Motion estimation of a spherical camera via self-supervised learning," *IEEE Access*, vol. 8, pp. 41 847–41 859, 2020.

[105] R. Yu, W. S. Lages, M. Nabiyouni, B. Ray, N. Kondur, V. Chandrashekar, and D. A. Bowman, "Bookshelf and bird: Enabling real walking in large vr spaces through cell-based redirection," in *2017 IEEE Symposium on 3D User Interfaces (3DUI)*, 2017, pp. 116–119.

[106] S. P. Sargunam, K. R. Moghadam, M. Suhail, and E. D. Ragan, "Guided head rotation and amplified head rotation: Evaluating semi-natural travel and viewing techniques in virtual reality," in *2017 IEEE Virtual Reality (VR)*, 2017, pp. 19–28.

[107] Y. Farmani and R. J. Teather, "Evaluating discrete viewpoint control to reduce cybersickness in virtual reality," *Springer Virtual Reality*, 2020.

[108] A. Pavel, B. Hartmann, and M. Agrawala, "Shot orientation controls for interactive cinematography with 360 video," in *Proceedings of the 30th Annual ACM Symposium*

on User Interface Software and Technology, ser. UIST '17. New York, NY, USA: Association for Computing Machinery, 2017, p. 289–297. [Online]. Available: https://doi.org/10.1145/3126594.3126636

[109] K. Rahimi Moghadam, C. Banigan, and E. D. Ragan, "Scene transitions and teleportation in virtual reality and the implications for spatial awareness and sickness," *IEEE Transactions on Visualization and Computer Graphics*, pp. 1–1, 2018.

[110] B. E. Riecke, M. V. D. Heyde, and H. H. Bülthoff, "Visual cues can be sufficient for triggering automatic, reflexlike spatial updating," *ACM Trans. Appl. Percept.*, vol. 2, no. 3, p. 183–215, Jul. 2005. [Online]. Available: https://doi.org/10.1145/1077399.1077401

[111] L. Sassatelli, A.-M. Pinna-Déry, M. Winckler, S. Dambra, G. Samela, R. Pighetti, and R. Aparicio-Pardo, "Snap-changes: A dynamic editing strategy for directing viewer's attention in streaming virtual reality videos," in *Proceedings of the 2018 International Conference on Advanced Visual Interfaces*, ser. AVI '18. New York, NY, USA: Association for Computing Machinery, 2018. [Online]. Available: https://doi.org/10.1145/3206505.3206553

[112] Y.-C. Lin, Y.-J. Chang, H.-N. Hu, H.-T. Cheng, C.-W. Huang, and M. Sun, "Tell me where to look: Investigating ways for assisting focus in 360° video," in *Proceedings of the 2017 CHI Conference on Human Factors in Computing Systems*, ser. CHI '17. New York, NY, USA: Association for Computing Machinery, 2017, p. 2535–2545. [Online]. Available: https://doi.org/10.1145/3025453.3025757

[113] T. Kjær, C. B. Lillelund, M. Moth-Poulsen, N. C. Nilsson, R. Nordahl, and S. Serafin, "Can you cut it? an exploration of the effects of editing in cinematic virtual reality," in *Proceedings of the 23rd ACM Symposium on Virtual Reality Software and Technology*, ser. VRST '17. New York, NY, USA: Association for Computing Machinery, 2017. [Online]. Available: https://doi.org/10.1145/3139131.3139166

[114] S. Dambra, G. Samela, L. Sassatelli, R. Pighetti, R. Aparicio-Pardo, and A.-M. Pinna-Déry, "TOUCAN-VR," *Software*, DOI: 10.5281/zenodo.1204442 2018. [Online]. Available: https://github.com/UCA4SVR/TOUCAN-VR

[115] Y. Zhang, P. Zhao, K. Bian, Y. Liu, L. Song, and X. Li, "Drl360: 360-degree video streaming with deep reinforcement learning," in *IEEE INFOCOM 2019 - IEEE Conference on Computer Communications*, 2019, pp. 1252–1260.

[116] S. Park, A. Bhattacharya, Z. Yang, M. Dasari, S. R. Das, and D. Samaras, "Advancing user quality of experience in 360-degree video streaming," in *2019 IFIP Networking Conference (IFIP Networking)*, 2019, pp. 1–9.

[117] L. Sassatelli, M. Winckler, T. Fisichella, and R. Aparicio, "User-adaptive editing for 360 degree video streaming with deep reinforcement learning," in *Proceedings of the 27th ACM International Conference on Multimedia*, ser. MM '19. New York, NY, USA: Association for Computing Machinery, 2019, p. 2208–2210. [Online]. Available: https://doi.org/10.1145/3343031.3350601

[118] J. Pineau, A. Guez, R. Vincent, G. Panuccio, and M. Avoli, "Treating epilepsy via adaptive neurostimulation: a reinforcement learning approach," *International journal of neural systems*, vol. 19, no. 4, pp. 227–240, 2009.

[119] T. Osa, J. Pajarinen, G. Neumann, J. Bagnell, P. Abbeel, and J. Peters, "An algorithmic perspective on imitation learning," *Foundations and Trends in Robotics*, vol. 7, no. 1-2, pp. 1–179, 2018.

[120] C. Chen, Y. Liu, S. Kreiss, and A. Alahi, "Crowd-robot interaction: Crowd-aware robot navigation with attention-based deep reinforcement learning," in *2019 International Conference on Robotics and Automation (ICRA)*. IEEE, 2019, pp. 6015–6022.

[121] A. Vaswani, N. Shazeer, N. Parmar, J. Uszkoreit, L. Jones, A. N. Gomez, Ł. Kaiser, and I. Polosukhin, "Attention is all you need," in *Advances in neural information processing systems*, 2017, pp. 5998–6008.

[122] O. Fabius and J. R. Van Amersfoort, "Variational recurrent auto-encoders," *arXiv preprint arXiv:1412.6581*, 2014.

[123] F. Marchetti, F. Becattini, L. Seidenari, and A. Del Bimbo, "Multiple trajectory prediction of moving agents with memory augmented networks," *IEEE Transactions on Pattern Analysis and Machine Intelligence*, 2020.

[124] L. Berlincioni, F. Becattini, L. Seidenari, and A. Del Bimbo, "Multiple future prediction leveraging synthetic trajectories," in *2020 25th International Conference on Pattern Recognition (ICPR)*. IEEE, 2021, pp. 6081–6088.

[125] F. Marchetti, F. Becattini, L. Seidenari, and A. Del Bimbo, "Mantra: Memory augmented networks for multiple trajectory prediction," in *Proceedings of the IEEE/CVF Conference on Computer Vision and Pattern Recognition*, 2020, pp. 7143–7152.

[126] Y.-C. Su and K. Grauman, "Learning spherical convolution for fast features from 360 imagery," *Advances in Neural Information Processing Systems*, vol. 30, pp. 529–539, 2017.

[127] J. Xu, W. Zhou, and Z. Chen, "Blind omnidirectional image quality assessment with viewport oriented graph convolutional networks," *IEEE Transactions on Circuits and Systems for Video Technology*, vol. 31, no. 5, pp. 1724–1737, 2020.

[128] R. Chen, Y. Rubanova, J. Bettencourt, and D. Duvenaud, "Neural ordinary differential equations (neurips)," 2018.

[129] J. Van Den Berg, S. J. Guy, M. Lin, and D. Manocha, "Reciprocal n-body collision avoidance," in *Robotics research*. Springer, 2011, pp. 3–19.

[130] L. Sassatelli, M. Winckler, T. Fisichella, A. Dezarnaud, J. Lemaire, R. Aparicio-Pardo, and D. Trevisan, "New interactive strategies for virtual reality streaming in degraded context of use," *Computers & Graphics*, vol. 86, pp. 27–41, 2020.

[131] L. Sassatelli, M. Winckler, T. Fisichella, R. Aparicio, and A.-M. Pinna-Déry, "A new adaptation lever in 360° video streaming," in *Proceedings of the 29th ACM Workshop on Network and Operating Systems Support for Digital Audio and Video*, 2019, pp. 37–42.

[132] B. J. Li, J. N. Bailenson, A. Pines, W. J. Greenleaf, and L. M. Williams, "A public database of immersive vr videos with corresponding ratings of arousal, valence, and correlations between head movements and self report measures," *Frontiers in psychology*, vol. 8, p. 2116, 2017.

[133] H. Jun, M. R. Miller, F. Herrera, B. Reeves, and J. N. Bailenson, "Stimulus sampling with 360-videos: Examining head movements, arousal, presence, simulator sickness, and preference on a large sample of participants and videos," *IEEE Transactions on Affective Computing*, 2020.

[134] W. Tang, S. Wu, T. Vigier, and M. P. Da Silva, "Influence of emotions on eye behavior in omnidirectional content," in *2020 Twelfth International Conference on Quality of Multimedia Experience (QoMEX)*. IEEE, 2020, pp. 1–6.

[135] S. Chaabouni and F. Precioso, "Impact of saliency and gaze features on visual control: gaze-saliency interest estimator," in *Proceedings of the 27th ACM International Conference on Multimedia*, 2019, pp. 1367–1374.

[136] S. Essid, S. Parekh, N. Q. K. Duong, R. Serizel, A. Ozerov, F. Antonacci, and A. Sarti, "Multiview approaches to event detection and scene analysis," in *Computational Analysis of Sound Scenes and Events*. Springer, 2018, pp. 243–276.

[137] S. Parekh, A. Ozerov, S. Essid, N. Q. K. Duong, P. Pérez, and G. Richard, "Identify, locate and separate: Audio-visual object extraction in large video collections using weak supervision," in *2019 IEEE Workshop on Applications of Signal Processing to Audio and Acoustics (WASPAA)*. IEEE, 2019, pp. 268–272.

[138] H.-N. Hu, Y.-C. Lin, M.-Y. Liu, H.-T. Cheng, Y.-J. Chang, and M. Sun, "Deep 360 pilot: Learning a deep agent for piloting through 360 sports videos," in *2017 IEEE Conference on Computer Vision and Pattern Recognition (CVPR)*. IEEE, 2017, pp. 1396–1405.

[139] W.-C. Lo, C.-L. Fan, J. Lee, C.-Y. Huang, K.-T. Chen, and C.-H. Hsu, "360 video viewing dataset in head-mounted virtual reality," in *Proceedings of the 8th ACM on Multimedia Systems Conference*, 2017, pp. 211–216.

[140] Y. Xu, Y. Dong, J. Wu, Z. Sun, Z. Shi, J. Yu, and S. Gao, "Github repository of: Gaze prediction in dynamic 360° immersive videos," https://github.com/xuyanyu-shh/VR-EyeTracking, 2018.

[141] M. Boyle, "The integration of angular velocity," *Advances in Applied Clifford Algebras*, vol. 27, no. 3, pp. 2345–2374, 2017.